Volume 12 Number 2
August 2013

ISBN No. 1607-9949

UNESCO

United Nations
Educational, Scientific and
Cultural Organization

Organisation
des Nations Unies
pour l'education,
la science et la culture

African Journal of Science and Technology (AJST)
Science and Engineering Series

Journal Africain de Science et de Technologie

The African Network of Scientific and Technological Institutions (ANSTI).

Réseau Africain d'Institutions Scientifiques et Technologiques (RAIST).

Science & Engineering Series

In pursuance of UNESCO/ANSTI's objective to facilitate the dissemination of research results and within the framework of the organization, the African Development Bank (AfDB) has provided a grant to the African Network of Scientific and Technological Institutions (ANSTI), for the publication of the African Journal of Science and Technology (AJST).

The African Journal of Science and Technology (AJST) is an annual technical publication of the African Network of Scientific and Technological Institutions (ANSTI).

Le Journal Africain de Science et de Technologie est une revue scientifique du Réseau Africain d'Institutions Scientifiques et Technologiques (RAIST).

African Journal of Science and Technology (AJST)
Science and Engineering Series

In pursuance of the objective to facilitate the dissemination of research results and within the framework of the organization's support for the African Network of Scientific and Technological Institutions (ANSTI), African Development Bank (AfdB) has provided a grant to continue the publication of the African Journal of Science and Technology (AJST).

The African Journal of Science and Technology (AJST) is a biannual technical publication of the African Network of Scientific and Technical Institutions (ANSTI).

Le Journal Africain de Science et de Technologie est une revue scientifique du Réseau Africain d'Institutions Scientifiques et Technologiques (RAIST).

For subscription and further information contact:
Pour tout renseignement complémentaire s'adresser au:

ANSTI/RAIST Secretariat
UNESCO-ROSTA, P.O. Box 30592-00100
Telephone: +254 20 7622619/20
E-mail: info@ansti.org

EDITORIAL BOARD

EDITOR-IN-CHIEF

Dr. Norbert Opiyo-Akech
Department of Geology
E-mail: opiyo-akech@uonbi. ac.ke
University of Nairobi
P.O.Box 30197
NAIROBI, KENYA

SUBREGIONAL/SUBJECT EDITORS

(Southern Africa/Afrique Australe)/(Chemistry/Chimie)
Prof. Victor S.B. Mtetwa,
Dean, Faculty of Science,
E-mail: mtetwa@science.uniswa.sz
University of Swaziland,
KWALUSENI, SWAZILAND

(Eastern Africa/Afrique de l'Est)/(Physics/Physique)
Prof. B. O. Aduda,
Department of Physics
E-mail: boaduda@uonbi.ac.ke
University of Nairobi
P.O.Box 30197
NAIROBI, KENYA

(French speaking Africa/Afrique Francophone)/(Earth Sciences/Science de la Terre)

Dr. I.K. Njilah
University of Yaunde I
E-mail: injilah@uycdc.uninet.cm
Department of Earth Sciences
E-mail: :njilah@hotmail.com
P.O. Box 812
Younde, CAMEROON

(Engineering/Technology/Technologie)
Prof F.A.O. Fred Otieno
E-mail: otienofao@tut.ac.za
Dean of Engineering
Tshwane University, Pretoria Campus
Pretoria
SOUTH AFRICA

(Mathematics/Mathematique)
Prof. Verdiana G. Masanja,
E-mail: vmasanja@maths.usdm.ac.tz
University of Dares- salaam
Department of mathematics
TANZANIA

(Biological and Agricultural Sciences)(Science de Biologie et Agriculture)
Dr. Ebenezer Oduro Owusu
Zoology Department
Email: eoowusu@ug.edu.gh
University of Ghana, Legon
ACCRA, GHANA.

CONTENTS
AJST, Vol. 12, No. 2: August, 2013

Page

African Journal of Science and Technology (AJST)
Science and Engineering Series Vol. 12, No. 2, pp. 1 - 6

EFFECT OF HEAT TREATMENT ON WEAR RESISTANCE OF A GRINDING PLATE

Odusote, J.K.[1], Talabi, S.I.[1] and Balogun, S.[2]

[1]Department of Materials and Metallurgical Engineering, University of Ilorin, Ilorin, Nigeria
[2]Department of Mechanical Engineering, University of Ilorin, Ilorin, Nigeria

Email: jamiukolawole@gmail.com; abduljamiuk@yahoomail.com

ABSTRACT: *The effects of heat treatment on the hardness and by extension the wear resistance of locally produced grinding plate of known composition were investigated. Specimens were prepared from the grinding plate and were heat treated at 840°C, 860°C and 880°C and quenched at different rate. Some of the specimens were quenched in water and palm oil, while some of the quenched specimens were tempered at 200°C. The results obtained were corroborated with the microstructure of the specimens examined under an optical microscope. The hardness values of the grinding plate specimens quenched in various media increased with increased heat treatment temperatures, and are higher than that of the as-cast specimen. Water quenched tempered specimens (WT) displayed higher hardness values than the as-cast, whereas oil quenched tempered specimens (OT) possessed lower hardness values. The presence of carbide was evident on the micrographs of the water quenched specimens at all the exposure temperatures, which corroborated the observed increased in the hardness values with increased heat treatment temperatures. However, there was significant reduction in the hardness value of the water quenched tempered specimens compared with the quenched specimens, which indicates a significant improvement in toughness. Thus, water quenched and tempered specimen with relatively high hardness value and improved toughness, will be suitable for use as grinding plate because of its relatively better wear resistance. The hardness of the specimens was found to depend on the formation of carbide precipitates within the matrix structure. There is also possibility of production of structure consisting of graphite embedded in a martensitic matrix through the heat treatment.*

Keyword: *carbide, heat treatment, hardness, microstructure, wear resistance*

INTRODUCTION

Grey iron is a class of cast iron that when broken, the fracture path will be along the graphite flakes. Their surface also has a grey, sooty appearance. The flakes act as stress raisers, thus greatly reducing ductility. Grey iron is weak in tension, although strong in compression, as are other brittle materials. On the other hand, the graphite flakes gives this material the capacity to dampen vibrations by the internal friction (hence energy dissipation) caused by these flakes. Grey iron is thus a suitable and commonly used material for constructing structures and machine tool bases, in which vibration damping is important [Serope, 2008]. The degree of hardness produced in cast iron depends upon the composition of cast iron, nature and properties of quenching medium, quenching temperature, size of the objective to be quenched, homogeneity of austenite, degree of agitation, and rate of cooling, surface condition of metal [Khanna, 2009].

Also, grey cast iron usually exhibit unique characteristics of a combination of good mechanical properties, good friction and wear behaviour, and economical manufacturing processes. The improved wear resistance of grey cast iron during dry sliding at low loading conditions has been attributed to the feeding of the contact surface by graphite ûakes and formation of a graphite ûlm on the contact surface. It has been observed that pearlitic structure of the matrix and an ASTM A type graphite ûake provides the best wear resistance for grey cast iron [White, 1992]. Despite the good characteristic offer by grey cast iron, it was observed that grinding plate made locally used in grinding machine, wear at a faster rate. Thus, this study was aimed at providing ways of improving the service life of these locally made grinding plates through heat treatment. Various heat treatment can be adopt for grey cast iron materials, but not all of this processes can optimize its properties. For example, annealing of grey iron consists of heating the iron to a temperature high enough to soften it and/or minimising or eliminating massive eutectic carbides, thereby improving its machinability. This heat treatment usually reduces mechanical properties substantially (Rajan et al., 1988). Hence, the choice of heat treatment operations used in this research excludes annealing the grey cast iron grinding plate. In this study, heat treatment operations were carried out at different temperatures and quenched using different quenching media (water and palm oil) with some of specimen also tempered. Metallography and hardness test were carried out before and after the heat treatments. The responses of this grinding plate to heat treatment, hardness test and microstructural examination are reported in the present paper.

RESEARCH METHODOLOGY

Chemical Composition Analysis

The grinding plate used was bought in a local market in Ilorin metropolis, Kwara state, Nigeria. The chemical composition of the grinding plate was carried out with an optical emission spectroscope (OES). The result obtained is presented in Table 1.

Heat Treatment

Fifteen specimens were prepared from the as-cast grinding plate. The fifteen specimens were grouped into three; each with five specimens. Each group of specimens was heated to 840°C, 860°C and 880°C respectively, and soaked at this temperature for 45 minutes. From the first group, one of the specimens was cooled in air (N_{840}); two out of the remaining four were quenched in water, while the remaining two were quenched in oil. One out of the two specimens quenched in water and oil were tempered for 30 minutes at 200°C and cooled in air. The above steps were repeated for the other groups. The specimens produced were tagged accordingly: heat-treated at 840°C and quenched in water (WQ_{840}), heat-treated at 840°C, quenched in water and tempered at 200°C (WT_{840}), heat-treated at 840°C, and cooled in air (N_{840}), heat-treated at 840°C and quenched in oil (OQ_{840}), heat-treated at 840°C, quenched in oil and tempered at 200°C (OT_{840}), heat-treated at 860°C and quenched in water (WQ_{860}), heat-treated at 860°C, quenched in water and tempered at 200°C (WT_{860}), heat-treated at 860°C, and cooled in air (N_{860}), heat-treated at 860°C and quenched in oil (OQ_{860}), heat-treated at 860°C, quenched in oil and tempered at 200°C (OT_{860}), heat-treated at 880°C and quenched in water (WQ_{880}), heat-treated at 880°C, quenched in water and tempered at 200°C (WT_{880}), heat-treated at 880°C, and cooled in air (N_{880}), heat-treated at 880°C and quenched in oil (OQ_{880}), heat-treated at 880°C, quenched in oil and tempered at 200°C (OT_{880}).

Hardness Test

The specimens which have been subjected to various heat treatment processes and the as-cast sample were prepared for hardness test. Brinell hardness tester was employed to determine the hardness of the specimens. The hardness of the specimens was indicated by the depth of penetration of the indenter on each of the specimens. The diameter of the impression was measured with the Brinell reading microscope and the corresponding Brinell hardness number was obtained from the standard hardness table. Average values were recorded after repeating the test for each one of the test specimens.

Metallography

The microstructures of the samples were examined using metallurgical optical microscope at X200 magnification after the samples have been prepared according to standard. After polishing, the specimens were etched with Natal and rinsed with water.

RESULTS AND DISCUSSION

Table 1 presents the chemical composition of the grey cast iron sample used for this investigation.

Table 1: Composition of the As-cast Grinding Plate Specimen

ELEMENTS	COMPOSITION (wt. %)
C	2.79
Si	1.46
Mn	0.24
P	0.09
S	0.1
Cu	0.18
Ni	0.06
Cr	0.57

Hardness

The hardness values of the specimens, which were subjected to different heat treatment processes, are presented in Tables 2 and 3. The graphical illustrations of the effect of the different heat treatment processes on the hardness of the specimens are shown in Figures 1-5. The hardness of the as-cast specimen is 341HB. The hardness values of the heat-treated specimens were found to be higher than that of as-cast specimen at all exposure temperatures except for the OT specimens (321HB). This shows that the heat treatment temperatures of the specimens quenched in oil and tempered at 200°C have no significant effect on the hardness of the specimens (Figure 5). Therefore, this heat treatment processes are not suitable for optimizing the wear resistance of the grinding plate, hence its performance in service. With respect to WT_{840}, $WT_{860,}$ and WT_{880} specimens, the hardness values increased with increased exposure temperatures, with highest value obtained for WT_{880} (454HB).This results showed that the hardness value is dependent on the heat treatment temperature. However, these specimens were tempered for stress relief and possible improvement in toughness. Water quenched specimens tempered at 200°C showed higher hardness values than both the as-cast and oil quenched tempered specimens. Although, there was a significant reduction in the hardness value of the water quenched tempered specimens compared with the untempered specimens, the reduction in hardness values indicates a significant improvement in toughness and consequently improved wear resistance of the specimens. Hence, WT specimen displayed relatively high hardness value with improved toughness, thereby making it more suitable for use as grinding plate with better wear resistance.

Table 2: Hardness Values of Quenched Specimens

Temperature °C	Brinell Hardness Number (HB)		
	Water	Oil	Air
840	421	363	350
860	441	363	363
880	454	444	388

Table3: Hardness Values of Tempered Specimens at 200°C

Temperature °C	Brinell Hardness Number (HB)	
	Water	Oil
840	388	321
860	388	321
80	363	321

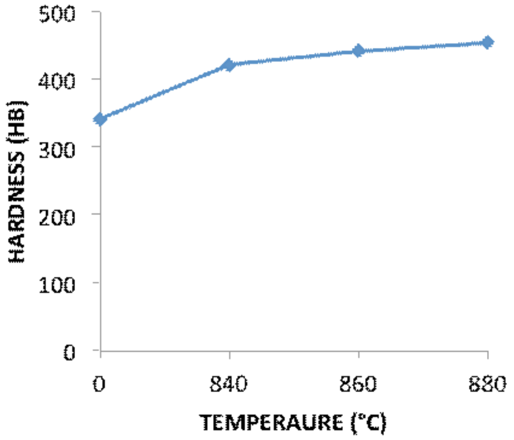

Figure 1. Effect of heat treatment temperatures on the hardness of water-quenched specimens

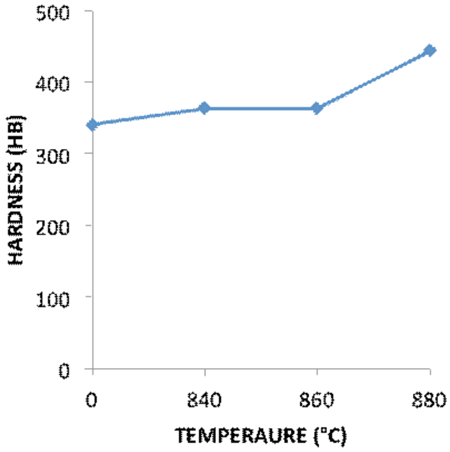

Figure 2. Effect of heat treatment temperatures on the hardness of oil-quenched specimens

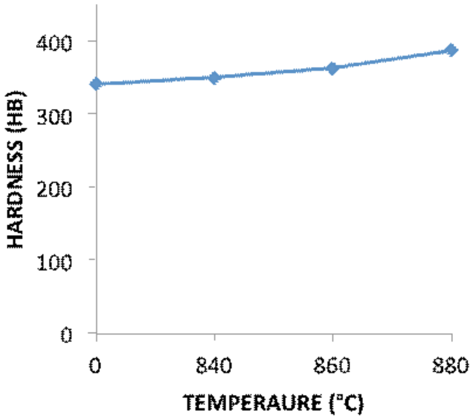

Figure 3. Effect of heat treatment temperatures on the hardness of AQ specimens

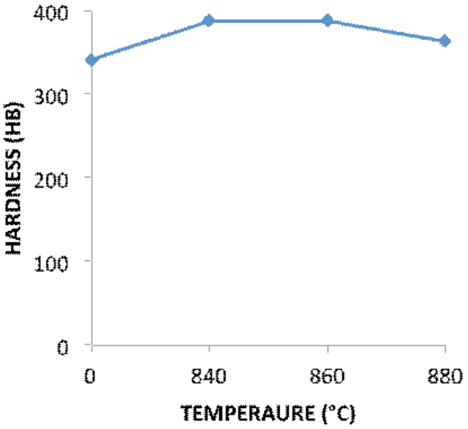

Figure 4. Effect of heat treatment temperatures on the hardness of water-quenched and tempered specimens

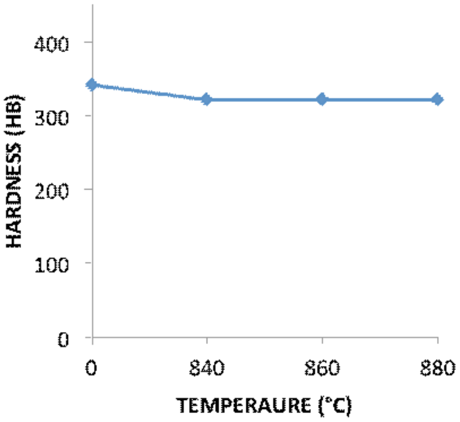

Figure 5. Effect of heat treatment temperatures on the hardness of oil-quenched and tempered specimens

MICROSTRUCTURE

The microstructural analysis results of the samples tempered at 200°C together with the as-cast specimen were presented as shown in Figure 6 (Plates 1 to 7). The hardness as well as the wear resistance properties of the specimens was found to depend on the formation of carbide precipitates within the matrix structure. There is also possibility of production of structure consisting of graphite embedded in a martensitic matrix through the heat treatment. The presence of graphite within the matrix structure usually improves wear resistance depending on its shape (Sugishita and Fujiyoshi, 1981). Heat treatment of grey iron usually alters the matrix microstructure with little or no effect on the size and shape of the graphite achieved during casting (www.key-to-steel). The microstructure of the unalloyed iron generally consists of M_3C carbides (Alp and Wazzan, 2005). Figure 6 (Plates 1-7) shows that the cooling rate of the heat treated specimens have dramatic effect on the size and distribution of the graphite crystals as well as the volume fraction of carbide precipitates. As shown in Plate 1, graphite flakes were formed in a ferritic or pearlitic matrix, depicting that a grey type of cast iron is formed. An evidence of carbide formation was also observed on the WQ_{880} and WQ_{860} specimens (Plates 2-3). The presence of chromium may be responsible for the formation of carbide in the matrix, which ultimately is responsible for the observed high hardness when compared with the as-cast specimen (Robert, 1994). As seen in Plate 4, the volume fraction of carbide in WT_{840} specimen reduces, hence the observed reduction in hardness value compared to the quenched specimens. Similarly, Plates 5-7 (OT_{840}, OT_{860} and OT_{880} specimens) also revealed reduction in the volume fraction of carbide, and hence the lower hardness values compared to the WT specimens as shown in Table 2.

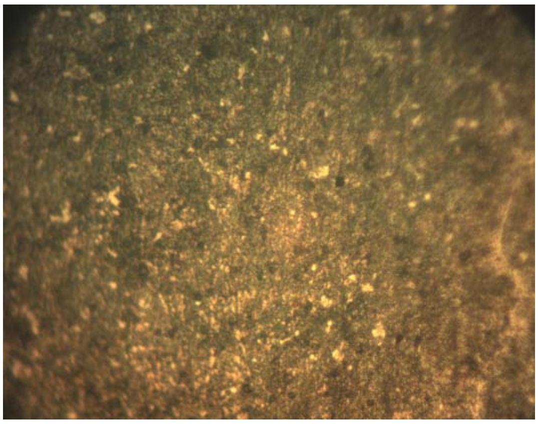

Plate 1: As- cast specimen

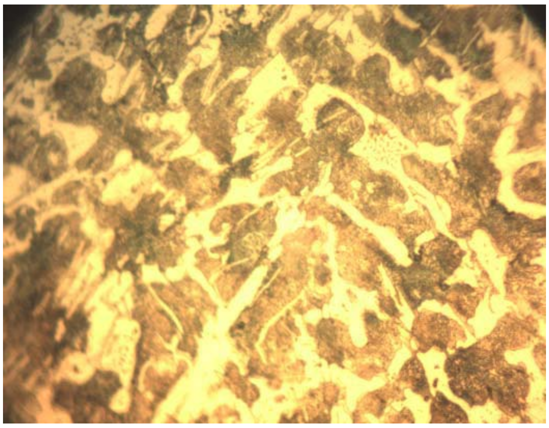

Plate 2: Water-Quenched specimen at 880°C

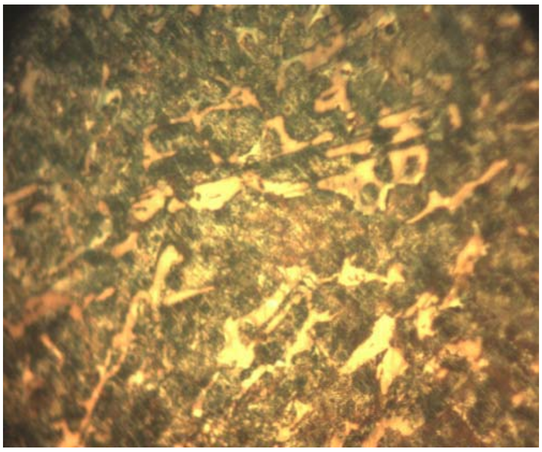

Plate 5: Oil Tempered at 880°C

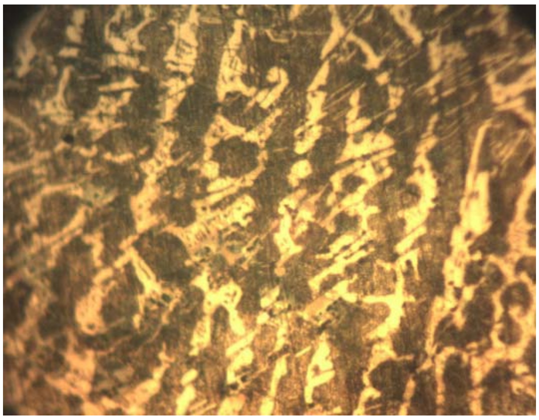

Plate 3: Water-Quenched specimen at 860^{0}C

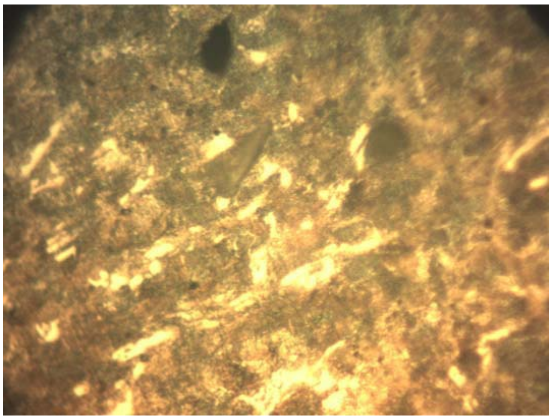

Plate 6: Oil Tempered at 860°C

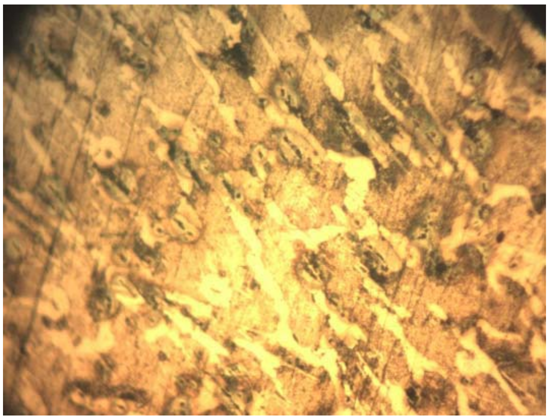

Plate 4: Water Tempered at 840°C

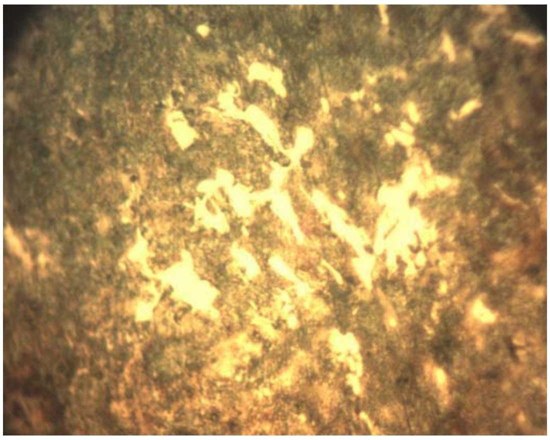

Plate 7: Oil Tempered 840°C

CONCLUSIONS

The hardness values of grinding plate specimens quenched in various media increased with increased heat treatment temperatures, indicating that both the heat treatment temperatures and quenching media has significant effect on the hardness values. However, these values are higher than that of the as-cast specimen.

Water quenched tempered specimens also displayed higher hardness values than the as-cast, whereas oil quenched tempered specimens possessed lower hardness values, which were constant throughout the exposure temperatures. Although, lower hardness value indicates a possible improvement in toughness but specimens with higher hardness values will likely possess better wear resistance.

The cooling rate of the heat treated specimens has dramatic effect on the size and distribution of the graphite crystals as well as the volume fraction of carbide precipitates. The presence of carbide was evident on the water quenched specimens at all the exposure temperatures, and hence the observed increased in the hardness values with increased heat treatment temperature. The highest hardness value was obtained on the water quenched specimen at 880°C, indicating better wear resistance. However, in an attempt to relief stresses developed during quenching and to balance between toughness and hardness, quenched specimens were tempered at 200°C. The results showed that the WT specimens still possessed high hardness value similar to air cooled specimens. Thus, the best heat treatment operation for better improvement in wear resistance of the grinding plate is heating at 840°C, followed by water quenching and tempering (for stress relief).

REFERENCES

[1] S. Gündüz, and A. Çapar, "Influence of forging and cooling rate on microstructure and properties of medium carbon microalloy forging steel". J. Mater Sci. 41(2): 561-564, 2006.

[2] T. Alp and A. A. Wazzan, "Microstructure–property relationships in cast irons". The Arabian Journal for Science and Engineering, Volume 30, Number 2B, 2005.

[3] J. Sugishita, S. Fujiyoshi, "The effect of cast iron graphites on friction and wear performance. 1. Graphite ûlm formation on grey cast iron surfaces". Wear 66 209–221, 1981.

[4] Robert, Reed-Hill. Principles of physical metallurgy, 3rd edition, PWS publishing, Boston, 1994.

[5] www.key-to - steel.com, Heat treating of gray irons, (part 1); Influence of alloying element on steel microstructure.

[6] T.V Rajan, C.P. Sharm, and A. Sharma. Heat treatment principles and techniques. Prentice Hall of India private Limited, New Delhi, 1988.

[7] Khanna O.P. (2009), Material science & Metallurgy

[8] Serope Kalpakjian and Steven R.Schmid, Manufacturing processes for Engineering and Materials, 5th edition, Prentice Hall Pearson Education, Singapore, 2008,

African Journal of Science and Technology (AJST)
Science and Engineering Series Vol. 12, No. 2, pp. 7 - 15

DETERMINATION OF THE PARAMETERS FOR DESIGN OF FLEXIBLE PLASTIC TANK

Langat, T. S., Mbuge, D.O. and Mutai, E. B. K.

Department of Environmental and Biosystems Engineering,
University of Nairobi, P.O. Box 30917, Nairobi, Kenya

E-mail : ebkmutai@uonbi.ac.ke

ABSTRACT: *The need to provide emergency water supplies in remote locations and to store water in small, irregular spaces was the main motivation for the research study. The flexible plastic tank provides a good solution to the challenges of efficient water supply to remote areas but has the disadvantage of creeping incessantly during use and does not recover its original dimensions after loading. This project sought to establish the limits within which the flexible HDPE tank may be used in hot tropical climates for water storage. The creep and recovery characteristics of the material were determined for the range of loads and temperatures at which the material is likely to be applied. A set of equations was developed from the creep and recovery curves to estimate the values of creep and recovery within the temperature range 30°C - 50°C and for stresses ranging from 0.781 to 1.563 MPa just by knowing only the applied stress and the operating temperature. Estimates were also provided for the expected permanent expansion of the material under load, when loaded once and when loaded and unloaded intermittently.*

INTRODUCTION

The Need for Flexible and Potable Water Storage Vessels

Slums, refugee camps present a special challenge to engineers and planners in that they are almost always not properly designed. Some of the big challenges in slum setups are water storage and rainwater harvesting because of the low height of buildings and inadequate space between buildings for construction of rainwater harvesting and storage structures, yet there is immense potential for rainwater harvesting in these places due to the vast roof area concentrated in one place as well as the fact that there is a high population density that is usually not connected to the regular municipal water system. Apart from being affordable to most slum dwellers, the flexible plastic tanks may fit in any shape of space as may be available in slums (Onyango, 2003)

In refugee, emergency and disaster camps, the most popular mode of water supply is by trucking, but the biggest problem is usually the water storage after it has arrived at the point of use. The flexible plastic tanks may easily be folded and supplied by helicopter and dropped off from the sky and may conveniently provide the required storage. For nomadic communities, water availability during their migration has been a major problem. A design of the flexible plastic storage in the model of the age old water skin to be carried by animals may alleviate this need (Kenya Rainwater Association, 2004)

This project was therefore the first step aimed at development of a tank that may contribute in part to the solution of the problem of water supply in Slums, arid and semi arid lands (ASALs) and refugee camps. Specifically, it seeks to test the feasibility of using HDPE, which is readily available and is currently used for lining water reservoirs, to fabricate flexible tanks that can fit in small and irregular spaces and may easily transported.

Despite the advantages of this tank, the material used is comparatively weak in strength, deforms with increasing intensity as temperature and loading rise and is subject to degradation on exposure to water and solar radiation Hence it is necessary to precisely define pertinent parameters under which this tank would operate. Of utmost importance is to determine the maximum amount of water that the tank may carry without deforming beyond allowable limits at the expected temperatures of operation. Moreover, it was necessary to determine the permanent deformation of the flexible tank after storage of water for a given period of time so as to set the limits of how much water the tank may store. Inevitably then, this design project was concerned with basic principles of viscoelasticity, specifically creep and recovery. Creep under load simulates stretching when loaded with water while recovery represents the contraction as the water is unloaded from the flexible tank.

Modeling Recovery

It was important to investigate creep recovery in this study since the material used was expected to be loaded intermittently, that is, the water tank would sometimes full of water in which case the HDPE material would exposed to high loads and creep and would sometimes empty, in which case recovery would proceed. This presents a case of creep in when the reservoir is loaded and recovery is assumed after it is emptied. The irreversible damage on the material is represented by un-recovered residual strain after loading. For a linear viscoelastic material in which strain recovery may be regarded as the reversal of creep, then the material behaviour may be represented as in Figure 1. Thus the time-dependent residual strain, $\varepsilon_r(t)$ may be expressed as (Crawford, 1998):

$$\varepsilon_r(t) = \varepsilon_c(t_c) - \varepsilon_c(t, t_c) \tag{1}$$

Where:

- ε_c is the creep strain during the specified period, denoted by (tc) or (t-tc).
- t_c is the specific time when the material is unloaded at the end of the creep period
- t is the specific time of taking a recovery reading

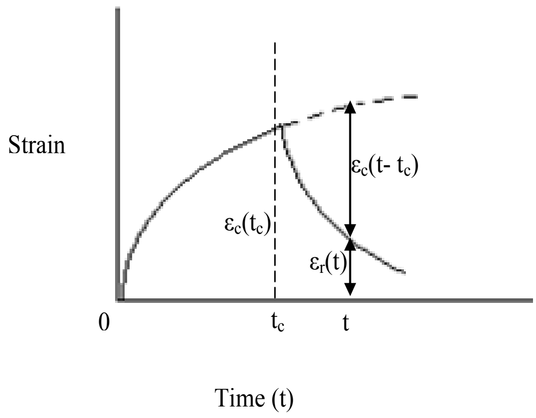

Figure 1: Typical Creep and Recovery Behaviour (Crawford, 2005)

According to Crawford (1998), there can be an infinite number of combinations of creep and recovery periods. It is therefore convenient to express this behaviour in terms of either fractional recovery or reduced time. Fractional recovery, Fr, is defined as:

$$F_r = \frac{\text{Strain Recovered}}{\text{CreepTime}} = \frac{\varepsilon_c(t_c) - \varepsilon_r(t)}{\varepsilon_c(t_c)} \tag{2}$$

Where:

$\varepsilon_c(t)$ is the creep strain at the end of creep period and

$\varepsilon_r(t)$ is the residual strain at any selected time during the recovery period.

Reduced time is a dimensionless variable defined as:

$$t_R = \frac{\text{Recovery Time}}{\text{Creep Time}} = \frac{t - t_c}{t_c} \tag{3}$$

It has been shown by Crawford (1998) that if the final creep strain is not large, then a graph of Fractional Recovery Vs Reduced Time is a master curve, which describes recovery behaviour with acceptable accuracy. The relationship between Fr and tR may be derived as follows. When creep curves are plotted on logarithmic strain and time scales they are approximately straight lines so that the creep strain $\varepsilon_c(t)$ may be expressed as:

$$\varepsilon_c(t_c) = At^n \tag{4}$$

Using the relationship in Equation (1),

$$\varepsilon_r(t) = At^n - A(t - t_c)^n \tag{5}$$

Therefore, the Equation (2) for Fractional Recovery may be written as;

$$F_r = \frac{At_c^n - \left[At_c^n - A(t - t_c)^n\right]}{At_c^n}$$

$$= 1 - \left(\frac{t}{t_c}\right)^n + \left(\frac{t}{t_c} - 1\right)^n \tag{6}$$

Hence,

$$F_r = 1 + t_R^n - (t_R + 1)^n \tag{7}$$

The relationship in Equation (7) is only good approximations since plastics are not linearly viscoelastic and do not completely obey the power law in Equation (4). However, the equation is favoured on account of its simplicity and is sufficiently accurate for most purposes and allows the analysis of intermittent loading.

From Equation (7) and the definition of Fractional Recovery, Fr in Equation (1), the residual strain is given by:

$$\varepsilon_r(t) = \varepsilon_c(t_c) - F_r.\varepsilon_c(t_c)$$

$$= \varepsilon_c(t_c)\left[\left(\frac{t}{t_c}\right)^n - \left(\frac{t}{t_c} - 1\right)^n\right] \tag{8}$$

If there are N cycles of creep and recovery, the accumulated residual strain would be:

$$\varepsilon_r(t) = \varepsilon_c(t_c)\sum_{x=1}^{x=N}\left[\left(\frac{t_pN}{t_c}\right)^n - \left(\frac{t_pN}{t_c} - 1\right)^n\right] \tag{9}$$

Where tp is the period of each cycle and thus the time for which total accumulated strain is being calculated is t = tpN. It is also noted that that the total accumulated strain after the load application for the (N+1)th time will be creep strain for the load-on period, given by $\varepsilon_c(t_c)$ plus the residual strain $\varepsilon_r(t)$, that is:

$$(\varepsilon_{N+1})_{\max}$$

$$= \varepsilon_c(t_c)\left\{1 + \sum_{x=1}^{x=n}\left[\left(\frac{t_pN}{t_c}\right)^n - \left(\frac{t_pN}{t_c} - 1\right)^n\right]\right. \tag{10}$$

Crawford (1998) has been clearly shown that when the total strain is plotted against the logarithm of the total creep time (that is, Nt or total experimental time minus the recovery time) the resultant is a linear relationship. This straight line includes the strain at the end of the first creep period and thus one calculation, for say the 10th cycle allows the line to be drawn. The total creep strain under intermittent loading can then be estimated for any combinations of loading/ unloading times.

The broad objective of the study was to determine the core parameters that would contribute to the design of an un-reinforced HDPE flexible tank for water storage. The specific objectives were:

1. To obtain the maximum amounts of water that an un-reinforced flexible HDPE tanks may carry when modeled as a thin cylindrical shell under pressure at different temperatures.

2. To determine the maximum lifespan of the HDPE tank when subjected to intermittent loading and unloading based on the residual unrecovered creep after loading.

MATERIALS AND METHODS

The specimens used in this project were obtained from HDPE plastic manufactured by A-Plus Ltd. in Nairobi at different times. The material used in the tests was 0.8mm thick. The rest of the dimensions are as shown in Figure 2 as per ASTM D 638 (2003) for Type II specimens. Specimens in both the axis parallel to the direction of extrusion and in the axis perpendicular to the direction of extrusion were used in the tests in equal proportions so as to cancel the effect of material orientation.

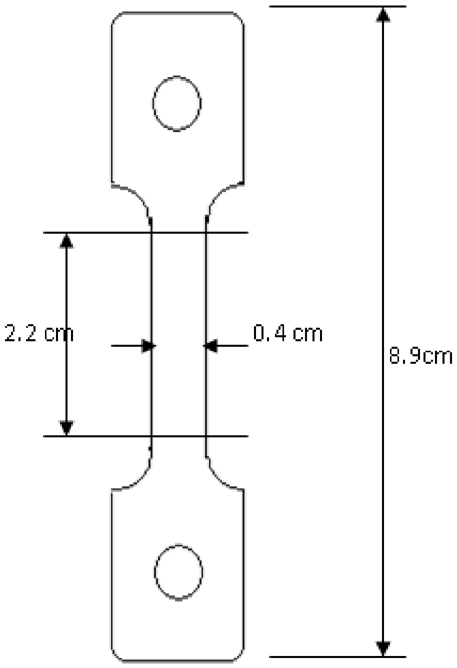

Figure 2: Specimen Geometry – Die Type II Dimensions used in the research study

The testing program comprised of exposing HDPE samples to the oven heated to prescribed temperatures. Three temperatures of 30°, 40°, 50° C were used. The temperatures were preset in the oven for a long time so as to stabilize. The specimens were then loaded in creep at stress levels of 1.56, 0.94 and 0.78 MPa for each of the temperature levels. These creep levels were taken to be about 10% of the material strength so as to mitigate excess creeping. The data was collected by measurements of extension of the specimen due to stress applied a period of 168 hours. Thereafter, the specimens were unloaded and allowed to undergo recovery. The readings of recovery were taken for a period of two weeks. The results were then analyzed so as to obtain the maximum water storage capacity at the given temperatures and the approximate length of time that the flexible tank may be used before its dimensions increase (due to permanent deformation) beyond acceptable levels.

To determine stress acting on the walls at any time, the equation of thin cylindrical shells was used as (Timoshenko and Goodier, 1983):

$$\sigma_c = \frac{\mathrm{Pr}}{t} \tag{11}$$

Where:

- P is the internal pressure exerted by the stored water
- t is the wall thickness
- r is the inside radius of the cylinder.
- σ_c is the hoop stress acting on the material.

Substituting for water pressure given as $\rho g h$ where ρ is density, g is gravitational pull and h is height substituted for radius r since the shape is cylindrical lying on the side, the equation becomes

$$\sigma_c = \frac{\rho g h^2}{t} \tag{12}$$

Hence for any applied stress σc, it was possible to calculate by Equation 13, the maximum radius and length of the cylindrical tank that would contain an amount of water that would cause the stress σc on the tank wall.

DATA ANALYSIS AND DISCUSSION

The tensile strength of the HDPE material had previously been determined as 12 MPa. The proposed shape of flexible tank to be used was a cylinder. The essence of the experiments was to relate the amount of water and the pressure there from to the stress acting on the walls of the cylindrical tank.

To find the maximum tank radius □c was taken as 12 Mpa , the material strength and substituted in equation (13) together with a material thickness, t of 0.8mm, this yielded a maximum tank radius of 0.989m, giving a maximum volume of 4.052 m3 per meter length at the specified thickness. Hence it was determined that the maximum amount of water that would cause instant breaking of the tank is 4,052 liters. By equation (13), an increase in thickness would increase the maximum radius and volume of water stored.

Each of these loads corresponds to a given volume of water in the tank so as to apply an equivalent pressure to induce the specified stress. From Equation (13) it was possible to calculate the corresponding maximum tank radii and volumes that will contain water to apply the equivalent of experimental loads. These are presented in Table 1.

Table 1: Maximum tank radii and volumes for applied creep loads

(a)	(b) Applied stress (MPa)	(c) Strain in 168 (hours)	(d) Unrecovered strain	(d) Maximum radius, r (m)	(e) Maximum Volume (m^3)	(f) Increase in volume (%)	(g) Permanent damage (%)
30 °C	1.563	1.80	0.55	0.422	0.530	965	27.38
	0.937	1.45	0.35	0.324	0.603	588	21.93
	0.781	0.95	0.22	0.255	0.695	427	20.26
40 °C	1.563	2.55	0.60	0.363	0.199	1070	30.46
	0.937	1.80	0.42	0.280	0.092	636	26.75
	0.781	1.65	0.38	0.255	0.069	445	23.41
50 °C	1.563	3.60	1.60	0.365	0.205	2989	20.07
	0.937	3.30	0.95	0.282	0.094	1321	19.77
	0.781	2.45	0.80	0.257	0.071	1085	17.00

Table 2: Variation of thicknesses with temperature under constant loading

Temperature	Lateral strain		
	0.7813 MPa	**0.9375 MPa**	**1.563 MPa**
25°C	0.000	0.025	0.063
30°C	0.063	0.088	0.150
40°C	0.100	0.125	0.188
50°C	0.213	0.250	0.375
60°C	0.313	0.375	0.438

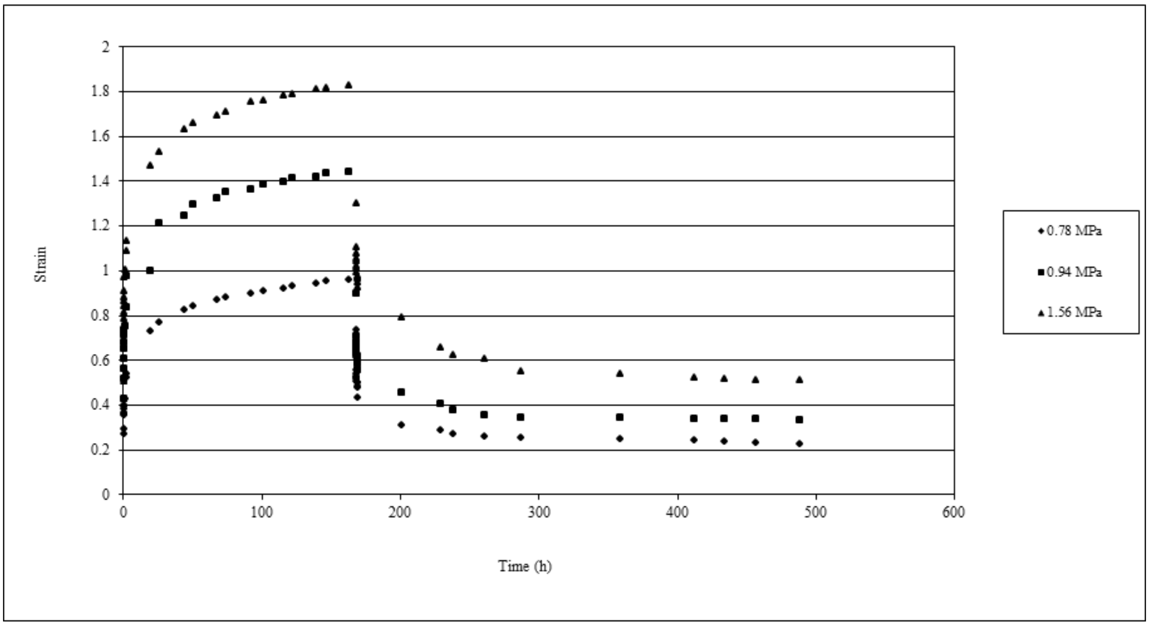

Figure 3: Creep and Relaxation curve at 30°C

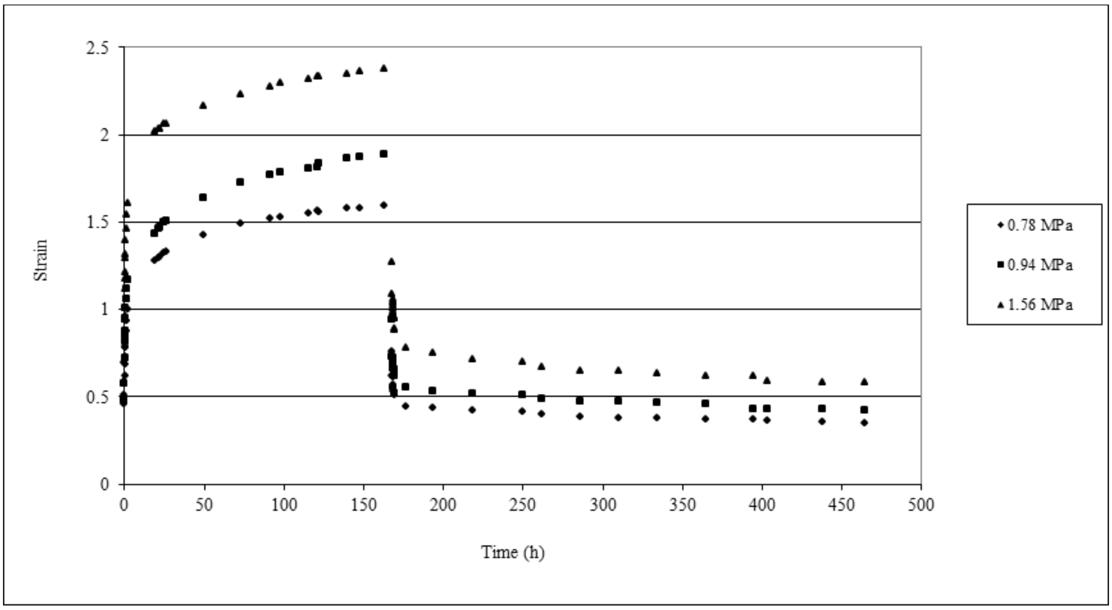

Figure 4: Creep and Relaxation curve at 40°C

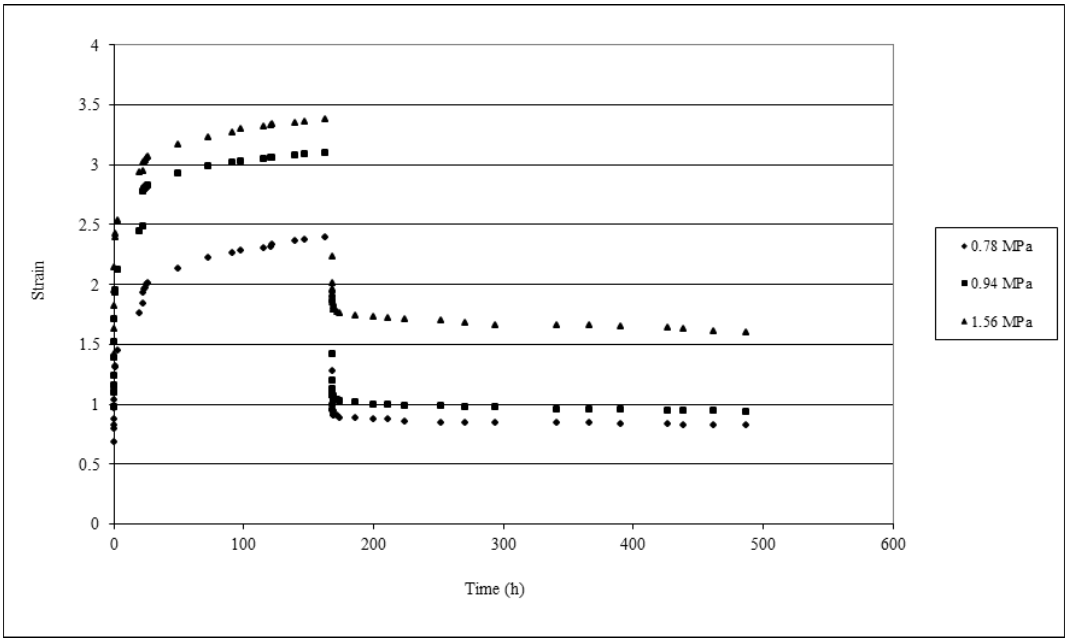

Figure 5: Creep and Relaxation curve at 50°C

Table 2 shows the results of variation in the thicknesses of specimen after elongation in different temperature conditions and varying loads. It was observed from Table 2 that the strain in the axis of loading was directly proportional to the lateral strain.

However, the research project used loads approximately 10% of the material strength so as to investigate the effect of creep namely 1.56, 0.94 and 0.78 MPa. The resulting creep and recovery curves are presented in Figures 3 – 5. The both the creep and recovery curves were fitted with power law to very high values of R2.

The power law was in the form of Equation (4), Where:

$\varepsilon_c(t_c)$ = Time dependant strain

A&n = Constants and be ± depending on whether the curve is of creep (+) or relaxation (-)

t = time elapsed (hours)

This implies that that theory on recovery presented in Crawford (1998) may be used in analysis of the data obtained in this project since in both cases, data may be described by the power law. The parameters A, n and R2 for each of the creep and relaxation curves at the specified temperatures and applied loads are presented in Table 2. It is usually important to obtain mathematical relationships for the different parameters so as to be able to interpolate or estimate values of different parameters for the temperatures and loads not actually used in the experiments. It was noted from Table 3 that the value of A generally increased with temperature for both creep and recovery. It was also noted that at a particular temperature, the values of A increased as the applied stress increased for both creep and recovery. To investigate this observation, curves of applied stress versus A values were plotted for both creep (Figure 6) and relaxation (Figure 7) data.

From Figure 6, the relationship between applied stress and values of A for creep at different temperatures was seen to be best represented by exponential equations as presented in the curves and yielded quite high value of R2. On the other hand, From Figure 7, the relationship between applied stress and values of A for recovery at different temperatures was seen to be best represented by linear equations as presented in the curves and yielded high value of R2.

Table 3: Summary of the parameters form the creep and relaxation curves

Temp °C	**Applied stress (MPa)**	**CREEP**				**RECOVERY**			
		A	**n**	**MEAN n**	**R^2**	**A**	**n**	**MEAN n**	**R^2**
30	**1.563**	0.991	0.126	0.137	0.964	0.931	-0.098	-0.105	0.971
	0.937	0.751	0.133		0.980	0.582	-0.098		0.986
	0.781	0.451	0.153		0.994	0.463	-0.121		0.994
40	**1.563**	1.341	0.124	0.127	0.939	0.941	-0.078	-0.070	0.986
	0.937	1.002	0.128		0.975	0.646	-0.067		0.984
	0.781	0.860	0.128		0.990	0.528	-0.066		0.989
50	**1.563**	2.161	0.097	0.115	0.956	1.855	-0.023	-0.023	0.960
	0.937	1.796	0.119		0.979	1.075	-0.022		0.948
	0.781	1.272	0.128		0.994	0.944	-0.024		0.948

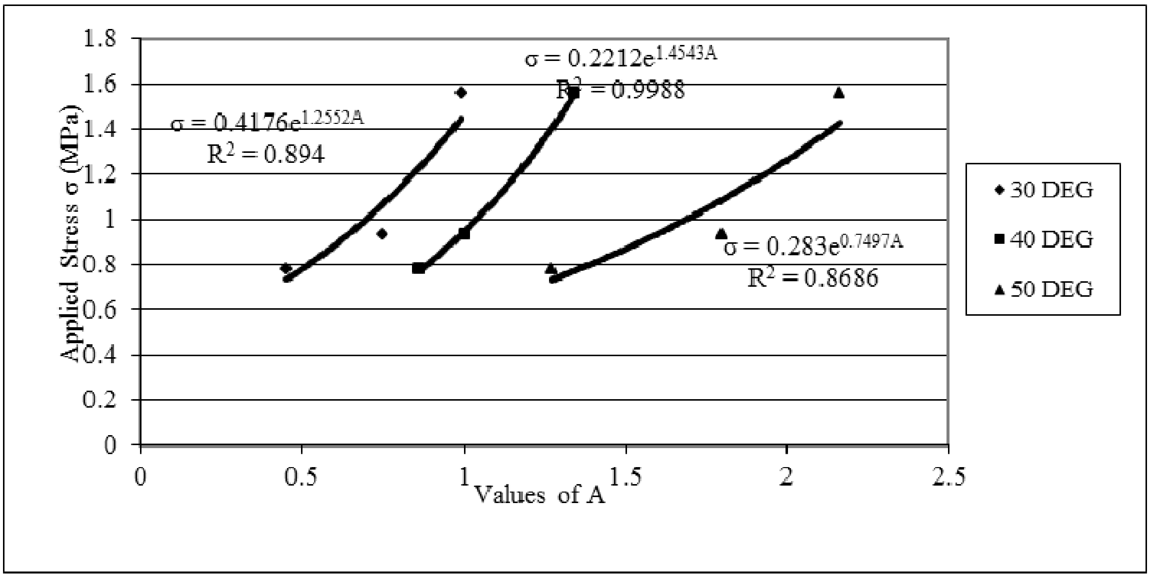

Figure 6: Relationship between applied stress and values of A for the creep curves at different temperatures

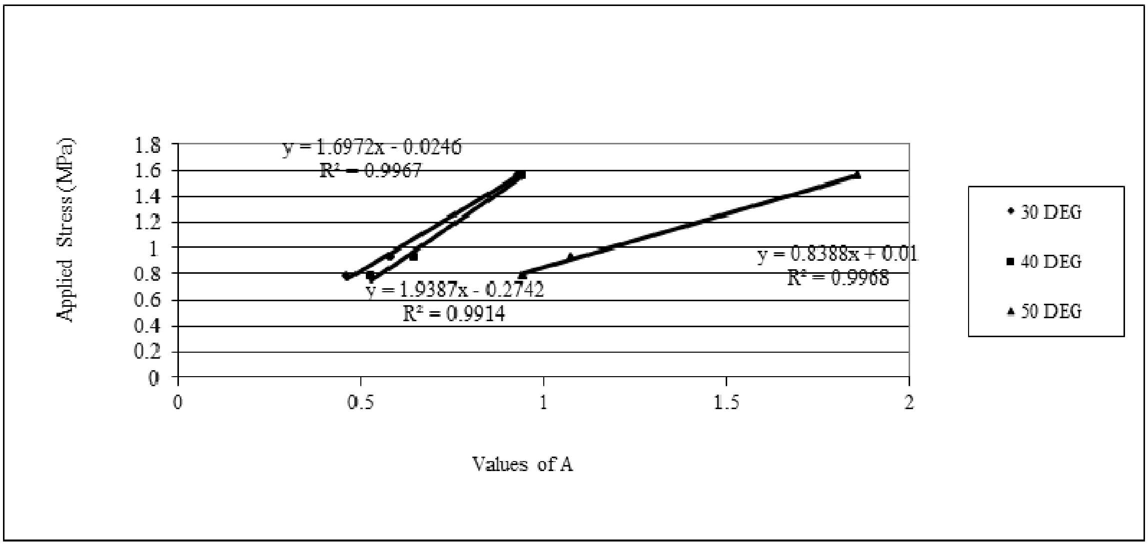

Figure 7: Relationship between applied stress and values of A for the relaxation curves at different temperatures

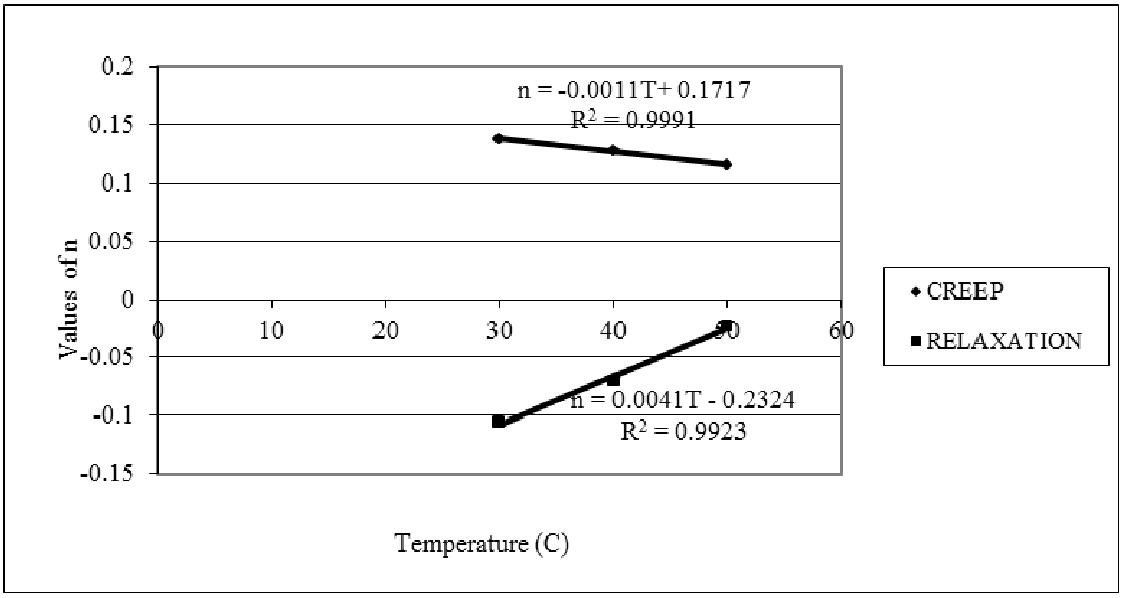

Figure 8: Relationship between values of n and temperature (T) for creep and relaxation

It was also noted in Table 3 that the values of n were almost constant for any applied stress at a particular temperature for both creep and recovery. Therefore for each temperature an average value of B was obtained. It was further observed that the average values of B decreased as temperature increased for creep and that the values of B increased as temperature increased during recovery. In Figure 8, a curve of the relationship between the values of B and temperature was plotted and yielded almost perfectly straight lines. It was therefore concluded that the values of B were independent of applied stress but were linearly related to the operating temperature.

It was concluded that, from the three curves presented in Figure 6, 7 and 8 it is possible to estimate the value of creep and recovery within the temperature range 30°C - 50°C and for stresses ranging from 0.781 to 1.563 MPa just by knowing only the applied stress and the operating temperature. This is because from either Figure 6 or 7, it is possible to obtain the values of A in creep and recovery by knowing the value of the applied stress (service loads) and from Figure 8, it is possible to obtain the values of n by knowing the operating temperature. These can then be used to estimate the expected creep and recovery strains from the power law in Equation (4) for the range of temperature and loads covered in the project.

It was further concluded that, by equations (10) and (11), by this project it is possible to obtain the expected permanent expansion of the material under load, when loaded once and when loaded and unloaded intermittently when given the expected volume of water to be stored. This is because from to be stored, the load that the water applies on the material may be calculated. Using Figures 6, 7 and 8, the values of constants A and n are obtained to be used in Equation (4) to calculate the corresponding value of $\varepsilon c(tc)$, which can be used together with tp, the period of each cycle and the number of cycles N, to obtain the accumulated residual strain in equation (10) and the total accumulated strain in equation (11)

REFERENCES

ASTM D638-2003 Standard Test Method for Tensile Properties of Plastics, ASTM International, West Conshohocken, PA, www.astm.org.

Onyango, D.M., 2003. Women at the Source of Life: The Experience of Kenya Rainwater Association, FAO Dimitra Newsletter, No. 8, October 2003, Brussels, Belgium.

Timoshenko, S.P. and J.N. Goodier, 1983. Theory of Elasticity, McGrawHill, New York.

Kenya Rainwater Association, 2004. Progress Report on Ndeiya Karai Project, Kenya Rainwater Association

Crawford, R.J., 1998. Plastics Engineering, Elsevier, Butterworth Heinemann, UK.

African Journal of Science and Technology (AJST)
Science and Engineering Series Vol. 12, No. 2, pp. 16 - 21

USE OF LIMITED HYDROLOGICAL DATA AND MATHEMATICAL PARAMETERS FOR CATCHMENT REGIONALIZATION: A CASE STUDY OF THE OSUN DRAINAGE BASIN, NIGERIA

Awokola, O.S.[1], Coker, A.O.[2,4], Fullen, M.A.[3] and Booth, C.A [4]

[1]Department of Civil Engineering, College of Engineering, University of Agriculture, P.M.B. 2240, Abeokuta, Nigeria.
[2]Department of Civil Engineering, Faculty of Technology, University of Ibadan, Ibadan, Nigeria.
[3]School of Applied Sciences, The University of Wolverhampton WV1 1LY, United Kingdom.
[4]School of Engineering and the Built Environment, The University of Wolverhampton WV1 1LY, United Kingdom.

ABSTRACT: *A protocol is proposed for the regionalization and subdivision of catchments based on hydrometric parameters. Such catchment regionalization may assist the development of appropriate catchment management strategies and policies. As a case study, the trends of variations in daily stage and discharge of seven gauging stations located in the 9,900 km^2 Osun Drainage Basin (South West Nigeria) were investigated. Linear regression models for all stations show the expected strong positive association of stage and discharge. The estimated daily changes explain only 1.44% of variations in stage, 0.25% variation in discharge and 99.5% in stage-discharge for station 5, 5.5% variation in stage, 0.7% variation in discharge and 99.7% in stage-discharge at station 25, and 10% variation in stage, 8.9% variation in discharge and 100% in stage-discharge at station 27. For the other studied stations, R^2 estimated from daily stage and daily discharge give widely varying patterns. R^2 estimated from daily stage and daily discharge is non-significant, but is significant for the daily stage-discharge relationship. The derived daily-stage and daily-discharge equations for the seven stations and their corresponding coefficients of determination can be used to classify the basin into three distinct zones. These are Zone I (coefficient of determination within the range of 0-6% for the daily-stage and daily-discharge), Zone II (coefficient of determination within the range of 7-10.5% for the daily-stage and daily-discharge), and Zone III (coefficient of determination within the range of 11-22% for the daily-stage and daily-discharge). The exponents of the stage-discharge equation can also be used for spatial classification. Zone A exponent is in the range of 1.3-1.7, Zone B exponent is in the range 2.2-2.3 and Zone C exponent is in the range 4.0-4.7. These can be combined to produce three hydrometric regions. It is proposed this regionalization protocol could be used as an initial step in dividing complex catchment systems into more homogeneous subunits, to assist subsequent catchment management and planning. The hydrometric regionalization protocol is now being evaluated on the Osun and other drainage basins in Nigeria.*

Keyword: *Derivation, Gauged and Ungauged Rivers, Drainage Basin, Power Equations*

INTRODUCTION

A proper understanding of the flow regime of rivers is essential for channel design and especially the estimation of flood discharges such structures could tolerate (Awokola and Martins, 2001). Solutions to such problems are necessary in any engineering activity connected with streams in which flow rates are stochastic in nature. Effective flood protection and erosion control schemes are among the challenges of hydraulic engineering, in which the inter-relationships between stream flow mechanics, dynamics and hydrology must be carefully studied and interpreted.

In Nigeria and other developing countries, there are problems of data inadequacy- frequent data gaps and non- existence of data at development sites - and these issues create serious design and project management problems (Sonuga, 1990). The most challenging situation exists when no flow records are available anywhere in the catchment. There are also other categories of ungauged catchment: (i) sites on a river where some tributaries are gauged, and (ii) sites on a river, which are gauged at one or more different locations upstream or downstream. In many aspects, even a site which has only several years of record must be evaluated as if it were an ungauged catchment, because the information usually requires augmentation. Even when models are constructed, they will require additional site-specific parameters to be defined for each application site (Beven, 2000; Awokola, 2001).

The derivation of relationships between hydrological variables is of great importance for the transfer of information from the few-gauged rivers to the many other rivers with hydrologically-similar catchments for which no stream flow data exist. We need an approach to ascertain the actual changes in hydrological response of a particular catchment within a drainage basin, which can reveal land transformations and interactions that occurred in the past. The 'region of influence' (ROI) approach adopted by Burn (1990) is limited to measures which do not rely on actual flow data. Regionalization or regional typification has been extensively analysed (Hosking *et al.,* 1985; Lettenmaier *et al.,* 1987; Chowdhury *et al.,* 1991; Hosking and Wallis, 1997). This approach entails inducing knowledge of the regional hydrological structure of the study territory on regional structure identified in a sample of gauged basins.

The aim of this study is to assess and evaluate the hydrologic response of seven gauging stations (catchment areas) in the Osun Basin of South West Nigeria that had one-year (1982) of complete hydrological record. Data analysis enabled the initial development of a regionalization protocol, based on analytically-determined hydrometric parameters. The results will hopefully be useful for engineers, conservationists and planners at gauged and ungauged sites and it will reveal the threshold of flood discharges required for the economic design of hydraulic structures and economic feasibility analysis of water resources management and environmental impact assessment of projects. In a previous study, Elkaduwa and Sakthivadivel (1998) observed that adverse environmental impacts were directly related to changes in flow regimes and that rapid runoff was responsible for high soil erosion rates, loss of land productivity and more frequent flash floods. The high rate of sediment supply due to accelerated erosion caused degradation of stream channels, increasing the likelihood of flash floods, deposition of coarse material and silting of irrigation canals.

THE STUDYAREA

The Osun River Basin occupies 9,900 km^2 and is located approximately between latitudes 6^{0}30'N-8^{0}20'N and longitudes 4^{0}E-5^{0}10'E (Figures 1a and 1b). The Osun River - a major drainage system in South West Nigeria- rises in the Oke-Mesi ridge ~5 km north of Effon-Alaye and flows through Itawure, before flowing first westward through Osogbo and Ede and then southward to enter Lagos Lagoon. The main tributaries are the Oba and Erinle. The basin's climate is strongly influenced by the movement of the Inter-Tropical Convergence Zone (ITCZ), a quasi-stationary boundary zone that separates the sub- tropical continental air mass over the Sahara and the equatorial maritime air mass over the Atlantic Ocean.

The ITCZ moves northwards beyond the basin at the peak of the rainy season in June and July, and southwards to the coast, in the middle of the dry season in December and January. Data obtained from stations in the basin show that February and March are the hottest months in the year. The mean daily maximum temperature for February is 31.4 ^{o}C in the south and as high as 34.6^{o}C in the north. The main feature of the rainfall pattern is its seasonal distribution. The rainy season begins earlier in the south, usually commencing in March, and continues until late October or early November.

Cretaceous sedimentary rocks are present in the southern section of the Osun Basin. The remaining sections are composed of crystalline rocks of the Basement complexes, which belong to the older Intrusive Series (Jones *et al*, 1964).

MATERIALSAND METHODS

There are 16 stream gauging stations in the Osun River Basin and 17 such stations in the Ona RivBasin and its tributaries Ibu and Omi (Tahal Consultants, 1982). The seven stations used in this study are shown in Fig.1a. They are monitored by Oyo and Osun State Water Corporations. Rating tables are available for all gauging stations (Table 1). Some 2,555 daily stage data for the seven stations were subjected to statistical analysis. All stage information was used with the available rating tables for each station to derive the rating equations in Table 2. The derived equations were used to predict discharge values for the range of daily stage available and the monthly maximum discharge for each station was calculated using the maximum stage and appropriate derived equation. The trend in daily stage and stream flow were analysed using the conventional techniques of linear regression models.

Table 1: List of Gauging Stations, Rivers and Locations

Rivers	Location	Gauging Station Number
Osun	Asejire	5
Osun	Iwo-Railway Station	25
Osun	Ede	27
Oba	Awe/Ife-Odan	35
Oba	Oyo/Ogbomosho	39
Osun	Ilase	52
Osun	Esa-Odo	64

RESULTS AND DISCUSSION

The power equations derived for stations 5, 25, 35 and 52 and the second-degree polynomial equations derived for stations 27 and 35 gave a perfect fit. Stations 39 and 64 showed good and perfect fit for the power and polynomial equations within the limits or range shown in Table 2. Analysis of Station 35 data showed that both power and polynomial equations gave a perfect fit, with coefficients of determination of $r^2 = 0.9988$ and 0.9995, respectively. Further investigations of physical and hydro-topographical parameters of the basin are required to ascertain the basis for the differences in the mathematical results between the stations. The trends of variations in daily stage and discharge are shown graphically in Figures 2-5; while the summary of the derived relations are reported in Table 3. The linear regression models for the entire stations show an increasing trend of both stage and discharge (Table 3). The coefficients of determination (R^2)

Table 2. The Derived Rating Equations for each Station

Stations	Derived Rating Equations (m^3/s)	Type of Equation	Remark
5	$Q_5 = 17.36H^{2.27}$	Power	Perfect Fit
25	$Q_{25} = 8.23H^{3.99}$	Power	Perfect Fit
27	$Q_{27} = 0.24H^{4.73}$	Power	Poor Fit
	$Q_{27} = 10.06H^2 +15.67H-62.39$ **($r^2 = 0.996$, $r = 0.998$), n = 2,555**	2nd Degree Polynomial	Perfect Fit
35	$Q_{35} = 7.44H^{1.59}$	Power	Perfect Fit
	$Q_{35} = 2.47H^2+8.02-2.78$ **($r^2 = 0.999$, $r = 0.9995$), n = 2,555**	2nd Degree Polynomial	Perfect Fit
39	$Q_{39} = 4.96H^{1.68}$	Power	Good Fit (Range 0.03-3.15 m)
	$Q_{39} = 6.87H^2-11.11H+5.71$ **($r^2 = 0.993$, $r = 0.9965$), n = 2,555**	2nd Degree Polynomial	Good Fit (Range 2.01m and above)
52	$Q_{52} = 2.56H^{2.24}$	Power	Perfect Fit
64	$Q_{64} = 6.25H^{1.25}$	Power	Good Fit (Range 0.03-2.4 m)
	$Q_{64} = 3.14H^2-0.14H-0.96$ **($r^2 = 0.9989$, $r = 0.999$), n =2,555**	2nd Degree Polynomial	Perfect Fit

All r coefficients significant at $P<0.001$.
Source: Awokola (2003).

Table 3. The Daily-Stage, Daily-Discharge and Stage-discharge Equations

Station	Stage-Discharge	Equation	Coefficient of Determination (R^2) %	Zone
5	Stage (m)	$H^{5} = 0.0005x + 0.3866$	1.44	I
	Discharge (m^3/s)	$Q^{5} = 0.0111x + 5.5639$	0.25	I
	Stage-Discharge (m^3/s)	$Q^{5} = 17.36H^{2.27}$	99.5	
25	Stage (m)	$H^{25} = 0.0012x + 1.0459$	5.51	I
	Discharge (m^3/s)	$Q^{25} = 0.101x + 37.657$	0.66	I
	Stage-Discharge (m^3/s)	$Q^{25} = 8.23\ H^{3.99}$	99.7	
27	Stage (m)	$H^{27} = 0.0016x + 2.4032$	10.05	II
	Discharge (m^3/s)	$Q^{27} = 0.1107x + 34.783$	8.89	II
	Stage-Discharge (m^3/s)	$Q^{27} = 0.24\ H^{4.73}$	100	
35	Stage (m)	$H^{35} = 0.0029x + 0.0843$	19.3	III
	Discharge (m^3/s)	$Q^{35} = 0.0349x - 2.2518$	17.1	III
	Stage-Discharge (m^3/s)	$Q^{35} = 7.44\ H^{1.59}$	100	
39	Stage (m)	$H^{39} = 0.0012x + 0.7247$	3.57	I
	Discharge (m^3/s)	$Q^{39} = 0.0094x + 3.9889$	2.64	I
	Stage-Discharge (m^3/s)	$Q^{39} = 4.96\ H^{1.68}$	96.7	
52	Stage (m)	$H^{52} = 0.0033x + 0.8655$	21.05	III
	Discharge (m^3/s)	$Q^{52} = 0.0369x + 1.6053$	14.67	III
	Stage-Discharge (m^3/s)	$Q^{52} = 2.56\ H^{2.24}$	99.9	
64	Stage (m)	$H^{64} = 0.0034x + 0.7541$	18.97	III
	Discharge (m^3/s)	$Q^{64} = 0.0332x + 0.838$	15.03	III
	Stage-Discharge (m^3/s)	$Q^{64} = 6.25\ H^{1.25}$	92.28	

estimated from daily stage and daily discharges are not significant, but are significant for the daily stage-discharge relationships.

The derived daily-stage and daily-discharge equations for the seven stations and their corresponding coefficients of determinations have been used to subdivide the basin into three distinct zones, based on the proposal of Solin (2005) that selected sets of gauged basins should represent the whole population of basins. These are Zone I (coefficient of determination within the range 0-6% for the daily-stage and daily-discharge), Zone II (coefficient of determination within the range 7-10.5% for the daily-stage and daily-discharge), and Zone III (coefficient of determination within the range 11-22% for the daily-stage and daily-discharge) (Table 4). The exponents of the stage discharge equation have been used as the basis of an additional classification system. Zone A exponent is in the range 1.3-1.7, Zone B exponent is in the range 2.2-2.3 and Zone C exponent is in the range of 4.0-4.7 (Table 4). The two methods of zoning were combined, as shown in Table 5, to produce a unitary zoning system. Thus, Zone A_u includes stations 35, 39 and 64; Zone B_u includes stations 5 and 52 and Zone C_u includes stations 25 and 27. The derived unitary zoning of hydrometrically-similar catchments within the Osun River Basin is presented in Figure 6.

Table 4: Classification of the Basin into Zones

Zone	Station number	Criteria
I	5,25 & 39	R^2: range 0-6%
II	27	R^2: range 7-10.5%
II	35,52 & 64	R^2: range 11-22%
A	35,39 & 64	Exponent: range 1.3-1.7
B	5 & 52	Exponent: range 2.2-2.3
C	25 & 27	Exponent: range 4.0-4.7

Table 5: Combination of the two derived zones

Station No.	Zone	Zone	Joint Zones	Groupings	Unitary Zone
5	I	B	IB	IB, IIIB	
				5,52	B_u
25	I	C	IC	IC, IIC	
				25,27	C_u
27	II	C	IIC		
35	III	A	IIIA	IIIA, IA, IIIA	
				35,39, 64	A_u
39	I	A	IA		
52	III	B	IIIB		
64	III	A	IIIA		

It is proposed that this regionalization protocol could be used as an initial step in dividing complex catchment systems into more homogeneous subunits, to assist subsequent catchment management and planning. The regionalization protocol is now being evaluated on the Osun and other drainage basins in Nigeria.

CONCLUSIONS

The derived daily-stage and daily-discharge equations for the seven stations and their corresponding coefficient of determinations were used to classify the Osun basin into three distinct hydrometric zones. These were Zone I (coefficient of determination within the range 0-6% for the daily-stage and daily-discharge), Zone II (coefficient of determination within the range 7-10.5% for the daily-stage and daily-discharge) and Zone III (coefficient of determination within the range 11-22% for the daily-stage and daily-discharge). The exponents of the stage-discharge equation were used for another classification, Zone A exponent in the range 1.3-1.7, Zone B exponent in the range 2.2-2.3 and Zone C exponent in the range 4.0-4.7. The combination of the two zoning methods resulted into three distinct unitary zones: A_u for stations 35, 39 and 64; B_u for stations 5 and 52, and Zone C_u is for stations 25 and 27. These results can be used for preliminary selection of hydrometrically-similar catchments within the Osun basin. Further investigations of basin hydrometric parameters are required to ascertain the basis for the difference in the mathematical results for the stations. An optimized hydrometric regionalization protocol could provide a useful tool for catchment evaluation and management in Nigeria and beyond.

ACKNOWLEDGEMENTS

The authors would like to thank the management of the Ogun-Osun River Basin Development Authority for their support during the data collection phase of the study. Dr. A.O. Coker gratefully acknowledges receipt of a Lady Wulfrun Visiting Research Fellowship from the School of Engineering and the Built Environment at The University of Wolverhampton, U.K.

REFERENCES

Awokola, O.S. and Martins, O. 2001. Regional Flood Frequency Analysis of Osun Drainage Basin, South Western Nigeria. *Nigerian Journal of Science,* Vol. 35, 37-44.

Awokola, O.S. 2001. Regional Flood Frequency Analysis for Ogun Drainage Basin South Western Nigeria. *The Nigerian Journal of Environmental Resources Management,* Vol. 1, 27-34.

Awokola, O.S. 2003. Derivation of Rating Equations For Gauged Rivers In Osun Drainage Basin, South Western Nigeria. *ASSET* Series A: 139-148.

Beven, K.J. 2000. Uniqueness of place and process representations in hydrological modelling. *Hydrology and Earth Systems Sciences,* 4(2), 203-213.

Burn, D.H. 1990. Evaluation of Regional Flood Frequency Analysis with a Region of Influence Approach. *Water Resources Research,* Vol. 26, No. 10, 2257-2265.

Chowdhury, J.U., Stedingen, J.R. and Lu Li-Hsiung (1991). Goodness-of-fit test for regional generalized extreme value flood distributions. Water Resources Research, Vol. 27, No. 7, 1765- 1776.

Elkaduwa, W.K.B. and Sakthivadivel, R. 1998. Use of historical data as decision support tool in watershed management: A case of the Upper Nilwala basin in Sri Lanka. Research Report 26. International Water Management Institute: Colombo, Sri Lanka.

Hosking, J.R.M. and Wallis, J.R. (1997). Regional Frequency Analysis. Cambridge University Press, Cambridge, UK.

Hosking, J.R.M., Wallis, J.R. and Wood, E.R. (1985). An appraisal of the regional flood frequency procedure in the UK. Hydrological Sciences Journal, 30(1), 85-109.

Jones, H.A., Phil, D. and Hockey, R.D. 1964. The Geology of Part of South-Western Nigeria. Published by the authority of The Federal Government of Nigeria, pp.72-75.

Lettenmaier, D.P., Wallis, J.R. and Wood, E.R. (1987). Effect of regional heterogeneity on flood frequency estimation. Water Resources Research, Vol. 23, No. 2, 313-323.

Solin, L. 2005. Identification of homogeneous regional classes for flood frequency analysis in the light of regional taxonomy. Hydrological Sciences Journal, 50(6), 1105-1118.

Sonuga, J.O. 1990. Hydrologic Decision Making for Design of Water Resources Systems. Proceedings of Nigerian National Committee for International Hydrological Programme (IHP), pp. 30-44.

Tahal Consultants, 1982. Oshun River Basin Feasibility Study. Vol. 7, Report submitted to Ogun-Oshun River Basin Development Authority.

African Journal of Science and Technology (AJST)
Science and Engineering Series Vol. 12, No. 2, pp. 22 - 30

SOLITARY ROSSBY WAVES IN THE LOWER TROPICAL TROPOSPHERE

A. Lenouo[1] and F. Mkankam Kamga[2]

[1]Department of Physics, Faculty of Science, University of Douala,
P.O. Box 24157 Douala, Cameroon
[2]Laboratory for Environmental Modelling and Atmospheric Physics,
Department of Physics, University of Yaounde 1, Yaoundé, Cameroon

E-mail: lenouo@yahoo.fr

ABSTRACT: *Weakly nonlinear approximation is used to study the theoretical comportment of large-scale disturbances around the inter-tropical mid-tropospheric jet. We show here that the Korteweg de Vries (KdV) theory is appropriated to describe the structure of the streamlines around the African easterly jet (AEJ) region. The introduction of the additional velocity* C_1 *permits to search the stage where the configuration of the wave will correspond in this zone to those of Rossby solitary waves. It was also shown that the configurations of disturbances can be influenced by this parameter so that we can look if the disturbances are in the control or not of their dispersive effects.*

Key words: *Soliton; Rossby waves; KdV equation; African easterly waves.*

INTRODUCTION

The Rossby waves are the most important in large-scale atmospheric flow processes (Holton, 2004). For their analysis, it is usually sufficient to study the horizontal structure of waves. Most theories treating the structure of these waves are based on linear models which only take into account their dispersive behaviour. Nonlinear processes are more interesting because they can help to explain, for example, the hurricane spiral bands observed in the tropical zone (Guinn and Schubert, 1993), and energy exchanges between different modes of the waves (Lenouo et al., 2005). Solitary Rossby waves in a zonal flow appear to have been discovered (analytically) by Long (1964) and have been studies subsequently by Larsen (1965), Benney (1966), Redekopp and Weidman (1978), Miles (1979), Hoskins and Ambrizzi (1993) and Luo (2004). All invoke Rossby's β-plane model, in which the northerly gradient of the vertical component of the earth's rotation is constant.

Many studies have dealt with nonlinear waves and particularly solitary waves in the atmosphere, stating with works by Tepper (1950) and Abdullah (1955). On the theoretical level, nonlinear waves have been examined by Lenouo et al. (2005) in the mid-atmosphere where the African Easterly waves (AEWs) are propagated. In the same region, Dobryshman (1982) showed that the Korteweg de Vries (KdV) theory is appropriate to describe Rossby solitary waves. But the physical interpretation of the results in terms of Rossby solitary waves is not evident and the roles that these waves could influence the structure and energy of these waves have not been examined. Moreover, Huang and Zhang (1988) established that the propagation of Rossby solitary wave has behaviour closer to those of ridges and troughs. They therefore showed that these waves can travel long distances in the northern Hemisphere without a change both in speed or structure, and for any hour.

The first well known studies of Rottman and Einaudi (1993) have helped to identify solitary wave connected to internal gravity waves in the atmosphere. They showed that these waves are described by KdV equations when they move in the upper atmosphere and by the Benjamin-David-Ono (BDO) equation when they appear in the lower level. They therefore correctly analysed the observations of Lin and Goff (1988) by using the KdV model, whereas the observation of Smith and Morton (1984) were better explained by the BDO model. This was the first evidence of these types of wave observed in the atmosphere and their comparison with theoretical models. The solution of the three-dimensional nonlinear Charney–Obukhov equation describing solitary pancake Rossby vortices was found by Kaladze (2000). Its solution was represented in the form of an axially symmetric cylindrical monopole (anticyclonic) vortical structure moving with constant velocity. Whereas the role of westward-travelling planetary (Rossby) waves in the block onset and the deformation of eddies during the interaction between synoptic-scale eddies and an incipient block was examined by Luo (2004). This author has constructed an incipient block that consists of a stationary dipole wave for zonal wavenumber and a westward-travelling monopole wave with constant amplitude for zonal wavenumber.

The role of nonlinear wave was also being studied in oceanography. Hence, time series observations of nonlinear internal waves in the deep basin of the South China Sea are used to evaluate mechanisms for their generation and evolution by Qiang and Farmer (2011). They showed that internal tides are generated by tidal currents over ridges in Luzon Strait and steeper as they travel west, subsequently generating high-frequency nonlinear waves. Although nonlinear internal waves appear repeatedly on the western slopes of the South China Sea, their appearance in the deep basin is intermittent and more closely related to the amplitude of the semidiurnal than the predominant diurnal tidal current in Luzon Strait.

In the present study, we will use the weakly nonlinear theory to examine the behaviour of the large-scale waves around the mid-tropospheric African Easterly Jet (AEJ), where the wave is more intense. Considering that the vertical extent of this jet is smaller than its horizontal extent (Lenouo et al. 2005), we admit in first approximation that the motion of the air in this region is dominated by the effects of the rotation of the earth. Under these assumptions, we will look for the stage where the configurations of these are similar to those having the form of solitary Rossby waves. This study is organised as follows. In Section 2, we will present method used to examine the nonlinear vorticity equation. In Section 3, the linear and nonlinear solutions are discussed whereas conclusion is presented in Section 4.

METHODOLOGY

Basics equations

Rossby solitary waves are sought by using a nonlinear vorticity equation in a barotropic model (Dobryshman, 1982). This equation integrates the horizontal shear in mean zonal wind that the profile permits to characterise the wave instability. We define a coordinate system (x,y,t) where t is the time component and the space components x and y are along the direction of wave propagation in east and north direction respectively. When the flow is no divergent, zonal and meridional components of the velocity can be written as a function of a streamfunction perturbation ψ as

$u = -\partial\psi / \partial y$ and $v = \partial\psi / \partial x$

Otherwise, in a barotropic model, the evolution of streamline is described by the equation (Holton, 2004)

$$\left[\frac{\partial}{\partial t} + U\frac{\partial}{\partial x}\right]\nabla^2\psi + J(\psi,\nabla^2\psi) + \left[\beta - \frac{d^2U}{dy^2}\right]\frac{\partial\psi}{\partial x} = 0 \qquad (1)$$

with the following boundary conditions:

ψ=0 at y=0 and y=L (2)

In equation (1), J is the Jacobian operator $J(a,b) = \frac{\partial a}{\partial x}\frac{\partial b}{\partial y} - \frac{\partial a}{\partial y}\frac{\partial b}{\partial x}$, $\nabla^2 = \frac{\partial^2}{\partial x^2} + \frac{\partial^2}{\partial y^2}$ the Laplacian operator, U the mean zonal wind component and β the meridional gradient of the coriolis parameter.

The effects of non linearity are introduced through the Jacobian term, which is nonlinear. In the case of weak amplitude waves, the individual oscillations can be represented in the form of linear or nonlinear wave superposition.

Theory

A soliton is localised wave, solution to a nonlinear partial derivatives equation without change of velocity or profile in a weakly dispersive area. By using a multiple scale method, we can write a stream function ψ in the form of a power expansion in a small parameter ϵ so that

$$\psi = \epsilon\,\psi_1 + \epsilon^2\,\psi_2 + \qquad (3)$$

It is necessary to introduce a convenient space and time variables ζ and τ, adapted to describe a weakly dispersive nonlinear system (Rottman and Einaudi, 1993). In this new Galilean reference frame, the transformations of Rottman and Einaudi (1993) are given by:

$$\zeta = \in^{1/2}(x - C_0 t) \text{ and } \tau = \in^{3/2} t \qquad (4)$$

where C_0 is the phase velocity of the eastward wave. The procedure consists in rewriting equation (1) using ζ and τ, and then seeks a solution in a power series expansion in the amplitude parameter ϵ. Then by collecting terms of order $O(\in^{3/2})$, we obtain the following linear equation in ψ_1:

$$(U - C_0)\frac{\partial}{\partial\zeta}\left(\frac{\partial^2\psi_1}{\partial y^2}\right) + \left[\beta - \frac{d^2U}{dy^2}\right]\frac{\partial\psi_1}{\partial\zeta} = 0 \qquad (5)$$

Also the terms of order $O(\in^{5/2})$ gives:

$$\frac{\partial}{\partial\tau}\left(\frac{\partial^2\psi_1}{\partial y^2}\right) + (U - C_0)\frac{\partial^3\psi_1}{\partial\zeta^3} + \frac{\partial\psi_1}{\partial\zeta}\frac{\partial^3\psi_1}{\partial y^3} - \frac{\partial\psi_1}{\partial y}\frac{\partial}{\partial\zeta}\left(\frac{\partial^2\psi_1}{\partial y^2}\right) = 0 \qquad (6)$$

Solutions of equations (5) and (6) are sought in the nonlinear waves form $A(\zeta,\tau)$, modulate by an amplitude function $\varphi(y)$, as given by the relation:

$$\Psi(\zeta,y,\tau)=A(\zeta,\tau)\,\varphi(y) \qquad (7)$$

a)- Determination of φ(y)

By substituting relation (7) into equation (5), we set the following eigenvalue equation for $\varphi(y)$:

$$\varphi''(y)+\frac{\beta-U''}{U-C_0}\varphi(y)=0 \qquad (8)$$

where the prime denotes differentiation with respect to y. The boundary conditions are the same as those given by relation (2)

$\varphi=0$ at $y=0$ and $y=L$.

Equation (8) is solved numerically by using GAUSS-SEIDEL's relaxation methods. The shape of horizontal shear is chosen such that the wind is zero at the boundaries. Using centred-difference differentiation, equation (8) is rewritten as:

$$\varphi_i=[\varphi_{i+1}+\varphi_{i-1}]/[2-F_i(\Delta y)^2] \qquad (9)$$

where Δy is the grid size; i=1, 2, …, N and $F_i=\left[\frac{\beta-U''}{U-C_0}\right]_i$.

b)- Nonlinear waves

By substituting relation (7) into equation (6), we can obtain a nonlinear equation as KdV-equation in the form

$$\frac{\partial A}{\partial\tau}+a_n\frac{\partial A}{\partial\zeta}+b_n\frac{\partial^3 A}{\partial\zeta^3}=0 \qquad (10)$$

where parameters a_n and b_n are determined by eigenfunctions φ and depend on the profile of U(y) (see appendix A for more detail). They are given by the following expression:

$$a_n=\frac{\int_0^L[\varphi\varphi'''-\varphi'\varphi'']dy}{\int_0^L\varphi''\,dy} \qquad (11)$$

and

$$b_n=\frac{\int_0^L(U-C_0)\varphi dy}{\int_0^L\varphi''\,dy} \qquad (12)$$

We now examine solutions of equation (10) in the form of nonlinear progressive waves (soliton) $A=A(\zeta+C_1\tau)$ where C_1 is the phase velocity of the soliton which is a weak contribution to the principal phase velocity C_0.

Thus, the total velocity of the system is:

$C=C_0+\epsilon C_1$

The solitary waves, solution of equation (10) is given by the following relation (see appendix B for more detail):

$$A(\zeta,\tau)=A_0\mathrm{Sech}^2[\kappa(\zeta+C_1\tau)] \qquad (13)$$

Where $A_0=3C_1/a_n$ is the nonlinear wave amplitude and $\kappa=(C_1/b_n)^{1/2}$. Going back to the original variable, we finally have:

$$A(x,t)=A_0Sech^2\left(\frac{x-Ct}{\Delta}\right)$$

(14)

where $\Delta=\sqrt{\frac{b_n}{\epsilon C_1}}$ is the soliton characteristic width.

The product of the soliton amplitude and the square of its characteristic width are independent of the soliton phase velocity C_1. It is however proportional to b_n and inversely proportional to a_n or ϵ and is expressed as:

$$\Delta^2A_0=\frac{3b_n}{\epsilon a_n} \qquad (15)$$

Since a_n and b_n are given by relation (11) and (12) respectively, the only known remaining is ϵ. Figure 1 shows some profiles of $A(x,t)/A_0$ for different values of additional phase velocity C_1 and $\epsilon=0.01$. For small C_1, the figure shows that A(x,t) is nearly constant in space but takes the form of a pulse when this parameter becomes important. It is to be noticed that this parameter appears explicitly in the expression of Δ. Thus, when C_1 is set to zero, Δ is even larger and the wave becomes evanescent. But as C_1 increases, e.g. $C_1=25\mathrm{m.s^{-1}}$, the wave propagate symmetrically below the plan which passed trough the origin where x=Ct. Hence, we can say that the wave amplitude A_0 grows with the additional phase velocity C_1 (Fig.2).This shows that the wave moves faster as its amplitude becomes larger. Fig.2 also shows that the soliton characteristic width Δ decreases with C_1.

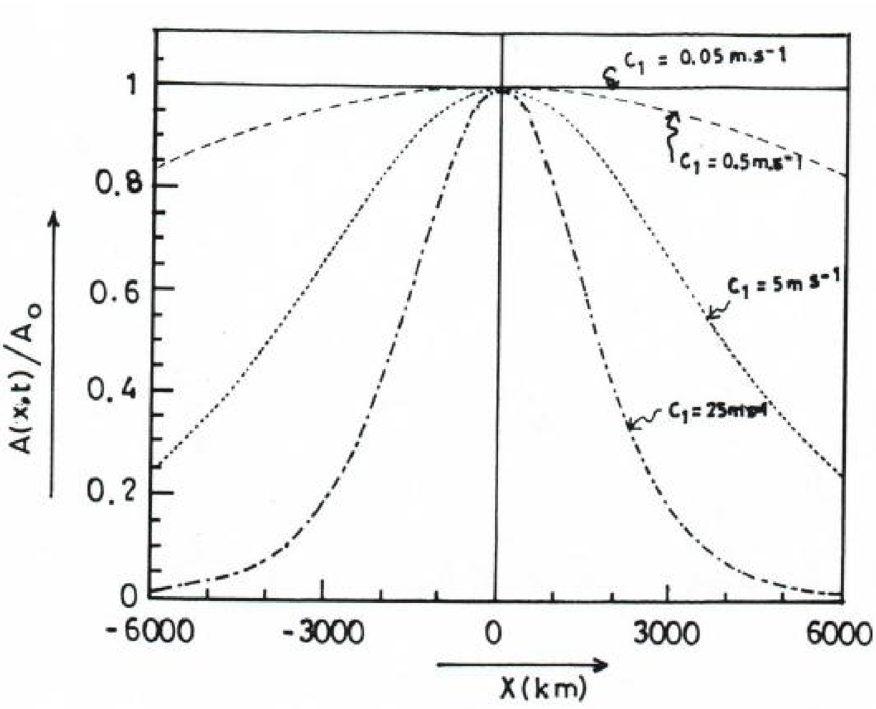

Figure 1: Variations of A(x,t)/A_0 in the propagation direction for different values of the additional wind velocity C_1.

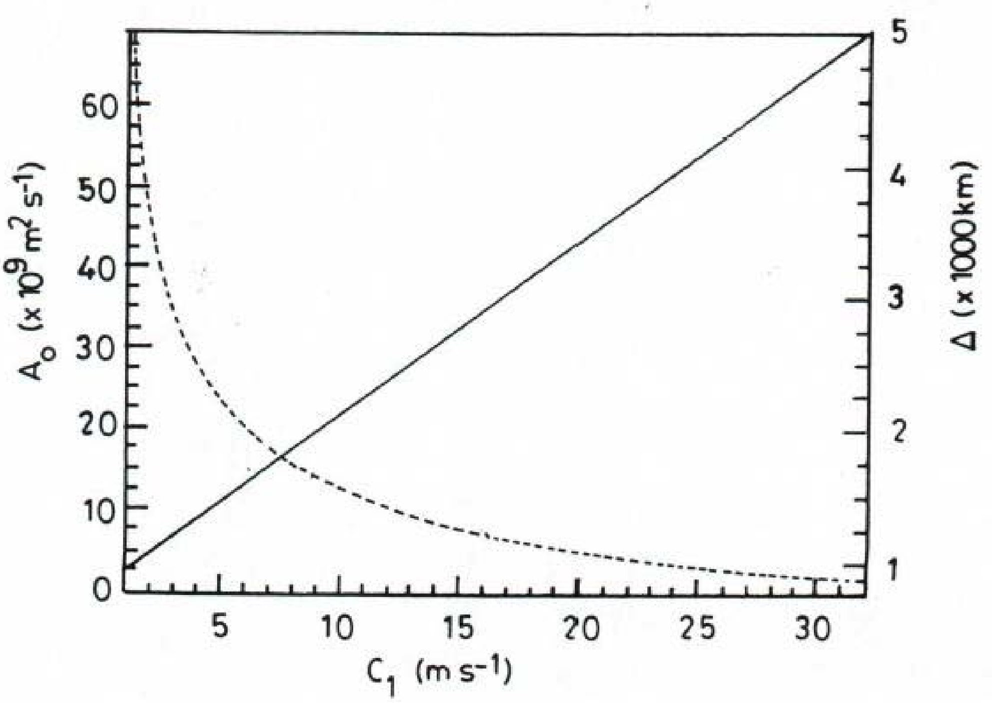

Figure 2: Variations of Amplitude A_0 (in solid line) and the width Δ (in dash line) of the soliton as function of the additional wind velocity C_1.

RESULTS AND DISCUSSIONS

As we know, the solitary wave can be considered only when we define a coordinates system which moves with the wave at the velocity C, for the soliton to appear stationary. At the origin X=0, where X=x-Ct, the amplitude solitary wave is maximal. This is due to the fact that in the translation X=x-Ct of a non fixed distance Ct, the maximum wave amplitude, initially at x=0 stays until we are at X=0.

Explicitly, the streamline depends on the soliton phase velocity C_1 and on the form of the mean zonal wind U(y). We adopt in this work a basic flow with a horizontal shear as proposed by Rennick (1976) to describe the mid-tropospheric jet in the West African Tropical zone. Based on observations the zonal wind can readily be represented in the functional form

$$U(y) = -U_0 \sin^2\left(\frac{\pi}{L} y\right) \tag{16}$$

where U_0=20m/s is the maximal value of wind at the centre of jet (15°N), L the distance between the Equator (y=0) and 30°N latitude (y=L). This jet corresponds to the one seen in the atmosphere during summer at an altitude of around 3000 m in the Northern African Troposphere. The principal phase velocity is found to be 7.0 m/s (Burpee 1972, Mass 1979, Lenouo and Mkankam 2008). Before examining the influence of the additional wind velocity C_1 in the present theory, let us first consider the case of linear waves.

Analysis of linear effects

In the linear theory case, the solution of equation (1) without the Jacobian term is sought in the normal mode:

$$\Psi(x,y,t) = Y(y) \exp[ik(x-Ct)] \tag{17}$$

Where k is the zonal wavenumber, k=2π/λ, λ the zonal wavelength; Y(y) is the amplitude function which depends only on y and solution to the following equation:

$$Y'' + \left[\frac{\beta - U''}{U - C_0} - k^2\right] Y = 0 \tag{18}$$

This equation differ from equation (8) by the presence of the k^2 term, but it still must verify the boundary conditions Y=0 at y=0 and y=L. The numerical solution of equation (18) is found as earlier by the GAUSS-SEIDEL's relaxation methods.

Figure 3 illustrates the configurations of streamlines in the (X,y) plane obtained from this approximation. We note that the region of instability corresponds to the depression located between two anticyclonics stones, whose centres are along the principal axes of the jet. These streamlines have a quasi-concentric form, on the one hand symmetric respect of the plan passing X=0 and on the other hand to the jet axis.

Nonlinear effects

The streamlines in the case of the weakly nonlinear approximation are presented in figure 4 for different values of the additional wind velocity C_1. We see that this velocity has a predominant role in the configuration of patterns in the domain under consideration.

For C_1=0.05 m.s^{-1} (Fig.4a), the patterns are essentially parallel to the zonal direction. Here, the perturbations are swamped by the mean flow and this explains why for weak value of C_1, one can not observe the track of the wave. The air flow can be assimilated in this case to the displacement of a solid that presents an axis of symmetric.

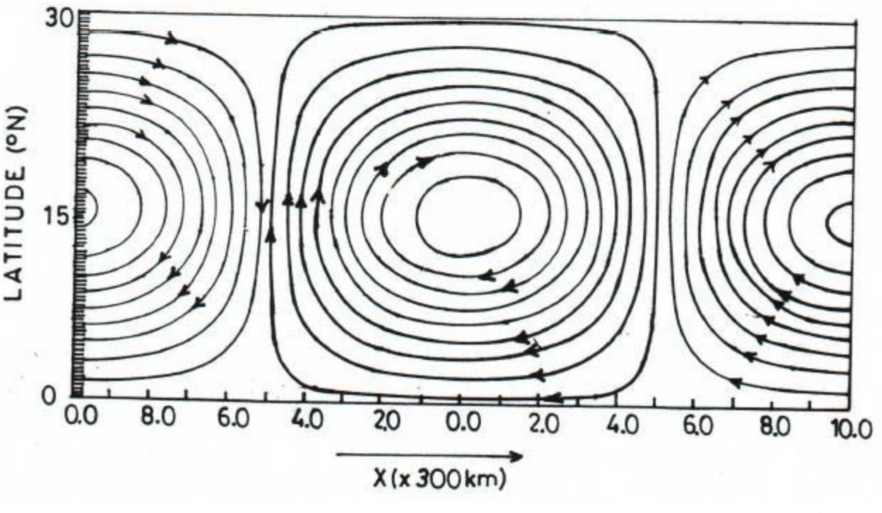

Figure 3: Configuration of streamlines in the case of linear approximation with C_0=7m.s^{-1}

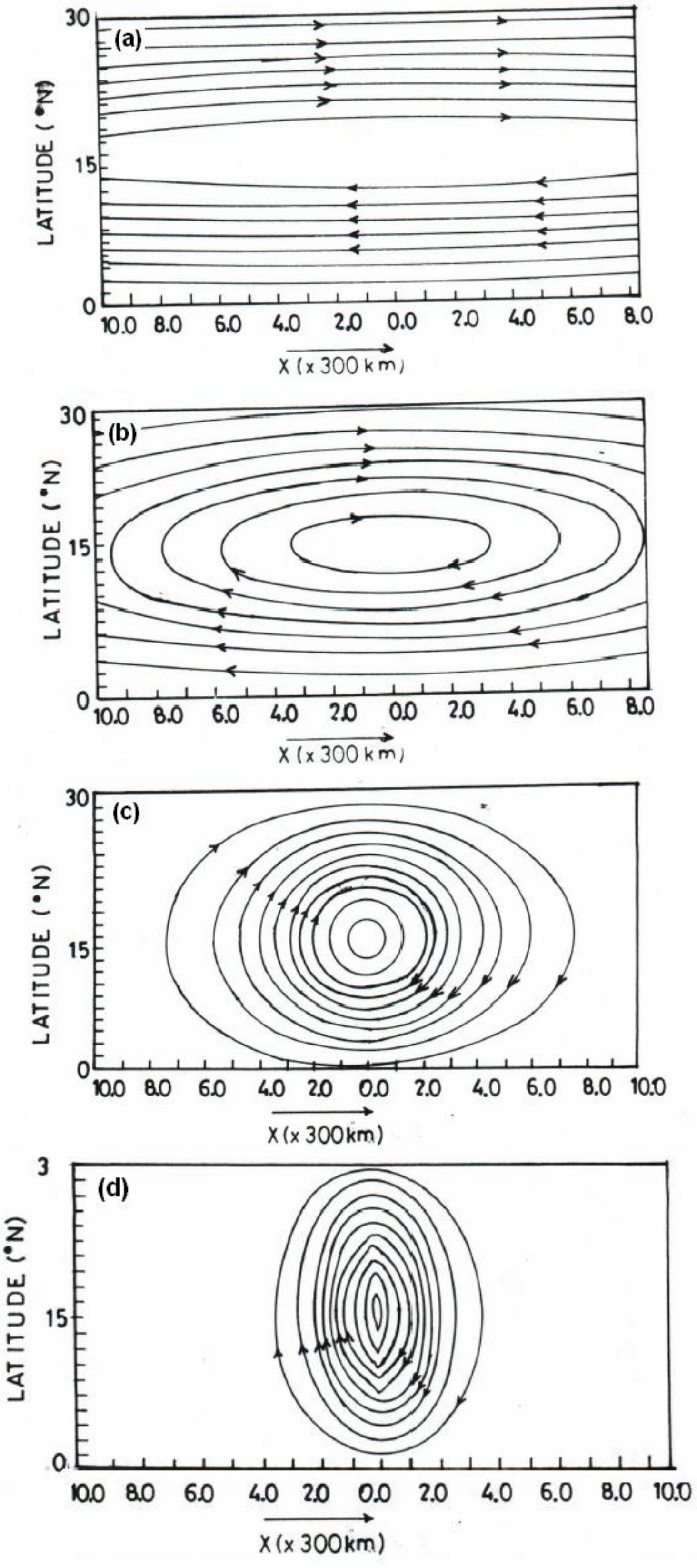

Figure 4: Configuration of streamlines in the case of weakly nonlinear approximation with C_0=7m.s^{-1} and ϵ=0.01 for (a) C_1=0.05m.s^{-1}; (b) C_1=0.5m.s^{-1}; (c) C_1=5m.s^{-1} and (d) C_1=25m.s^{-1}.

When the value of the parameter C_1 is increased, the streamlines have a new configuration as shown in figure 4b. We can deduce that the streamlines tend to unclose and stretch in the zonal direction isolating a depression centred at the region of maximum shear. The presence of a depression characterises the linear effects in the system. The fact that it is presently limited to the maximum disturbance region shows that these effects are in their early stages. This is why the little felt at the boundary of the domain, where only weak deformations of streamlines are observed.

We can continue to increase the value of the phase velocity of the soliton in order to determine a value that for which the weakly nonlinear theory, leads to the same structure of linear waves as given by normal mode theory. Fig. 4c presents the streamlines for C_1=5m.s^{-1}. We note that all the patterns have concentric ovoidal form around the region of maximal instability region where the amplitude of the nonlinear wave is high. The difference with previous configurations is the fact that these patterns are zonally limited at X=±2100 km. Contrary to the streamline of Fig.3, the absence of anticyclonic zone here is due to the shape of the solitary wave amplitude A(x,t), obtained in the weak nonlinear approximation. Since our interest is to study the behaviour of wave around the jet, this result is not in contradiction with those obtained in the case of the linear approximation, but matter confirm that the maximum instability of the jet is located in depressionnary area. As also shown in the Fig.4c, this streamline can be superposed to those given by linear approximation (Fig.3). Hence the nonlinear wave is strongly governed by its linear effects. The first manifestation of the nonlinearity effects appear here, as noted by Kadomek (1979), the presence of a weak nonlinearity in the system can produce important effects capable to countering those due to the dispersion. According to the weakly nonlinear approximation, the soliton result from a balance between linear and nonlinear effects. In other term, it is for the value of C_1 equal to 5m.s^{-1} that the Rossby soliton may be observed. Its profile described by relation (14) is represented in Fig.1.

As the parameter C_1 increases, the nonlinear effects grow and the wave patterns are concentrated around the region where their amplitudes grow (Fig.4d). Here, the streamlines tend to stretch along the meridional direction while being confined in a small zonal domain. This shows that the nonlinear waves became strongly localised.

For energy consideration, we admit the principle that the energy of the perturbation is proportional to the square of amplitude of the wave. So, for weak values of C_1, the energy of the wave is dissipated in the space x-Ct. For C_1=5 m.s^{-1}, we found that the energy spread in the space x-Ct but in a reasonable interval compared to the purely linear case. However, Fig. 4c shows that nonlinearity, though weak, leads to live for the perturbation.

CONCLUSION

We have presented a nonlinear theory to study the evolution of perturbation due to the shear mean wind in the midtropospheric African jet. Its formulation is necessarily complicated, but we have carefully described all the stages which permit to obtain the final result, so that one can use, in some conditions, these results seem applicable to description of Rossby solitary waves. This requires the choice of additional wind speed C_1. The use of Gardner and Murikawa (1965) transformations help us to introduce the phase velocity of the soliton C_1. Its influence on the structure and the amplitude for streamline is important. Hence, the weakly nonlinear approximation through KdV theory explains how the solitary Rossby waves are propagated over West Africa. The weakly nonlinear theory leads to the same structure of linear waves as given by normal mode theory for C_1=5 m.s^{-1} where the presence of a weak nonlinearity in the system can produce important effects capable to countering those due to the dispersion.

In the tropical zone, the cyclones are some time presented as the soliton. Its interesting to confront this theory with observations since the nonlinear amplitude function A(x,t) which is proportional to pressure, presents a maximum when the eastern wave propagation arrives at X=0.

REFERENCES

Abdullah, A.J., 1955: The atmospheric solitary wave. *Bull. Amer. Meteo. Soc.*, **10**, 511-518.

Benney, D.J., 1966: Long nonlinear waves in fluid flows. *J. Math. Phys*., **45**, 52-63.

Burpee, R. W., 1972: The origin and structure of easterly waves in the lower troposphere of North Africa. *J. Atmos. Sci.*, **29**, 77–90.

Dobryshman, E. M., 1982: Theoretical studies of tropical waves. *GATE Pub.,* **25**, 121–177.

Guinn, T.A. and Wayne H. Schubert, 1993: Hurricane spiral bands. *J. Atmos. Sci.*, **50**, 3380-3403.

Holton, J. R., 2004: An introduction to dynamic meteorology. *Inter. Geoph. Series***16**, 4th ed.,pp 535.

Hoskins, B. J. and Ambrizzi, T., 1993: Rossby wave propagation on a realistic longitudinally varying flow. *J. Atmos. Sci*, **50**, 1661– 1671.

Huang, S. and Zhang Ming, 1988: Periodic, solitary and discontinuous periodic solution of nonlinear waves in the atmosphere and their existence. Part I and II. *Scientie Sinica*, Serie B, Vol. **XXXI**, N°12.

Kadomtsev, B. B., 1979: Phénomènes collectifs dans le plasmas. *Ed. MIR*, Moscou, 161–187.

Kaladze, T.D, 2000: New solution for nonlinear pancake solitary Rossby vortices. *Physics Letters A,* **270**. 93–95

Larsen, L.H., 1965: Comments on “Solitary waves in the westerlies”. *J. Atmos. Sci*, **22**, 222-224.

Lenouo A., F Mkankam Kamga and E Yepdjuo, 2005: Weak interaction in the African easterly jet. *Annales Geophysicae*, **23**, 1637–1643.

Lenouo **A.** and F Mkankam Kamga, 2008: Sensitivity of African Easterly Waves to Boundary Layer Condition. *Annales Geophysicae*, **26,** 1355-1363.

Lin, Y.L. and R.C. Goff, 1988: A study of mesoscale solitary wave in the atmosphere originating near a region of deep convection. *J. Atmos. Sci*, **45**, 194-205.

Long, R.R., 1964: Solitary waves in the westerlies. *J. Atmos. Sci*, **21**, 197-200.

Mass, C., 1979: A linear equation model of African wave disturbances. *J. Atmos. Sci*, **36**, 2075–2092.

Luo, D., 2004: A Barotropic Envelope Rossby Soliton Model for Block–Eddy Interaction. Part II: Role of Westward-Traveling Planetary Waves. *J. Atmos. Sci*, **62**, 22-62.

Miles, J.W., 1979: On solitary Rossby waves. *J. Atmos. Sci*, **36**, 1236-1238.

Qiang, Li and David M. Farmer, 2011: The Generation and Evolution of Nonlinear Internal Waves in the Deep Basin of the South China Sea. *J. Phys. Oceanogr.*, **41**, 1345–1363.

Redekopp, L.G and P.D. Weidman, 1978: Solitary Rossby waves in zonal shear flows and their interactions. *J. Atmos. Sci*., **35**, 790-804.

Rennick, A. M., 1976: The generation of African wave. *J. Atmos. Sci*, **33**, 1955–1969.

Rottman, J. W. and F. Einaudi, 1993: Solitary waves in the atmosphere. *J. Atmos. Sci*., **50**, 2116–2131.

Smith, R.K and B.R. Morton, 1984: An observational study of north-easterly “morning glory” wind surges. *Aust. Meteor. Mag*., **32**, 155-175.

Tepper, M., 1950: A proposed mechanism of squall line. The pressure jump line. *J. Meteo*., **7**, 21-29.

APPENDIX

Appendix A: Determination of parameter a_n and b_n

By substituting relation (7) in to equation (6), we obtain

$$\varphi''\frac{\partial A}{\partial\tau}+\left(U-C_0\right)\varphi\frac{\partial^3 A}{\partial\zeta^3}+\varphi\frac{\partial A}{\partial\zeta}A\varphi'''-\varphi' A\varphi''\frac{\partial A}{\partial\zeta}=0 \qquad \text{(A-1)}$$

or

$$\varphi''\frac{\partial A}{\partial\tau}+\left(U-C_0\right)\varphi\frac{\partial^3 A}{\partial\zeta^3}+\left(\varphi\varphi'''-\varphi'\varphi''\right)A\frac{\partial A}{\partial\zeta}=0 \qquad \text{(A-2)}$$

and if we integrate this equation into meridional domain, we have:

$$\int_O^L\varphi''\frac{\partial A}{\partial\tau}dy+\int_0^L\left(U-C_0\right)\varphi\frac{\partial^3 A}{\partial\zeta^3}dy+\int_0^L\left(\varphi\varphi'''-\varphi'\varphi''\right)A\frac{\partial A}{\partial\zeta}dy=0 \qquad \text{(A-3)}$$

by setting $\int_0^L \varphi''\,dy$, (A-3) can be rewritten at last as:

$$\frac{\partial A}{\partial\tau}+a_n\frac{\partial A}{\partial\zeta}+b_n\frac{\partial^3 A}{\partial\zeta^3}=0 \qquad \text{(A-4)}$$

with

$$a_n=\frac{\int_0^L\left[\varphi\varphi'''-\varphi'\varphi''\right]dy}{\int_0^L\varphi''\,dy} \quad \text{and} \quad b_n=\frac{\int_0^L\left(U-C_0\right)\varphi dy}{\int_0^L\varphi''\,dy} \qquad \text{(A-5)}$$

Appendix B: solution of KdV-equation

To solve the equation (10), we introduce the following Galilee transformation:
$s=\zeta-C_1\tau$ (B-1)
In this new referential where the wave is propagated with the velocity C_1, the equation (10) becomes:

$$-C_1\frac{\partial A}{\partial s}+a_nA\frac{\partial A}{\partial s}+b_n\frac{\partial^3 A}{\partial s^3}=0 \qquad \text{(B-2)}$$

The integration of (B-2) with respect to s gives

$$-C_1A+a_n\frac{A^2}{2}+b_n\frac{\partial^2 A}{\partial s^2}=0 \qquad \text{(B-3)}$$

By multiplying this last equation by dA/ds and integrating, we have:

$$-C_1\frac{A^2}{2}+a_n\frac{A^3}{6}+\frac{b_n}{2}\left(\frac{dA}{ds}\right)^2=0 \qquad \text{(B-4)}$$

or

$$\frac{dA}{ds}=\left(\frac{C_1}{b_n}\right)^{1/2}A\sqrt{1-\frac{a_n}{3C_1}A} \qquad \text{(B-5)}$$

By setting $\tilde{A}=a_nA/(3C_1)$, we obtain the integral:

$$\int\frac{d\tilde{A}}{\tilde{A}\left(1-\tilde{A}\right)^{1/2}}=\left(\frac{C_1}{b_n}\right)^{1/2}(s-s_0) \qquad \text{(B-6)}$$

If we assume $s_0=0$, (B-6) can be written as:

$$ArgSech\tilde{A}=\left(\frac{C_1}{b_n}\right)^{1/2}s \qquad \text{(B-7)}$$

And at last:

$$A=\frac{3C_1}{a_n}Sech^2\left[\left(\frac{C_1}{b_n}\right)^{1/2}s\right] \qquad \text{(B-8)}$$

African Journal of Science and Technology (AJST)
Science and Engineering Series Vol. 12, No. 2, pp. 31 - 43

TRANSMISSION DYNAMICS OF HIV/AIDS WITH SCREENING AND NON-LINEAR INCIDENCE

Kung'aro, M.[1], Massawe, E. S.[1] and Makinde, O.D.[2]

[1]Mathematics Department, University of Dar es Salaam,
P. O. Box 35062, Dar es Salaam, Tanzania
[2] Institute for Advance Research in Mathematical Modelling and Computations,
Cape-Peninsula University of Technology, P. O. Box 1906, Bellville 7535, South Africa

ABSTRACT: *This paper examines the transmission dynamics of HIV/AIDS with screening using non-linear incidence. A nonlinear mathematical model for the problem is proposed and analysed qualitatively using the stability theory of the differential equations. The results show that the disease free equilibrium is locally stable at threshold parameter less than unity and unstable at threshold parameter greater than unity. Globally, the disease free equilibrium is not stable due existence of forward bifurcation at threshold parameter equal to unity. However numerical results suggest that screening of unaware infectives has the effect of reducing the transmission dynamics of HIV/AIDS. Also, the effect of non-linear incidence parameters showed that transmission dynamics of HIV/AIDS will be lowered when infectives after becoming aware of their infection, do not take part in sexual interaction or use preventive measures to prevent the spreading of the infection. Numerical simulation of the model is implemented to investigate the sensitivity of certain key parameters on the transmission dynamics of HIV/AIDS with screening using non-linear incidence.*

Keywords*: HIV/AIDS, Screening, Non-linear incidence, Reproduction number, Stability*

INTRODUCTION

HIV/AIDS has become a global problem. Its infection which emerged in 1981 has become a famous sexual transmitted disease throughout the world. It has started getting attention as it has become a death sentence and fear to a lot of people mainly because there is no cure available till to date (Naresh, *et al,* 2008).

HIV belongs to a class of viruses known as retroviruses, which contain ribonucleic acid (RNA) as their genetic material. After infecting a cell, HIV uses an enzyme called reverse transcriptase to convert its RNA into deoxyribonucleic acid (DNA) and then proceeds to replicate it using the cells machinery (Anderson and May R., 1991).

Early detection of HIV through voluntary screening is important for intervention and for reducing HIV transmission. Early identification can provide the opportunity for timely treatment of infected individuals, thus reducing morbidity and mortality. Additionally, the decrease in risky behaviour resulting from HIV counselling and the reduction in infection due to the use of antiretroviral therapy (ART) can translate into a significant benefit from reduced HIV transmission (Tole *et al*, 2009). However, increasing the number of people who know their HIV status especially among most at risk populations through HIV testing and counselling is key to expanding access to HIV prevention, treatment and care. The fundamental principle of HIV testing is that it must be accompanied by basic pre-test information to enable the client make an informed and voluntary decision to be tested.

The essential assumption in most classical compartmental epidemic models is that the individuals are homogeneously mixed and each individual has the same chance of getting infected when a small number of infectives are introduced to the susceptible populations (Yuan and Wang, 2009). The rate of new infections, known as the incidence rate, thus takes the bilinear form (mass action). In reality, populations may not be homogeneously mixed and thus it is more realistic to take heterogeneities in population mixing into consideration in modelling the spread of infectious diseases.

It has been suggested by several authors that the disease transmission process may have nonlinear incidence rate. This allows one to include behavioural changes and prevent unbounded contact rates (Liu *et al*, 1987; Moghadas and Gumel, 2002). A particular example of such an incidence rate is given by $\alpha I^s \big/ \left(1+\beta I^k\right)$, with $s, k, \alpha, \beta > 0$ (Kyrychko and Blyuss, 2005).

Tripathi *et al*. (2007) established and analyzed a mathematical model on the effect of screening of unaware infectives on the spread of HIV infection. However the integration of screening using non-linear incidence rates was not incorporated. In this paper, it is therefore intended to establish and analyze a model which will incorporate the aspect of non-linear incidence in assessing transmission dynamics of HIV/AIDS with screening. We thus study and analyze a deterministic model of Transmission Dynamics of HIV/AIDS with screening using non-linear incidence rates. The model assumes that susceptibles become infected via sexual contacts with both types of infectives and individuals will die due to disease after reaching the full blown AIDS stage.

MODEL FORMULATION

In modelling the disease dynamics, the population is subdivided into four population compartments depending on the HIV status of the individuals: The susceptibles or HIV negatives $S(t)$, HIV positives or infectives who do not know whether they are infected $I_1(t)$, HIV positives or infectives who know that they are infected $I_2(t)$ and those with full blown AIDS $A(t)$ (Tripathi *et a*l, 2007).

In formulating the model, the following assumptions are taken into consideration:

(i) The mode of transmission is assumed to be via heterosexual contacts as this represents the single major primary mode of HIV infection globally,

(ii) Susceptible individuals are considered to be heterogeneously mixed, and it is assumed that unaware and aware infectives will move to full blown AIDS at the rate δ,

(iii) Unaware infectives can be transferred to aware infective class after screening by the rate θ.

(iv) Unaware infectives and aware infectives can infect susceptibles at different rates β_1 and β_2 respectively,

(v) Individuals will die due to disease after reaching the full blown AIDS stage by the rate α,

(vi) The population under consideration comprise persons with at least 18 years of age,

(vii) All parameters and variables of the model are considered to be positive.

Taking into account of the above consideration, we then have the following transfer diagram of the model:

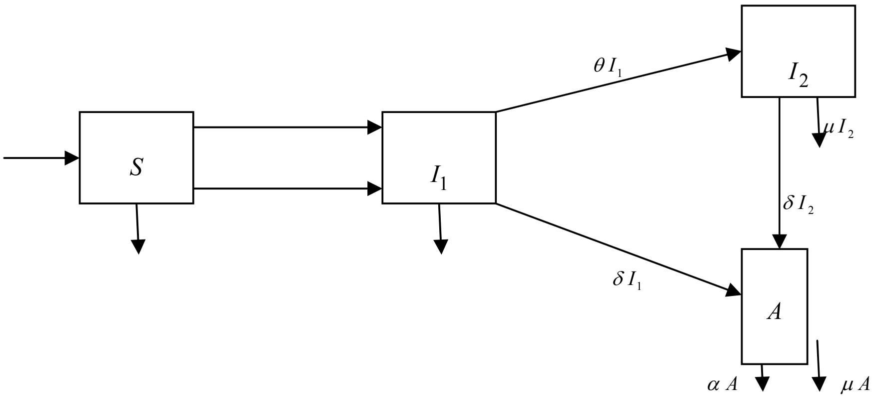

Figure 1: A compartmental model for transmission dynamics of HIV/AIDS

The model is thus governed by the following system of non linear ordinary differential equations:

$$\frac{dS}{dt}=\lambda N-\left[\frac{\beta_1 I_1}{N+a_1 I_1}+\frac{\beta_2 I_2}{N+a_2 I_2}\right]S-\mu S$$

$$\frac{dI_1}{dt}=\left[\frac{\beta_1 I_1}{N+a_1 I_1}+\frac{\beta_2 I_2}{N+a_2 I_2}\right]S-\left(\theta+\delta+\mu\right)I_1 \qquad (1)$$

$$\frac{dI_2}{dt}=\theta I_1-\left(\delta+\mu\right)I_2$$

$$\frac{dA}{dt}=\delta I_1+\delta I_2-\left(\alpha+\mu\right)A$$

with nonnegative initial conditions

$$S(0)>0,\ I_1(0)\geq 0,\ I_2(0)\geq 0,\ A(0)>0$$

where

λ is the recruitment rate,

α is the disease (AIDS) related death rate,
μ is the background mortality rate unrelated to HIV/AIDS,
θ is the transfer rate from the asymptomatic to the symptomatic compartment,
δ is the AIDS progression rate,

$\beta_i\left(i=1,2\right)$ are the per capital contact rates for susceptible with unaware infectives and aware infectives respectively,

$a_i\left(i=1,2\right)$ are non-linear incidence parameters with respect to unaware and aware infectives respectively.

The total population at any time t is then given by

$$N(t)=S(t)+I_1(t)+I_2(t)+A(t).$$

It is reasonable to assume that $\beta_2<\beta_1$ because on becoming aware of the infection, one may choose to use preventive measures and change behaviour.

Since the variable A of system (1) does not appear in the first three equations, in the subsequent analysis we can analyze qualitatively the following subsystem (Cai *et al*, 2009):

$$\frac{dS}{dt}=\lambda N-\left[\frac{\beta_1 I_1}{N+a_1 I_1}+\frac{\beta_2 I_2}{N+a_2 I_2}\right]S-\mu S$$

$$\frac{dI_1}{dt}=\left[\frac{\beta_1 I_1}{N+a_1 I_1}+\frac{\beta_2 I_2}{N+a_2 I_2}\right]S-\left(\theta+\delta+\mu\right)I_1 \qquad (2)$$

$$\frac{dI_2}{dt}=\theta I_1-\left(\delta+\mu\right)I_2.$$

In terms of the total population N, the subsystem model becomes

$$\frac{dN_1}{dt}=\lambda N-\mu N_1-\mu\left(I_1+I_2\right)$$

$$\frac{dI_1}{dt}=\left[\frac{\beta_1 I_1}{N+a_1 I_1}+\frac{\beta_2 I_2}{N+a_2 I_2}\right]S-\left(\theta+\delta+\mu\right)I_1 \qquad (3)$$

$$\frac{dI_2}{dt}=\theta I_1-\left(\delta+\mu\right)I_2$$

where

$$N_1\left(t\right)=S\left(t\right)+I_1\left(t\right)+I_2\left(t\right)$$

The system (3) is well posed for $N_1\left(0\right)>0$, since solutions remain the non-negative initial conditions.

Model analysis

The nonlinear system in Equation (3) will be qualitatively analyzed so as to find the conditions for existence of stability disease free equilibrium points (Gomes *at el*, 2004). Analysis of the model allows us to determine the impact of screening and non-linear incidence. Threshold condition(s) which govern elimination or persistence of HIV/AIDS transmission will be determined and studied. Also on finding the reproductive number R_0 one can determine if the disease become endemic in a population or not.

Positivity of solutions

It is necessary to prove that all solutions of system (3) with positive initial data will remain positive for all times $t > 0$. This will be established by the following theorem.

Theorem 1

Let $S(0) > 0$, $I_1(0) \geq 0$, $I_2(0) \geq 0$, . Then solutions $S(t)$, $I_1(t)$ and $I_2(t)$ of system (3) are positive $\forall t \geq 0$.

Proof

To prove theorem 1, we use all equations of the model (3). From the system (3), we obtain the inequality expression

$$\frac{dI_1}{dt} \geq -(\theta + \delta + \mu) I_1$$

which gives

$$I_1(t) \geq C \exp\{-(\theta + \delta + \mu)t\} > 0.$$

As $t \to \infty$ we obtain $0 \leq I_1(t) \leq 1$. Hence all feasible solution of system (3) enter region $\Gamma = \{(S,\ I_1,\ I_2,)\}$. Similar proofs can be established for the positivity of the other solution.

Disease-free equilibrium point (DFE) and its stability

The disease free equilibrium of the model (3) is obtained by setting

$$\frac{dS}{dt} = \frac{dI_1}{dt} = \frac{dI_2}{dt} = 0. \tag{4}$$

At disease-free equilibrium, we have

$$I_1 = I_2 = 0$$

so that model (3) becomes

$$\lambda N - \mu S = 0 \tag{5}$$

Therefore, the disease-free equilibrium (DFE) denoted by E_0 of the model (3) is given by

$$E_0 = (S,\ 0,\ 0) = \left(\frac{\lambda N}{\mu},\ 0,\ 0\right),\ \mu > 0 \tag{6}$$

Local stability of DFE

The disease free equilibrium of the model (3) was given by

$$E_0 = (S,\ 0,\ 0) = \left(\frac{\lambda N}{\mu},\ 0,\ 0\right) \tag{7}$$

In order to assess the local stability of the E_0 established by next generation method on the system (3), computation of basic reproduction number is essential. The basic reproduction number R_0 is defined as the effective number of secondary infections caused by typical infected individual during his entire period of infectiousness (Diekman *et al*, 1990). This definition is given for the models that represent spread of the infection in a population. It is obtained by taking the dominant eigenvalue (spectral radius) of

$$\left[\frac{\delta F_i(E_0)}{\delta x_j}\right] \cdot \left[\frac{\delta V_i(E_0)}{\delta x_j}\right]^{-1} \tag{8}$$

where

F_i is the rate of appearance of new infection in compartment i,

V_i^+ is the transfer of individuals into compartment i,

V_i^- is the transfer of individuals out of compartment i by all other means,

E_0 is the disease-free equilibrium.

Consequently

$$\begin{pmatrix} f_1 \\ f_2 \end{pmatrix} = \begin{pmatrix} \dfrac{\beta_1 I_1 S}{N + a_1 I_1} + \dfrac{\beta_2 I_2 S}{N + a_2 I_2} \\ 0 \end{pmatrix}$$

By linearization approach, the associated matrix at disease-free equilibrium is given by

$$\mathbf{F}=\begin{pmatrix}\frac{\delta f_1}{\delta I_1}(E_0) & \frac{\delta f_1}{\delta I_2}(E_0)\\ \frac{\delta f_2}{\delta I_1}(E_0) & \frac{\delta f_2}{\delta I_2}(E_0)\end{pmatrix} \tag{9}$$

which gives

$$\mathbf{F}=\begin{pmatrix}\frac{\beta_1\lambda}{\mu} & \frac{\beta_2\lambda}{\mu}\\ 0 & 0\end{pmatrix}$$

and

$$\begin{pmatrix}v_1\\ v_2\end{pmatrix}=\begin{pmatrix}(\theta+\delta+\mu)I_1\\ -\theta I_1+(\delta+\mu)I_2\end{pmatrix}$$

Again by linearization we get

$$\mathbf{V}=\begin{pmatrix}\frac{\delta v_1}{\delta I_1}(E_0) & \frac{\delta v_1}{\delta I_2}(E_0)\\ \frac{\delta v_2}{\delta I_1}(E_0) & \frac{\delta v_2}{\delta I_2}(E_0)\end{pmatrix}$$

yielding

$$\mathbf{V}=\begin{pmatrix}\theta+\delta+\mu & 0\\ -\theta & \delta+\mu\end{pmatrix}$$

with

$$\mathbf{V}^{-1}=\begin{pmatrix}\frac{1}{\theta+\delta+\mu} & 0\\ \frac{\theta}{(\theta+\delta+\mu)(\delta+\mu)} & \frac{1}{\delta+\mu}\end{pmatrix}.$$

Therefore

$$\mathbf{FV}^{-1}=\begin{pmatrix}\frac{\beta_1\lambda}{\mu(\theta+\delta+\mu)}+\frac{\beta_2\lambda\theta}{\mu(\theta+\delta+\mu)(\delta+\mu)} & \frac{\beta_2\lambda}{\mu(\delta+\mu)}\\ 0 & 0\end{pmatrix}$$

The eigenvalues of $\mathbf{FV}^{-1}$ are

$$\left(0,\ \frac{\beta_1\lambda}{\mu(\theta+\delta+\mu)}+\frac{\beta_2\lambda\theta}{\mu(\theta+\delta+\mu)(\delta+\mu)}\right)$$

The basic reproduction number for the model (3) with non-linear incidence denoted by R_0 is

$$R_0=\frac{\beta_1\lambda(\delta+\mu)+\beta_2\lambda\theta}{\mu(\theta+\delta+\mu)(\delta+\mu)} \tag{10}$$

Thus the disease free equilibrium of the transmission dynamics of HIV/AIDS model (3) with screening and non-linear incidence is locally asymptotically stable if $R_0<1$ and unstable if $R_0>1$. This can be realized when one tries to assess the contribution of I_1 and I_2 in terms of β_1 and β_2 respectively from equation (10) above. Let

$$R_{0a}=\frac{\beta_1\lambda}{\mu(\theta+\delta+\mu)} \text{ and}$$

$$R_{0b}=\frac{\beta_2\lambda\theta}{\mu(\theta+\delta+\mu)(\delta+\mu)} \tag{11}$$

where

$$R_0=R_{0a}+R_{0b}. \tag{12}$$

It is clear from equations (11) that $R_{0a}>R_{0b}$ which implies that for large infective population, the unaware infectives I_1 have a significant contribution on the transmission of the infection and keep the disease endemic in the population via β_1 compared to aware infectives I_2 via β_2.

Endemic equilibrium

To find endemic equilibrium, denoted by $E_1\left(I_1^*,I_2^*,S_1^*\right)$, we set the right hand side of each equation of the system (3) equal to zero and express the other dependent variables in terms of I_1^* at equilibrium point and to obtain

$$I_2^*=\frac{\theta I_1^*}{(\delta+\mu)},$$

Substituting I_2^* and S^* in the second equation of (3) at steady state, we obtain after some calculations that I_1^* must satisfy the following equation

$$S^* = \frac{\left[N(\delta+\mu)+a_2\theta I_1^*\right]\left[N+a_1 I_1^*\right]\lambda N}{I_1^{*2}\left(\mu a_1 a_2\theta+\beta_2 a_1\theta+\beta_1 a_2\theta\right)+I_1^*\left(\mu N\theta a_2+\mu N\delta a_1+\mu^2 N a_1+N\delta\beta_1+N\beta_1\mu\right)+N^2\left(\mu\delta+\mu^2\right)} \tag{12}$$

$$I_1^* f\left(I_1^*\right) = I_1^*\left(A I_1^{*2} + B I_1^* + C\right) = 0 \tag{13}$$

where

$$A = \beta_1 a_2\theta^2 + \mu a_1 a_2\theta^2 + \beta_2 a_1\theta^2 + \mu^2 a_1 a_2\theta + \delta\mu a_1 a_2\theta + \delta\beta_1 a_2\theta$$
$$+\delta\beta_2 a_1\theta + \mu\beta_1 a_2\theta + \mu\beta_2 a_1\theta$$

$$B = \beta_2 N\theta^2 + \mu N a_2\theta^2 + \beta_1 N\delta^2 + \mu^3 a_1 N + \beta_1 N\mu^2 + \delta^2 a_1\mu N$$
$$+\mu^2 N a_2\theta + \mu a_1 N\delta\theta + \mu^2 N a_1\theta + \beta_1\theta N\delta + \beta_1 N\mu\theta + \delta\mu N a_2\theta$$
$$+2\delta a_1 N\mu^2 + 2\delta\beta_1 N\mu + \delta\beta_2\theta N + \mu\beta_2\theta N - \theta\beta_1\lambda N a_2 - \theta\beta_2\lambda N a_1$$

$$C = \mu N^2\delta^2 + 2\delta N^2\mu^2 + \theta N^2\mu^2 + N^2\mu^3 + \theta\mu N^2\delta$$
$$-\beta_1\lambda\delta N^2 - \beta_1\lambda\mu N^2 - \beta_2\theta\lambda N^2$$

$$f_1\left(I_1^*\right) = \frac{\beta_1 I_1^*}{N + a_1 I_1^*}$$

From equation (13) it can be seen that the root for $I_1^* = 0$ corresponds to the DFE. The relationship $f\left(I_1^*\right) = 0$ corresponds to the existence of multiple equilibria. The model also exhibits a forward bifurcation for some estimated parameters as seen in figure 2 below:

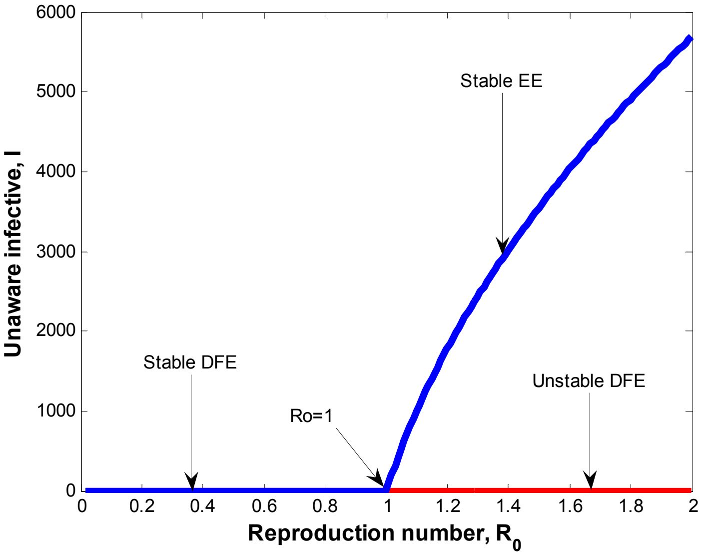

Figure 2 Forward bifurcation in the (R_0, I) plane

From the bifurcation figure, it can be seen that, the EE point being locally asymptotically stable, the disease can invade the population and transmission dynamics can persist if no purposive interventional measures are subjected to the population for the purpose of reducing the disease or if possible to eradicate it. Hence control of the epidemic depends on the enhancement of the behavioural changes among the subgroups of populations where the spreading of the disease occurs and optimum use of the available therapy for those infected.

Global stability analysis

The global stability analysis of the epidemic models is generally difficult to carry out. Consequently, the literature on global analysis of dynamical systems is very little. Busenberg and van den Driessche (1990) proposed an elegant technique for proving the non-existence of certain type of solutions such as periodic orbits, homoclinic orbits and polygons associated with SIR models. In this regard, using the Busenberg and van den Driessche technique it can be shown that the global stability analysis of model (3) is given as follows. We set

$$\Gamma_1=\left\{(S,I_1,I_2)\in\Gamma : S+\frac{(\mu+\delta)}{\mu}I_1+\frac{(\mu+\delta)}{\mu}I_2>\frac{\lambda N}{\mu}\right\}$$

$$\Gamma^*=\left\{(S,I_1,I_2)\in\Gamma : S+\frac{(\mu+\delta)}{\mu}I_1+\frac{(\mu+\delta)}{\mu}I_2=\frac{\lambda N}{\mu}\right\}$$

$$\Gamma_2=\left\{(S,I_1,I_2)\in\Gamma : S+\frac{(\mu+\delta)}{\mu}I_1+\frac{(\mu+\delta)}{\mu}I_2<\frac{\lambda N}{\mu}\right\}$$

Thus Γ_1, Γ^*, Γ_2 are pair wise disjoint subsets of Γ, and $\Gamma=\Gamma_1\cup\Gamma^*\cup\Gamma_2$.

Let $N_1=S+I_1+I_2,\ (S,I_1,I_2)\in\Gamma$. From system (3), the equation for the total population N_1 satisfies

$$\frac{dN_1}{dt}=\lambda N-\mu N_1-\delta(I_1+I_2). \tag{14}$$

Consequently, in $\Gamma_1,\Gamma^*,\Gamma_2$, we have $\frac{dN_1}{dt}>0,\ \frac{dN_1}{dt}=0,\ \frac{dN_1}{dt}<0$, respectively. It then follows that Γ^* is a positively invariant set in Γ.

Numerical simulations

In order to illustrate some of the analytical results of the study, numerous numerical simulations of the model (3) are carried out using a set of reasonable parameter values given in table 1 below and the following estimated initial conditions $S=500,\ I_1=250,\ I_2=100$

However these parameters may (or may not) be biologically feasible.

Figure 4.1 below shows variation of the S, I_1 and I_2 with time when $R_0=0.7058$,

Table 1: Parameter values used in numerical simulations

Parameter symbol	**Parameter value $(yr)^{-1}$**	**Source**
λ	0.0100	Estimated
μ	0.0200	Tripathi *et al* (2007)
θ	0.6000	Issa *et al* (2010)
δ	0.0500	Nyabadza *et al* (2010)
α	1.0000	Naresh *et al* (2009)
a_1	0.0900	Estimated
a_2	0.0100	Estimated
β_1	0.8600	Estimated
β_2	0.1500	Tripathi *et al* (2007)

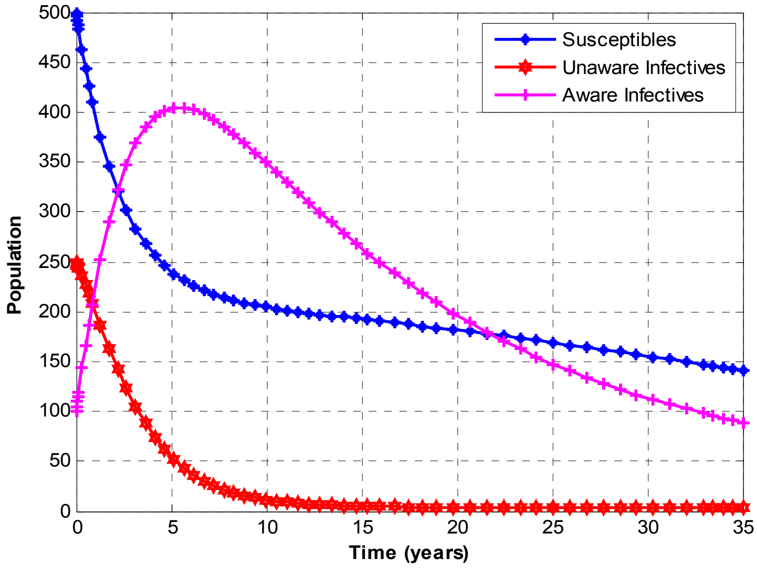

Figure 4.1: General variation of population in different classes

In Figure 4.1 it is seen that the number of susceptibles and unaware individuals decrease with time. Initially aware infective class increase with time and then reaches its equilibrium position. This is due to an increase in screening rate in which unaware individuals are moved to this class by the rate θ. This explains why unaware infectives decrease rapidly to zero, susceptibles decrease to a certain level but do not diminish to zero. This means that we can control the epidemic through promoting behavioural change and taking necessary precautions while having sexual interaction.

As it can be seen in Figure 4.2, when screening rate becomes zero, the infectives who do not know that they are infected, continue maintaining sexual relationship in the community leading to persistance of the disease as far as $R_0 > 1$. But when the rate of screening increases, there is a possibility of the disease to cease because individuals may use prenventive measures after knowing their HIV status.

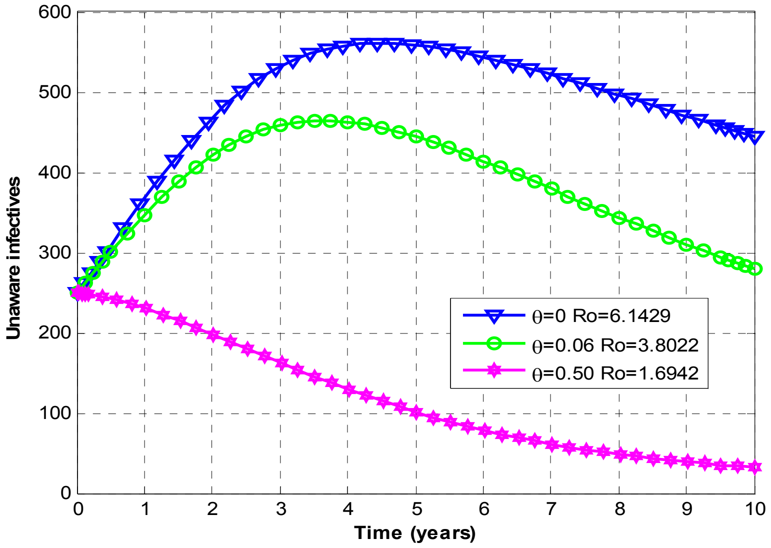

Figure 4.2 : Variation of unaware infectives with time for different values of θ

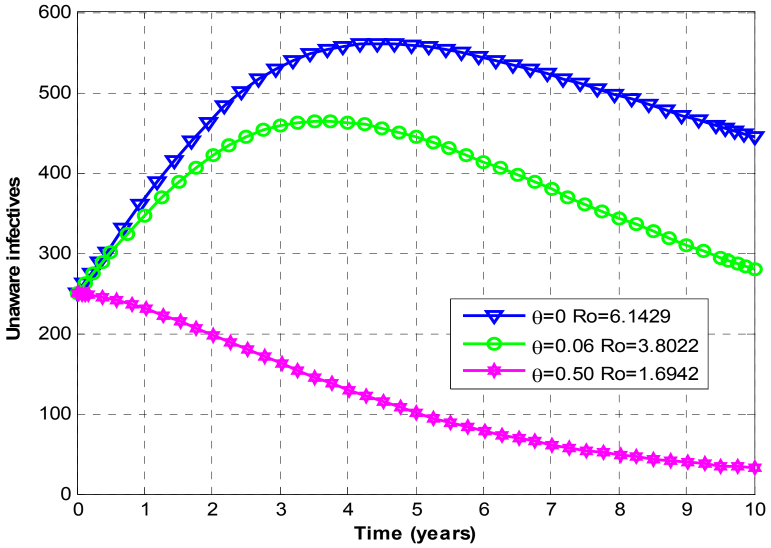

Figure 4.3 : Variation of aware infectives with time for different values of θ.

Figure 4.3 reveals that if screening rate θ is increased, aware (symptomatic) individuals also increase. Symptomatic infectives after knowing their HIV status may change their behaviour and continue surviving and thus reduce the AIDS population. It is therefore suggested that, to minimize the spread of the disease, the population under consideration should be encouraged to attend medical screening for the purpose of changing their behaviour and use preventive measures.

Figures 4.4 (a) and 4.4(b) above show the role of contact rate β_2 of aware HIV infectives and susceptible respectively. It can be seen that as aware HIV infectives continue maintaining sexual interaction without exposing themselves, the susceptible population decrease rapidly leading to an increase in aware HIV infectives thus increasing transmission dynamics and hence disease persists in the population as the number of AIDS individuals increase.

The effect of non-linear incidence parameter $a_{i=1,2}$, are observed in the following figures using the following estimated initial conditions $S = 1500,\ I_1 = 700$ and $I_2 = 300$.

Figure 4.5 assess the impact of non-linear incidence parameters against susceptibles. As it can be seen from the figure, the susceptibles decrease very slowly with time for a very high non-linear incidence rate. This means that if the infected individuals manage to change their behaviour and stop spreading the disease, the epidemic can go to extinction as long as very few susceptibles are infected.

Figure 4.6 shows that infectives who are not aware of their status decrease rapidly whenever saturation effects are achieved, that is conditions under which the disease can persists in the population are well known to them. Intervention strategies are then used to infected individuals and behavioural changes are well achieved within the society.

The rate of new infection plays a very important role in the investigation of disease dynamics. As seen in figure 4.7, if aware infected individuals do not interact with others, that is, non-linear incidence rate is zero, the number of infected individuals increase rapidly with time hence increasing transmission dynamics. However, the speed of increasing changes if infected individuals interact with others and positive response to intervention programs are effective.

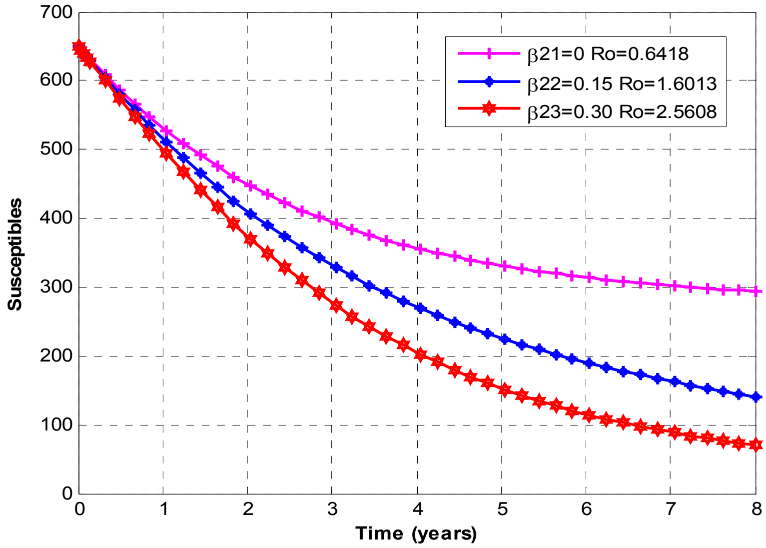

Figure 4.4(a) **Variation of sucseptibles for different values of** β_2

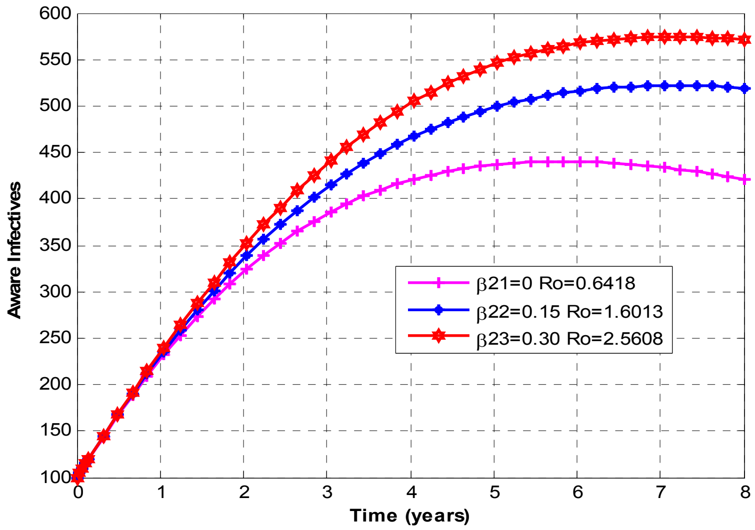

Figure 4.4(b): Variation of aware infectives for different values of β_2

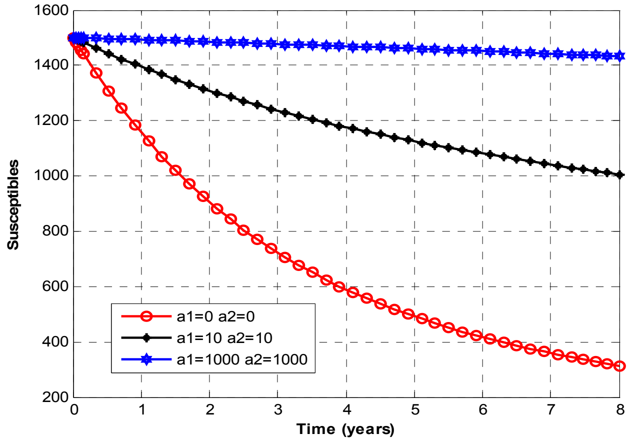

Figure 4.5: Variation of susceptible individuals for different values of $a_{i=1,2}$

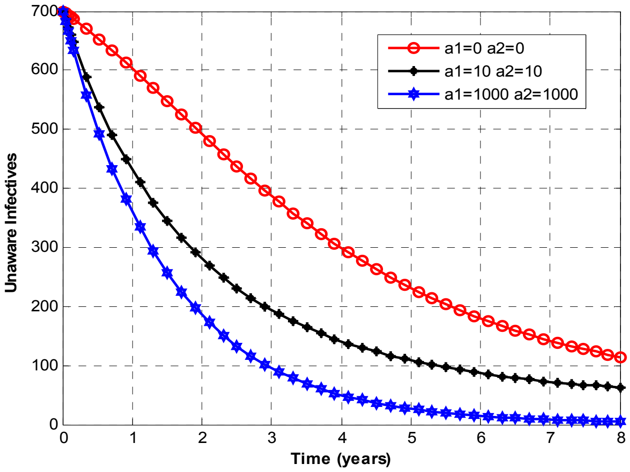

Figure 4.6: Variation of unaware infectives for different values of $a_{i=1,2}$

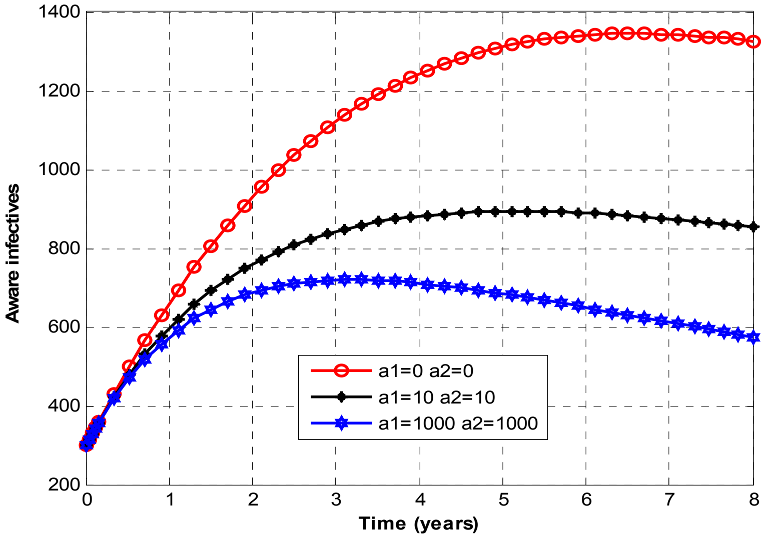

Figure 4.7: Variation of aware infectives for different values of $a_{i=1,2}$

Thus, to maintain the spread of the epidemic at control, the detected infective individuals should be provided with thorough education with respect to their behavioural changes so as to either abstain from sexual interaction or use preventive measures to stop spreading the infection.

DISCUSSION AND CONCLUSION

In this paper, a non-linear mathematical model has been established to study the transmission dynamics of HIV/AIDS with screening and non-linear incidence. The main objective of the study was to assess the transmission dynamics of HIV/AIDS with screening using non-linear incidence. In the study it was assumed that there is no vertical transmission of the disease and mode of transmission is assumed to be via heterosexual contacts. Susceptibles are considered to be heterogeneously mixed and disease related death rate is assumed to occur to individuals after reaching the full-blown AIDS stage. Both qualitative and numerical analyses of the model were done. Qualitative analysis of the model involved computation of the basic reproduction number. The model showed that the disease free equilibrium is locally stable at threshold parameter less than unity and unstable at threshold parameter greater than unity, but globally the disease free equilibrium is not stable due existence of forward bifurcation at threshold parameter equal to unity. Also the model analysis showed the existence of unique endemic equilibrium, that is, locally stable under certain conditions when the threshold parameter exceeds unity due to existence of forward bifurcation at threshold parameter equal to unity. The endemic equilibrium is found to be globally stable under certain conditions.

A numerical study of the model was performed to see the effects of certain key parameters on the spread of the disease. The analysis shows that the screening of unaware HIV infectives and treatment of screened HIV infectives have the effect of reducing the transmission of the disease. It is observed that when the screened infectives and treated infectives do not participate in the transmission of the infection, the AIDS population is significantly reduced in comparison to the case where there is no screening and treatment. In the absence of screening, the endemicity of the infection increases results in the increase of AIDS population.

Based on the results of the study, it is concluded that the most effective approach that can be used to possibly reduce transmission dynamics of the disease and lower the incidence rate is emphasis on information campaign in order to reduce HIV prevalence. Furthermore people should be educated and be aware of preventive measures for the the spread of the disease to be under control. Thus, education campaign must reach the community at all social levels, especially in lower classes and to the high risk groups so as to increase the awareness about the disease and protection measures so as to enhance the control of the disease. The HIV/AIDS eradication remains a challenge to all parts of the world particularly in most developing countries. Hence, there is a need to strengthen the control strategies at hand as well as putting more emphasis on the behavioural changes among individuals.

REFERENCES

Anderson R. M. and May R. M., Infectious diseases of humans, dynamiccs and control. Oxford University Press, pp 237-239, 1991

Busenberg S. and van den Driessche P., Analysis of a disease transmission model in a population with varying size, J. Math. Biol. 28, pp. 257-270, 1990.

Cai L., Xuezhi L., Ghosh M and Guo B., “Stability analysis of an HIV/AIDS epidemic model with treatment”, Journal of computational and applied mathematics, 229, pp. 313-323, 2009.

Diekmann O., Heesterbeek J.A.P. and Metz J.A.P., On the definition and computation of the basic reproduction ratio in the model of infectious disease in heterogeneous populations, Journal of Math. Biol. 2(1), 265-382, 1990.

Driessche, V. P., Some epidemiological models with non-linear incidence, J Math.Biol., 29: pp. 271-287, 1991.

Gomes M. G. M., White L. J., Medley G. F., Infection, reinfection, and vaccination under suboptimal immune protection: Epidemiological perspectives, J. Theor. Biol. 228, pp. 539-549, 2004.

Issa S., Modelling the effect of screening on the spread of HIV infection in a homogeneous population with infective immigrants., Scientific Research and Essays, Vol. 6(20), pp. 4397-4405, 2010.

Kyrychko Y. N and Blyuss, K. B., Global properties of a delayed SIR model with temporary immunity and nonlinear incidence rate. Nonlinear analysis: Real world applications 6, pp. 495-507, 2005.

Liu W. M., Hetchote H. W and Levin S. A., Dynamical behaviour of epidemiological models with non-linear incidence rates, J. Math. Biol. 25 pp. 359-380, 1987.

Moghadas S. M. and Gumel A. B., Global stability of a two-stage epidemic model with generalized non-linear incidence”. Mathematics and computers in simulation, 60, pp. 107–118, 2002.

Naresh R., Tripathi A., Biazar J. and Sharma D., Analysis of the effects of vaccination on the spread of AIDS epidemic using a domian decomposition method”. In nature science and technology yearbook 2008/2009, M. Ratiqul Islam (Ed), Nova science publishers, Inc, NY, 2008.

Nyabadza, F., Chiyaka, C., Mukandavire, Z. and Musekwa, S. D. H., Analysis of an HIV/AIDS model with public health information campaigns and individual withdrawal”. Journal of Biological Systems, Vol. 18, No 2, pp. 1-19, 2010.

Tole S. P., Sanders, G. D., Bayoumi A. M., Galvin C. M., Vinichenko T. N., Brandeau M. L., Owens D. K., Cost-effectiveness of voluntary HIV screening in Russia, International journal of STD & AIDS, Vol 20, 2009.

Tripathi A., Naresh R and Sharma D., Modelling the effect screening of unaware infectives on the spread of HIV infection”. Applied mathematics and computation 184, pp. 1053-1068, 2007.

Yuan Z and Wang L., Global stability of epidemiological models with group mixing and nonlinear incidence rates. Nonlinear analysis: Real world applications, 11, pp. 995-1004, 2009.

African Journal of Science and Technology (AJST)
Science and Engineering Series Vol. 12, No. 2, pp. 44 - 54

COMPARATIVE STUDY OF THE EFFECTS OF TREATMENT TECHNIQUES ON THE THERMAL AND FRICTIONAL PROPERTIES OF KENAF (*Hibiscus canabinus*) FIBRE REINFORCED BRAKE PADS

Namessan, N.O.[1], Maduako, J.N.[2] and Iya, S.[2]

[1]Department of Agronomy, Taraba State University, P.M.B 1167 Jalingo, Nigeria

[2]Department of Agricultural and Environmental Engineering,
Modibbo Adama University of Technology, Yola

Email address: naneekee@yahoo.com

ABSTRACT: Asbestos fibre has been used as the traditional base material in brake pads manufacture, but due to its health hazard, non-renewability, cost, non-biodegradability and difficulty in processing, its replacement has been sought. This paper reports the effects of some fibre treatment techniques namely: mercerization, acetylation and semi-carbonisation on the performance of Kenaf fibres. The treated kenaf fibres which are considered biodegradable, cost effective, renewable and user friendly have been used as a possible base friction material for brake pad production. Results indicated that the four kenaf brake pad samples behave differently during during performance evaluation. semi-carbonized samples had high thermal conductivity with an average value of 0.6215 W/m. K than all the samples investigated in this study.

Keywords: *treatment techniques, kenaf fibre, comparative study, brake pads, thermal properties*

INTRODUCTION

Brake pads for an automotive brake system are friction complex composites because they contain numerous ingredients that are diverse in physical, mechanical and chemical properties. These brake pads or friction composites comprise many disparate ingredients such as binders, fibres and fillers. According to Marthur et al (2004), asbestos fibres, which occurred naturally as mineral, have been used as traditional fibrous ingredient to reinforce the constituents in the friction material or to provide mechanical strength and also to inhibit catastrophic failure of the structure. However, due to its non-biodegradability, non-renewability, difficulty in processing, high cost, high density and most especially its risk of causing cancer, asbestos – based friction materials were banned and the search for safer and cheaper alternative sources started as reported by NICNAS (1999) and Warren (1992). Several treatment techniques intended to improve the natural fibre-matrix adhesion in brake pad composites were reported in literature. Some of the techniques considered in this paper are mercerisation, acetylation and semi-carbonisation of kenaf fibre as compared to using the crude. The objectives of this study is to compare the effects of these fibre treatment techniques on the physical properties (namely; density, water absorption and porosity) of Kenaf Brake Pad samples.

Materials and Methods

Materials for kenaf brake pad production

The materials used in this study include binder or polyester, fillers (rubber crumbs, fine grain iron filings, graphites, barium sulphate), rolls of decorticated kenaf fibre, sodium hydroxide, ammonium oxalate, hydrochloric acid, hydrogen peroxide, tools and equipment include; furnace, oven, drier, hardness tester, compression moulding rig, friction test rig, impact tested, digitizer, camera fitted light microscope, microtome, stop watch, weighing balance and intsrone machine.

2.1.1 Binder

The Unsaturated Polyester Binder that was used was obtained from the Northern Scientific Laboratory Located here in Yola.Ten litres of this binder were purchased for the purpose of this research.

Fillers

Rubber crumbs

These are the other black particles that are seen in commercial brake pads. They are produced from scrap rubber from used tires of 50 μm and are relatively inexpensive. The low specific weight of rubber was an advantage in the final product. In this work 500 g of rubber crumbs was ground to 0.5 mm particle size and was used.

Fine grained metal iron

Fine grain metal iron or iron powder was used in this research as an abrasive. About 1.5 kg of fine-grain metal iron was sieved which was obtained as waste from Machine Shops in Jimeta, Yola. This was sieved into fine grain of 2 μm size

Graphite

Graphite occurs naturally in places like Gayama village in Taraba State, Nigeria. From this village, which is about 289 km from the state capital, Jalingo, 1.2 kg of graphite stone was mined or dug from the deposit for the purpose of this study. Thereafter, it was milled and the product, which is a fine powder, was sieved through a 200 mesh (75 um).

Barium sulphate

Like graphite, Barium Sulphate also called barite was obtained locally from the mines at Lau village of Taraba State. This filler was ground into powder by means of a plate mill; thereafter it was sieved through a 345 mesh (5 μm). A Total of 1.5 kg of this material was used in this study.

Kenaf fibre

Ten rolls of decorticated Kenaf fibre were used in this study, it was procured from Jimeta Market, Yola. These fibres have been decorticated, dried and packed in form of rolls. The material represents a matured fibre and the best of its type available in the locality. These fibres were purified and transformed into better fibre through some innovative chemical treatments discussed previously. Using a plate mill, I kg each of the four fibre Treatments was ground and sieved into an average length of 2 - 4 mm and an average diameter of 12 ɥm. According to Jang *et al* (2001and 2005); Marthur *et al* (2004), 10 % - 20% fibre reinforcement was used in brake padding (Pre trials to determine the fibre volume fraction were also carried out). Thereafter, 15% by weight of kenaf fibre was considered adequate for reinforcement in this study.

Methods

Acetylation of kenaf fibre.

To 1 g of mercerized fibre, 5.5 cm^3 of acetic acid; 2.5 cm^3 acetic anhydride 0.65 cm^3 conc. H_2SO_4 were added. The content was warmed gently to 45 ^0C for 1 h. 0.65 cm^3 of H_2SO_4 was again added and stirred using a magnetic stirrer at 43-45 ^0C for another 1 h. The dark colored solution was poured into 50 cm^3 of water and allowed to stand for 48 h. The precipitate was dried and the yield determined. The water absorptions characteristics was conducted on the acetylated fibre samples

Surface modification by mercerization.

About five batches of 1.0 g each of 10% treated ammonium oxalate and 10% hydrogen peroxide and bleached samples of cellulose fibre were immersed in beakers containing 10%, 15% 18%, 22% and 25% sodium hydroxide concentrations. The temperatures in these beakers were kept at 5^0C by means of ice blocks for a period of 45 mins. Thereafter mercerized samples were washed very thoroughly in 5% solution of acetic acid. The water absorptions characteristics was conducted on the mercerised fibre samples

Surface modification by semi – carbonization or heat treamtent

Crude fibre having been retted and bleached was semi-carbonised using a laboratory oven as shown on Figure 5a, b, and c. An equal weight of 0.300 g of the above kenaf fibre sample was weighed. And using a heating rate of 2.21 ^0C/min, each batch was heated to temperatures of 100^0C 150^0C, 200^0C, 250^0c and 300^0C respectively. It was then soaked for 5 mins at each temperature threshold as was done by Rowell *et al* (1995).

Production of kenaf brake pads

Experimental design

The experiments were of the randomised 1 x 3 x 3 factorial design for four different types of kenaf fibre at 15 % weight each.. Table 1 shows the outline of the experimental design for the four types of kenaf fibers with three levels of polyester binder and filler.

Main treatment: $\mathbf{T_1}$ (Untreated fibre); $\mathbf{T_1}$ (Mercerized fibre); $\mathbf{T_1}$ (Acetylated fibre); T_1 (Semi – Carbonized fibre) at 15 % weight each. **Sub-treatment**s: $\mathbf{S_1}$ (15 % polyester (Binder)); $\mathbf{S_2}$ (20% polyester); $\mathbf{S_3}$(25% polyester), then filler at $\mathbf{R_1}$ (60 %), $\mathbf{R_2}$ (65 %), and $\mathbf{R_3}$ (70 %) by weight

Table 1 Experimental design for kenaf brake pad samples

		Treatment			
S/N	Sample code	Kenaf Fibre Type (1 level)	Polyester (3 levels)	Filler (3 levels)	Replications
1	T1S1R1	1	1	1	5
2	T1S1R2	1	1	2	5
3	T1S1R3	1	1	3	5
4	T1S2R1	1	2	1	5
5	T1S2R2	1	2	2	5
6	T1S2R3	1	2	3	5
7	T1S3R1	1	3	1	5
8	T1S3R2	1	3	2	5
9	T1S3R3	1	3	3	5
10	Control (commercial sample)	NA	NA	NA	NA

NA = Not Available

Treatment combination = for the four types of fiber treatments = 1 Level of fibre × three levels of binder (Polyester) x three levels of Filler = 1 x 3 x 3 = 9 (T1S1R1, T1S1R2, T1S1R3, T1S2R1, T1S2R2, T1S2R3, T1S3R1, T1S3R2 and T1S3R3)

Total experiments conducted = 9 treatments x 4 Fibre Types × 5 replications = 108 experiments.

T, S and **R** were mere letters chosen to represent fibre treatment, binder (polyester) and Filler, respectively The numbers 1, 2, 3 were used to denote the levels of the factors. This exercise was done this way for convenience only.

1 Kg of rubber crumbs, 1 Kg of iron filings, 1 Kg of barium sulphate and 1 Kg graphite to give 4 Kg of Fillers.

Total Raw Materials used in this study = 100g x 1 treatment x 5 replications = 500g

Where the treatment combination does not give exactly 500g, calcium carbonate was used as a space filler to adjust the remaining percentage during replications as was done by Marthur et al (2004). Then the materials used in this study is approximately, 500g x 9 Treatments x 4 Fibre Types = 18,000g

Mixing of raw materials

In order to assist fiber dispersion, kenaf fibres were fiberized in a double-bladed kitchen blender for 8 mins. The fiberized kenaf fibers were dried at 60^0C for 24 h and stored in a desiccator, prior to compounding. A total of 9 samples with five replicates for each formulation of the four fibre treatments were mixed batch by batch.

The mixing was done at a temperature of 380C, mixing time of 5 mins, and rotor speed of 600 rpm as was done by Jang et al (2001). The first treatment mixing was carried out in this manner: the binder resin (unsaturated polyester (15 % of the Total weight) was first added inside the mixing chamber then another 15 % by weight of the fibre type was added, and finally 70 % by weight of the last component (filler) was also added. The mixer containing 100 g of kenaf fibre, polyester and filler was started and run for 5 mins until the three components were mixed. Thereafter the mixed material was removed for the next process.

Compression moulding

The mixed material was molded on a Hydraulic press into pads with dimensions of 6 cm x 4 cm x 2 cm. The mold was first preheated to raise the temperature to175 0C. As shown in Figure 1 and Figure 2, the mixed material was then placed in the mould and heated for 1 min under a constant pressure of 32.5 MPa; thereafter the moulded material was removed and cooled at room temperature for 8 mins as outlined on Figure 2a-d.

The pressed samples were then cured in an Oven for 8h, thereafter it was finished and prepared for performance properties (Booker., 1992 and Jang et al., 2001).

Figure 1 Compression moulding process using the CMR Equipment

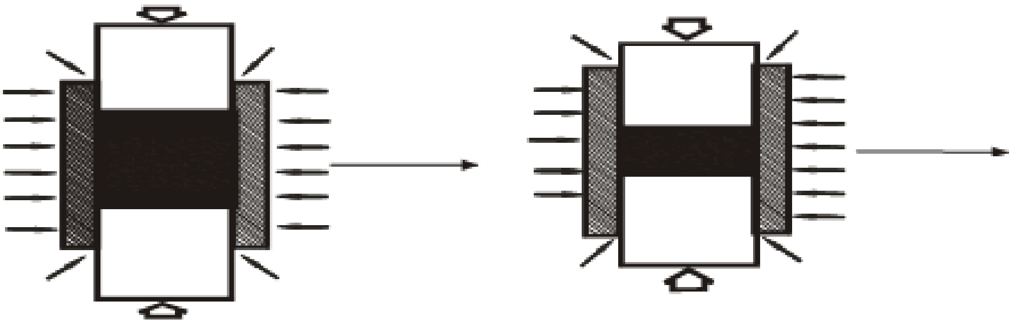

(a) Charging and heating

b) Heating and moulding

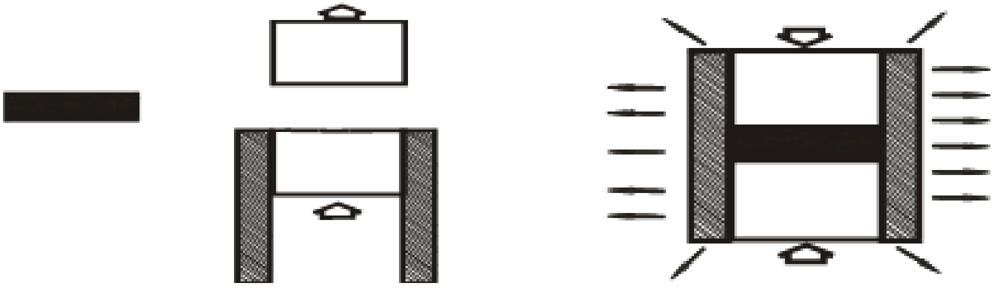

(c) Cooling brake pad sample

(d) Demoulding

Figure.2 a, b, c and d. Compression Molding process for kenaf brake pad

Plate 1 Kenaf brake pad samples

Thermal conductivity of kenaf brake pads

Test specimens of 0.002 m^2 and thickness of 0.01m were cut from their respective mother samples as was done by Ugheoke *et al* (2006). The test specimens were tested one after the other. Each specimen was fixed in the space provided within the thermal conductivity apparatus fabricated by the Mechanical Engineering Department. A conical flask containing 50 ml of water was placed directly above and in contact with the specimen. A cork having a thermometer passing through it was used to cork the mouth of the conical flask. The thermometer read the temperature changes of the water in the flask. The test section was then closed and the initial water temperature was noted. A second thermometer with the aid of a cork was inserted into the steam outlet pipe offset to monitor the steam temperature so as to ensure constant base temperature of 100 ^{0}C

The boiler water outlet valve was closed while 5 litres of water was measured and poured into the boiler cover remaining opened. The boiler was switched on. Immediately the water started boiling, the boiler, cover was closed, while the steam inlet valve was fully opened with all the remaining valves closed. Timing commenced with the aid of a stopwatch immediately the steam inlet valve opened.

The testing was timed in each case for 10 mins and final temperature of the water in the beaker was noted at the end of time. Each specimen was tested twice and a mean temperature value was obtained. At the end of each experiment, the steam outlet valve was opened to release steam. The water in the boiler was refilled to maintain 5 litres and the experiment was repeated as stated above for other specimens

The values of the Thermal Conductivity, K for each of the specimen was determined using the formular as suggested by Ugheoke *et al* (2006).

$$K = 2.303\, MCL / A\, [\log(\Theta_1/\Theta_2)]/t \qquad (1)$$

Where

k = thermal conductivity of the specimens
Θ_1 = initial temperature of the water in the conical flask (^{0}K)
Θ_2 = Final temperature in the conical flask (^{0}K)
C = specific heat capacity of water in conical flask {J/kg},
A = specimen are, (m^2)
M = mass of water in conical flask {kg}
t = Time (mins)

Testing for static coefficient of friction

Coefficient of Static friction is tangent of the friction angle of the material, which is the angle at which the material starts moving down the inclined plane with minimum resistance. This was carried out as was done by Kabri (2002). In his method, the sample whose friction angle is to be measured was placed on the inclined plane (galvanized sheet) surface of the friction test device lined with dry steel sheet. The inclined plane was raised gently with the help of the screw until material started to slide down the device. The angle at this point was noted from the protractor attached on the device. The procedure was repeated five times and the corresponding readings were noted and calculated from the following formula.

$$\mu = \tan \Phi \quad (2)$$

Where

μ = coefficient of static friction
Φ = angle recorded when the material started to slide (^{0})

Testing for dynamic coefficient of friction

Dynamic friction tests on the kenaf brake pads were carried out using the laboratory scale friction and wear test rig, FTR as shown on Figure 2 and the data generated is presented in Appendix D. This equipment, which was designed and constructed in the course of this work, is equipped with a brake assembly of a medium size passenger car (Mazda Model). Using a continuous sliding test (ASTM G99) method as was done by Marthur et al (2004), when the brake was applied, a brake pressure of 3.5 g/cm2 was delivered to the calliper(Pcal) and the the force on the calliper (Fclamp) was calculated as in equation 3, the torgue and the friction force(Ffriction) were calculated from equation 5.

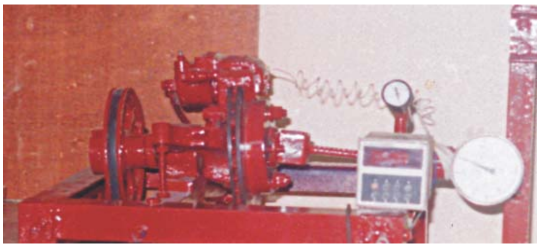

Figure 3. Experimental set up of the Friction Test Rig (FTR)

Thereafter, the coefficient of dynamic friction was calculated from equation 7. For every fresh experiment 5 min 'running-in' period was allowed for the FTR to allow the fresh test samples to bed very well, the reason being that the dynamic coefficient of friction changes significantly during the initial stages of testing and only becomes relatively stable after running in.

The rotational speed of 1500 rpm and a contact time of 1 s were maintained for the rotor or brake disc through out the experiment, the changes in the speed of the rotor after brake application and the power delivered to the rotor was used to determine the torgue on the brake disc. Also, temperature of the rotor surface was measured using a temperature sensor.

$$Fcal = Pcal \times Acal \quad (3)$$

$$Fclamp = Fcal \times 2 \text{ (back plates)} \quad (4)$$

$$Tr = Pem \times \omega r \quad (5)$$

$$F_{friction} = \frac{T_r}{R_{eff.rotor}} \quad (6)$$

$$\mu_{bp} = \frac{F_{friction}}{F_{clamp}} \quad (7)$$

Where

T_r = Torque on rotor radius (Nm),

P_{cal} = brake pressure delivered to the calliper (kg/cm2),

P_{em} = Power delivered to the rotor by the electric motor (hp)

ω_r = angular velocity (rad/s),

$F_{friction}$ = force of friction generated by the brake pads opposing the rotation of the rotor (N),

$R_{eff.\ rotor}$ = effective radius of the rotor(cm),

F_{clamp} = force generated by the clamp (Nm), μ_{bp}= coefficient of dynamic friction of kenaf brake pads, F_{cal}= the one sided force generated by the calliper (Nm),

A_{cal} = effective area of the calliper hydraulic pistons (cm^2)

Testing for thermal stability (wear loss) of kenaf brake pads

The wear tests were performed on the designed and constructed test rig, using a grey cast iron rotor disc of a passenger car. The friction test rig delivers 2.0 hp to the rotor rotating at 1500 rpm. A pair of test sample of 4 cm x 6 cm x 2 cm was bonded on both sides of the disc as required in SAE J – 661a test method and reported by Marthur *et al* (2004).

Figure 4.Worn samples of Kenaf Brake Pads fitted on back plates

The rig was allowed to run for some time to allow the samples to bed-in to allow at least 80% of the conformal contact, which was confirmed through visual inspection of the rubbed surface (Figure 4) prior to every experiment. The braking load of 3.5 kg/cm^2 was applied once the required speed (1500 rpm) of the disc was attained; the change in speed was recorded as well as temperature. This was done for 10, 20 and 30 braking cycles of 10 seconds each; and using a venier calliper measurements were recorded, afterwards the wear loss was obtained by the following expression:

$$W_{loss} = T_1 - T_2 \qquad (8)$$

Where

W_{loss} = thickness loss (mm),

T_1 = initial material thickness (mm)

T_2 = final thickness of the material (mm)

RESULTS AND DISCUSSION

Evaluation for thermal properties of kenaf brake pads reinforced with crude fibres

Table 2 shows the average values of thermal conductivity of crude brake pads which range from 0.298 W/m. ^{0}K in T1S1R1 sample code to as high as 0.424W/m. ^{0}K in T1S3R1. The percentage weight loss evaluation in crude brake pad samples revealed an almost close range of 31.080 % in T1S3R1 to a much higher average value of 32.672 % in T1S3R3. Thermal conductivity values also range from 0.298 W/m. ^{0}K in T1S1R1 and rises to a higher value of 0.424 W/m. ^{0}K in T1S3R1 crude kenaf brake pad formula. This value of thermal conductivity falls short by about 33 % of the value obtained in the commercial sample (control).

Evaluation for thermal properties of kenaf brake pads reinforced with mercerised fibres.

The average values of thermal conductivity and percentage weight loss of mercerised brake pads is presented on Table 3.These values range from 0.408 W/m. ^{0}K in T1S1R3 sample code to as high as 0.510 W/m. ^{0}K in T1S2R3. The percentage weight loss evaluation in crude brake pad samples revealed an increase of 18.890 % in T1S3R1 to a much higher average value of 22.298 % in T1S1R2.

Evaluation for thermal properties of kenaf brake pads reinforced with acetylated fibres

Table 4. shows the average values of thermal conductivity of acetylated brake pads which range from 0.394 W/m. 0K in T1S1R2 sample code to as high as 0.430 W/m. 0K in T1S2R3. The percentage weight loss evaluation in acetylated brake pad samples range from 14.948 % in T1S1R1 to a much higher average value of 16.820 % in T1S3R2.

Table 2. Thermal Properties of brake pads reinforced with crude kenaf fibre

		Treatment			Thermal properties	
S/N	Sample code	Crude Fibre (1 level)	Polyester (3 levels)	Filler (3 levels)	Thermal conductivity W/m. ^{0}K	Percentage Weight Loss
1	T1S1R1	1	1	1	0.298± 0.013	31.562± 1.583
2	T1S1R2	1	1	2	0.306± 0.045	32.344 ± 1.228
3	T1S1R3	1	1	3	0.310± 0.022	31.928 ± 2.058
4	T1S2R1	1	2	1	0.3400± 0.05	31.760 ± 1.639
5	T1S2R2	1	2	2	0.394± 0.023	31.854 ± 2.021
6	T1S2R3	1	2	3	0.400± 0.015	33.228 ± 1.886
7	T1S3R1	1	3	1	0.424± 0.034	31.080 ± 1.231
8	T1S3R2	1	3	2	0.408+ 0.0342	31.434 + 1.296
9	T1S3R3	1	3	3	0.418+ 0.043	32.672 + 1.679
10	Control	NA	NA	NA	0.68 ± 0.01	13.43 ± 1.04

NA = Not Available

Table 3. Thermal Properties of brake pads reinforced with Mercerised kenaf fibre

		Treatment			Thermal properties	
S/N	Sample code	Mercerised Fibre (1 level)	Polyester (3 levels)	Filler (3 levels)	Percentage Weight Loss	Thermal conductivity W/m. 0K
1	T1S1R1	1	1	1	21.804 ± 0.654	0.412 ± 0.063
2	T1S1R2	1	1	2	22.298 ± 1.030	0.430 ± 0.045
3	T1S1R3	1	1	3	21.870 ± 0.919	0.408 ± 0.047
4	T1S2R1	1	2	1	21.068 ± 0.324	0.490 ± 0.035
5	T1S2R2	1	2	2	21.316 ± 0.585	0.498 ± 0.025
6	T1S2R3	1	2	3	20.222 ± 0.813	0.510 ± 0.023
7	T1S3R1	1	3	1	20.154 ± 1.1683	0.424 ± 0.045
8	T1S3R2	1	3	2	20.550 ± 0.3474	0.434 ± 0.040
9	T1S3R3	1	3	3	18.890 ± 0.734	0.430 ± 0.041
10	Control	NA	NA	NA	0.68 ± 0.01	13.43 ± 1.04

NA = Not Available

Table 4. Thermal Properties of brake pads reinforced with Acetylated kenaf fibre

		Treatment			Thermal properties	
S/N	Sample code	Acetylated Fibre (1 level)	Polyester (3 levels)	Filler (3 levels)	Thermal conductivity W/m. ^{0}K	Percentage Weight Loss
1	T1S1R1	1	1	1	0.400 ± 0.010	14.948 ± 0.223
2	T1S1R2	1	1	2	0.394 ± 0.011	15.042 ± 0.565
3	T1S1R3	1	1	3	0.400 ± 0.010	15.280 ± 0.468
4	T1S2R1	1	2	1	0.402 ± 0.016	16.044 ± 0.240
5	T1S2R2	1	2	2	0.406 ± 0.018	16.048 ± 0.412
6	T1S2R3	1	2	3	0.422 ± 0.031	16.264 ± 0.427
7	T1S3R1	1	3	1	0.406 ± 0.020	16.450 ± 0.418
8	T1S3R2	1	3	2	0.414 ± 0.018	16.820 ± 0.340
9	T1S3R3	1	3	3	0.430 ± 0.037	16.506 ± 0.720
10	Control	NA	NA	NA	0.68 ± 0.01	13.43 ± 1.04

NA = Not Available

Evaluation for thermal properties of kenaf brake pads reinforced with semi-carbonised fibres

The results of evaluation of thermal properties of brake pads reinforced with semi-carbonised fibres is presented on Table 5. The average values of thermal conductivity of crude brake pads which range from 0.568 W/m. ^{0}K in T1S1R1 sample code to as high as 0.676 W/m. ^{0}K in T1S3R3.

The percentage weight loss evaluation in crude brake pad samples revealed an almost close range of 13.870± 0.565 % in T1S3R2 to a much higher average value of 15.672± 0.156% in T1S3R2.

Evaluation for tribological properties of kenaf brake pads reinforced with crude fibres

Table 6 shows the average values of Static and Dynamic coefficient of friction and Wear behaviour of crude brake pad samples. Static coefficient of friction of crude samples ranges from 0.410 in T1S1R1 sample code to as high as 0.426 in T1S2R1. Dynamic coefficient of friction also ranges from 0.312 in T1S1R1 to a much higher average value of 0.372 in T1S1R1. Also, Wear behaviour of crude brake pad samples range with the lowest value of 2.377mm occurring in T1S3R1 and T1S2R1 having the highest value of 3.353 mm.

Table 5. Thermal Properties of brake pads reinforced with Semi-carbonised kenaf fibre

		Treatment			Thermal properties	
S/N	Sample code	Semi-carbonised Fibre (1 level)	Polyester (3 levels)	Filler (3 levels)	Thermal conductivity W/m. 0K	Percentage Weight Loss
1	T1S1R1	1	1	1	0.568 ± 0.008	15.076 ± 0.223
2	T1S1R2	1	1	2	0.580 ± 0.008	15.672± 0.156
3	T1S1R3	1	1	3	0.606 ± 0.011	15.516± 0.448
4	T1S2R1	1	2	1	0.620 ± 0.010	14.502 ± 0.447
5	T1S2R2	1	2	2	0.612 ± 0.008	14.402 ± 0.346
6	T1S2R3	1	2	3	0.614 ± 0.005	14.156± 0.374
7	T1S3R1	1	3	1	0.652 ± 0.008	14.124± 0.400
8	T1S3R2	1	3	2	0.664 ± 0.008	13.870± 0.565
9	T1S3R3	1	3	3	0.676 ± 0.005	14.018± 0.134
10	Control	NA	NA	NA	0.68 ±0.01	13.43 ±1.04

NA = Not Available

Table 6 Evaluated tribological properties of brake pads reinforced with Crude kenaf fibre

		Treatment			Triobological properties		
S/N	Sample code	Crude Fibre (1 level)	Polyester (3 levels)	Filler (3 levels)	Static Coeff of friction	Dynamic coeff. of friction	Wear Loss (mm) at 30Braking cycles
1	T1S1R1	1	1	1	0.410 ± 0.040	0.312± 0.037	3.353± 0.257
2	T1S1R2	1	1	2	0.420 ± 0.033	0.338± 0.032	3.006± 0.112
3	T1S1R3	1	1	3	0.418 ± 0.040	0.330± 0.028	3.113± 0.092
4	T1S2R1	1	2	1	0.426 ± 0.023	0.348± 0.030	2.422± 0.107
5	T1S2R2	1	2	2	0.416 ± 0.024	0.354± 0.034	2.512± 0.016
6	T1S2R3	1	2	3	0.410 ± 0.027	0.342± 0.027	2.475± 0.162
7	T1S3R1	1	3	1	0.414 + 0.028	0.356+ 0.020	2.377+ 0.044
8	T1S3R2	1	3	2	0.422± 0.022	0.372± 0.021	2.967± 0.170
9	T1S3R3	1	3	3	0.416 ± 0.031	0.340± 0.015	2.514± 0.137
10	Control	NA	NA	NA	0.380 ±0.084	0.398 ±0.081	1.434 ±0.026

NA = Not Available

Evaluation for tribological properties of kenaf brake pads reinforced with mercerised fibres

The results of Static and Dynamic coefficient of friction and Wear behaviour of mercerised brake pad samples is presented on Table 7. Static coefficient of friction of mercerised samples ranges from 0.386 in T1S1R1 sample code to as high as0.417 in T1S3R3.

Evaluation for tribological properties of kenaf brake pads reinforced with acetylated fibres

Table 8 shows the average values of Static and Dynamic coefficient of friction and Wear behaviour of Acetylated brake pad samples. Static coefficient of friction of Acetylated samples ranges from 0.388 in T1S3R2 sample code to as high as 0.404 in T1S1R2. Dynamic coefficient of friction also ranges from 0.354 in T1S1R1 to a much higher average value of 0.388 in T1S3R2. Also, Wear behaviour of Acetylated brake pad samples range with the lowest value of 2.130 mm occurring in T1S3R3 and T1S2R1 having the highest value of 3.248 mm.

Evaluation for tribological properties of kenaf brake pads reinforced with semi-carbonised fibres

The results of Static and Dynamic coefficient of friction and Wear behaviour of semi-carbonised brake pad samples is presented on Table 9. Static coefficient of friction of semi-carbonised samples ranges from 0.402 in T1S3R3 sample code to as high as 0.410 in T1S1R1. Dynamic coefficient of friction also ranges from 0.378 in T1S2R3 to a much higher average value of 0.416 in T1S1R1. Also, Wear behaviour of semi-carbonised brake pad formulae range with the highest value of 1.814 mm in T1S1R1 while lowest value of 1.588 mm occurred in T1S3R2.

Table 7. Evaluated tribological properties of brake pads reinforced with Mercerised kenaf fibre

		Treatment			Triobological properties		
S/N	Sample code	Crude Fibre (1 level)	Polyester (3 levels)	Filler (3 levels)	Static Coeff of friction	Dynamic coeff. of friction	Wear Loss (mm) at 30Braking cycles
1	T1S1R1	1	1	1	0.386+ 0.018	0.364+ 0.293	2.2300+ 0.324
2	T1S1R2	1	1	2	0.398+ 0.019	0.360 + 0.046	2.462+ 0.148
3	T1S1R3	1	1	3	0.401+ 0.010	0.352 + 0.046	2.562 + 0.043
4	T1S2R1	1	2	1	0.385+ 0.016	0.352 + 0.029	3.098 + 0.042
5	T1S2R2	1	2	2	0.345+ 0.029	0.352 + 0.038	3.344 + 0.034
6	T1S2R3	1	2	3	0.394+ 0.010	0.340 + 0.038	3.324 + 0.073
7	T1S3R1	1	3	1	0.394+ 0.022	0.366 + 0.037	2.540 + 0.095
8	T1S3R2	1	3	2	0.413+ 0.014	0.360 + 0.033	2.322 + 0.003
9	T1S3R3	1	3	3	0.417+ 0.028	0.370 + 0.033	2.722+ 0.076
10	Control (commercial sample)	NA	NA	NA	0.380 + 0.084	0.398 + 0.081	+ 0.026

NA = Not Available

Table 8. Evaluated tribological properties of brake pads reinforced with Acetylated kenaf fibre

		Treatment			Triobological properties		
S/N	Sample code	Crude Fibre (1 level)	Polyester (3 levels)	Filler (3 levels)	Static Coeff of friction	Dynamic coeff. of friction	Wear Loss (mm) at 30Braking cycles
1	T1S1R1	1	1	1	0.400± 0.024	0.354± 0.040	3.248 ± 0.023
2	T1S1R2	1	1	2	0.404± 0.015	0.356± 0.020	3.016± 0.0 17
3	T1S1R3	1	1	3	0.394± 0.021	0.362± 0.017	2.964± 0.056
4	T1S2R1	1	2	1	0.394± 0.016	0.378± 0.021	3.202± 0.062
5	T1S2R2	1	2	2	0.394± 0.027	0.382± 0.016	3.170± 0.037
6	T1S2R3	1	2	3	0.394± 0.013	0.384± 0.008	3.192± 0.0 43
7	T1S3R1	1	3	1	0.394± 0.015	0.386± 0.011	2.538± 0.050
8	T1S3R2	1	3	2	0.388± 0.019	0.388± 0.008	2.962± 0.005
9	T1S3R3	1	3	3	0.394± 0.015	0.382± 0.008	2.130± 0.031
10	Control	NA	NA	NA	0.380 ±0.084	0.398 ±0.081	1.434 ±0.026

NA = Not Available

Table 9. Evaluated tribological properties of brake pads reinforced with Semi-carbonized kenaf fibre

		Treatment			Triobological properties		
S/N	Sample code	Semi-carbonised Fibre (1 level)	Polyester (3 levels)	Filler (3 levels)	Static coeff of friction	Dynamic coeff. of friction	Wear Loss (mm) at 30 Braking cycles
1	T1S1R1	1	1	1	0.410± 0.007	0.416± 0.005	1.814 ± 0.021
2	T1S1R2	1	1	2	0.408± 0.003	0.416 ± 0.008	1.716 ± 0.084
3	T1S1R3	1	1	3	0.406± 0.005	0.406± 0.008	1.638 ± 0.043
4	T1S2R1	1	2	1	0.404± 0.011	0.404 ± 0.005	1.68 ± 0.023
5	T1S2R2	1	2	2	0.406± 0.005	0.378 ± 0.010	1.714± 0.015
6	T1S2R3	1	2	3	0.406± 0.005	0.378 ± 0.013	1.686 ± 0.049
7	T1S3R1	1	3	1	0.404± 0.005	0.386 ± 0.005	1.670± 0.004
8	T1S3R2	1	3	2	0.404± 0.005	0.384 ± 0.008	1.588± 0.078
9	T1S3R3	1	3	3	0.402± 0.008	0.386 ± 0.005	1.654± 0.002
10	Control	NA	NA	NA	0.380 ±0.084	0.398 ±0.081	1.434 ±0.026

NA = Not Available

CONCLUSION

From the results obtained in this study, it can be concluded that semi-carbonised fibre based brake pad samples exhibited higher thermal conductivity with an average value of 0.625 W/m. K than all the other samples investigated.

REFERENCES

ASTM, (1999) ASTM Standard D570-99: Standard Test Method for Water Absorption of

Plastics. American Society forTesting and Materials Standards 08 (01)1271-1285.

Booker, B.U(1992). Compression moulding method of making brake Linings. US Patent 5156787, United States patent and trademark office. pp 123-127

Jang, H., Lee, J.S. and Fash, J.W (2001). compositional effects of the brake friction Material on creep groans phenomena. Journal of wear. 251 (14)1477 – 1483.

Mathur, R.B; P. Thiyagarajan and T. L. Dhami (2004): Controlling the Hardness and Tribological Behaviour of Non-asbestos Brake Lining Materilas for Automobiles. Journal of Carbon Science. 5 No. (1): 6-11

National industrialChemical Notification and Assessment Scheme for asbestos, NICNAS (1999). Priority Existing chemical Report 9, Common Wealth of Austrialia, P. 8

Rowell, R.M., Kawai, S. and M. Inoue. (1995). Dimensionally Stabilized, Very Low Density Fiberboard. Wood and Fiber Science, Vol. 27, No. 4, pp. 428-436.

Ugheoke, B.I; E.O Onche; N.O Namessan and G.A Asikpo (2006). Property Optimizaton

of Kaolin – Husk Insulating Fire – Bricks. Leonardo Electronic Journal of Practices and Technologies, 9 (34):167-177.

Warren, R. (1992). ceramic- matrix composite, UK asbestos ban in Journal of Sealing technology.72(12):16.

African Journal of Science and Technology (AJST)
Science and Engineering Series Vol. 12, No. 2, pp. 55 - 64

ON OPTIMUM DISPATCH OF ELECTRIC POWER GENERATION VIA NUMERICAL METHOD

Y.O .Aderinto and O. M. Bamigbola

epartment of Mathematics , University of Ilorin, Ilorin, Nigeria.
Email: moladerinto2007@yahoo.com

ABSTRACT: *In this work we develop an optimum dispatch / generating strategy by presenting economically the best load flow configuration in supplying load demand among the generators. The main aim is to minimize the total production / generation costs, with minimum losses and at the same time satisfy the load flow equation without violating the inequality constraints.*

Key Words: *Generation, power flow, generator limits, power losses,Chironomidae, River Niger, Niamey, water quality*

INTRODUCTION

The industrial growth of any nation depends greatly on the reliability of a large interconnected electric power system. Electric power system is a significant form of modern energy source, because of its application in nearly all spheres of human endeavour aimed at socio-economic development. In an interconnected power system, the objective is to find the output power and load shedding of each power plant in such a way as to minimize the operating cost. Manafa(1978), Laden(2008), Country profile(2006).

The factors influencing power generation at minimum cost are operating efficiencies of generators, fuel cost and transmission losses. The most efficient generator in the system may not guarantee minimum cost as it may be located in an area where fuel cost is high. Olle(1987), Power Sector Reform(2005). Also, if the plant is located far from where the load is, transmission losses may be considerably higher and hence the plant may be uneconomical.

The purpose of this work is to minimize the total production / generation costs, with minimum losses and at the same time satisfy the load flow equation without violating the inequality constraints.

Optimal Power Flow as an Optimization method for an energy management system control centre was developed in the 1960s by Carpenter, and since then it has been an

MOTIVATION FOR THE STUDY

important function as a standard application. A generalized nonlinear mathematical programming formulation of the economic dispatch problem including voltage and other operating power constraint which was named the Optimal Power Flow Problem, was introduced by Carpenter 1962, Dammel and Tinney, Oct, 1968. Since then, a great deal of research has been done and various optimization techniques have been used in order to find efficient solutions to this optimization problem. In 2005, Adejumobi looked at the effectiveness and efficiency of the electrical power distribution system in Nigeria by making use of power system security. In 1998, Arthur et al, worked on Optimization for load management scheduling. Also, in 1986 Lee et al, worked on optimization technique for power operation.

Similarly, in 1989, Youssef et al, looked at the transmission planning model for a power system. In 1988, Lee et al, looked at the transmission planning model for a power system. However, little or no attention has been paid to the production cost; they emphasized more on the operational aspect (design aspect) rather than the economical aspect of optimal power flow problem (OPF).

The purpose of this work is to develop an optimum dispatch / generating strategy by presenting economically the best load flow configuration in supplying load demand among the generators. The main aim is to minimize the total production / generation costs, with minimum losses and at the same time satisfy the load flow equation without violating the inequality constraints

MATHEMATICAL FORMULATION

The standard optimal electric power generation problem (optimal power flow problem), is formulated mathematically as follows. Olle(1987), Rao(1998).

Minimize

$$
\begin{aligned}
&C = C_i(x,u)\ Subject\ to\\
&g_i(x,u) = 0\\
&f_i(x,u) \le 0 \qquad (1)\\
&u_{\min} \le u \le u_{\max},\quad x_{\min} \le x \le x_{\max},\\
&x \in \Re^n, u \in \Re,\quad i = 1.....n\ \ bus
\end{aligned}
$$

$C_t, g_i\ and\ f_i$ are continuous differentiable, vector x contains independent variables consisting of bus voltage magnitudes and phase angle, reference bus angle, fixed bus voltage, e.t.c. The vector consists of controls variables, including real and reactive power generations, phase – shifter angles, direct transmission line flows, controls voltage settings, e.t.c.

Where, $C_i(x,u)$ represent the objective function, $g_i(x,u)$ represent non - linear equality constraint, the equality $g_i(x,u)$ is the load flow equation, $f_i(x,u)$ is the non - linear inequality constraint of vector argument x and u. The inequality $f_i(x,u)$ is the limit on the control variable u and the operating limits on the power system bus voltage limits. Limits on the control variables are known as "hard" limits (i.e. violation is not allowed, e.g. upper and lower band on the active power generation at the generator buses) and operating limits are known as " soft" limits (i.e. small violation is tolerable, e. g. voltage limit at load buses, maximum line loading limit). The vector x contains dependent or state variables (such as voltage magnitude, phase angle, e.t.c.), and u consists of control variables such as generated active and reactive power e. t. c. , Olle, (1987).

OPTIMIZATION OF REAL POWER GENERATION INCLUDES THE LIMIT AND TRANSMISSION LOSSES

When transmission distances are long with low density area, transmission losses are not neglected. The idea is to include the effect of transmission losses which can be expressed as a quadratic function of the generation power outputs, Burchett, R.S ., et al(1982), Charles, A.G.(1986). The simplest quadratic form is

$$
P_L = \sum_{i=1}^{ng}\sum_{j-1}^{ng} P_i B_{ij} P_j \quad or
$$

$$
P_L = \sum_{i=1}^{ng}\sum_{j-1}^{ng} P_i B_{ij} P_j \ + \sum_{i=1}^{ng} B_{01} P_i + B_{00}
$$

The coefficients B_{ij} are called loss coefficient or B – coefficient, which are assumed constants.

Statement of the problem

The problem can now be stated as:

Minimize the overall generation cost C_t

$$
C_t(pg_i) = \sum_{i=1}^{n}\left(\alpha_i + \beta_i pg_i + \gamma_i pg_i^2\right)
$$

subject to the constraints

$$
\begin{aligned}
&\sum_{i=1}^{ng} Pg_i = P_D + P_L, \qquad (2)\\
&pg_{i\min} \le Pg_i \le Pg_{i\ \max},\ i = 1,\quad ....ng
\end{aligned}
$$

Where $Pg_{i\min}$ and $Pg_{i\max}$ are the minimum and maximum generating limit respectively, for plant i.

Solution to the Problem

Using the Langrange Multiplier and adding additional terms to include the constraints

we have,

$$
\begin{aligned}
L = C_t(pg_i) &+ \left(P_D + P_L - \sum_{i-1}^{ng} Pg_i\right)\\
&+ \sum_{i=1}^{ng} \mu_{i\max}\left(Pg_i - Pg_{i(\max)}\right) \qquad (3)\\
&+ \sum_{i=1}^{ng} \mu_{i(\min)}\left(Pg_i - Pg_{i(\min)}\right)
\end{aligned}
$$

Note: $\mu_{i(\max)=0}\ \ when\ \ Pg_i < Pg_{i(\max)},$

$\mu_{i(\min)=0}\ \ when\ \ Pg_i > Pg_{i(\min)}$

This simply means that if the constraint is not violated then the associated μ variable is zero.

$$
\begin{aligned}
L &= \sum_{i=1}^{ng}\left(\alpha_i+\beta_i pg_i+\gamma_i pg_i^2\right)\\
&+\lambda\left(P_D+P_L-\sum_{i=1}^{ng}Pg_i\right)\\
&+\sum_{i=1}^{ng}\mu_{i\max}\left(Pg_i-Pg_{i(\max)}\right)\\
&+\sum_{i=1}^{ng}\mu_{i(\min)}\left(Pg_i-Pg_{i(\min)}\right)
\end{aligned}
\qquad (4)
$$

The solution to the Langrange equation is found by obtaining the following

$$
\left.
\begin{aligned}
&\frac{\partial L}{\partial Pg_i}=0,\quad \frac{\partial L}{\partial \lambda}=0\\
&\frac{\partial L}{\partial \mu_{i(\max)}}=Pg_i-Pg_{i(\max)}=0,\\
&\frac{\partial L}{\partial \mu_{i(\min)}}=Pg_i-Pg_{i(\min)}=0
\end{aligned}
\right\}
\qquad (5)
$$

Hence, we have

$$\beta_i+2\gamma_i Pg_i+\lambda\left(0+\frac{\partial P_L}{\partial Pg_i}-1\right)=0$$

which is equivalent to

$$\frac{\partial C_t\left(Pg_i\right)}{\partial Pg_i}+\lambda\frac{\partial P_L}{\partial Pg_i}=\lambda,$$

$$where\ \ \frac{\partial P_L}{\partial Pg_i}=2\sum_{j=1}^{ng}B_{ij}P_j+B_{oi}$$

Therefore, we have

$$2\gamma_i Pg_i+\beta_i+2\lambda\sum_{j=1}^{ng}B_{ij}P_j+B_{0i}\lambda=\lambda$$

or

$$\left(\frac{\gamma_i}{\lambda}+B_{ii}\right)Pg_i+\sum_{\substack{j=1\\ i=1}}^{ng}B_{ij}P_j=\frac{1}{2}\left(1-B_{0i}-\frac{\beta_i}{\lambda}\right) \qquad (6)$$

Expanding the above result in linear matrix, we have,

$$
\begin{bmatrix}
\frac{\gamma_i}{\lambda}+B_{11} & B_{12} & .\ . & B_{ing}\\
B_{21} & \frac{\gamma_2}{\lambda}+B_{22} & .\ . & B_{2ng}\\
. & . & .\ . & .\\
. & . & .\ . & .\\
B_{ng1} & B_{ng2} & .\ . & \frac{\gamma_{ng}}{\lambda}+B_{ngng}
\end{bmatrix}
\begin{bmatrix}
Pg_i\\ Pg_i\\ .\\ .\\ Pg_n
\end{bmatrix}
=
$$

$$
\frac{1}{2}
\begin{bmatrix}
1 & -B_{01} & -\frac{\beta_1}{\lambda}\\
1 & -B_{02} & -\frac{\beta_2}{\lambda}\\
. & . & .\\
. & . & .\\
1 & -B_{0ng} & -\frac{\beta_{ng}}{\lambda}
\end{bmatrix}
$$

$$i.e \qquad E \quad P \quad = \quad D$$

$$i=1,.........ng \qquad (7)$$

To find the optimal dispatch for an estimated value of $\lambda^{(k)}$ ' equation (7) is solved using the iterative method. The iterative continues until the load flow equation is satisfied. Thus from (6), we have,

$$\left(\frac{\gamma_i+\lambda B_{ii}}{\lambda}\right)Pg_i+\sum_{\substack{i=1\\ j\pm i}}^{ng}B_{ij}P_j=\frac{1}{2}-\frac{1}{2}B_{0i}-\frac{1}{2}\frac{\beta_i}{\lambda}$$

$$\Rightarrow\left(\frac{\gamma_i+\lambda B_{ii}}{1}\right)Pg_i+\lambda\sum_{\substack{i=1\\ j\pm i}}B_{ij}P_j=\frac{\lambda}{2}-\frac{\lambda}{2}B_{0i}-\frac{1}{2}\beta_i$$

Therefore,

$$P^{(k)}g_i=\frac{\lambda^{(k)}\left(1-B_{0i}\right)-\beta_i-2\lambda^{(k)}\sum_{\substack{i=1\\ j\pm i}}B_{ij}P_j^{(k)}}{2\left(\gamma_i+\lambda^{(k)}B_{ii}\right)}$$

Since,

$$\sum_{i=1}^{ng}pg_i=P_D+P_L$$

$$\frac{\sum_{j=1}^{ng}\lambda^{(k)}\left(1-B_{oi}\right)-\beta_i-2\lambda^{(k)}\sum_{j\pm i}B_{ij}P_j^{(k)}}{2\left(\gamma_i+\lambda^{(k)}B_{ii}\right)}=P_D+P_L^{(k)}$$

L If we denote $pg_i^{(k)}$ by $f(\lambda)^k$, and using Taylor series expansion, we have,

$$f(\lambda)^k + \left(\frac{df(\lambda)}{d\lambda}\right)^{(k)} \Delta\lambda^{(k)} + \left(\frac{d^2 f(\lambda)}{d\lambda^2}\right)^{(k)} \Delta^2\lambda^{(k)} + ... = P_D + P_L^{(k)}$$

Neglecting second and higher degree, we have,

$$f(\lambda)^k + \left(\frac{df(\lambda)}{d\lambda}\right)^{(k)} \Delta\lambda^{(k)} = P_D + P_L^{(k)}$$

where

or

$$\Delta\lambda^{(k)} = \frac{P_D + P_L^{(k)} - f(\lambda)^k}{\left(\frac{df(\lambda)}{d\lambda}\right)^{(k)}} \qquad (8)$$

Let

$\Delta P^{(k)} = P_D + P_L^{(k)} - f(\lambda)^{(k)}$, then

$$\Delta\lambda^{(k)} = \frac{\Delta P^{(k)}}{\left(\frac{df(\lambda)}{d\lambda}\right)^{(k)}} = \frac{\Delta P^{(k)}}{\sum_{i=1}^{n}\left(\frac{dPg_i}{d\lambda}\right)^{(k)}} \qquad (9)$$

Minimize

$$\begin{aligned} &C = C_i(x,u)\ Subject\ to \\ &g_i(x,u) = 0 \\ &f_i(x,u) \le 0 \qquad (1) \\ &u_{\min} \le u \le u_{\max},\quad x_{\min} \le x \le x_{\max}, \\ &x \in \Re^n, u \in \Re,\quad i = 1.....n\ \ bus \end{aligned}$$

,

C_t, g_i *and* f_i are continuous differentiable, vector x contains independent variables consisting of bus voltage magnitudes and phase angle, reference bus angle, fixed bus voltage e.t.c. The vector consist of controls variables, including real and reactive power generations, phase – shifter angles, direct transmission line flows, controls voltage settings e.t.c.

Where, $C_i(x,u)$ represent the objective function, $g_i(x,u)$ represent non - linear equality constraint, the equality $g_i(x,u)$ is the load flow equation, $f_i(x,u)$ is the non - linear inequality constraint of vector argument x and u. The inequality $f_i(x,u)$ are the limit on the control variable u and the operating limits on the power system. bus voltage limits. Limits on the control variables are known as "hard" limit (i.e. violation is not allowed, e.g. upper and lower band on the active power generation at the generator buses) and operating limits are known as " soft" limits (i.e. small violation is tolerable, e. g voltage limit at load buses, maximum line loading limit). The vector x contains dependent or state variables (such as voltage magnitude, phase angle etc), and u consist of control variables such as generated active and reactive power etc , Olle, (1987).

OPTIMIZATION OF REAL POWER GENERATION INCLUDES THE LIMIT AND TRANSMISSION LOSSES

When transmission distances are long with low density area, transmission losses are not neglected. The idea is to include the effect of transmission losses which can be expressed as a quadratic function of the generation power outputs, Burchett,R.S, et al(1982),Charles,A.G.(1986). The simplest quadratic form is

$$P_L = \sum_{i=1}^{ng}\sum_{j-1}^{ng} P_i B_{ij} P_j \quad or$$

$$P_L = \sum_{i=1}^{ng}\sum_{j-1}^{ng} P_i B_{ij} P_j + \sum_{i=1}^{ng} B_{01} P_i + B_{00}$$

4.1: Statement of the problem

The problem can now be stated as:

$$C_t(pg_i) = \sum_{i=1}^{n}\left(\alpha_i + \beta_i pg_i + \gamma_i pg_i^2\right)$$

subject to the constraints

$$\sum_{i=1}^{ng} Pg_i = P_D + P_L, \qquad (2)$$

$$pg_{i\min} \le Pg_i \le Pg_{i\max},\ i = 1, \ \ ....ng$$

Where $Pg_{i\min}$ and $Pg_{i\max}$ are the minimum and maximum generating limit, respectively for plant i.

4.2: Solution to the Problem

Using the Langrange Multiplier and adding additional terms to include the constraints.

We have,

$$\begin{aligned} L = C_t(pg_i) &+ \left(P_D + P_L - \sum_{i-1}^{ng} Pg_i\right) \\ &+ \sum_{i=1}^{ng} \mu_{i\max}\left(Pg_i - Pg_{i(\max)}\right) \qquad (3) \\ &+ \sum_{i=1}^{ng} \mu_{i(\min)}\left(Pg_i - Pg_{i(\min)}\right) \end{aligned}$$

Note: $\mu_{i(\max)=0}$ $when\ Pg_i < Pg_{i(\max)}$,
$\mu_{i(\min)=0}$ $when\ Pg_i > Pg_{i(\min)}$

This simply means that if the constraint is not violated then the associated variable is zero.

$$\begin{aligned} L &= \sum_{i=1}^{ng}\left(\alpha_i + \beta_i pg_i + \gamma_i pg_i^2\right) \\ &+ \lambda\left(P_D + P_L - \sum_{i=1}^{ng} Pg_i\right) \\ &+ \sum_{i=1}^{ng} \mu_{i\max}\left(Pg_i - Pg_{i(\max)}\right) \\ &+ \sum_{i=1}^{ng} \mu_{i(\min)}\left(Pg_i - Pg_{i(\min)}\right) \end{aligned} \qquad (4)$$

The solution to the Langrange equation are found by obtaining the following

$$\left.\begin{aligned} &\frac{\partial L}{\partial Pg_i} = 0, \quad \frac{\partial L}{\partial \lambda} = 0 \\ &\frac{\partial L}{\partial \mu_{i(\max)}} = Pg_i - Pg_{i(\max)} = 0, \\ &\frac{\partial L}{\partial \mu_{i(\min)}} = Pg_i - Pg_{i(\min)} = 0 \end{aligned}\right\} \qquad (5)$$

Hence, we have

$$\beta_i + 2\gamma_i Pg_i + \lambda\left(0 + \frac{\partial P_L}{\partial Pg_i} - 1\right) = 0$$

Which is equivalent to

$$\frac{\partial C_t(Pg_i)}{\partial Pg_i} + \lambda\frac{\partial P_L}{\partial Pg_i} = \lambda,$$

$$where\ \ \frac{\partial P_L}{\partial Pg_i} = 2\sum_{j=1}^{ng} B_{ij}P_j + B_{oi}$$

Therefore, we have

$$2\gamma_i Pg_i + \beta_i + 2\lambda\sum_{j=1}^{ng} B_{ij}P_j + B_{0i}\lambda = \lambda$$

or

$$\left(\frac{\gamma_i}{\lambda} + B_{ii}\right)Pg_i + \sum_{\substack{j=1 \\ i=1}}^{ng} B_{ij}P_j = \frac{1}{2}\left(1 - B_{0i} - \frac{\beta_i}{\lambda}\right) \qquad (6)$$

Expanding the above result in linear matrix, we have,

$$\begin{bmatrix} \frac{\gamma_i}{\lambda} + B_{11} & B_{12} & . \ . & B_{ing} \\ B_{21} & \frac{\gamma_2}{\lambda} + B_{22} & . \ . & B_{2ng} \\ . & . & . \ . & . \\ . & . & . \ . & . \\ B_{ng1} & B_{ng2} & . \ . & \frac{\gamma_{ng}}{\lambda} + B_{ngng} \end{bmatrix} \begin{bmatrix} Pg_i \\ Pg_i \\ . \\ . \\ Pg_n \end{bmatrix} =$$

$$\frac{1}{2}\begin{bmatrix} 1 & -B_{01} & -\frac{\beta_1}{\lambda} \\ 1 & -B_{02} & -\frac{\beta_2}{\lambda} \\ . & . & . \\ . & . & . \\ 1 & -B_{0ng} & -\frac{\beta_{ng}}{\lambda} \end{bmatrix}$$

$$i.e \qquad E \quad P \quad = \quad D$$

$$i = 1,.........ng \qquad (7)$$

To find the optimal dispatch for an estimated value of $\lambda^{(k)}$, equation (7) is solved using the iterative method. The iterative continues until the load flow equation is satisfied. Thus from (6), we have,

$$\left(\frac{\gamma_i + \lambda B_{ii}}{\lambda}\right)Pg_i + \sum_{\substack{i=1 \\ j\pm i}}^{ng} B_{ij}P_j = \frac{1}{2} - \frac{1}{2}B_{0i} - \frac{1}{2}\frac{\beta_i}{\lambda}$$

$$\Rightarrow \left(\frac{\gamma_i + \lambda B_{ii}}{1}\right)Pg_i + \lambda\sum_{\substack{i=1 \\ j\pm i}} B_{ij}P_j = \frac{\lambda}{2} - \frac{\lambda}{2}B_{0i} - \frac{1}{2}\beta_i$$

Therefore,

$$P^{(k)}g_i = \frac{\lambda^{(k)}(1 - B_{0i}) - \beta_i - 2\lambda^{(k)}\sum_{\substack{i=1 \\ j\pm i}} B_{ij}P_j^{(k)}}{2\left(\gamma_i + \lambda^{(k)}B_{ii}\right)}$$

Since,

$$\sum_{i=1}^{ng} pg_i = P_D + P_L$$

$$\sum_{j=1}^{ng} \frac{\lambda^{(k)}(1 - B_{oi}) - \beta_i - 2\lambda^{(k)}\sum_{j\pm i} B_{ij}P_j^{(k)}}{2\left(\gamma_i + \lambda^{(k)}B_{ii}\right)} = P_D + P_L^{(k)}$$

L If we denote $pg_i^{(k)}$ by $f(\lambda)^k$, and using Taylor series expansion, we have,

$$f(\lambda)^k+\left(\frac{df(\lambda)}{d\lambda}\right)^{(k)}\Delta\lambda^{(k)}+\left(\frac{d^2f(\lambda)}{d\lambda^2}\right)^{(k)}\Delta^2\lambda^{(k)}+.........=P_D+P_L^{(k)}$$

Neglecting second and higher degree, we have,

$$f(\lambda)^k+\left(\frac{df(\lambda)}{d\lambda}\right)^{(k)}\Delta\lambda^{(k)}=P_D+P_L^{(k)}$$

where

$$\Delta\lambda^{(k)}=\frac{P_D+P_L^{(k)}-f(\lambda)^k}{\left(\frac{df(\lambda)}{d\lambda}\right)^{(k)}} \qquad (8)$$

Let

$\Delta P^{(k)}=P_D+P_L^{(k)}-f(\lambda)^{(k)}$, then

$$\Delta\lambda^{(k)}=\frac{\Delta P^{(k)}}{\left(\frac{df(\lambda)}{d\lambda}\right)^{(k)}}=\frac{\Delta P^{(k)}}{\sum_{i=1}^{n}\left(\frac{dPg_i}{d\lambda}\right)^{(k)}} \qquad (9)$$

$$\sum_{i=1}^{n}\left(\frac{dPg_i}{d\lambda}\right)^{(k)}=\frac{\sum_{i=1}^{ng}2\left(\gamma_i+\lambda^{(k)}B_{ii}\right)\left[(1-B_{0i})-2\sum_{j=i}B_{ij}P_j^{(k)}\right]-\left[\lambda^{(k)}(1-B_{0i})-2\lambda^{(k)}\sum_{j=i}B_{ij}P_j^{(k)}\right]2B_{ii}}{4\left(\gamma_i+\lambda^{(k)}B_{ii}\right)^2}$$

$$=\frac{\sum_{j=i}^{ng}\gamma_i(1-B_{0i})+\lambda^{(k)}B_{ii}(1-B_{0i})-2\gamma_i\sum_{j=i}B_{ij}P_j^{(k)}-2\lambda^{(k)}B_{ii}\sum_{j=i}B_{ij}P_j^{(k)}-\lambda^{(k)}B_{ii}(1-B_{0i})+2B_{ii}\lambda^{(k)}\sum_{j=i}B_{ij}P_j^{(k)}}{2\left(\gamma_i+\lambda^{(k)}B_{ii}\right)^2}$$

$$=\frac{\left(\sum_{j=i}^{n}\gamma_i(1-B_{0i})-\sum 2\gamma_iB_{ij}P_j^{(k)}\right)}{2\left(\gamma_i+\lambda^{(k)}B_{ii}\right)^2} \qquad (10)$$

And therefore,

$\lambda^{(k+1)}=\lambda^{(k)}+\Delta\lambda^{(k)}$,

where $\Delta P^{(k)}=P_D+P_L^{(k)}-\sum_{i-1}^{ng}Pg_i^{(k)}$

The process continues until $\Delta P^{(k)}$ is less than a specified accuracy.

If an approximate loss formula expressed by $P_L=\sum_{i=1}^{ng}B_{ii}P^2g_L$ is used, $B_{ij}=0,\quad B_{0i}=0,$ and solution of the equation becomes

$$P_i^{(k)}=\frac{\lambda^{(k)}-\beta_i}{2\left(\gamma_i+\lambda^{(k)}B_{ii}\right)} \qquad (3.16a)$$

Hence,

$$\sum_{i=1}^{ng}\left(\frac{dP_i}{d\lambda}\right)^{(k)}=\frac{2\left(\gamma_i+\lambda^{(k)}B_{ii}\right)-\left[\left(\lambda^{(k)}\right)\left(2B_{ii}\right)\right]}{4\left(\gamma_i+\lambda^{(k)}B_{ii}\right)^2}$$

$$=\frac{\gamma_i+\lambda^{(k)}B_{ii}-\lambda^{(k)}B_{ii}}{2\left(\gamma_i+\lambda^{(k)}B_{ii}\right)^2}$$

$$=\sum_{i=1}^{ng}\frac{\gamma_i}{2\left(\gamma_i+\lambda^{(k)}B_{ii}\right)^2} \qquad (11)$$

4.3: Solution Algorithm

1. Assume an initial value for $\lambda^{(k)}$.
2. Calculate Pg_i. using equation

A.
$$Pg_i^{(k)} = \begin{bmatrix} \frac{\gamma_i}{\lambda} + B_{ii} & B_{12} & . \;\; . & B_{1n} \\ B_{21} & \frac{\gamma_2}{\lambda^{(k)}} + B_{22} & . \;\; . & B_{2n} \\ . & . & . \;\; . & . \\ . & . & . \;\; . & . \\ B_{01} & B_{ng2} & . \;\; . & \frac{\gamma_n}{\lambda^{(k)}} + B_{nn} \end{bmatrix} \begin{bmatrix} Pg_1^{(k)} \\ Pg_2^{(k)} \\ . \\ . \\ Pg_n^{(k)} \end{bmatrix}$$

$$= \begin{bmatrix} 1 & -B_{01} & -\frac{\beta_1}{\lambda^{(k)}} \\ 1 & -B_{02} & -\frac{\beta_2}{\lambda} \\ . & . & . \\ . & . & . \\ 1 & -B_{0n} & -\frac{\beta_{ng}}{\lambda^{(k)}} \end{bmatrix}$$

or

B. $$Pg_i^k = \frac{\lambda^{(k)} - \beta_i}{2\left(\gamma_i + \lambda^{(k)} B_{ii}\right)}$$

3. Calculate $P_L^{(k)}$ using

$$P_L = \sum_{i=1}^{n} \sum_{j=1}^{n} P_i B_{ij} P_j + \sum_{i=1}^{n} B_{0i} P_i + B_{00} \quad \text{for 2.A}$$

above and $P_L^{(k)} = \sum_{i=1}^{n} B_{ii} P_i^2$ for 2B.

4. Check if the relationship $\sum_{i=1}^{n} Pg_i^{(k)} = P_D + P_L^k$ is satisfied if not go to 5.
5. Calculate $\Delta Pg_i^{(k)}$ from

$$\Delta Pg_i^{(k)} = P_D + P_L - \sum_{i=1}^{n} Pg_i^k$$

6. Calculate $\Delta\lambda^{(k)}$ from

$$\Delta\lambda^{(k)} = \frac{\Delta Pg_i^{(k)}}{\frac{\left(\sum \gamma_i (1 - B_{0i}) - \sum 2\gamma_i B_{ij} P_j^{(k)}\right)}{2\left(\gamma_i + \lambda^{(k)} B_{ii}\right)^2}} \quad for \;\; 2A$$

$$or \; = \frac{\gamma_i}{2\left(\gamma_i + \lambda^{(k)} B_{ii}\right)^2} \quad for \; 2B.$$

7. Obtain a new value of λ from $\lambda^{(k+1)} = \lambda^k + \Delta\lambda^{(k)}$
8. Repeat step 2 – 7 until $\Delta Pg_i^{(k)} = 0$ or when $\Delta Pg_i^{(k)}$ is less than a specified accuracy.
9. Check for the value of Pg_i when the equality is met, plants that exceed their upper limit are kept at the specified limit.
10. Continue from step 4 – 7 when the equality constraints are met again check limit of the plants.
11. Calculate the total Production Cost $C_t(Pg_i) = C_1 + C_2 + ... + C_{n,}$ where n the number of generator.

5. Numerical Results and Interpretation

In this section we give some numerical examples and the interpretation of the results obtained.

5.1 Numerical Results

Problem 5. 1

Consider the following generator parameters of 5 bus system with three generating bus.

Table 7.1

Bus No	P_{min}	P_{max}	α	β	γ
1	5.5	39.5	150	7.0	0.008
2	10	80	160	6.3	0.009
3	10	70	140	6.8	0.007

Given that the real power losses is expressed as

$$P_L = \sum_{i=1}^{n} B_{ii} P_i^2,$$

$$\text{where } B_{ii} = \begin{bmatrix} 0.000218 \\ 0.00228 \\ 0.00179 \end{bmatrix}, i = 1....,3$$

Determine the optional dispatch of generator and the cost of generation when the total system load demand is 180MW.

Solution:

The problem can be stated as

Minimize,

$$C_t(Pg_i)=\sum_{i=1}^{3}\alpha_i+\beta_i Pg_i+\gamma_i Pg_i$$

Subject to

$$\sum_{i=1}^{3}Pg_i-P_D-P_L=0$$

$$P_{i(\min)}\le P_i\le P_{i(\max)}$$

$$P_{2(\min)}\le P_2\le P_{2(\max)}$$

$$P_{3(\min)}\le P_3\le P_{3(\max)}$$

$P_L=\sum_{i=1}^{n}B_{ii}P_i^2$, where

$$B_{ii}=\begin{bmatrix}0.000218\\0.00228\\0.00179\end{bmatrix}, i=1....,3,\quad P_D=180MW$$

Follow the algorithm above,

Assume $\lambda^{(1)}=7.5$ and obtain Pg_i from $Pg_i^{(k)}$

Obtain $Pg_i^{(k)}=\dfrac{\lambda^{(k)}-\beta_i}{2(\gamma_i+\lambda^{(k)}B_{ii})}$

$$P_1^{(1)}\cong 25.95MW,\quad P_2^{(1)}=56.02MW,\quad P_3^{(1)}=41.95MW$$

$$P_L^{(1)}=B_{11}\overset{(1)}{P_1^2}+B_{22}\overset{(1)}{P_2^2}+B_{33}\overset{(1)}{P_3^2}$$
$$=0.000218(25.95)^2+0.000228(56.02)^2+0.000179(41.95)^2$$

=1.18MW

Since $P_D=180MW$, we compute

$$\Delta P^{(1)}=180+1.18-(25.95+56.02+41.95)=57.26MW$$

$$\Delta\lambda^{(1)}=\frac{\Delta P^{(1)}}{\sum_{i=1}^{3}\frac{\gamma_i}{2(\gamma_i+\lambda^{(1)}B_{ii})^2}}\cong 0.43$$

$$\lambda^{(2)}=\lambda^{(1)}+\Delta\lambda^{(1)}=7.93$$

Hence, we obtain, $P_i^{(2)},\quad i=1,.....,3$,

$P_i^{(2)}\cong 47.80MW$, $P_2^{(2)}\cong 75.41MW$, and $P_3^{(k)}\cong 67.11MW$

Note that P_1 has exceeded the upper limit, so that from P_1 at the upper limit of 39.5MW and obtain P_L and $\Delta P^{(2)}$.

$$P_L^{(2)}\cong 2.44MW$$

$$P_L^{(2)}\cong 2.44MW$$

$$\Delta P^{(2)}=180+2.44-(39.5+75.41+67.1)=0.42$$

With P_1 fixed, compute $\Delta\lambda^{(2)}$ and $P_1^{(3)}$

$$\Delta\lambda^{(3)}=\frac{\Delta P^{(2)}}{\sum_{i=1}^{3}\frac{\gamma_i}{2(\gamma_i+\lambda^{(1)}B_{ii})^2}}\cong 0.003$$

$$\lambda^{(3)}=7.93+0.003=7.933$$

$P_1=39.5MW, P_2^{(3)}\cong 75.54$ $P_3^{(3)}\cong 67.28$, $P_L^{(3)}\cong 2.45MW$.

$$\Delta P^{(3)}=0.13$$

Compute $\Delta\lambda^{(4)}$ and $P_i^{(4)}$, using:

$$\Delta\lambda^{(4)}=\frac{\Delta P^{(3)}}{\sum_{i=1}^{3}\frac{\gamma_i}{2(\gamma_i+\lambda^{(2)}\beta_{ii})^2}}\cong 0.001 \text{ and}$$

$\lambda^{(4)}=7.934$.

Hence,

$P_1^{(3)}=39.5MW$, $P_2^{(4)}\cong 75.56MW$, $P_3^{(4)}\cong 67.34MW$ $P_L^{(4)}\cong 2.45MW$.

$$\Delta P^{(4)}=180+2.45-(39.5+75.56+67.34)=0.05<1$$

Since the difference between $\Delta P^{(i)}$ is getting very smaller compare to 1, we stop here and compute the cost of generation for each plant and the total cost of generation.

Thus, the optimal dispatch is

$$P_1 = 39.5MW,\ P_2 \cong 75.56MW,\ P_3 \cong 67.34MW,$$
$$\lambda = 7.934,\ P_L \cong 2.45MW,$$
$$C_1 = 438.98\#/h,\ C_2 = 687.41\#/h,\ C_3 = 629.66\#/h,$$
$$\text{and } C_t = 1756.05\#/h,$$

Problem 5.2

Consider the generator parameters given below,

Table 5.2.

Bus No	P_{min}	P_{max}	α	β	γ
1	5	25	45	7.820	0.00140
2	5	20	50	7.60	0.00292
3	5	10	30	7.85	0.00480

Given that, $P_L = \sum_{i=1}^{n}\sum_{j=1}^{n} P_i B_{ij} P_j + \sum^{n} B_{0i} P_i + B_{00}$,

Where,

$$B_{ij} = \begin{bmatrix} 0.00067 & 0.00095 & 0.00050 \\ 0.00095 & 0.0012 & 0.00090 \\ 0.00050 & 0.00090 & 0.00029 \end{bmatrix},$$

$$B_{ii} = \begin{bmatrix} 0.00016 \\ 0.0014 \\ -0.0082 \end{bmatrix}, \qquad B_{00} = 0.00403,$$

Determine the optimal dispatch of the generator and the optimal cost of generation, when the total load demand is 31MW

The problem can be stated as,

Minimize,

$$C_t(P_i) = \sum_{i=1}^{3}\left(\alpha_i + \beta_i P_i + \alpha_i P_i^2\right)$$

Subject to

$$P_{i(\min)} \le P_i \le P_{i(\max)},\quad i = 1,\ldots,3$$

$$P_D + P_L - P_i = 0$$

where, $P_L = \sum_{i=1}^{3}\sum_{j=1}^{3} P_i B_{ij} P_j + \sum^{3} B_{0i} P_i + B_{00}$,

with

$$B_{ij} = \begin{bmatrix} 0.00067 & 0.00095 & 0.00050 \\ 0.00095 & 0.0012 & 0.00090 \\ 0.00050 & 0.00090 & 0.00029 \end{bmatrix},$$

$$B_{ii} = \begin{bmatrix} 0.00016 \\ 0.0014 \\ -0.0082 \end{bmatrix}, \qquad B_{00} = 0.00403,$$

$$P_D = 31MW$$

Follow the algorithm above, obtaining P_i using

$$\begin{bmatrix} \frac{\gamma_i}{\lambda} + B_{11i} & B_{12} & B_{13} \\ B_{21} & \frac{\gamma_2}{\lambda} + B_{22} & B_{23} \\ B_{31} & B_{32} & \frac{\gamma_3}{\lambda} + B_{33} \end{bmatrix} \begin{bmatrix} P \\ {}^{1}P_2 \\ P_3 \end{bmatrix} = \frac{1}{2}\begin{bmatrix} 1 - B_{01} + \frac{\beta_1}{\lambda} \\ 1 - B_{02} + \frac{\beta_2}{\lambda} \\ 1 - B_{03} + \frac{\beta_3}{\lambda} \end{bmatrix}$$

Assume $\lambda^{(1)} = 8.2$, we obtain

$$\begin{bmatrix} 0.841 & 0.95 & 0.5 \\ 0.95 & 1.556 & 0.9 \\ 0.5 & 0.9 & 0.875 \end{bmatrix} \begin{bmatrix} P_1 \\ P_2 \\ P_3 \end{bmatrix} = \begin{bmatrix} 23.091 \\ 36.52 \\ 25.44 \end{bmatrix},$$

Using Gausian elimination method, we have,

$$\left[\begin{array}{ccc|c} 0.841 & 0.95 & 0.5 & 23.091 \\ 0.95 & 1.556 & 0.9 & 36.52 \\ 0.5 & 0.9 & 0.875 & 25.44 \end{array}\right],$$

$$M_{21} = \frac{0.95}{0.841},\quad M_{31} = \frac{0.5}{0.541}$$

$$\left[\begin{array}{ccc|c} 0.841 & 0.95 & 0.5 & 23.091 \\ 0 & 0.4829 & 0.3352 & 10.44 \\ 0 & 0.3352 & 0.5777 & 11.712 \end{array}\right],$$

$$M_{32} = \frac{0.3352}{0.4829}$$

$$\left[\begin{array}{ccc|c} 0.841 & 0.95 & 0.5 & 23.091 \\ 0 & 0.4829 & 0.3352 & 10.44 \\ 0 & 0 & 0.3450 & 4.465 \end{array}\right],$$

$$\begin{bmatrix} 0.841 & 0.95 & 0.5 \\ 0 & 0.4829 & 0.3352 \\ 0 & 0 & 0.3450 \end{bmatrix} \begin{bmatrix} P_1 \\ P_2 \\ P_3 \end{bmatrix} = \begin{bmatrix} 23.091 \\ 10.44 \\ 4.465 \end{bmatrix},$$

$$P_3^{(1)} = 12.94MW,\quad P_2^{(1)} = 12.64MW,\quad P_1^{(1)} = 5.49MW$$

$$P_L^{(1)} = (5.49)^2(0.00067) + (12.64)^2(0.0012) + (12.94)^2(0.00029) +$$
$$(5.49)(0.00016) + 12.64(0.00014) + 12.94(-0.0082) + 0.00403$$
$$= 0.161046031 \cong 0.16$$

Since $P_D = 31MW$

$$\Delta P_i^{(1)} = 0.09$$

Compute

$$\Delta\lambda^{(1)} = \frac{\Delta P_1^{(1)}}{\dfrac{\left[\sum_{i=1}^{3}\gamma_i\left(1-B_{01}\right)-\sum_{\substack{i=1\\j=1}}^{3}2\gamma_i B_{ij}P_j^{(1)}\right]}{2\left(\gamma_i+\lambda^{(1)}B_{ii}\right)^2}} ,i=1,2,3$$

$$= 0.0000466$$

$$\lambda^{(2)} = 8.2 + 0.0000466 = 8.2000466$$

Compute $P_i^{(2)}$, we have the same value as $P_i^{(1)}$, and ΔP_i, is very small, so we stop and compute $C_t\left(P_i\right)$,

$$C_3 = 73.24\#/h, and, \quad C_t = 366.20\#/h$$

$$C_1 = 146.43\#/h, \quad C_2 = 146.53\#/h,$$

Thus, the optimal dispatch is given by

$$P_1 = 5.49MW,\ P_2 = 12.64MW,\ P_3 = 12.94MW,$$

$$\lambda = 8.2,\ P_L = 0.16MW.$$

INTERPRETATION

It is observed that when generating limit is included, generators are capable of dispatch more power under the secured atmosphere. It is also observed that plants with higher actual capacity should not be placed very far from the National Control Center (Grid Center) in order to minimize power losses.

CONCLUSION

We give, mathematical formulation of the Optimization problems involving electric power generation with generator limit plus power losses was established. An Algorithms was tested via iterated numerical method and numerical examples were considered for better understanding of the concept. Finally we present interpretation of the result folowed by conclusion.

REFERENCES

[1] Abadie, J and Carpenter , J, (1969), Generalization of the Wolfe reduced gradient method to the case of nonlinear Constraints Optimization, R. Fletcher. Ed. Academic Press, New York.

[2] Adejumobi, I.A. (2005). Optimizing the effectiveness and efficiency of electrical system in Nigeria. Ilorin Metropolis as case study. A Ph. D dissertation, Department of Electrical Engineering, University of Ilorin, Ilorin. Nigeria.

[3] Arthur I.C. and Connie, C.W. (1988). An Optimization for load Management Scheduling, IEEE Transactions on Power System, Vol.3, No.2.pp612- 618.

[4] 34th Annual Electric Utility Forecast (1983), Electrical World, Vol. 197, No 9, 55 - 62.

[5] Burchett, R. S. Happ, H.H. and Wirgau,K.A. (1982), Development in Optimal power flow, IEE Trans, Power Application and System. PAS – 101, 406 - 414.

[6] Charles, A. G. (1986), Power System Analysis, John Wiley and Sons, New York Santa Barbara, Churchester, Brisbane Toronto.

[7] Country Profile, Nigeria June 2006, Library of Congress, Federal Research Division.

[8] Dommel, H.W and Tinney, W (1968) Optimal Power Flow Solution, IEEE Trans. Power Application and System PAS -87, 1866-1876.

[9] Duncan, Glover. J and Muluktla Sarma, (1986), Power System Analysis and Design, PWS-KENT Publishing Company, 20m Park Plaza, Boston, Massachusetts. [.

[10] Laden U.S. (2008). Achieving Steady Power Supply, Daily Sun, Monday, July 7, 2008

[11] Lee, K.Y. Ortiz, J.L Park Y.M. and Pond, L.G. (1986). An Optimization Technique for power operation, IEEE Transaction on Power Systems, Vol PWRS-1 No; 2. pg 153-159.

[12] Lee, K.Y. Ortiz J.L. Mohtadi M.A. and Park, Y.M. (1988). Optimal Operation of Large –scale Power Systems IEEE Transactions on Power systems, Vol 3, No 2, pg 413-4

African Journal of Science and Technology (AJST)
Science and Engineering Series Vol. 12, No. 2, pp. 65 - 69

ADDITIVE MAIN EFFECTS AND MULTIPLICATIVE INTERACTIONS ANALYSIS OF HARVEST INDEX PERFORMANCES IN CASSAVA (*Manihot esculenta,* Crantz) GENOTYPES ACROSS 4 ENVIRONMENTS

Adomako, W.[1], Asante I. K.[2] and Carson G. C.[3]

[1]University of Education Winneba Ashanti-Mampong Campus;
[2]Department of Botany, P.O. Box LG55, University of Ghana, Legon. Ghana
[3]University of Cape Coast, Department of Crop Science, School of Agriculture, Cape Coast.

Email: ikasante@ug.edu.gh

ABSTRACT: *Eight cassava genotypes were evaluated for harvest index performance across four environments. Data analysis was performed using MATMODEL and GGEbiplot. AMMI analysis of variance showed that 10.02% of the total sum of squares was attributable to environmental effects, 3.99% to genotypic effects and 50.13% to GEI effects. The GEI sum of squares contained approximately 76.52% (0.30709) pattern and 23.48% (0.09442) noise of the total GEI. The mean squares for IPCA 1 and IPCA 2 were significant at P = 0.000 and 0.002 respectively; all together they contributed 94.18% of the total GEI. Therefore, the post-dictive evaluation using an F-test at 0.000 and 0.002 suggested that two principal axes of the interaction were significant for the model with 16 degrees of freedom. The predictive assessment measured by the average root mean square predictive difference (RMS PD), selected AMMI1 with the first interaction PCA axis as the most predictively accurate. The AMMI1 model had the lowest average RMS PD (9.996). Mean performance and stability of the genotypes assessed by biplot analysis showed that the most stable genotypes were G2, G1 and G7. However G5 was highly unstable followed by G8 and G3. Two mega-environments were defined namely: G5-winning niche and G3-winning niche. The current study has demonstrated that the GGE biplot is a useful tool for the analysis of multi-environment trial (MET) data.*

Key Words*: AMMI, GGEbiplot, stability, harvest index, mega-environment*

INTRODUCTION

Yield performance of a number genotypes evaluated across a number of environments is always affected by genotype x environment interaction (GEI). Difference in genotype ranking across environments may depend on the magnitude of the interactions or the differential responses to environments. Interaction effect can be quantified by using a combined analysis of variance. However analysis of variance is not informative for explaining GEI.

The additive main effect and multiplicative interaction (AMMI) model is a useful model for understanding GEI. The model integrates additive main effects and multiplicative components, extracting first the additive main effects and then using principal components analysis to investigate the GEI. Accuracy of estimates of genotypic yields in multi-location trials is the main focus of plant breeding. This method has been referred to as yield prediction assessment and functions by splitting the data into modelling and validation data, with the values expected by the model compared with the validation data (Gauch and Zobel 1988).

Visual examination of GEI can be done by a biplot where both genotypes and locations occur on the same scattergram. It clearly shows which genotype won in which environment and therefore facilitates mega-environment identification (Mohammadi and Haghparast 2007).

MATERIALS AND METHODS

This study was carried out to determine the harvest index performance of 8 cassava genotypes across four environments in the 2004-2005 growing season. Environments comprised two locations and two different harvest times. The two locations were Bunso and Legon.

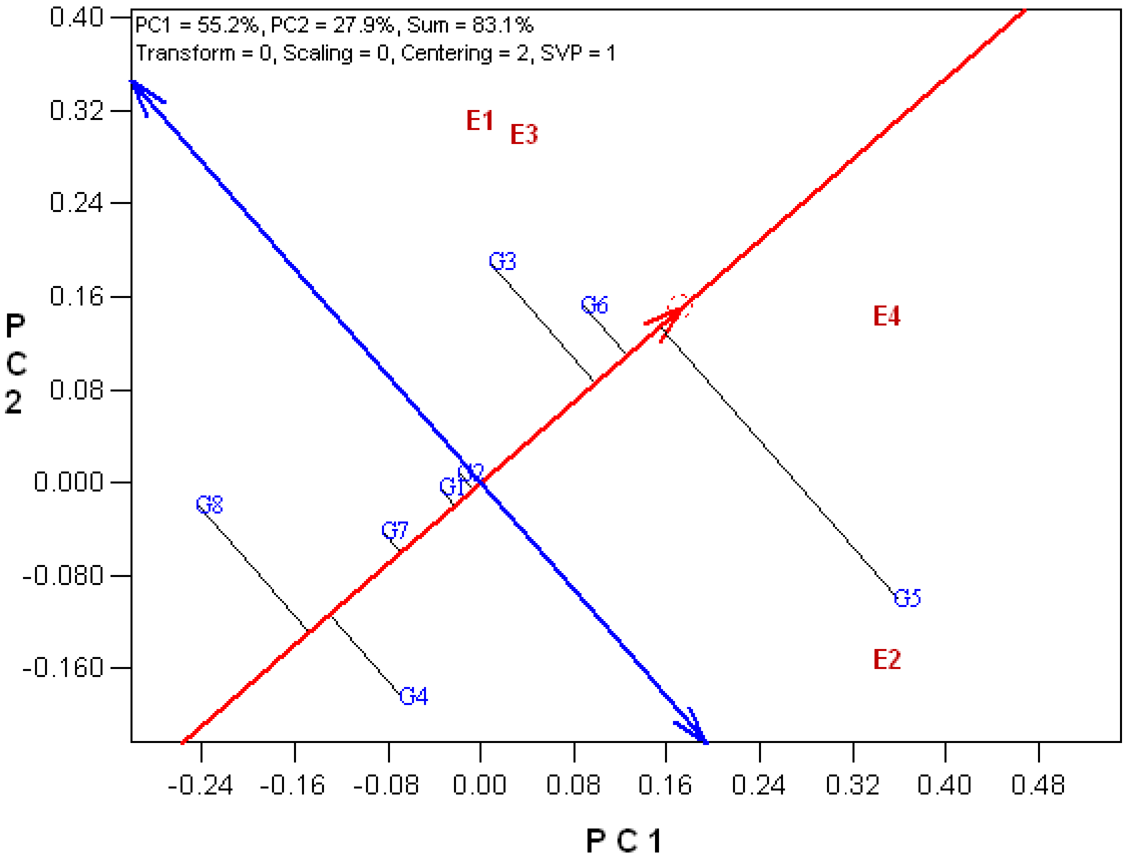

Figure1. Mean performance and stability of 8 cassava genotypes for harvest index

Table 1. Origin, code and source of cassava genotypes

Cassava genotype	Genotype Code	Origin
Afisiafi	G1	Released variety
HO001	G2	Volta Region
Bosome Nsia	G3	Local material
UCC90	G4	Western Region
DMA030	G5	Dormaa Ahenkro
UG126	G6	University of Ghana
HO015	G7	Volta Region
HO008	G8	Volta Region

Bunso is located in the semi-deciduous agroecological zone in the Eastern region of Ghana and Legon is located in the coastal savannah agroecological zone in the Greater Accra region of Ghana. Description and designations of the four environments are shown in Table 2. The experimental materials (Table 1) were the top 8 genotypes of 32 early bulking cassava genotypes stored at the research farm of the Department of Crop Science University of Ghana Legon. The experimental layout was a randomized complete block design with three replications. The experimental area was divided into three blocks with inter-block distance of 2 m. Each block measured 23 m long and 11 m wide. Each block was further divided into eight 5 m by 5 m plots with 1 m spacing between plots. Harvest index was calculated as weight of cassava storage roots divided by sum of top weight and storage root weight.

The MATMODEL (Version 3.0, Gauch, 2007) was used to perform analysis of AMMI on the data. Biplot analysis was carried out by using the GGEbiplot (version 4.1)

RESULTS AND DISCUSSION

The AMMI analysis of variance of cassava harvest index of the 8 cassava genotypes tested in the four environments showed that 10.02% of the total sum of squares was attributable to environmental effects, 3.99% to genotypic effects and 50.13% to GEI effects (Table 2). The magnitude of the GEI sum of squares was 2.5 times larger than that for genotypes, indicating that there were some levels of differences in genotypic response across environments. The noise sum of squares in the interaction can be estimated as GEI degrees of freedom multiplied by the Error MS. Accordingly, the GEI sum of squares contains approximately 76.52% (0.30709) pattern and 23.48% (0.09442) noise of the total GEI.

Results of the AMMI analysis (Table 3) further showed that the first principal component axis (PCA 1) of the interaction captured 66.53% of the interaction sum of squares in 42.86% of the interaction degrees of freedom. Similarly, the second principal component axis (PCA 2) explained a further 27.65% of the GEI sum of squares. Furthermore, the sums of squares for PCA 1 and PCA 2 were greater than that of genotypes. The mean squares for PCA 1 and PCA 2 were significant at P = 0.000 and 0.002 respectively; cumulatively they contributed to 94.18% of the total GEI. Therefore, the post-dictive evaluation using an F-test at 0.000 and 0.002 suggested that two principal axes of the interaction were significant for the model with 16 degrees of freedom.

The most accurate model for AMMI can be predicted by using the first two PCAs (Gauch and Zobel, 1996; Yan et al., 2002). Predicitive PCA axis cannot be specified a priori without AMMI model-validation for predictive assessment (Gauch, 2007). In the current study, predictive assessment measured by the average root mean square predictive difference (RMS PD), selected AMMI1 with the first interaction PCA axis as the most predictively accurate. The AMMI1 model had the lowest average RMS

Table 2. Designation of the environments

Environment	Environment code	Location	Harvesting period
1	E1	Bunso	12MAP
2	E2	Legon	12MAP
3	E3	Bunso	8MAP
4	E4	Legon	8MAP

Table 3. Additive main effects and multiplicative interaction analysis of variance for harvest index including the first three interaction principal component analysis (PCA) axes.

Source of variation	df	Sum of squares	Mean squares	Explained %
Treatment combination	31	0.5135	0.0166***	
Genotype (G)	7	0.032	0.0046	
Environment (E)	3	0.0802	0.0267***	
G-E	21	0.4013	0.0191***	
Interaction PCA 1	9	0.267	0.0297***	66.53
Interaction PCA 2	7	0.111	0.0159**	27.65
Intearction PCA 3	5	0.0234	0.0047	5.83
Residual	64	0.2671	0.0045	
Total	95	0.8006	0.0084	

PD (9.996) (Table 4) based on 1000 runs having 32000 validations with actual treatment data. This model has 19 df (3 for environments plus 7 for genotypes plus 9 for interaction PCA axis 1) and is 1.4 times parsimonious (few df) as AMMI2, which was selected for postdictive success (i.e., AMMI2 contains 1.4 times as many df as AMMI1).

Table 4. Average root mean square predictive difference (RMS PD) for four models constructed based on harvest index from the cassava trial.

Model	df	RMS PD
AMMI0	10	0.0921
AMMI1	19	0.0839
AMMI2	26	0.0812*
AMMI3	31	0.0824

Mean performance and stability of the genotypes were assessed by biplot analysis (Fig. 1). On the biplot the single-arrowed line, the average-environment coordination (AEC) abscissa points to higher mean harvest index across environments. The double-arrowed line is the AEC ordinate and it points to greater variability (poor stability) in either direction. Genotype G5 had the highest value of harvest index followed by G6 and G3. Genotype G8 had the lowest value. The most stable genotypes were G2, G1 and G7. However G5 was highly unstable followed by G8 and G3.

A biplot was generated using genotypic and environmental sources of the first two AMMI components (Vargas and Crossa, 2000). The biplot was used to identify winning genotypes and mega-environments (Fig. 2). On the biplot, some corner or vertex genotypes, which are the most responsive ones, can be visually identified. These are either the best or the poorest genotypes at some or all environment (Weikai *et al*., 2006). The vertex genotypes for the present work were G1, G4, G8, G3 and G6 (Fig. 2). Genotypes G1, G2, and G7 were located within the polygon and were found less responsive (Weikai *et al*., 2006). Two mega-environments were defined namely: G5-winning niche and G3-winning

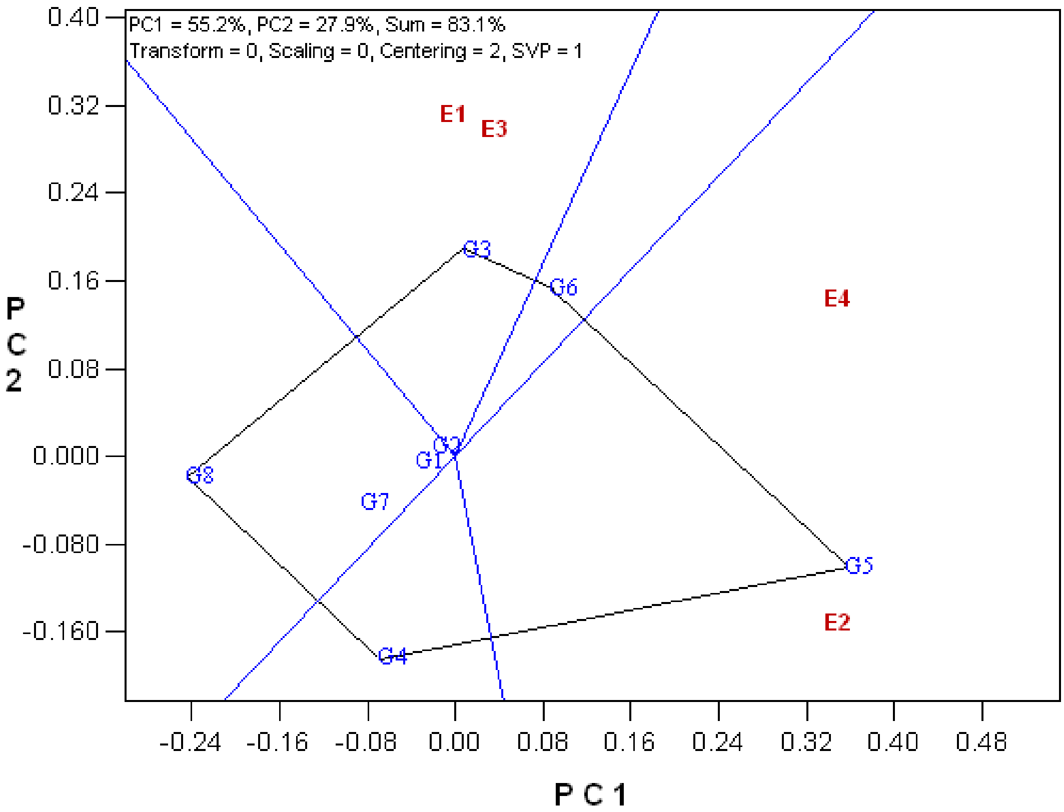

Figure 2. Mega-environment defined by different winning cassava genotypes for harvest index

niche. No environments fell in the sectors with G4, G6 and G8 as vertex genotypes. This indicates that these vertex genotypes were not the best in any of the test environments, but the poorest in some or all of the environments.

The current study has shown that the GGE biplot is a useful tool for the analysis of multi-environment trial (MET) data. On the basis of a drawn-to-scale, two-dimensional GGE biplot, the similarities and differences among environments in their discrimination and genotypes, the similarities and differences among the genotypes in their response to the environments and the nature and magnitude of interaction between any genotype and any environment can be readily visualized (Yan *et al*, 2000). Year-to-year variation may limit the value of a single year data, however biplot analysis of single year MET data is worthwhile and its reasons have been described in detail by Yan *et al* (2001). Although conclusions from a single year MET may not be conclusive, they may be valuable suggestions (Yan *et al*, 2001). Even if the which-won-where pattern is proven to be unrepeatable over years, the researcher would still want to know the average yield and the stability of the cultivars based on each year's MET.

REFERENCES

Gauch H. G. and Zobel, R. W. 1988. Predictive and postdictive success of statistical analyses of yield trials. *Theor. Appl. Genet*. 76:1-10.

Mohammadi, R and Haghparast, R. 2007. Biplot analysis of multi-environment trials for identification of Winter wheat mega-environments in Iran. *World Journal of Agricultural Sciences* 3 (4): 475-480.

Yan, W., L.A Hunt, Q. Sheng and Z. Szlavnics, 2000. Cultivar Evaluation and Mega-Environment Investigation Based on the GGE Biplot. *Crop Science*, 40: 597-605.

Yan, W., P.L. Cornelius, J. Crossa and L.A Hunt, 2001. Two Types of GGE Biplots for Analysing Multi-Environment Trial Data. *Crop Science*, 41: 656-663.

African Journal of Science and Technology (AJST)
Science and Engineering Series Vol. 12, No. 2, pp. 70 - 79

ETUDE PHENOMENOLOGIQUE SUR LA CONVECTION NATURELLE AU DESSUS D'UN DISQUE RAINURE PAR VOIE OPTIQUE

Boussoukaia, T.[1], Hammouda, M.[2] et Draoui, B.[3]

[1]Laboratoire LDDI, Université d'Adrar, Algérie
[2]Unité de Recherche en Energies Renouvelables en Milieu Saharien (URER /MS), Adrar
[3]Laboratoire d'Energétique en Zones Arides (LEZA), Université de Bechar, Algérie

E-mail : Tboussoukaia@Gmail.coma.

RÉSUMÉ: *Parmi toutes les méthodes expérimentales, l'optique a toujours occupé une place de choix grâce à son caractère non intrusif : la traversée d'un écoulement par un faisceau lumineux n'entraine pas de perturbation dans les conditions requises par la visualisation ou la mesure. C'est ce qui explique l'importance de la technique que nous allons décrire. Cette étude vise la mise en place d'un banc d'essai en vue de visualiser et traiter numériquement la convection naturelle induite par un disque rainuré et chauffée par le bas dans un système ouvert. La méthode de visualisation choisie est l'ombroscopie comme méthode non intrusive afin de ne pas perturber la convection. Il est utile aussi de rappeler que cette dernière technique délivre en fait des images qu'il faudra lire et éventuellement traiter. Ainsi, dans pratiquement tous les cas de contrôle optique, il faut, pour obtenir des images reconstituées de bonne qualité et envisager une vision nette, mettre en œuvre un système élaboré de traitement d'images. Ce système a pour premier but d'améliorer la qualité de l'image sur le plan du contraste et du niveau de bruit; il doit en seconde lieu très souvent prendre en compte la morphologie des objectifs recherchés afin de rendre l'image reconstituée parfaitement exploitable.*

Mots clés: *Convection naturelle, Disque rainuré, Ombroscopie, Traitement d'image, thermographie*

ABSTRACT: *Among all the experimental methods, optics always occupied a choice place thanks to its nonintrusive character: the line of a flow by a beam of light does not involve a disturbance under the requirements by visualization or measurement. It is what explains the importance of the technique that we will describe. This study is based on the design and use of an experimental set-up dedicated to make visible and treat the natural convection above a heated horizontal grooved disk in ambient air. The shadowgraph technique is used in order to visualize the flow and get quantitative data. It's also useful to recall that's the last technique delivers images which will have to be read and possibly treat. Therfore, it's necessary in sight check, to implement an elaborate system of image processing in order to obtain reconstituted images of good quality and clear vision . The first purpose of this system is to improve quality of the image within contrast and noise level, it must in the second place very often, take into account the morphology of the required objectives in order to make the image reconstituted perfectly exploitable.*

Key words: *Natural convection, grooved Disc, shadowgraph, Image processing, thermal imaging*

INTRODUCTION

La convection est un mode de transport d'énergie par l'action combinée de la conduction, de l'accumulation de l'énergie et du mouvement du milieu. La convection est le mécanisme le plus important de transfert d'énergie entre une surface solide et un fluide. Le transfert d'énergie par convection d'une surface dont la température est supérieure à celle du fluide qui l'entoure s'effectue en plusieurs étapes. D'abord la chaleur s'écoule par conduction de la surface aux molécules du fluide adjacentes. L'énergie ainsi transmise sert à augmenter la température et l'énergie interne de ces molécules du fluide. Ensuite les molécules vont se mélanger avec d'autres molécules situées dans une région à basse température et transférer une partie de leur énergie. Dans ce cas l'écoulement transporte le fluide et l'énergie. L'énergie à présent; emmagasinée dans les molécules du fluide et elle est transportée sous l'effet de leur mouvement. [1]

Parmi toutes les méthodes expérimentales, l'ombroscopie a toujours occupé une place de choix grâce à son caractère non intrusif : la traversée d'un écoulement par un faisceau lumineux nous permet de percevoir la présence et le comportement des courants convectifs par des manifestations indirectes naturelles. Toutes les techniques optiques sont fondées sur la mise en évidence ou sur l'amplification de ces manifestations. La mesure optique est une méthode de mesure utilisant la lumière pour quantifier des distances, des déformations et des déplacements. On distingue les mesures utilisant des cibles optiques placées sur le sujet, des mesures utilisant du traitement d'images à partir d'images ou de vidéos du sujet. Alors que les cibles optiques sont largement utilisées depuis le milieu des années 1990, la deuxième méthode restait expérimentale au milieu des années 2000. [2]

L'objectif de l'étude est de caractériser expérimentalement la convection naturelle générée par un disque rainuré, chauffé par le bas, et à axe vertical dans un système ouvert (air ambiant). Pour cela un moyen de visualisation et de traitements en temps réel est mis en place.

METHODE DE VISUALISATION PAR OMBROSCOPIE

Principe Général [1]

Le principe de l'ombroscopie consiste à utiliser les variations spatiales de l'indice optique n(T) comme traceur de la dépendance spatiale du champ de température T. par exemple, un indice optique périodique dans le domaine où se développe la convection conduit à une déviation périodique d'un faisceau de lumière initialement parallèle. Sous certaines conditions, l'on peut récupérer en aval sur un écran un signal dont l'intensité reproduira la dépendance spatiale de la température. Les courants convectifs ascendants ont une dépendance spatiale selon les grandes directions verticales et il est naturel d'éclairer le domaine de convection par un faisceau de lumière parallèle vertical.
L'indice de réfraction d'un milieu transparent pour une radiation de longueur d'onde λ est lié à la masse volumique ρ de ce milieu par la relation de Lorentz :

$$\frac{n^2 - 1}{n^2 + 2} = \mathrm{b}.\rho \qquad (1)$$

Où la grandeur b ne dépend que de la longueur d'onde λ et du milieu considéré.

Dans le cas de l'air, l'indice n est très voisin de l'unité et la relation précédente (1) devient la loi d'Aragot-Biot :

$$\frac{n-1}{\rho} = \frac{3}{2} b \qquad (2)$$

Introduisons la masse volumique normale ρ_n (température, zéro degré Celsius ; pression, 76 cm de mercure) ; la loi (2) s'écrit :

$$n - 1 = k\frac{\rho}{\rho_n} \qquad (3)$$

*Où **k** est un nombre sans dimension qui ne dépend que du milieu transparent et de la longueur d'onde.*
Des variations locales de masse volumique et, par suite, d'indice de réfraction, se produisent dans tout l'écoulement non uniforme de l'air. La mise en évidence des variations locales d'indice de réfraction est possible par l'ombroscopie, laquelle constitue, de ce fait, un procédé d'étude de la convection.

ETUDE EXPERIMENTALE

Description du Dispositif (Fig.1)

Le système se compose d'une source lumineuse S, punctiforme mais très brillante, est placé au foyer d'une lentille L. le faisceau de rayons parallèles ainsi obtenu traverse les zones d'intérêts *(plan au voisinage immédiat du disque chauffé : couche limite thermique, la région* correspond *au régime laminaire et l'amorçage du régime turbulent)* et vient rencontrer un écran.

Un examen visuel direct de l'image qui vient d'apparaitre sur l'écran (*belle à voir*) peut constituer un contrôle suffisant pour la détection des hétérogénéités locales et superficielles développée sur le plan vertical du disque. Toutefois, l'examen purement visuel présent des limitations de différentes natures qui justifient l'éclosion de toute une gamme de procédés de contrôle optique, dont, parmi les principaux la visualisation automatique par traitement d'images. D'où la nécessité.

Figure1 : prise de vue du banc d'essai

Positionnement et mise au point de la caméra

Une bonne visualisation ainsi que des mesures précises nécessitent un positionnement soigneux et minutieux de la caméra, et la possibilité d'ajuster ces coordonnées à tout moment. Pour répondre à ce besoin, la caméra et la source lumineuse sont portées sur le même rail afin de les préserver toujours orthogonal à l'écran. Le rail permet de translater de manière linéaire la caméra vers la zone d'intérêt. Le positionnement vertical est réalisé au moyen de deux ascenseurs métriques de précision, sur lesquels est fixé le rail. Un déphasage en hauteur entre la caméra et la source de lumière est exigent pour éviter l'ombre de la caméra.

Le réglage du diaphragme de la caméra est réalisé de manière à obtenir un bon contraste entre la prise de vue de la zone d'intérêt et le bruit de fond, nécessaire pour optimiser le produit de corrélation.

Télévision

On ne peut se satisfaire d'un examen visuel dont nous avons souligné les limites liées en particulier à la fatigue du l'expérimentateur. Pour cela, la télévision, munie d'une palette riche en option, apporte une aide précieuse au control visuel. La TV raccordée à la caméra via son port TV permettant une observation à distance en temps réel de ce qui se passe au dessus du disque chauffé par le biais de l'image induite sur l'écran ayant pour but d'améliorer suffisamment les contrastes de l'image d'un phénomène détecté, de façon que sa présence puisse être automatiquement signalée ou enregistrée.

Traitement d'image

Le traitement d'image associé aux : (caméra numérique HD ; logiciel de traitement) est indispensable. En effet, le signal vidéo sortant de toute caméra de prise de vue est pratiquement toujours bruité pour qu'un traitement analogique simple suffise à délivrer un signal défaut fiable.

Ainsi, dans pratiquement tous les cas de visualisation optique, il faut, pour obtenir des images reconstituées de bonne qualité et envisager une détection automatique des anomalies sur celles-ci, mettre en œuvre un système élaboré de traitement d'images. Ce système a pour premier but d'améliorer la qualité de l'image sur le plan de contraste et du niveau de bruit ; il doit en second lieu très souvent prendre en compte la morphologie de l'hétérogénéité recherchée en vue de rendre l'image reconstituée parfaitement exploitable.

Ces traitements, qui peuvent être relativement complexes, ne peuvent être mis en œuvre que par voie numérique, ce qui entraine la nécessité de disposer derrière la caméra d'un système de numérisation rapide, d'une ou plusieurs mémoires d'image (vidéo-RAM, carte CSD,…) et d'un mini-ordinateur adapté au traitement d'images en temps réel. Les outils mathématiques utilisables sont nombreux et variés, nous nous contenterons de mentionner ici les opérateurs matriciels linéaires (filtre cardinal, filtre de Laplace), et non linéaire (filtre de Sobel, de Kirsh, de Prewitt) et statistiques (Markovien), la convolution bidimensionnelle, l'analyse fréquentielle de Fourrier,…etc.

Résultats Expérimentaux

1- Avant d'aborder la phase de convection ; on a voulu s'assurer que le régime de conduction soit établit en tout point de la surface supérieure du disque. Pour répondre à ce besoin, on a fait appel à la thermographie pour justifier et prouver toutes les hypothèses qui peuvent être cité dans la littérature: FIG. (2,3)

* le disque intérieurement chauffé est placé dans une salle d'expérimentation dont la vitesse de l'air ambiant est faible.

* la conduction thermique sur le disque est assez grande pour que tous les points de la surface du disque soient à la même température T_s .

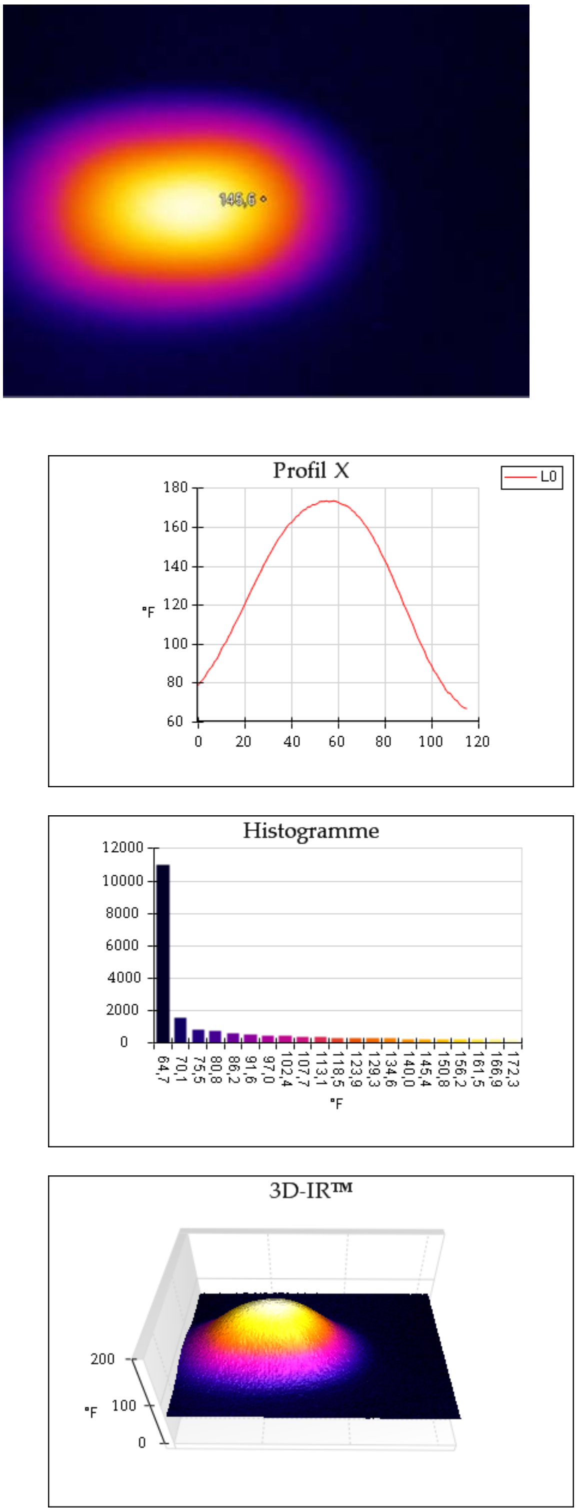

Figure 2: Régime transitoire de la conduction au dessus du disque

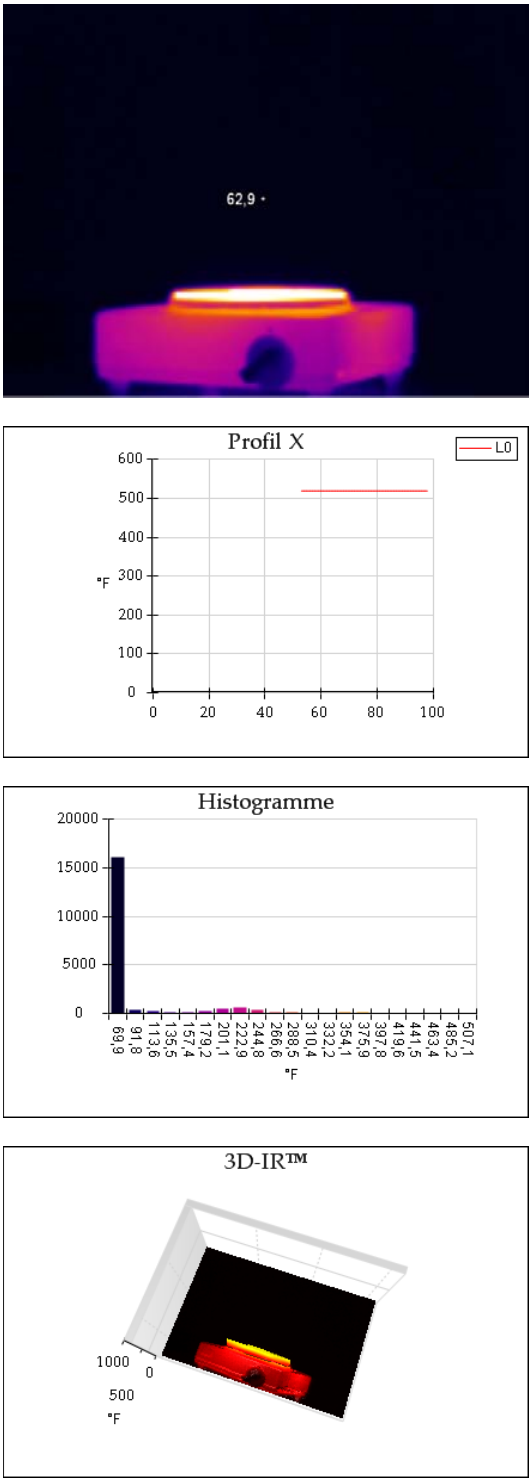

Figure 3: Régime stationnaire de la conduction au dessus du disque

2- Essayons de décrire de façon purement phénoménologique le comportement temporel de la perturbation de température qui conduit à l'établissement de l'image de la Fig. (4).

Figure 4: image ombroscopique temporelle brute temporelle

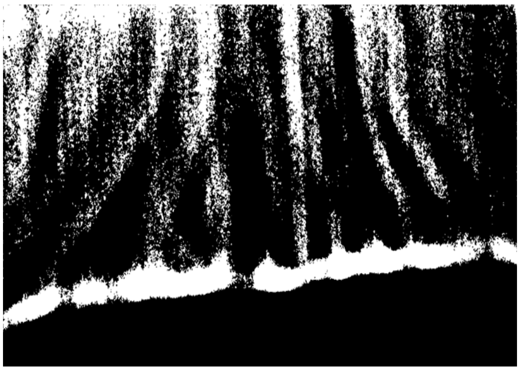

Figure 5: image ombroscopique traiteée

Les Fig. (4,5) représentent l'ombre du disque ainsi que les masses d'air déplacées par convection sur l'écran placé à une distance bien calculée. Cette image illustre la concentration de la lumière au dessus du disque sous la forme d'une mince bande lumineuse. Ce phénomène optique est dû aux effets de la réfraction sur les rayons lumineux et permet de matérialiser la frontière de la couche limite thermique. Ainsi le montage permet, par l'observation de l'éclairement de l'écran, de localiser les régions où varie le gradient de masse volumique et de connaitre dans quel sens s'effectue la variation.

L'image illustre un mécanisme très intuitif. L'air au repos subit une fluctuation de température, la densité varie et s'accentue quand on s'élève dans le fluide: cette situation est potentiellement instable, car dans le champ de pesanteur, la tendance naturelle est de mettre le lourd en bas et le léger en haut .*cette redistribution se traduit par l'apparition d'une circulation sous forme d'une alternance de région où l'air monte et descend. Ce rebondissement est bien illustré dans la Fig.(6)*.

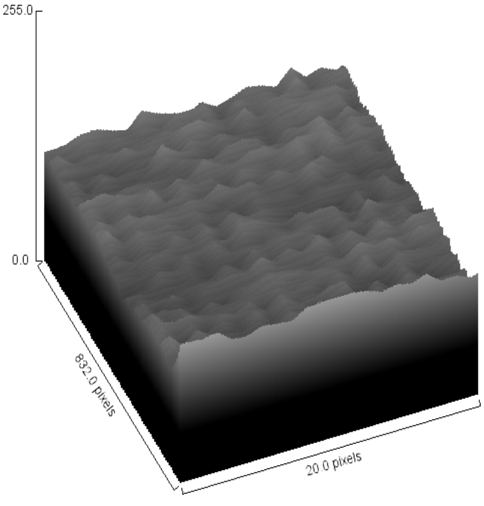

Figure 6: Plot 2D de la zone de covection

Ces régions sont caractérisées par des courants convectifs qui apparaissent sous l'effet de la poussée d'Archimède différentielle.la morphologie de ces courants varie d'une région à l'autre selon la verticale Fig.(9,10) et l'horizontale Fig.(7,8). Cela se traduit par la compétition entre le mécanisme d'amplification de la perturbation et le mécanisme d'amortissement combinant les effets de viscosité et de diffusion de chaleur. Si l'écart de température appliqué entre le disque et le milieu ambiant est trop petit, l'accélération vers le haut est faible et les processus dissipatifs l'emportent. La couche d'air retourne à son état de base. Quant l'écart de température augmente, le mécanisme déstabilisant augmente d'intensité. Il finit par l'emporter au-delà d'un écart critique ΔT_c appelé seuil de convection. L'expérience montre que, suffisamment prés de seuil, cette circulation s'organise en courants de longueur h qui représente la hauteur de la couche d'air sur laquelle les trajectoires de ces courants deviennent tous parallèles à la verticale et asymptotique.

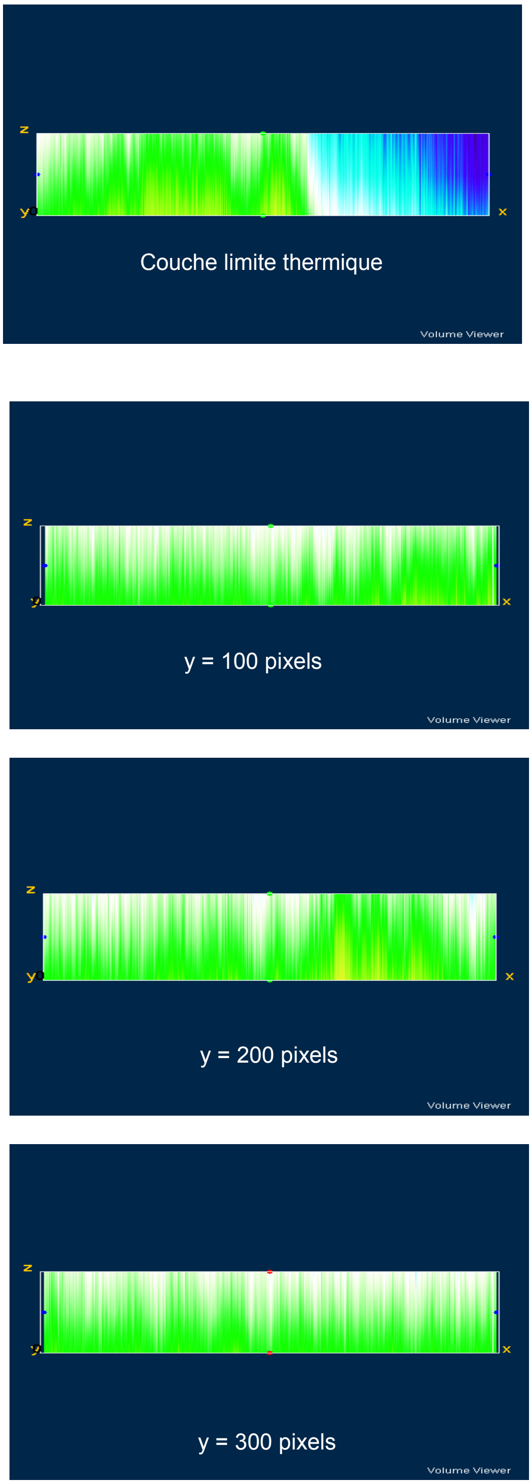

Figure 7: Echantillons temporels pour la répartition horizontale de l'intensité lumineuse le long de la zone de convection

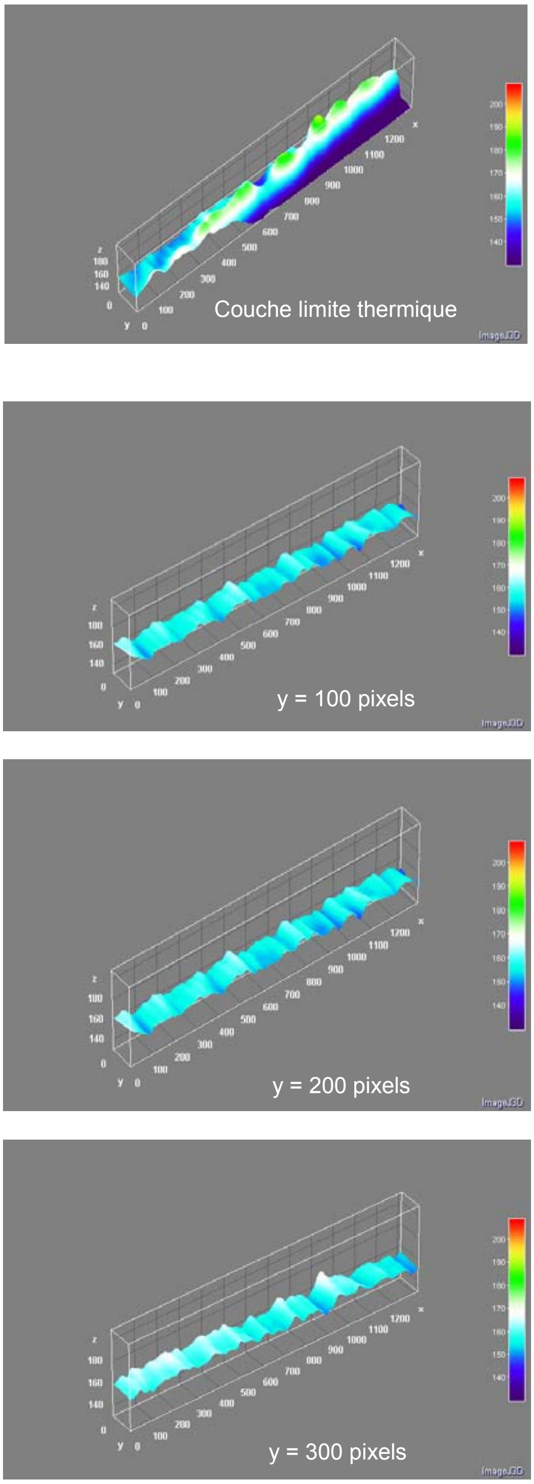

Figure 8: Echantillons temporels pour les profils horizontaux de l'intensité lumineuse le long de la zone de convection

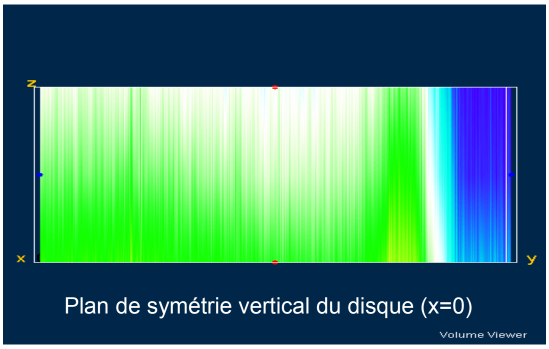

Gauche/ Plan de symétrie

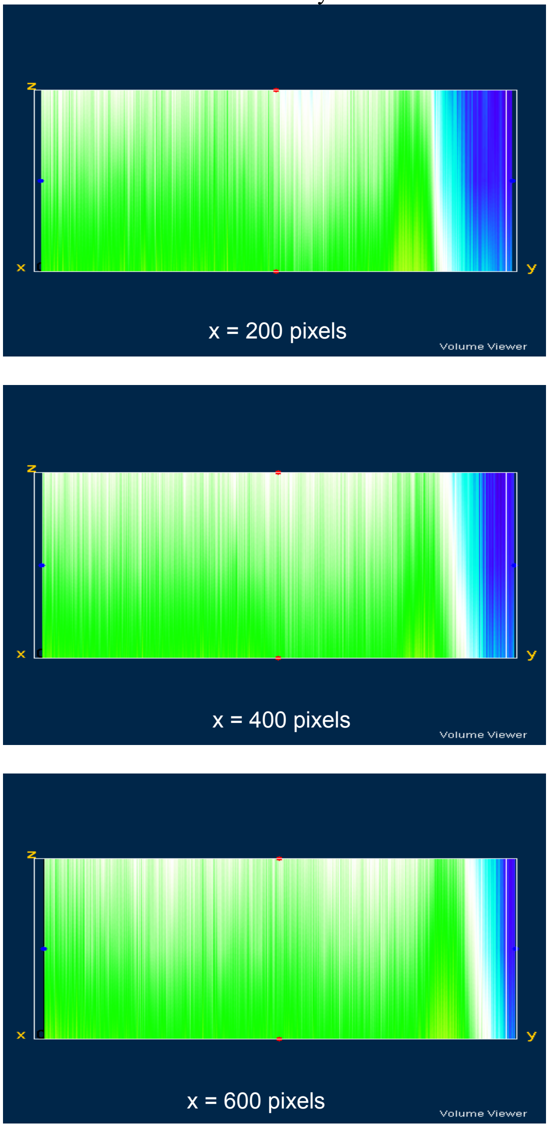

Figure 9-a : Echantillons temporels pour la répartition verticale de l'intensité lumineuse le long de la zone de convection à gauche du plan de symétrie du disque

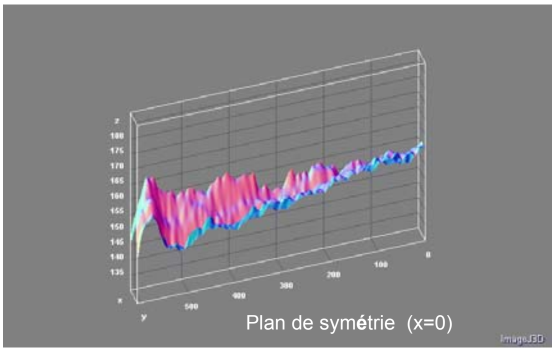

Gauche/ Plan de symétrie

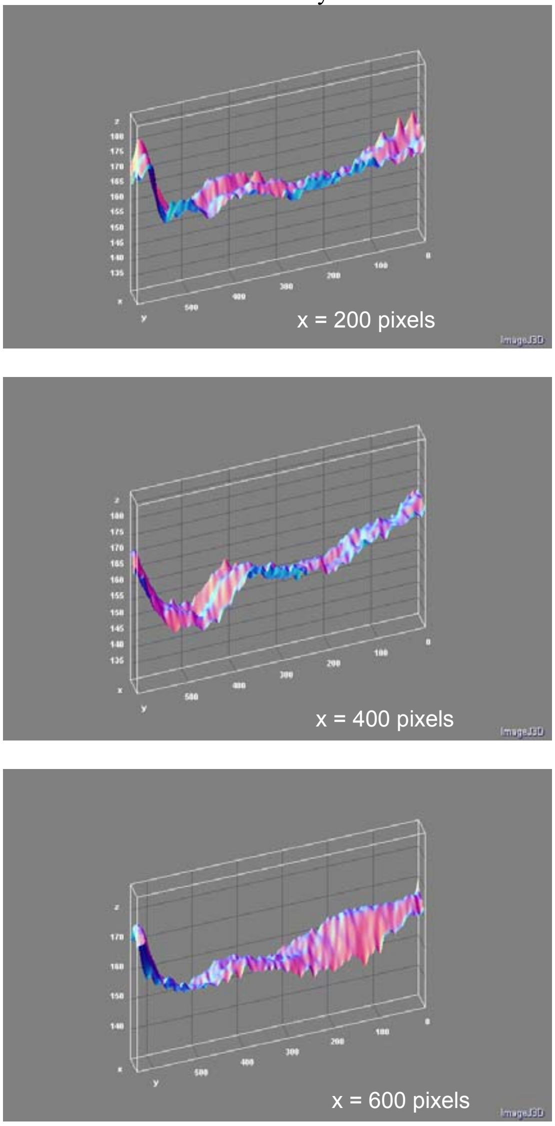

Figure10-b: Echantillons temporels pour les profils verticaux de l'intensité lumineuse le long de la zone de convection à gauche du plan de symétrie du disque

Droite/ Plan de symétrie

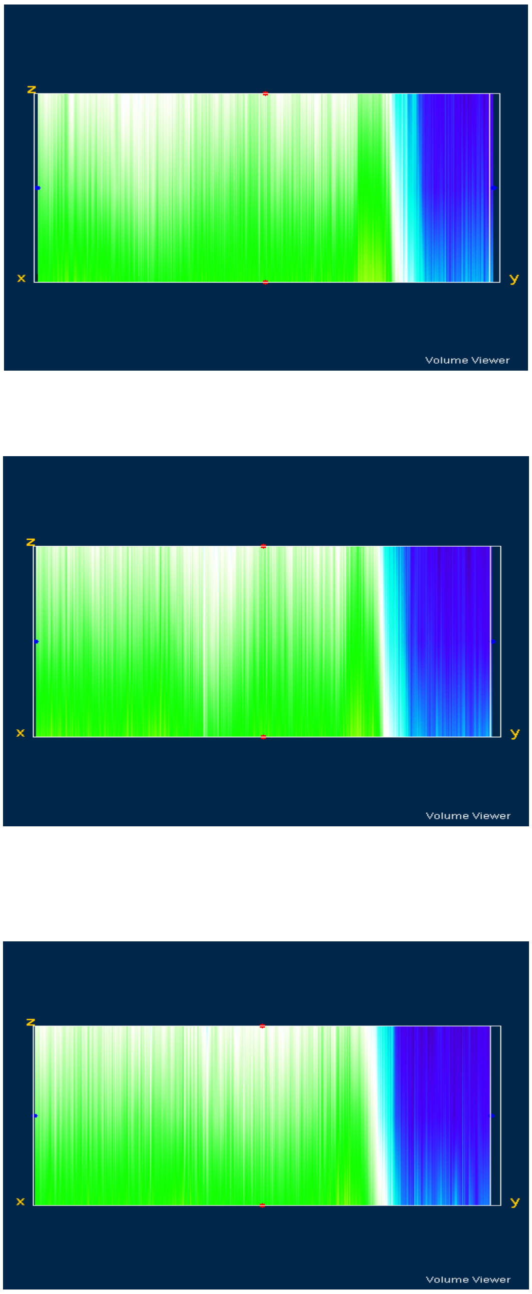

Figure 9-a’: Echantillons temporels pour la répartition verticale de l’intensité lumineuse le long de la zone de convection à droite du plan de symétrie du disque

Droite/ Plan de symétrie

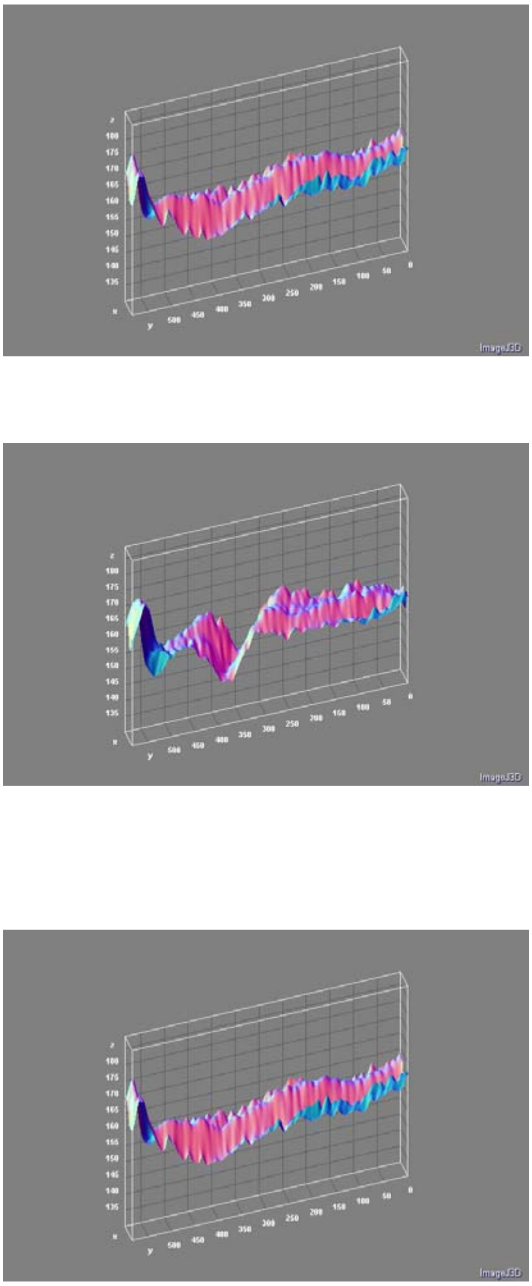

Figure 10-b’ : Echantillons temporels pour les profils verticaux de l’intensité lumineuse le long de la zone de convection à droite du plan de symétrie du disque

Autrement dit, appelant $\dot{x}$ la direction perpendiculaire au plan des courants convectifs, il semble légitime selon la Fig.(11) de représenter le champ de vitesse verticale associé aux courants sous la forme [2]:

$$v_z = X(t).f_v(z).\sin(kx), k = 2\pi/h \qquad (4)$$

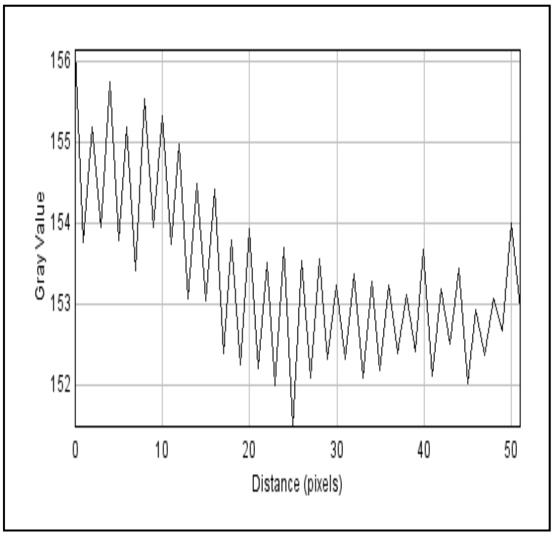

Figure 11 : Profil temporel vertical de la vitesse

Dans cette expression, la périodicité en $\dot{x}$ a été explicitée et la dépendance spatiale séparée de la dépendance temporelle. La forme analytique de $f_v(z)$ est sans importance bien que calculable. La variable $X(t)$ mesurant l'intensité de la convection est donc supposée rendre compte de la dépendance temporelle. Pour ce qui est de la fluctuation de vitesse associée, le mécanisme illustré dans la Fig.(11) suggère fortement d'admettre une dépendance horizontale en phase avec celle de $v(z)$, i.e. $\sim sin(kx)$. Naturellement les deux perturbations (température et vitesse) sont couplées, mais cette fois ci, *essayons de décrire de façon purement phénoménologique le comportement temporel de la perturbation de vitesse* qui conduit à l'établissement des courants convectifs décrits par la relation (4).

En dessous du seuil, celle-ci est amortie, tandis qu'au dessus elle est amplifiée. Son taux de croissance σ passe donc de valeurs négatives en des valeurs positives lorsque l'écart de température ΔT , le paramètre de contrôle de notre problème, atteint puis dépasse la valeur critique ΔT_c.

Définissons un paramètre de contrôle réduit :

$$r = \frac{\Delta T - \Delta T_c}{\Delta T_c} \qquad (5)$$

L'évolution de X , amplitude de la perturbation, est alors décrite par :

$$\frac{d}{dt} X = \sigma X \qquad (6)$$

Où σ est à priori fonction de r

En $r = 0$ c'est-à-dire au seuil $\Delta T = \Delta T_C$ les perturbations ne sont ni amorties ni amplifiées et $\sigma = 0$

Pour r suffisamment petit, on peut se contenter du premier terme d'un développement de σ en puissance de r soit :

$$\sigma = r/\tau_0 \qquad (7)$$

Où τ_0*, homogène à un temps, caractérise l'évolution naturelle des fluctuations.*

L'équation (7) assortie de (6) décrit, selon le signe de r, l'amortissement ou l'amplification de petites perturbations initiales. Lorsque r est négatif, celles-ci régressent et l'état de base correspond à la solution triviale $X = 0$ est stable, sinon il est instable. *Cette évolution des perturbations est exponentielle ce qui est justifié par la Fig. (12)*.

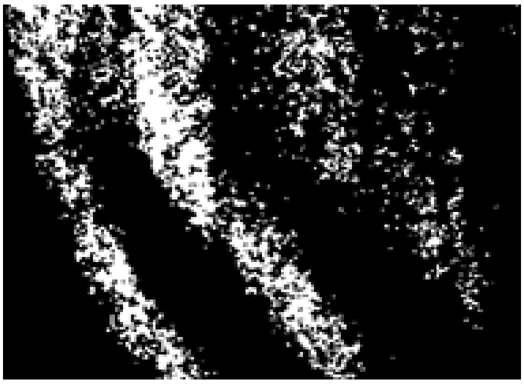

Figure 12 : Région exponentielle

Autant dire que, si elles sont amplifiées, elles ne restent pas longtemps petites et qu'il va falloir tenir compte des effets non linéaires.

Réduisant la fonction X au premier terme significatif de son développement en puissance de X on obtient :

$$\tau_0\sigma_{eff} = r - gX^2 \qquad (8)$$

Où la constante g est homogène à $1/X^2$, ce que l'on peut formaliser en écrivant :

$$g = 1/\bar{X}^2$$

Où $\bar{X}$ représente une certaine amplitude caractéristique mesurant l'intensité des couplages non-linéaires. Lorsque la convection se développe, la chaleur transportée par les courants convectifs augmente au détriment de celle transportée par le flux conductif. Or le mécanisme d'instabilité résulte de la poussée d'Archimède différentielle dans le gradient de température local. Celui-ci est lié au flux conductif par la loi de Fourrier. Ce gradient étant affaibli au cœur de la couche fluide, on admettra sans difficulté que le taux de croissance effectif se trouve diminué par le développement du mode d'instabilité, ce qui correspond à $g > 0$ avec les notations introduites par la formule (5).

Le modèle non linéaire décrivant la convection au voisinage du seuil va donc s'écrire :

$$\begin{aligned}\tau_0\frac{d}{dt}X &= F_r(X) \qquad (9)\\ &= r.X - g.X^3\end{aligned}$$

L'expression F_r définit sur l'espace des phases un champ de vecteurs qui rend compte de la dynamique du système dans cet espace. Son étude, élémentaire, est en voie de finilisation.

CONCLUSION

Cette contribution expérimentale présente une grande concordance avec les résultats publiés dans [1] et la description théorique de la convection naturelle éditée par Paul Manneville dans son livre [3] ainsi que la référence [5] .*l'expérience a montrée et la théorie a justifiée l'allure de la distribution de la température, dans les plans parallèles et verticaux au disque, sous forme des régions alternées.* Cette initiative apporte un complémentaire aux résultats obtenus par des méthodes numériques qui illustrent le champ de température sous formes des droites parallèles au disque.

REFERENCES

[1] E.A. Brun, A.M.Lagarde, J. Mathieu; Mécanique des Fluides, Tome I, III, Deuxième édition, Dunod, Paris (1968, 1970).

[2] Image processing and analysis with ImageJ and MRI Cell Image Analyzer Montpellier RIO Imaging Volker Baecker 30.04.2010

[3] P. Manneville, Dynamique non-linéaire et chaos, Paris VI- Ecole polytechnique

[4] W. Merzkirch; Flow Visualization Academic Press, New-York (1974).

[5]W. Hauf, U.Grigull ; Optical Methods in Heat Transfer, in Advances in heat Transfer, Vol 6, J.P Hartnett, (1970).

[6] M.Cagnet, *Optique instrumentale. Aberration.* Cours, École supérieure d'optique, 1995.

[7] L.Dettwiller, *Les instruments d'Optique : Étude théorique, expérimentale et pratique.* 1997 Ellipses.

[8] J.-L.Meyzonnette, *Radiométrie et sources non cohérentes.* E 4 010, traité Électronique, 1995.

[9] M. Henry, *Optique géométrique.* A 190, traité Sciences fondamentales, 1981.

[10] C.Véret, *Enregistrement rapide des images. Introduction.* R 6 728, traité Mesures et Contrôle, Techniques de l'Ingénieur, oct. 1993.

[11] J.C. Miquel, *Caméras DCP.* EDISCOM (1989).

[12] M.Wetzel, *Cinématographie ultra-rapide. Caméras mécano-optiques à haute résolution* 6 730, traité Mesures et Contrôle, Techniques de l'Ingénieur, avril 1993.

[12] N.Fleurot, *Cinématographie ultrarapide. Caméras électroniques.* R 6 732, traité Mesures et Contrôle, Techniques de l'Ingénieur, avril 1993.

[13] J.C.Miquel, *L'observation en vidéo rapide (de 50 à 25000 trames par seconde).*Tec et Doc. Lavoisier (1985).

African Journal of Science and Technology (AJST)
Science and Engineering Series Vol. 12, No. 2, pp. 80 - 90

ETUDE BATHYMETRIQUE, SEDIMENTOLOGIQUE ET ENVIRONNEMENT DE DEPOTS DES SABLES SUPERFICIELS DE LA LAGUNE DE FRESCO (ZONE OUEST DU LITTORAL IVOIRIEN)

[\] N'guessan ,Y. A., Adopo, L., Amani, E.M., Konan, K.B.
Toure,M. Monde, S. et Aka, K.

[1]Université de Cocody, UFR des Sciences de la Terre et des Ressources
Minières Laboratoire de Géologie Marine et de Sédimentologie.
22 BP 528 Abidjan 22, Côte d'Ivoire.
E-mail: alestouxis@yahoo.fr

RESUME: *Les études granulométriques et les levés bathymétriques effectués en lagune de Fresco, ont permis de caractériser les sédiments et la morphologie du fond de cette lagune. Sur le fond, les sédiments sont constitués de vases localisées dans les bras de la lagune alors que dans la lagune de Fresco proprement dite, on rencontre essentiellement des sables. Les galets et les graviers se localisent par endroit, sur la rive Nord de la lagune, au Sud-Est de la ville de Fresco. L'essentiel des sables de la lagune de Fresco provient d'un environnement de type continental fluviatile. La majorité des sables se déplace par saltation. Le mode de transport des silts, des argiles et des sables très fins est exclusivement par suspension. Les sables fins ont un mode de transport dominé par le transport par suspension. Les sables moyens se déplacent exclusivement par saltation. Le transport par roulement est le mode de transport dominant des sables grossiers. Cette étude a permis de réaliser les cartes bathymétriques et de répartition des sédiments, ainsi que la détermination de l'environnement de dépôts des sables.*

Mots clés : *Morphologie, Sédimentologie, Environnement de dépôts, Lagune de Fresco, Côte d'Ivoire.*

INTRODUCTION

Les lagunes sont le lieu de transit de la plus grande partie des apports continentaux. La compréhension des interrelations entre les continents et l'océan passe par l'étude des milieux saumâtres qui jouent un rôle d'interface essentiel puisqu'ils sont le siège de phénomènes complexes liés aux échanges entre eaux douces et marines. (Kouassi, 2005).

La Côte d'Ivoire possède un système lagunaire situé dans la zone littorale au Sud. Il forme l'interface entre les milieux continental, fluvial et marin et s'étend parallèlement au rivage du Golfe de Guinée sur près de 300 km. Entre les 2°50' et 5°45' de longitude Ouest sa superficie totale est de 1200 km^2 (Varlet, 1978). La lagune de Fresco objet de la présente étude, est située entre les 5°32' et 5°38' de longitude Ouest et les 5°40' et 5°70' de latitude Nord, avec une superficie de 17 km^2 (Figure 1). Elle est alimentée en eaux douces par les rivières Bolo et Niouniourou (Sankaré et al., 1999 ; Egnankou et al., 2004). Le plan d'eau lagunaire s'étire d'Est en Ouest, sur une longueur d'environ 6 km et une largeur comprise entre 2 et 4 km. La lagune de Fresco et les autres lagunes ivoiriennes constituent, avec les écosystèmes adjacents, de véritables supports de subsistance pour les populations environnantes. Ces populations installées sur les rives des lagunes ont entre autres, pour activité économique principale la pêche. Ces activités entraînent un changement défavorable des caractéristiques naturelles de ces milieux saumâtres. Les investigations menées sur ces lagunes se sont intéressées entre autres à l'hydrodynamisme, à la morphobathymétrie, à la circulation des masses d'eau, à la géochimie, à la physico-chimie, à l'hydroclimat et à la modélisation de la dispersion du sel et de l'eau douce (Affian, 2003 ; Monde, 2004 ; N'guessan, 2008 ; Wango, 2009). Les études antérieures sur la lagune de Fresco portent essentiellement sur la biologie (Egnankou, 1985 ; Egnankou et al., 2004 ; Nicole et al., 1987) et sur la géochimie des sédiments superficiels (Issola et al., 2008). Toutefois, la morphologie du fond et l'environnement de dépôts des sédiments superficiels de la lagune de Fresco restent encore méconnus. Cette étude traitera de la bathymétrie, de la sédimentologie et de l'environnement de dépôt des sables superficiels de la lagune de Fresco. L'analyse bathymétrique permettra de mettre en évidence la morphologie du fond. Ensuite l'étude s'intéressera à la sédimentologique, et à la granulométrique afin de dégager le comportement hydrodynamique des grains de sable en tenant compte à la fois de leur répartition, de leur taille, de leur nature et de leur origine. Elle se terminera par l'examen du mode de transport de ces sables afin de dégager leur environnement de dépôt.

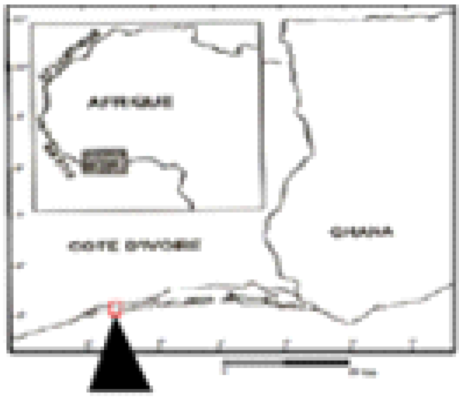

MATERIELETMETHODES

Levés et traitements de sondes bathymétriques

Les levés bathymétriques ont été effectués le long des radiales à partir d'un échosondeur de type Lowrance, modèle LMS-160 et Global Map^{TM} 1600, couplé à un récepteur GPS pour l'acquisition des sondes (Diner et Marchand, 1995 in Monde, 1997). Elles ont été mesurées avec une fréquence de 160 kHz qui permet aux signaux émis de ne pas pénétrer les vases (Lowrance, 1998) et la lecture faite directement sur l'écran de l'unité centrale. Les corrections sont effectuées afin de déterminer la profondeur réelle à chaque point. Ces corrections concernent la profondeur d'immersion du transducteur et la marée dynamique (Abé, 2005). Les sondes réelles sont traitées et analysées afin de tracer des contours de cartes, des courbes d'isovaleurs dans un plan de la lagune de Fresco.

Prélèvements et traitements des sédiments superficiels

L'échantillonnage des sédiments de la lagune de Fresco, s'est déroulé à l'aide d'une benne Van Veen. Ces prélèvements ponctuels (31 au total)(Figure 2) ont été positionnés par un récepteur GPSGARMIN dont la précision est environ de 2 m (Wognin, 2004). Pour l'étude granulométrique, les sédiments meubles, après conditionnement (lavage et séparation de la fraction supérieure à 63 ìm ; attaques chimiques à l'acide chlorhydrique et à l'eau oxygénée pour l'élimination respective des carbonates et de la matière organique; séchage à l'étuve) ont subi un tamisage sur une colonne de seize tamis vibrants de la série AFNOR, de mailles comprises entre 63 ìm et 5 mm (N'guessan et al., 2008). La cartographie des faciès des sédiments superficiels de la lagune de Fresco a été réalisée. A partir des formules de Folk et Ward (1957) basées sur l'unité F (où F = -log2 d, avec d désignant le diamètre des particules en millimètre), six paramètres de distribution granulométriques ont été calculés. Ce sont : la médiane (Md), le mode (Mo), le grain moyen (M), l'indice de tri (IT), l'écart type ou classement ou Sorting (So) et l'asymétrie ou le Skewness (Sk). Des cartes de répartition des sédiments (galets et graviers, sables, vases) ont été réalisées.

Le test de Visher a permis de mettre en relation la granulométrie et le mode de transport. L'auteur Visher (1969) porte en ordonnées les pourcentages cumulés et en abscisses la taille (en unité phi (F)) des classes granulométriques correspondantes. Cette méthode permet de définir trois modes de transport qui sont : la suspension, la saltation et le roulement (ou reptation, ou charriage ou encore "surface creep").

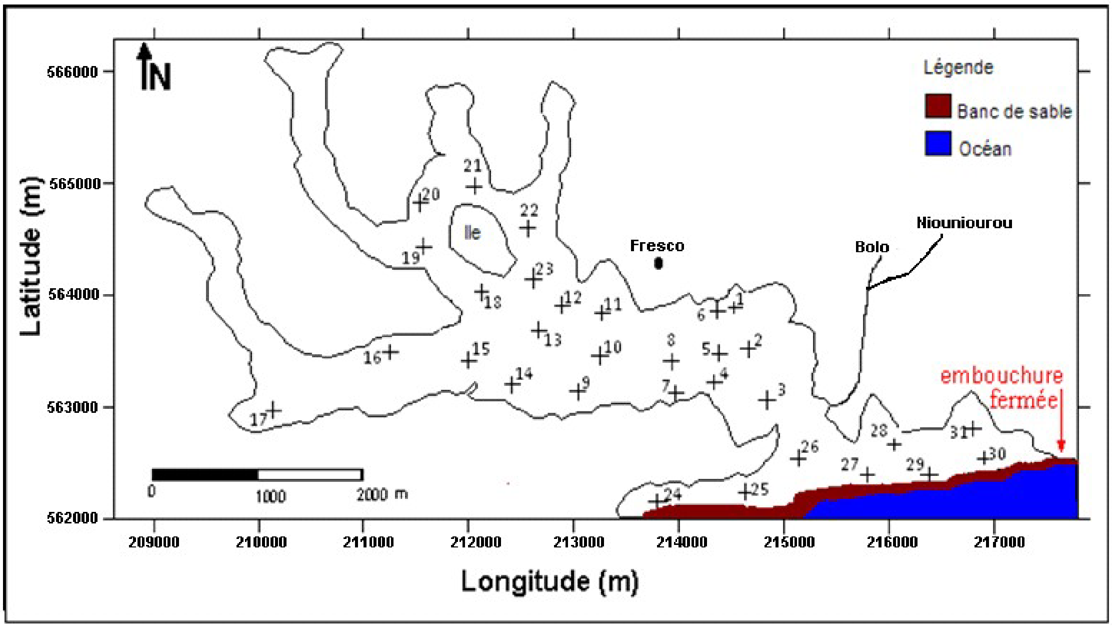

Figure 2 : Localisation des points de prélèvement

RESULTATS ET DISCUSSION

3.1 Morphologie de la lagune de Fresco

L'examen de la carte bathymétrique de la lagune de Fresco (Figure 3) montre que les profondeurs varient de 0 à 3,5 m. Sur 17 km^2 de la superficie totale de la lagune de Fresco les profondeurs ne dépassent guère les 1,8 m surtout dans les environs de l'île. Les profondeurs les plus élevées s'observent à l'exutoire de la rivière Bolo où elles atteignent 3,5 m. Deux dépressions lagunaires sont nettement identifiables à l'Est, au débouché du Bolo. Ce sont : la dépression principale de 3,2 m de profondeur, située au niveau de la longitude 215 000 m, au Sud-Est de la lagune. Elle se situe à proximité du banc de sable entre la lagune et l'Océan Atlantique ; un peu plus au Nord de la dépression principale, une dépression profonde de 2,8 m maximum, située à proximité de la rivière Bolo. La présence de ces deux dépressions pourrait s'expliquer par le fort courant de la rivière Bolo pendant la période de crue, qui empêche le dépôt des sédiments, facilitant ainsi la mise en place de celles-ci. Le modèle numérique d'élévation du fond de la lagune de Fresco (Figure 4) a permis de mettre en évidence quelques hauts-fonds. Ils se rencontrent dans la zone centrale de la lagune à proximité de l'île. Ils correspondraient au prolongement sous lagunaires des alluvions provenant des eaux de ruissellement et des différents bras de la lagune de Fresco. Ainsi ils se localisent dans un environnement vaseux, traduisant les conditions hydrodynamiques assez calmes. Leur formation pourrait être due à l'accumulation des sédiments provenant du continent à travers les bras de la lagune de Fresco.

L'étude des profils bathymétrique de la lagune de Fresco montre des chenaux en forme de "V" qui résultent d'un processus d'érosion (Aka, 1991). Les chenaux en forme de "U" observés traduisent un équilibre d'action entre les agents d'érosion et d'accumulation. Les formes intermédiaires mis en évidence montrent que les agents d'érosion ont donc une action plus intense que celle des agents d'accumulation (Derruau, 1962).

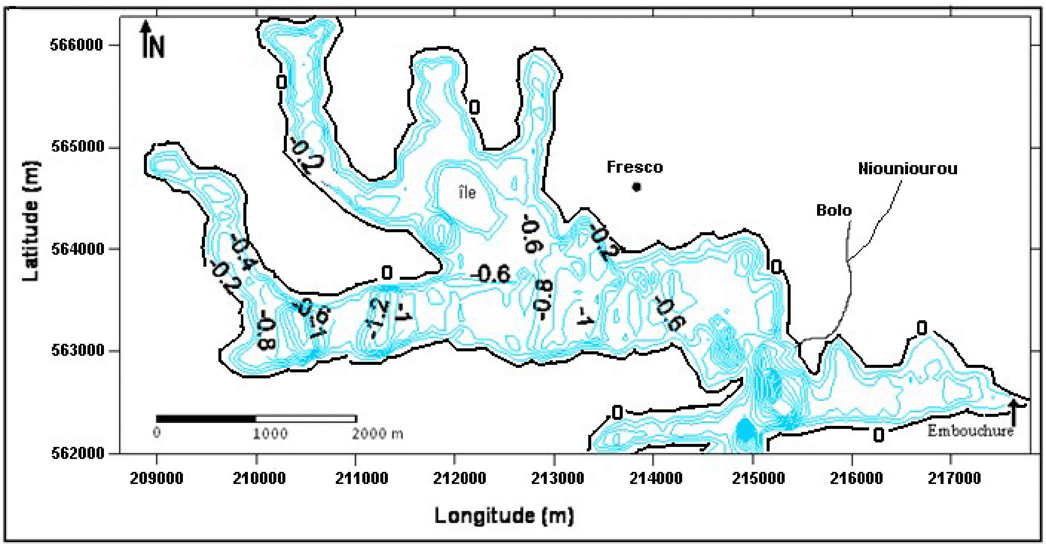

Figure 3 : Carte bathymétrique de la lagune de Fresco

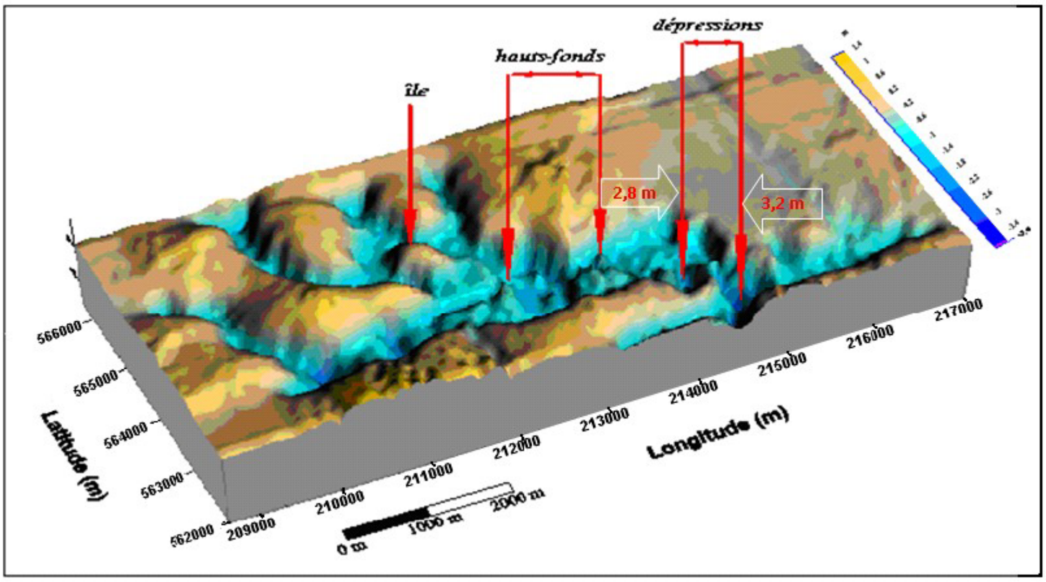

Figure 4 : Modèle numérique d'élévation de la lagune de Fresco

Sédimentologie des sédiments superficiels de la lagune de Fresco

Description lithologique des sédiments superficiels

L'analyse macroscopique des sédiments superficiels de la lagune de Fresco met en évidence quatre faciès lithologiques. Il s'agit de galets et graviers, de sables, de vase et de sédiments "mixtes", caractéristique des lagunes ivoiriennes (N'guessan *et al.*, 2011) :

- les galets et les graviers sont de couleur brun ;
- les sables vont de très fins à grossiers. Leur couleur est jaune ocre, jaune roux et gris clair. On y trouve, quelques débris coquilliers et végétaux ;
- les vases sont de couleur variable, du noir au gris et avec une compacité variable. Cette couleur sombre des vases pourrait être due en partie à l'apport de la matière organique produite par la dégradation des débris végétaux provenant de la forêt et des mangroves sur les berges de la lagune de Fresco. Elles sont peu plastiques et moins cohésives. Néanmoins la vase organique d'aspect crémeux ou "crème" de vase a été identifiée (Tastet, 1979 ; N'guessan, 2008).
- les sédiments "mixtes" sont constitués de sables vaseux et de vases sableuses. Leur coloration varie du noir au gris, épousant ainsi la couleur de la vase. Ils contiennent des débris végétaux et coquilliers.

Répartition des faciès superficiels de la lagune de Fresco

La figure 5 présente la répartition des faciès sédimentaires de la lagune de Fresco. Les galets et les graviers se localisent, sur la rive Nord de la lagune, au Sud-Est de la ville de Fresco. A ce niveau la lagune est en contact avec les terrains nus, à proximité de la ville. Les eaux de ruissellement provenant de ces terrains alimentent la lagune en sédiments, en particulier en galets et en graviers. Ces zones correspondent à la proximité de la ville de Fresco. Ces sédiments se concentrent à des faibles profondeurs de moins de 0,5 m. Les sables occupent la lagune de Fresco proprement dite, dans sa zone Est, Sud et Centre. Ils se concentrent à proximité de la ville de Fresco et du banc sableux séparant la lagune de l'océan Atlantique. Les sables se concentrent aussi à l'exutoire de la rivière Bolo et dans les zones proximales (Issola *et al.*, 2008). Les sables proviennent des formations sableuses encaissantes soit par remaniement à partir des berges, soit par des apports de rivières, notamment des rivières Bolo et Niouniourou. Ils peuvent provenir en partie du cordon sableux, contact avec l'océan. Ces sédiments sableux se concentrent essentiellement à des profondeurs faibles à élevées, pouvant atteindre les profondeurs maximales de 3,5 m, dans les dépressions. Cela pourrait s'expliquer par le fait que les eaux de ruissellement et les rivières qui transportent la plupart des sables atteignent une vitesse presque nulle au contact de la lagune. Vu

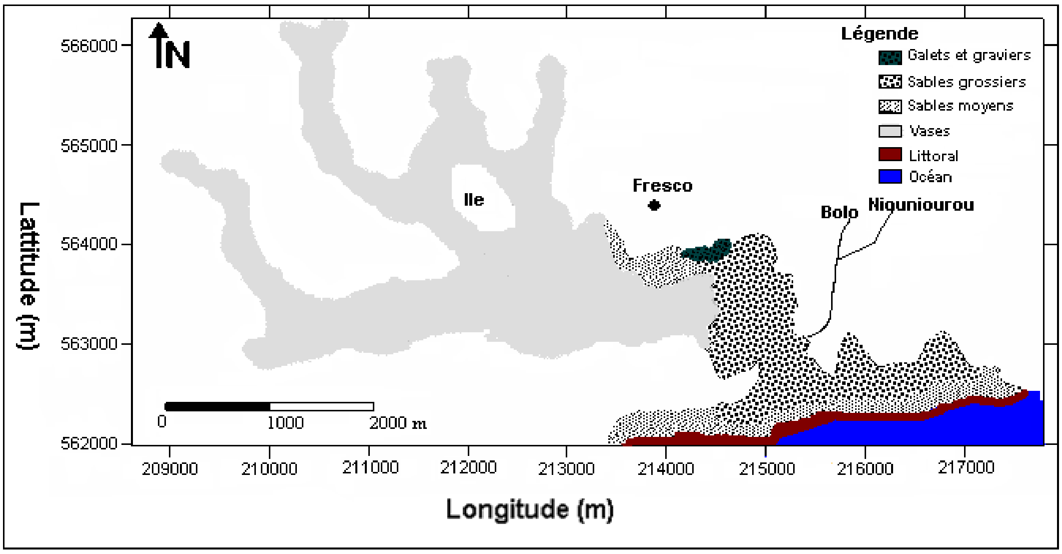

Figure 5 : Carte de répartition des faciès sédimentaires de la lagune de Fresco

l'interruption de leur avancée par le banc de sable, le courant n'étant plus fort et donc incapable de transporter les grains de sables de taille plus importante, les déposes sur les berges et dans les dépressions à des profondeurs de 0 à 3,5 m. Les vases s'accumulent aux profondeurs inférieures à 1,8 m sur les 2/3 du fond lagunaire. Elles se localisent dans les bras, dans la zone centrale et à proximité de l'île de la lagune (figure 5). Cette accumulation est due au dépôt par décantation et au remaniement des zones de bordure des bras par le clapot (Tastet & Guiral, 1994). Les vases, de taille plus petite restent en suspension dans l'eau et se déposent par décantation sur les fonds lagunaires (Sanchez & Levacher, 2007).

Mode de transport et environnement de dépôt des sédiments de la lagune de Fresco

Mode de transport des sédiments

Le test de Visher (1969) réalisé sur les sédiments superficiels de la lagune de Fresco donne les résultats présentés par la figure 6. Il permet de montrer la relation entre la granulométrie des sédiments et leur mode de transport. Ainsi trois populations de sables se distinguent :

- la population A est marquée par le transport des grains par suspension ;
- la population B rassemble les sables transportés par saltation ;
- la population C regroupe les sables transportés par roulement.

L'analyse des résultats montre que la population B est la plus importante (Tableau 1). Elle représente une proportion de 47%. Les deux autres cas restant se repartissent entre la population A (28%) et la population C (25%). Cette analyse quantitative montre que la majorité des sédiments se déplace par saltation. Néanmoins, certains sédiments sont transportés par suspension et par charriage.

Tableau 1 : Proportion de sédiment selon les différents modes de transport

	Population A (90-100%)	Population B (20-90%)	Population C (0-20%)
Effectif par population	37	61	33
% par population	28%	47%	25%

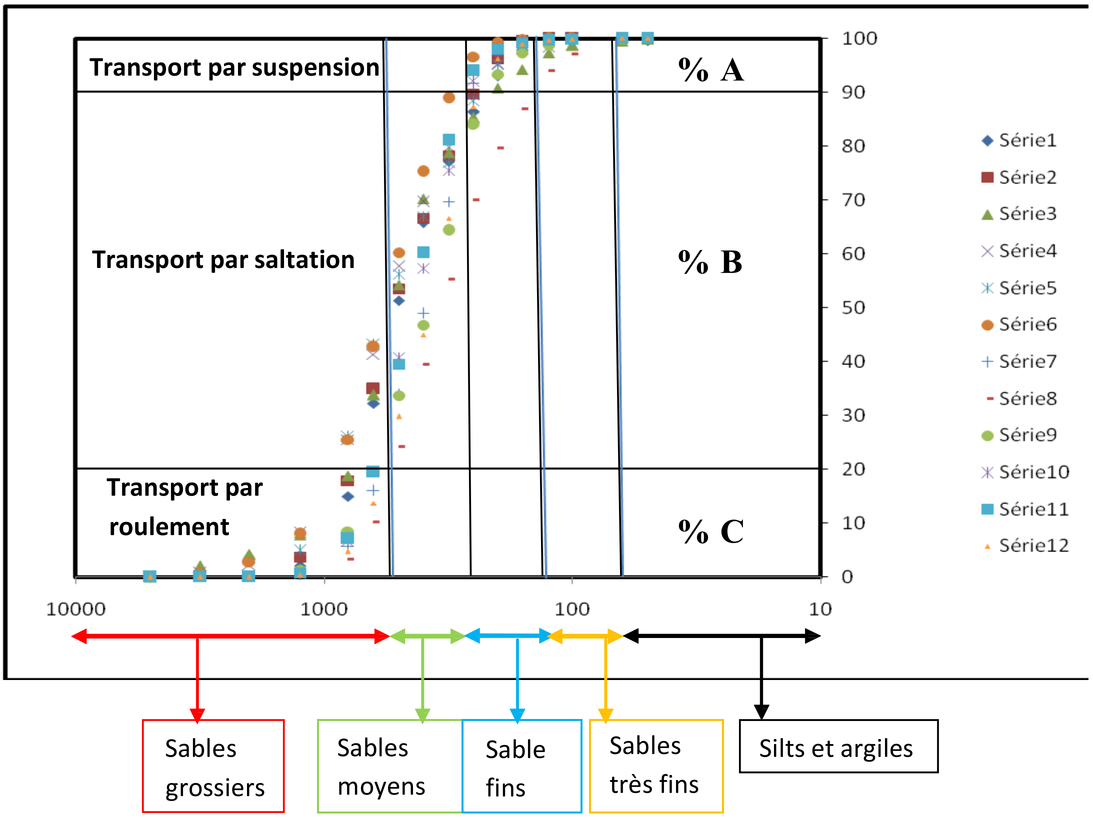

Figure 6 : Diagramme de répartition des sables selon le test de Visher

Par ailleurs, la caractérisation du type de transport dans les différentes classes granulométriques représentée par le tableau 2 montre que :

- les silts, les argiles et les sables très fins (Ø<0,20 mm) ont pour mode exclusif de transport la suspension ;
- le mode de transport des sables fins (Ø<0,315 mm) est dominé par le transport par suspension (70% du matériel fin). Néanmoins 30% de ces sables fins sont portés par saltation.
- les sables moyens de taille comprise entre 0,315 et 1,25 mm se déplacent exclusivement par saltation (100% du matériel moyen) ;
- le transport par charriage (ou roulement) est le mode de transport dominant des sables grossiers (Ø>1,25 mm) avec une proportion de 75% du matériel grossier. Par ailleurs 25% de ce matériel grossier est transporté par saltation.

Tableau 2 : Caractérisation du type de transport selon les classes granulométriques

	Roulement (%)	Saltation (%)	Suspension (%)
Sables grossiers	75%	25%	0%
Sables moyens	0%	100%	0%
Sables fins	0%	30%	70%
Sables très fins	0%	0%	100%
Silts et Argiles	0%	0%	100%

Environnement de dépôts des sédiments de la lagune de Fresco

Les diagrammes Md-So et Sk-Md de l'évolution des paramètres granulométriques des sables de la lagune de Fresco permettent de déterminer leur milieu de dépôt. Le diagramme Md-So de la figure 7 présente la dispersion des points. Elle se fait entre le domaine de plages et le domaine de rivières. A l'analyse, tous les points sauf deux sont regroupés dans le domaine des rivières. Ceci signifie que 91% des grains sont issus des rivières (Tableau 3). Les sédiments pourraient dans ce cas être des sables d'origine fluviatile (Moiola & Weiser, 1968). En effet ils seraient transportés par les rivières Bolo et Niouniourou avant d'être déposés en lagune. La majorité de ces sables provient des rivières Bolo et Niouniourou et de la rive Nord de la lagune de Fresco (figure 7). Toutefois, une quantité insuffisante (9%) des sables provient des plages. Ainsi, l'essentiel des sables de la lagune de Fresco provient d'un environnement de type rivières.

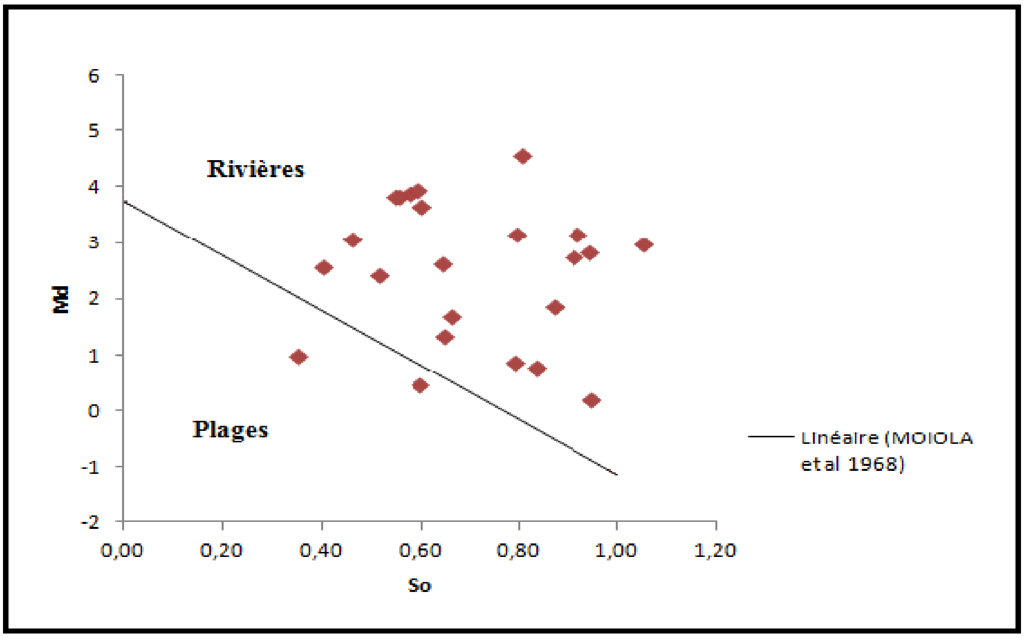

Figure 7 : Diagramme Md-So (Moiola et Weiser, 1968)

Tableau 3 : Proportion de sédiment selon l'environnement de dépôt (Diagramme Md-So)

	Rivières	Plages
Effectif par environnement	20	2
% par environnement	90,90%	09,10%

La figure 8 présente le diagramme de dispersion Sk-Md. La répartition des points se fait dans le milieu des dunes continentales (59%) et dans le milieu des dunes côtières (41%). Ces proportions (Tableau 4) ne permettent pas de caractériser l'origine de ces sables. Cela pourrait s'expliquer par le fait que la lagune de Fresco joue un rôle d'interface entre le milieu continental et le milieu marin. La lagune est alimentée par un bassin principal qui draine les régions du socle précambrien, auxquels s'ajoutent les apports des rivières Bolo et Niouniourou. Les sédiments pourraient être drainés des dunes côtières (41%) par les rivières et par les eaux de ruissellement avant d'être déposés en lagune. Toutefois, le domaine des dunes continentales serait l'environnement de dépôt des sables de la lagune de Fresco (Moiola & Weiser, 1968). En somme les sédiments de la lagune de Fresco proviennent essentiellement d'un environnement de type continental fluviatile.

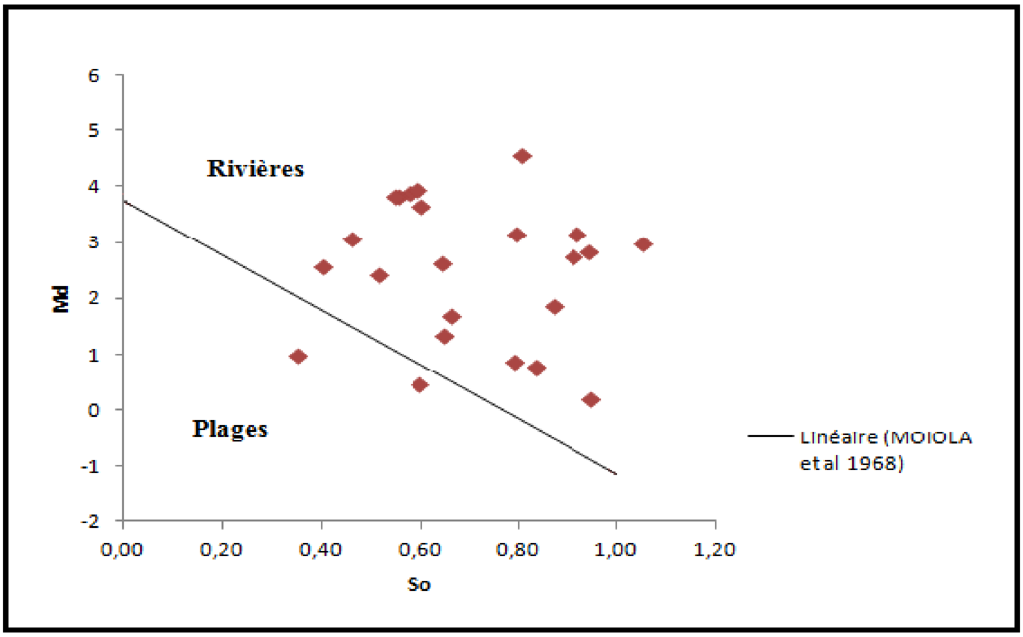

Figure 8 : Diagramme Sk-Md (Moiola et Weiser, 1968)

Tableau 4 : Proportion de sédiment selon l'environnement de dépôt (Diagramme Sk-Md)

	Dunes côtières	Dunes continentales
Effectif par environnement	9	13
% par environnement	40,91%	59,09%

Analyse minéralogique et morphoscopie des grains de sables de la lagune de Fresco

Analyse minéralogique des sédiments

L'analyse minéralogique des sédiments a donné les minéraux suivants :

Amphibole (2,16 %), Biotite (3,75 %), Chlorite (0,16 %), Feldspath (0,38 %), Muscovite (5,62 %), Plagioclase (1,44 %), Pyroxène (0,65 %) et Quartz (85,6 %). Une abondance remarquable du quartz est notée.

Morphoscopie des grains de sables

Les sables observés montrent une morphoscopie variant des arrondis aux anguleux. Aussi les variantes (sub-anguleux et les sub-arrondis) sont très abondantes. Cesrésultats montrent que les sédiments ont été transportés sur une distance plus ou moins importante avant de se déposer en lagune. Leurs aspects luisants montrent qu'ils ont subi un transport en milieu aqueux. La plupart des sédiments sont transportés et déposés en lagune par les rivières Bolo et Niouniourou. Ils sont d'origine fluviatile.

CONCLUSIONS

La lagune de Fresco est caractérisée par des profondeurs de 0 à 3,5 m. Les profondeurs les plus élevées correspondent aux dépressions situées à l'exutoire de la rivière Bolo. Les hauts-fonds qui s'y trouvent se rencontrent dans la zone centrale de la lagune à proximité de l'île. L'étude lithologique et granulométrique des sédiments superficiels, indique que les galets et les graviers, se localisent sur la rive Nord de la lagune, au Sud-Est de la ville de Fresco. Les sables occupent la lagune de Fresco proprement dite dans sa zone Sud, Est et centre et à l'exutoire du Bolo à des profondeurs variables (0 à 3,5 m). Les vases se concentrent aux profondeurs inférieures à 1,8 m. Elles se localisent dans les bras, dans la zone centrale et à proximité de l'île de la lagune. L'étude de l'environnement de dépôts nous amène à dire que, l'essentiel des sables de la lagune de Fresco provient d'un environnement de type rivières. En effet ils sont transportés par les rivières Bolo et Niouniourou avant d'être déposés en lagune. La majorité de ces sables proviennent des rivières Bolo et Niouniourou et de la rive Nord de la lagune de Fresco. Les sédiments pourraient être drainés des dunes côtières (41%) par les rivières et par les eaux de ruissellement avant d'être déposés en lagune. Toutefois, le domaine des dunes continentales serait l'environnement de dépôt des sables de la lagune de Fresco. L'analyse quantitative montre que la majorité des sédiments se déplace par saltation. Toutefois, certains sédiments se déplacent par suspension et par charriage. Le mode de transport des silts, des argiles et des sables très fins est exclusivement par suspension. Celui des sables fins est dominé par le transport par suspension (70% du matériel fin). Les sables moyens se déplacent exclusivement par saltation (100 % du matériel moyen). Le transport par roulement est le mode de transport dominant des sables grossiers avec une proportion de 75% du matériel grossier. Les sables très bien classés varient des grains arrondis aux grains anguleux. Les sub-anguleux et les sub-arrondis sont abondants et leurs aspects est luisants, preuve qu'ils ont été transportés en milieu fluviatile sur une distance plus ou moins longue. La minéralogie des sédiments superficiels nous donne une forte proportion des grains de quartz avec plus de 85 %.

REFERENCES BIBLIOGRPHIQUES

ABE J. (2005). *Contribution à la connaissance de la morphologie et de la dynamique du littoral ivoirien (cas du littoral d'Abidjan).* Essais de modélisation en vue d'une gestion rationnelle. Thèse Doctorat d'Etat, Université Cocody, Abidjan, Côte d'Ivoire, 345 p.

AFFIAN K. (2003). *Approche environnementale d'un écosystème lagunaire microtidal (la lagune Ebrié en Côte d'Ivoire), par des études géochimiques, bathymétriques et hydrologiques: contribution du S.I.G. et de la télédétection.* Thèse Doctorat d'Etat, ès Sc. Nat., Université de Cocody, Abidjan, Côte d'Ivoire, 222p.

AKA K. (1991). *La sédimentation quaternaire sur la marge de la Côte d'Ivoire : Essai de modélisation.* Thèse doc. Etat es sc. Nat. Unv. Abidjan Cocody n°146, 320p.

DERRUAU M. (1962). *Précis de Géomorphologie* – Librairies de l'Académie de Médecine. Masson & Cie. Editeurs. 120, Boul. Saint Germain, Paris, 1er Trim. 1962, 391p.

DINER N. & MARCHAND P. (1995). *Acoustique et pêche maritime*, Masson, Paris, 300p. 69 fig.

EGNANKOU W. M. (1985). *Etude des mangroves de Côte d'Ivoire: Aspect écologique et recherches sur les possibilités de leur aménagement*. Thèse de Doctorat de 3è Cycle, Université Paul -Sabatier Toulouse III, N° 3196: 176p.

EGNANKOU W. M., SANKARE Y., CONARAMS-CI. (2004). *Fiche descriptive sur les zones humides Ramsar (FDR), Fresco (Côte d'Ivoire).*

ETILE N. R. (2004). *Etude de l'environnement hydroclimatique d'une lagune tropicale(lagune de Grand-Lahou, Côte d'Ivoire).* DEA Université de Cocody, 48p.

FOLK R.L., WARD W.C. (1957). *Brazos river bar, a study in the significance of grain size parameters*. Journal of Sedimentary Petrology, n° 27, pp 3- 26.

ISSOLA Y., KOUASSI A. M., DONGUI K. B., BIEMI J. *Caractéristiques physico chimiques d'une lagune côtière tropicale : lagune de Fresco (Côte d'Ivoire).* Afrique Science, Vol.4, N°3 (2008), 1 septembre 2008, 10p.

KOUASSI A. M. (2005). *Hydrochimie et qualité des eaux de deux lagunes tropicales de Côte d'Ivoire (Ebrié, Grand-Lahou).* Thèse de Doctorat, Université ce Cocody : 147p.

LOWRANCE (1998). *LMS-160 et Global Map 1600 ; Directive d'installation et notetechnique.* Lowrance Electronics, Inc. 75 p.

MOIOLA R.J. et WEISER D. (1968). *Textural parameters: an evaluation*. Journal of Sedimentary Petrology, n° 38, pp 45- 53.

MONDE S. (1997). *Nouvelles approches de la cartographie du plateau continental de la Côte d'Ivoire : Aspects morphologiques et sédimentologiques*. Thèse Doctorat 3^{ème} Cycle, 175p. Université Abidjan, Côte d'Ivoire.

MONDE S. (2004). *Etude de la circulation des masses d'eau dans la lagune Ebrié (Côte d'Ivoire). Modélisation hydrodynamique 2DH*. Thèse Doctorat Etat, ès Sc. Nat., Université de Cocody, Abidjan, Côte d'Ivoire, 238 p.175p.

N'GUESSAN Y.A. (2008). *Analyse morphologique, sédimentologique et environnement de dépôts des sédiments superficiels des lagunes Adjin et Potou (Zone littorale de la Côte d'Ivoire).* Thèse Unique, Université Cocody, Abidjan, Côte d'Ivoire 171 p.

N'GUESSAN Y.A., MONDE S., AKA K. (2008*). Sedimentological analysis and paleoenvironment of the* surface *sediments of the Adjin and Potou lagoons*. European Journal of Scientific Research, Vol. 19, n° 2, pp 391- 404.

N'GUESSAN Y.A., WOGNIN V., COULIBALY A., MONDE S., WANGO T.E., AKA K. (2011*). Analyse granulométrique et environnement de depots des sables superficiels de la lagune Adjin (Côte d'Ivoire).* Revue Paralia, Vol. 4, pp 6.1- 6.14.

NICOLE M. EGNANKOU W. M. SCHMIDT M. (1987). *Les zones humides côtières de Côted'Ivoire*. 73p.

SANCHEZ M., LEVACHER D. (2007). *The influence of particle size of the dispersed mineral fraction on the settlement of marine and estuarine muds*. Geo-Marine Letters. Vol. 27, n° 5, pp 303-313.

SANKARE Y. AVIT J-BLF. EGNANKOU W. M. SAENGER P. (1999). *Etude floristique des mangroves des milieux margino-littoraux de Côte d'Ivoire*. Bull. Jard. Bot. Nat. Belg. 67:335-360.

TASTET J.P. (1979). *Environnements sédimentaires et structuraux quaternaires du littoral du golfe de Guinée (Côte d'Ivoire, Togo et Bénin).* Thèse Doctorat d'Etat, Université Bordeaux I, France, 175 p.

TASTET J.P., GUIRAL D. (1994). *Géologie et sédimentologie. in : Environnement et ressources aquatiques de Côte d'Ivoire*, t. II. Les milieux lagunaires, édition ORSTOM, pp 35- 58.

VARLET F. (1978). *Le régime de la lagune Ebrié (Côte d'Ivoire), Traits physiques essentiels*. Travaux et Documents ORSTOM, n° 83, 110 figs., 164 p.

VISHER G.S. (1969). *Grain size distributions and depositional processes.* Journal ofSedimentary Petrology, Vol. 39, n° 3, pp 1074-1106.

WANGO T. E. (2009). *Modélisation de l'hydrodynamisme, de la dispersion du sel et de l'eau douce dans le complexe lagunaire de Côte d'Ivoire*. Thèse Unique, Université Cocody, Abidjan, Côte d'Ivoire, 173 p.

WOGNIN A.V.I. (2004). *Hydrologie et sédimentologie à l'embouchure du fleuve Bandama.* Thèse de Doctorat, Université Cocody, Abidjan, Côte d'Ivoire, 195 p.

African Journal of Science and Technology (AJST)
Science and Engineering Series Vol. 12, No. 2, pp. 91 - 98

ÈVALUATION DE LA VIROSE DU JAUNISSEMENT ET DE L'ENROULEMENT EN CUILLERE DES FEUILLES DE TOMATE (Lycopersicon esculentum Mill) SUR DIVERS CULTIVARS AU SENEGAL

\Mouhameth CAMARA[1], Abdou Aziz MBAYE[2], Samba Arona Ndiaye SAMBA[3], Tala GUEYE[3], Kandioura NOBA[4], Samba DIAO[2] et Christian CILAS[5]

[1]Département Productions Végétales, Institut Supérieur de Formation Agricole et Rurale (ISFAR), Université de Thiès, BP 54, Bambey, Sénégal,
[2]Laboratoire de Phytopathologie, Centre pour le Développement de l'Horticulture (CDH), ISRA BP 3120, Dakar, Sénégal,
[3]École Nationale Supérieure d'Agriculture (ENSA), Université de Thiès. BP 967, Dakar, Sénégal
[4]Département de Biologie Végétale, Université Cheikh Anta DIOP de Dakar (UCAD), BP 5005, Sénégal,
[5]Centre International de Recherche Agricole pour le Développement (CIRAD), TA A31/02, 34398, Montpellier Cedex 5, France

E-mail: moucamara2001@yahoo.fr

RÉSUMÉ: *La tomate est le second plus important légume après l'oignon au Sénégal. Elle est très sensible au virus du TYLC (Tomato Yellow Leaf Curl)***.** *Douze variétés issues d'un criblage de résistance au TYLC et deux témoins sensibles (Roma VF et Xina) ont été testés pour confirmer cette résistance. L'incidence, la sévérité de la maladie et les variables de rendement ont été évaluées aux stades de floraison, fructification et après la première* ***récolte****. Les résultats ont confirmé ceux du criblage chez toutes les variétés. Les témoins ont fortement été attaqués par le virus. Lety F1 a produit plus de fruits. Le nombre de fruits/grappe a varié entre les variétés. La masse unitaire des fruits a été plus élevée pour Bybal, Roma VF et Lety F1. La longueur des fruits de Thoriya et Lety F1 a été plus importante. Roma VF et Bybal ont présenté les plus gros diamètres des fruits. TY75 et Ponchita ont produit les rendements consommables les plus élevés. Roma VF et Lety F1 ont produit les rendements non consommables les plus élevés. Globalement, les plus fortes productions ont été obtenues par TY75 et Roma VF. Ces résultats pourraient aider à faire le bon choix des variétés à cultiver dans des conditions similaires à celles des Niayes.*

Mots-clés : *Tomate, variétés, Lycopersicon esculentum, virus, résistance, TYLC, Xina, Roma VF, Sénégal*

Title: Effect of Yellow Leaf Curl Disease (TYLC) on different tomato cultivars (*Lycopersicon esculentum* Mill) in Senegal

ABSTRACT: *Tomato is the second most important vegetable, after onion, in Senegal. The species is very sensible to the TYLC virus. Twelve promising varieties of tomato, from a resistance to the Tomato Yellow Leaf Curl (TYLC) screening and two susceptible checks (Roma VF and Xina) were tested to confirm their resistance to the virus. The variables measured were: incidence and severity of the disease and yield variables. Observations were made during the flowering, fruiting and at first harvest stages. Our results confirmed the screening results. The susceptible checks were strongly attacked by the virus. Lety F1 has produced more fruits per plant. Fruits number per cluster showed significant differences between varieties. Bybal, Roma VF and Lety F1 recorded the highest fruit weight. Mean fruit length was higher with Thoriya and Lety F1. Roma VF and Bybal exhibited the largest fruit diameter. TY75 and Ponchita have produced the highest consumable yields while Roma VF and Lety F1 produced the highest non consumable yield. The largest overall yields were obtained by TY75 and Roma VF. These results could be used to make the best variety choice for areas that have similar conditions to those of the Niayes region.*

Key words*: Tomato, Lycopersicon esculentum Mill., virus, resistance, TYLCV, Xina, Roma VF, Senegal*

INTRODUCTION

La tomate est l'un des légumes les plus consommés dans le monde; elle occupe la deuxième place derrière la pomme de terre. Au Sénégal, elle vient en seconde position après l'oignon. Les rendements moyens sont de l'ordre de 20 t/ha, alors que des rendements d'environ 100 t/ha sont obtenus dans d'autres pays (Laterrot, 1994). Malgré son importance dans l'économie nationale, cette culture connaît de nombreux facteurs limitants dont les plus importants sont d'ordres physiologique et phytosanitaire.

En effet, plus de 200 maladies de cette culture sont recensées à travers le monde (Gry, 1994). Aux maladies cryptogamiques et/ou bactériennes s'ajoutent les ravageurs et les maladies virales dont *Tomato Yellow Leaf Curl* (TYLC) constitue la plus importante et la plus dangereuse (Belen et *al*., 1996 ; Moriones et Navas - Castillo, 2000). TYLC est une maladie qui provoque l'enroulement et le jaunissement des feuilles de tomate. Le virus de *Tomato Yellow Leaf Curl Virus* (TYLCV) est transmis par une mouche blanche, *Bemisia tabaci Gennadius*, qui appartient au groupe des «Géminivirus» (Cohen et Harpaz, 1964 ; Czosnek et Laterrot, 1997 ; Nzi et *al*., 2010). Après transmission, le virus est localisé le plus souvent dans les tissus de la plante et perturbe sa croissance. La plante se nanifie et prend un aspect buissonnant, les folioles s'enroulent, jaunissent et leur taille est réduite (Cohen et *al*., 1974). Les symptômes sont d'autant plus accentués que la variété est sensible et les conditions édapho-climatiques difficiles.

Les récoltes sont presque nulles lorsque le virus est transmis avant la floraison. Lorsque la transmission intervient après la floraison, les quelques fleurs formées donnent des fruits de calibre très réduit débouchant sur des pertes de 75% (Anonyme, 1998). La récolte est presque nulle quand l'attaque se déclare en pépinière (Laterrot, 1994). Les dégâts causés par TYLCV peuvent être de 50 à 70% si l'attaque est tardive et de 100% si elle se produit en pépinière (Belen et *al*., 1996 ; Vidavsky et Czosnek, 1998 ; Moriones et Navas-Castillo, 2000 ; Ciss, 2004).

Au Sénégal, la maladie est apparue en 1980 dans les régions de Kaolack et Ziguinchor (Ciss, 2004). L'apparition de cette maladie est probablement due à la proximité de la culture du coton qui héberge l'insecte vecteur, *Bemisia tabaci*. Aujourd'hui, elle a gagné tout le territoire national et constitue une menace sérieuse pour la production de la tomate dans le pays, voire dans la sous région (Huat, 2006). La lutte chimique, longtemps préconisée, n'a pas apporté une solution satisfaisante et durable; de plus, elle est onéreuse et polluante (Mason et *al*., 2000). Il semble que l'amélioration génétique pour la résistance, avec la mise au point de variétés tolérantes ou résistantes, reste la meilleure approche (Pilowsky et Cohen, 1990 ; Belen et *al*., 1996 ; Lapidot et *al.,* 1997 ; Santana et *al*., 2001). Cette approche, associée à une bonne connaissance de la dynamique de la mouche blanche en rapport avec l'épidémiologie de la maladie, permettrait de définir un contrôle intégré de cette virose (Moriones et Navas - Castillo, 2000).

En 2006, un essai préliminaire de criblage a été effectué sur 41 variétés de tomate d'origines diverses à Sangalkam (Sénégal), pour évaluer leur comportement vis-à-vis du TYLCV. Une vingtaine de variétés se sont révélées résistantes ou tolérantes au virus à l'issue de ce screening. Il s'agit de *FTC 6236*, *FTC 6231 Favi 9*, *HA 3060*, *Nadira*, *FTC 7088*, *Nirouz*, *HMX*, *Sasya 0202* , *Yassemen TH99802*, *TY75*, *Realeza*, *Thoriya*, *Bybal*, *Atak*, *Ponchita*, *Chenoa*, *Yosra*, *Gempride*, *Lety F1*, *Industry DR 1040* et *F1 3019 Galina*. L'objectif de la présente étude était de confirmer cette résistance/tolérance au virus chez les douze dernières variétés et d'évaluer leur productivité.

MATÉRIEL ET MÉTHODES

Site expérimental

Le site expérimental était situé à Sangalkam (Lalitude 14° 46' 44.30" N, Longitude 17° 13' 33.65" O, Altitude 19 m), département de Rufisque dans la zone écologique des *Niayes* où le climat est de type subcanarien (Figure 1) et les sols de type sablo- argileux, riche en matières organiques. La température moyenne de la zone varie entre 20 et 30°C avec une amplitude de 5 à 12° C. La pluviosité moyenne annuelle est d'environ 400 mm.

Dispositif expérimental

Il était en blocs de Fisher randomisés avec trois répétitions. La parcelle élémentaire avait une surface de 9,75 m^2 (6,5 m x 1,5 m). Les plants de tomates ont été plantés en lignes avec des écartements de 0,5 m sur la ligne et de 1,20 m entre les lignes. Chaque parcelle élémentaire comptait ainsi 36 plants.

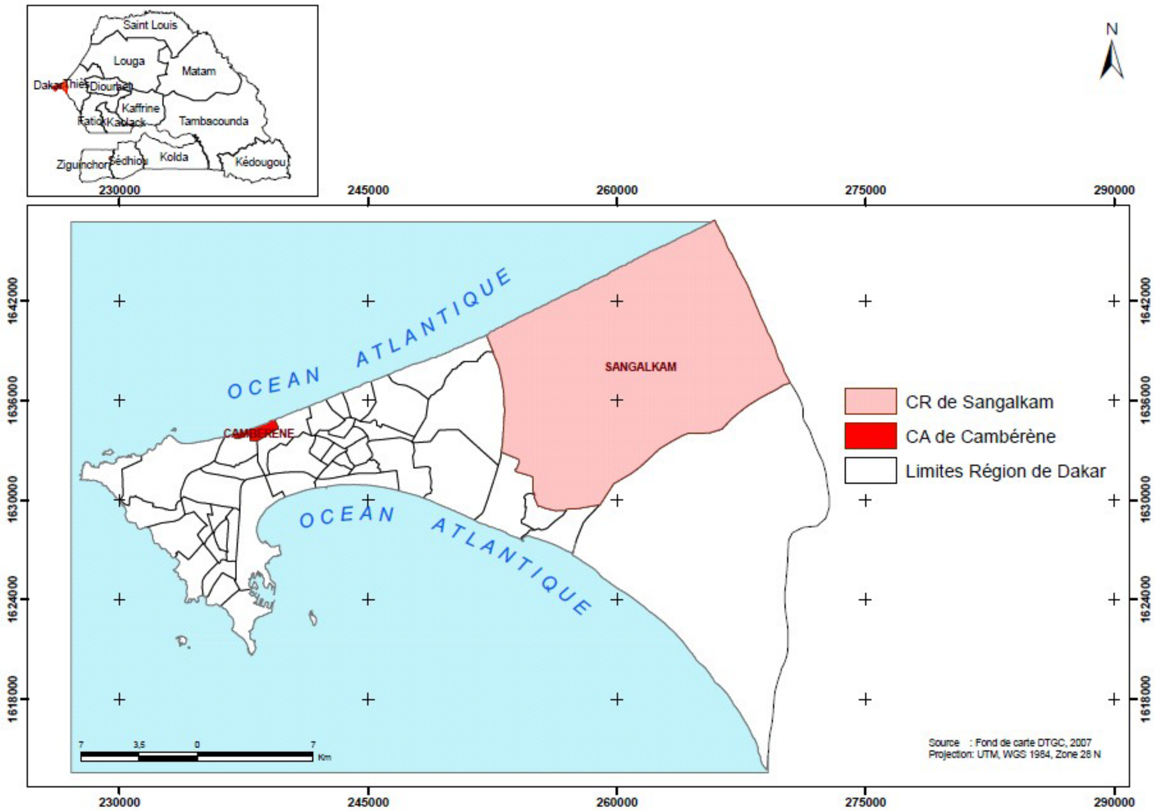

Figure 1. La station de recherche ISRA - CDH de Sangalkam dans la région de Dakar

Matériel végétal

Douze (12) variétés pré - sélectionnées à partir d'un essai préliminaire ont été utilisées (Tableau 1). Il s'agissait des variétés *Atack*, *Bybal*, *Chenoa*, *TY75*, *Gempride*, *Industry DR 10403*, *Lety F1*, *Ponchita*, *Realeza*, *Thoriya*, *Yosra* et *FTC6236*, auxquelles ont été ajoutées deux variétés sensibles (*Roma VF* et *Xina*), soit au total 14 entrées. Les observations ont été faites sur 10 plants/parcelle, localisés à l'intérieur des lignes centrales pour éviter les plants de bordure. L'incidence a été calculée à partir de la formule:

$$\left[\% = \frac{PA}{PT} \text{ x } 100\right]$$

I% = Incidence en pour cent, PA = nombre de plants attaqués, PT = nombre total des plants.

Pour la sévérité, une échelle de 5 classes (0-4) a été utilisée: 0 = pas de symptôme; 1 = léger jaunissement du bord des feuilles; 2 = jaunissement et enroulement du bord des feuilles; 3 = jaunissement prononcé, enroulement et rabougrissement des feuilles, la plante continue sa croissance; 4 = sévère rabougrissement avec enroulement des feuilles, la plante ne croît plus.

L'incidence moyenne de sévérité (Sm) a été calculée à partir de la formule:

$$Sm = \frac{\Sigma Si \text{ x } Ni}{\Sigma Ni}$$

Si : i$^{\text{ème}}$ note de l'échelle; Ni : nombre de plants ayant reçu la note Si. Les notes de sévérité ont été attribuées comme suit: Résistant (R): 0,0 = Sm = 1,0; Modérément Résistant (MR): 1,0 = Sm = 2,0; Sensible (S): 2,0 = Sm = 3,0; Hautement sensible (HS): 3,0 < Sm = 4,0.

Tableau 1 : Caractéristiques des variétés présélectionnées

Variétés	Formes	Provenance	Rendements (T/ha)
Atack	aplatie	Enza Zaden	25,80
Bybal	légèrement aplatie	De Rinter Seeds	18,9
Chenoa	aplatie	Enza Zaden	21,65
F^{1}3019 Galina	ovoïde	Tropicasem	19,10
Gempride	aplatie	Seminis	19,6
Industry DR 1040	légèrement aplatie	De Rinter Seeds	31,00
Lety F1	ovoïde	Harris Moran	12,50
Ponchita	aplatie	Enza Zaden	21,20
Realeza	pyriforme	De Rinter Seeds	31,05
Roma VF	ovoïde	Tropicasem	20,30
Thoriya	globuleuse	De Rinter Seeds	27,35
TY 75	aplatie	Takii	34,50
Xina	globuleuse	CDH/ISRA	12,40
Yosra	globuleuse	Enza Zaden	34,90

Pour les composantes du rendement comme le nombre de fruits par plante et le nombre de fruits par grappe, trois (3) plants de tomate ont été choisis au hasard par parcelle. En ce qui concerne la longueur moyenne, la largeur moyenne et la masse moyenne des fruits, les données ont été obtenues sur 15 plants par parcelle, choisis au hasard. Les rendements globaux ont été calculés en faisant la somme de la masse des fruits consommables et de celle des fruits non consommables.

Analyse des données

L'analyse de variance a été réalisée avec le logiciel MSAT.C pour étudier l'existence ou non de différences significatives ($p < 0{,}05$) entre les traitements. Le test de Student Newman Keuls a ensuite été utilisé pour identifier les traitements significativement différents ($p < 0{,}05$).

RÉSULTATS

Taux de levée

Les taux de levée se situaient en moyenne autour de 90% avec un minimum de 73,0% pour *Industry DR 1040* et un maximum de 98,7% pour *Thoriya*. Sur les 14 variétés, 11 avaient plus de 90% de levée (Tableau 2).

Incidence et sévérité de la maladie

A part les témoins sensibles (*Roma VF* et *Xina*) qui étaient respectivement à 86,7% et 81,2% d'incidence, les autres variétés ont eu une incidence nulle. Par conséquent la sévérité de la maladie (Sm) a également été nulle chez toutes les variétés sauf chez ces témoins, avec des valeurs respectives de 3,66 (*Roma VF*) et 4,00 (*Xina*). Ces deux variétés ont ainsi été hautement sensibles. Les symptômes se sont manifestés par un sévère rabougrissement avec enroulement des feuilles et arrêt de la croissance des plantes.

Longueur des fruits

La longueur moyenne des fruits a pratiquement varié du simple au double en passant de 26,8 mm (*Ponchita*) à 56,81 mm (*Thoriya*). Neuf groupes ont été identifiés par le test de Newman - Keuls (Tableau 2).

Tableau 2 : Effets du *Tomato Yellow Leaf Curl Virus* (TYLCV) sur les variables : Taux de levée (%), Incidence (%), Sévérité, Longueur moyenne d'un fruit (mm), Diamètre moyen d'un fruit (mm) de 14 variétés de tomate

Variétés	Taux de levée (%)	Incidence (%)	Sévérité	Longueur moyenne d'un fruit (mm)	Diamètre moyen d'un fruit (mm)
Atack	98,4	0	0	41,6 e	59,0 ab
Bybal	96,0	0	0	47,7 c	61,7 a
Chenoa.	95,4	0	0	44,9 cde	55,6 b
TY 75	96,7	0	0	52,7 b	45,9 de
Gempride	92,8	0	0	47,5 c	50,0 cd
Industry DR 1040	73,0	0	0	44,9 cde	50,3 c
Lety F1	98,7	0	0	54,9 ab	58,5 ab
Ponchita	97,6	0	0	26,8 g	30,2 h
Realeza	95,4	0	0	43,1 de	56,8 b
Roma VF	92,1	86,7	3,7	46,4 cd	61,8 a
Thoriya	98,7	0	0	56,8 a	38,0 g
Yosra	91,4	0	0	46,5 cd	42,8 ef
FTC 6236	75,6	0	0	44,7 cde	58,1 ab
Xina	86,2	82,2	4	38,4 f	38,7 fg

Légende: Les moyennes ayant des lettres communes ne sont pas significativement différentes au seuil de 5% (Test de Student Newman Keuls).

Diamètre des fruits

Le diamètre moyen des fruits a également doublé entre les différentes variétés en passant de 30,2 mm à 61,8 mm. Dix groupes ont été différenciés par le test de Newman - Keuls dont le premier était constitué par *Roma VF* et *Bybal* et le dernier par *Ponchita* (Tableau 2).

Nombre de fruits par plant et par grappe

Le nombre de fruits par plant a significativement varié (p < 0,0001) de 26 en moyenne pour le groupe homogène du test de Newman - Keuls constitué des variétés *Xina* (témoin sensible), *Yosra*, *Chenoa* et *Bybal* à 105 pour Lety F1 (Tableau 3). Le nombre de fruits par grappe a suivi la même tendance (p < 0.0007) avec un maximum de 5,0 pour *Lety F1* et un minimum de 2,6 en moyenne pour le reste des variétés qui constituent un seul groupe homogène (Tableau 3).

Masse unitaire des fruits

La masse unitaire moyenne d'un fruit a significativement varié (p < 0,0001) entre 15,5 g et 117,1 g (Tableau 3). Le test de Newman - Keuls a différencié 10 groupes dont le premier était constitué par le groupe *Bybal*, *Roma VF* et *Lety F1* et le dernier par *Ponchita*.

Masse de fruits consommables

La masse de fruits consommables a fortement varié (p < 0,0001) entre les différentes variétés de tomate, passant de 38,4 T/ha à 8,3 T/ha. Cinq groupes ont été identifiés par le test de Newman Keuls : le meilleur était constitué par *Roma SF* et le dernier par *Xina* (témoin sensible) (Tableau 3).

La masse des fruits non consommables a varié (p = 0.0147) entre 20,4 T/ha pour *TY75* et 6,7 T/ha pour *Ponchita*. Globalement la variété la plus productive a été *Roma VF* (55,8 T/ha) et la moins productive *Xina* (17,9 T/ha). A l'exception de *Xina*, toutes les autres variétés ont exprimé des potentiels de rendement variant entre 30 et 45 T/ha.

Tableau 3: Effets du *Tomato Yellow Leaf Curl Virus* (TYLCV) sur les variables : Nombre de fruits/plante, Nombre de fruits/grappe, Masse moyenne d'un fruit (g), Masse des fruits consommables (T/ha), Masse des fruits non consommables (T/ha) et Rendement (T/ha) de 14 variétés de tomate

Variétés	Nombre de fruits/plante	Nombre de fruits/grappe	Masse moyenne d'un fruit (g)	Masse des fruits consommables (T/ha)	Masse des fruits non consommables (T/ha)	Rendement (T/ha)
Atack	38,0 de	3,0 b	93,1 b	24,0 bc	14,0 abcde	38,0 bc
Bybal	24,6 e	2,8 b	117,1 a	18,4 bc	17,1 abcd	35,4 bc
Chenoa	26,2 e	2,3 b	85,8 bc	21,1 bc	9,9 cde	31,0 c
TY 75	84,0 b	3,3 b	61,5 def	38,4 a	17,4 abc	55,8 a
Gempride	81,8 b	2,7 b	66,9 de	17,1 c	13,8 abcde	30,9 c
Industry DR 1040	41,6 de	2,5 b	72,7 cd	18,6 bc	15,9 abcd	34,6 bc
Lety F1	105,2 a	5,0 a	112,2 a	18,6 bc	17,8 ab	36,4 bc
Ponchita	37,2 de	2,6 b	15,5 h	26,4 b	6,7 e	33,1 bc
Realeza	68,3 bc	2,9 b	90,5 bc	24,1 bc	14,3 abcd	38,4 bc
Roma VF	66,6 bc	3,0 b	115,2 a	24,5 bc	20,4 a	44,9 ab
Thoriya	53,9 cd	2,9 b	47,2 fg	17,8 bc	12,3 bcde	30,1 c
Yosra	28,2 e	2,8 b	52,7 efg	23,5 bc	13,0 abcde	36,6 bc
FTC 6236	38,7 de	2,7 b	93,9 b	22,3 bc	13,8 abcde	36,0 bc
Xina	24,2 e	2,4 b	37,5 g	8,3 d	9,7 de	17,9 d

Légende: Les moyennes ayant des lettres communes ne sont pas significativement différentes au seuil de 5% (Test de Student Newman Keuls).

DISCUSSION

Les 12 variétés prometteuses issues de l'essai préliminaire ont confirmé leur caractère résistant vis-à-vis du TYLCV. En effet, l'incidence et la sévérité de la maladie ont été nulles chez ces dernières. Le virus, présent sur les feuilles malades des plantes de tomate, a été identifié en 2006 à Corneil University (Anonyme, 2006) et par le CIRAD (2009).

Des études similaires effectuées simultanément dans cinq pays d'Afrique de l'Ouest (Bénin, Burkina Faso, Ghana, Mali et Togo) et utilisant les mêmes variétés ont montré des comportements différents de ces entrées d'un pays à l'autre. Par exemple *Bybal* a été sensible au Bénin, hautement sensible au Togo et au Ghana, modérément résistante au Burkina et résistante au Mali et au Sénégal. De même, *Gempride* a été sensible au Bénin et au Burkina Faso, hautement sensible au Togo, modérément résistante au Ghana, au Mali et au Sénégal (Anonyme, 2006). Le comportement des variétés testées permet de penser que la pression parasitaire (présence du virus et du vecteur *Bemisia tabaci*) n'était peut être pas la même partout. A cela s'ajoutent les facteurs édapho-climatiques différents dans ces pays. On note cependant de manière générale que les variétés étudiées présentent les mêmes comportements de résistance ou de sensibilité à l'intérieur de deux groupes de pays: Sénégal-Mali et Bénin-Togo. Au Burkina Faso, les comportements se rapprochent de ceux observés dans le groupe Sénégal-Mali, alors qu'au Ghana ils sont plus proches du groupe Bénin-Togo. Toutefois, le concept de variété sensible, tolérante ou résistante doit ainsi être considéré avec beaucoup de réserve à cause des conditions écologiques différentes qui ont une influence sur le comportement variétal.

En utilisant la quantité d'ADN viral présent dans des plantes infectées pour cribler des variétés de tomate, Zakay et *al.* (1991) ont observé une corrélation négative entre la quantité d'ADN viral et le degré de résistance et entre le degré de résistance et le rendement. Fargette et *al.* (1996) ont confirmé l'existence de cette corrélation. Plus récemment Laterrot (1994), en travaillant sur les variétés *TY172* et *TY197*, a montré leur résistance au TYLCV et leur faible perte de récolte par rapport à d'autres variétés commerciales sensibles à la maladie.

Cette corrélation n'est cependant pas toujours vérifiée. En effet ces mêmes auteurs ont trouvé des plantes à faible taux d'ADN viral, présentant des rendements plus faibles que des plantes dont la quantité d'ADN viral était plus importante. Ceci semble montrer que la résistance variétale pourrait inhiber l'effet du virus mais qu'elle ne suffit pas à elle seule pour expliquer le niveau des rendements obtenu.

La différence de comportement des variétés ne doit pas être liée uniquement à la quantité d'ADN dans les plantes et aux conditions édapho-climatiques mais également aux espèces de TYLC présentes et aux biotypes de l'insecte vecteur. D'après Ueda *et al.* (2009), cinq souches de TYLCV sont maintenant reconnues par le Comité International sur la Taxonomie des Virus (ICTV): Tomato yellow leaf curl virus - Gezira (TYLCV-Gez), Tomato yellow leaf curl virus - Israel (TYLCV-IL), Tomato yellow leaf curl virus - Mild (TYLCV-Mld), Tomato yellow leaf curl virus - Oman (TYLCV-OM) et Tomato yellow leaf curl virus - Iran (TYLCV-IR).

De nombreuses autres espèces de bégomovirus provoquent des symptômes d'enroulement des feuilles avec plus ou moins de jaunissement : *Tomato yellow leaf curl Axarquia virus* (TYLCAxV), *Tomato yellow leaf curl China virus* (TYLCCN), *Tomato yellow leaf curl Guangdong virus* (TYLCGuV), *Tomato yellow leaf curl Kanchanaburi virus* (TYLCKaV), *Tomato yellow leaf curl Indonesia virus* (TYLCIDV), *Tomato yellow leaf curl Malaga virus* (TYLCMalV), *Tomato yellow leaf curl Mali virus* (TYLCMLV), *Tomato yellow leaf curl Sardinia virus* (TYLCSV), *Tomato yellow leaf curl Thailand virus* (TYLCTHV) et *Tomato yellow leaf curl Vietnam virus* (TYLCVNV) (Fauquet *et al.,* 2008).

Par ailleurs, dans de nombreux pays, l'arrivée successive de différentes espèces de TYLCV a été observée Cette situation a contribué par la suite à l'émergence de virus recombinants tout au long de ces 10 dernières années. Il est à signaler que la recombinaison génère une diversité génétique dans les populations virales. Cette diversité génétique sera d'autant plus grande dans le cas de co-infection de plantes par des souches ou espèces différentes, avec un risque d'émergence de recombinants présentant des propriétés biologiques et pathologiques imprévisibles. Ces recombinants présentent une gamme d'hôtes plus large que chacun de leurs parents ce qui leur a vraisemblablement offert un avantage sélectif pour permettre leur émergence.

En conclusion nous pouvons affirmer que toutes les variétés testées ont confirmé les résultats de l'essai préliminaire en ce qui concerne la résistance au TYLCV et que les témoins sensibles, *Roma VF* et *Xina*, ont fortement été attaqués.

La variété *Lety F1* a produit plus de fruits que toutes les autres variétés mais le nombre de fruits par grappe n'a pas varié entre les variétés. *Bybal*, *Roma VF* et *Lety F1* ont enregistré les meilleurs poids par fruit. En ce qui concerne la longueur moyenne d'un fruit, *Thoriya*, *Lety F1* et *TY75* se sont le plus illustrés. Pour le diamètre des fruits, *Roma VF* et *Bybal* ont présenté les plus gros calibres. Pour les rendements en fruits consommables, *TY75*, *Ponchita* et *Atack* ont donné les meilleurs scores. Enfin, les plus fortes productions ont été obtenues avec *TY75* et *Roma VF*.

RÉFÉRENCES BIBLIOGRAPHIQUES

Anonyme, (1998), Les problèmes du maraîchage au Sénégal, *Direction de la Protection des Végétaux (DPV)*, 4 pages.

Anonyme, (2006), Agricultural Biotechnology Support Project (ABSP) II - Application of Biotechnology to the Tomato Virus Crisis in West Africa, *Quarterly Progress Report,* April - June 2006, Corneil University (USA).

Pico B., Diez M.J., Nuez F., (1996), Viral diseases causing the greatest economic losses to the tomato crop, II, The Tomato yellow leaf curl virus - a review *Scientia Horticulturae,* **67:**151-196.

Ciss I., (2004), Epidémiologie comparée du TYLCV chez les variétés sensibles et tolérantes de tomate (*Lycospersicon esculentum* Mill.), Mémoire de fin d'études pour le Diplôme d'Ingénieur des Travaux Agricoles, E.N.C.R de Bambey, Sénégal, 43 pages + annexes.

Cohen S., Harpaz I., (1964), Periodic, rather than continual acquisition of a new tomato virus by its vector, the tobacco white fly (*Bemisia tabaci Gennadius*) *Entomol. Exp. Appl.,* **7:**155-166.

Cohen S., Melamed-Madjar V., Hameiri J., (1974), Prevention of the spread of tomato yellow leaf curl virus transmitted by *Bemisia tabaci* in Israel, *Bulletin of Entomological Research,* **64:**19-37.

Czosnek H., Laterrot H., (1997), A worldwide survey of tomato yellow leaf curl viruses, *Archive of virology* **142:**1391-1406.

Fargette D., Leslie M., Harrison B.D., (1996), Serological studies on the accumulation and localization of three tomato leaf curl geminiviruses in resistant and susceptible *Lycopersicon* species and tomato cultivars, *Ann. Appl. Biol.,* **128:**317-328.

Fauquet C.M., Briddon R.W., Brown J.K., Moriones E, Zerbini M., Zjou X., (2008), Geminivirus strain demarcation and nomenclature. Archives Virology – ARCH VIROL, vol 153, n° 4, pp. 783-821.

Gry L., (1994), La tomate en révolution permanente, *Semences et progrès,* **78:**21-34.

Huat J., (2006), Facteurs limitatifs du rendement de la tomate industrielle en périmètres irrigués au Nord Sénégal, *Cahiers Agricultures,* **15**(3), mai - juin 2006.

Lapidot M., Friedmann M., Lachman O., Yehezkel A., Nahon S., Cohen S., Pilowsky M., **(**1997), Comparison of Resistance Level to Tomato Yellow Leaf Curl Virus Among Commercial Cultivars and Breeding Lines, *Plant Disease,* **81**(12):1425-1428.

Laterrot H., (1994), Création de populations sources pour la sélection de variétés de tomates résistantes à la virose de l'enroulement foliaire dans les pays Méditerranéens subtropicaux et tropicaux, *INRA-Station d'amélioration des plantes maraîchères*, BP 94-84143 MontFavet-France, 25 p. et annexes.

Mason G., Rancati M., Bosco D.**, (**2000), The effect of thiamethoxam, a second generation neonicotinoid insecticide, in preventing transmission of tomato yellow leaf curl geminivirus (TYLCV) by the white fly *Bemisia tabaci* (*Gennadius*), *Crop Protection,* **19:** 473-479.

Moriones E., Navas-Castillo J., (2000), Tomato yellow leaf curl virus, an emerging virus complex causing epidemics worldwide, *Virus Research,* **71:**123-134.

Nzi C.J., Kouame C., Nguetta A.S.P., Fondio L., Djidji A.H., Sanghare A.**, (**2010), Evolution des populations de *Bemisia tabaci Genn*. selon les varieties de tomates (*Solanum lycopersicum*) au centre de la Côte d'ivoire, *Sciences et Nature,* **7**(1):31-40.

Pilowsky M., Cohen S., (1990), Tolerance to Tomato Yellow Leaf Curl Virus Derived from *Lycopersicon peruvianum, Plant Disease,* **74**(3):248-250.

Santana M.F., Ribeiro S.G., Moita A.W., Moreira D.J., Giordano L.B., **(**2001), Sources of resistances in *Lycopersicon* spp. to a bipartite whitefly-transmitted geminivirus from Braszil, *Euphytica,* **122**(1):45-51.

Ueda S., Onuki M., Kijima K., Futagani K., Kinjo K., Murayama Y., Taniguchi M. and Kawano S., (2009), Introduction and modecular characterization of Tomato yellow leaf curl virus in Okinawa, Japan, JARQ 43 (1):19-24, http: //www.jicas.affrc.go.jp

Vidavsky F., and Czosnek H., (1998), Tomato Breeding Lines Resistant and Tolerant to Tomato Yellow Leaf Curl Virus Issued from *Lycopersico hirsutum*. *Phytopathology,* **l88** (9):910-914.

Zakay Y., Navot N., Zeidan M., Kedar N., Rabinowitch H., Czosnek H., Zamir D., (1991), Screening *Lycopersicon* accessions for resistance to tomato yellow leaf curl virus: Presence of viral DNA and symptom development, *Plant Disease,* **75**:279-281.

African Journal of Science and Technology (AJST)
Science and Engineering Series Vol. 12, No. 2, pp. 99 - 104

ON THE PRESSURE VELOCITY AND TEMPERATURE FACTORS AND THE EFFECT OF VISCOSITY ON THE ARTERIAL BLOOD FLOW IN RELATION TO THE HYPERTENSION PATIENT, PART 1 – FLOW WITHOUT OUTFLOW

Okuyade, W. I. A.
Department of Mathematics/Statistics, University of Port Harcourt,
P.M.B 5323, Choba, Port Harcourt, Nigeria

E-mail: wiaokuyade@yahoo.com

ABSTRACT: *In this paper, we examine the effects of viscosity on the blood pressure, velocity and temperature distributions in the arterial blood flow in the absence of outflows. The governing continuity, momentum and energy equations are solved analytically by method of characteristics. Using the wavefront expansions, an equation of the form of the Riccatti equation is derived. By this, explicit results about the pressure, velocity and temperature distributions are obtained. It is observed that viscosity reduces the pressure, hence, the velocity and temperature distributions. Our results may find relevance in the medical treatment of high blood-pressure problem*

Key words*: Viscosity pressure, velocity, temperature, arterial blood flow, hypertension.*

INTRODUCTION

Man is plagued with many internal flow problems. Among others, he has the problem of stenosis of the arteries and the situation where the aortic value fail to close properly. With emphasis, the latter can lead to hypertension and hypothermia in the patient. Because of the importance of human life, it becomes necessary to join hands, inter-disciplinarily to attack problem of hypertension and hyperthermia in relation to blood flow An understanding of blood flow in the arteries, dynamically, must be based on a good knowledge of physical laws governing the behaviour of the physical fluids at rest and in motion.

The mathematical theory of blood flow in the arteries is based on an unsteady one-dimensional model in which the pressure and fluid velocity are average over the cross-sectional area of the arteries. The equations describing the flow are sets of nonlinear first-order partial differential equations, which are hyperbolic and resemble those of the one-dimensional gas dynamics [5]. The equations arising from the forgoing are solved by method of wavefront expansions. As a result of a result of omitting from the model some aspects of the system that become significant at rapid flow changes, shock discontinues may develop. Therefore, the possibility of shock discontinues is a direct consequence of the non-linearity of the system [12]. [2] and [3] envisioned shock waves in the form of abrupt rise in pressure, velocity and temperature, or as spike–type perturbations which may evolve from relatively gradual changes in pressure.

Much work have been done at different dimensions on the flow of blood in the arteries. For example, [2] used the numerical approach to consider the steady flow pulses all shock wave of the arteries. They compared the linearized and nonlinearized analysis and their effect on the wavefront. [10], examined shock waves in the mathematical models of the aorta for the inviscid flow through a semi-infinite uniform distensible tube. Using the method of characteristics he obtained the distance at which shock discontinuities may occur. [4] extended problems in [10] to viscous flow in non-uniform tubes. They investigate the, conditions under which a, shock wave will form, the time and distance from the entrance of the tube wherein this will happen. They found that for a tapered tube, the shocks form earlier and nearer to the entrance than for a uniform tube, and that viscosity has a delaying effect on shock formation.

In line with [4], [l] examined the conditions under which shock is formed, however, they left out. According to [3], the energy equation need not be examined (temperature being approximately constant throughout the circulatory system) if the energy stored in the elastic walls of the artery is not accompanied by thermal effect (and in which case, the viscosity will be zero). [13] gave a relationship between heat transfer and the rheological properties of blood. They showed that the viscosity of blood in the circulatory system is a function of temperature. Allowing viscosity to depend on temperature, [4] showed that viscosity delays shock formation. What was not clear is the effect of variable viscosity on shock formation. Responding to this, [3] presented an asymptotic analysis of the temperature equation and investigated the effect of variable viscosity on the temperature distribution in a sickle cell anemia patient. They showed that a local hot spot exist in the sickle–cell anemia patient since the velocity becomes infinite at (xs, ts) and for practical purpose, the viscosity is greater than zero.

The aim of this paper is to investigate the effect of viscosity on the pressure and velocity, temperature distributions in the arterial blood flow (without side branches) in the high - blood patient.

PHYSICS OF PROBLEM

As a living organ, certain malfunctioning conditions due to diseases may arise in the artery. These are times when he aortic valve fails to close properly (i.e incompetent). Because of this, a large proportion of the blood ejected by the ventricle in systole (ventricular contraction) flows back to it in diastole (auricular contraction). The heart naturally adjusts itself to maintain peripheral circulation. In this situation, the heart is greatly enlarged, thus increasing the volume of blood ejected from it. The amplitudes of the pulse is then, very large and strong, thus, giving rise to arterial “pistol” shot. The pistol shot is the manifestation of hydraulic jump or shock in the arterial system. The jump in the pressure variable may lead to a crisis called hypertension (a body pressure that is above normal), which is invariably accompanied by hyperthermia (a body temperature that is above normal) in the patient.
We shall examine the effect of viscosity on the pressure, and hence, the velocity and temperature distributions of the flow in relation to the hypertension patient.

MATHEMATICAL FORMULATION

In line with [I], an unsteady one-dimensional model for arterial blood flow is presented and examined. The model is developed on the basis of the following assumptions: blood is compressible and newtonian. The arteries are straight elastic tubes (without side branches) of circular cross-sections constrained from longitudinal motions, so that only the axisymmetric bulging motions of the tube walls are considered. Since the radius of the artery is usually much smaller than the typical axial wavelength of flow, the radial acceleration and pressure force are neglected and only the longitudinal pressure gradient and axial fluid acceleration are considered. The flow and pressure pulses propagate with the local speed of sound c. The viscosity of blood vary with temperature. And, the blood constituents (solid corpuscles and plasma) flow with the same velocity.
The flow being one-dimensional, the only independent variables in the model are the axial coordinate, x and time, t. The governing continuity, momentum and energy equations for a segment x1 ≤ x ≤ x2 are:

$$\frac{d}{dt}\int_{X_1}^{X_2}\rho A dx = -\rho u A\Big|_{x_1}^{x_2} \tag{3.1}$$

$$\frac{d}{dt}\int_{x_1}^{x_2}\rho u A dx = -\left(\rho u^2 A + pA\right)\Big|_{x_1}^{x_2} + \int_{x_1}^{x_2} p\frac{\partial A}{\partial x} - \int_{x_1}^{x_2} A\frac{\partial \eta}{\partial x}dx \tag{3.2}$$

$$\frac{d}{dt}\int_{x_1}^{x_2}\left(\tfrac{1}{2}\rho u^2 + \rho C_v T\right)A dx = -\left(\tfrac{1}{2}\rho u^2 + \rho C_v T\right)uA\Big|_{x_1}^{x_2} - \int_{x_1}^{x_2} Ap\frac{\partial u}{\partial x}dx - \int_{x_1}^{x_2} Ak\frac{\partial^2 T}{\partial x} - \int_{x_1}^{x_2} A\eta\frac{\partial u}{\partial x}dx \tag{3.3}$$

Equation (3.1) – (3.3) can be written in differential form as:

$$\frac{d}{dt}(\rho A) + \frac{d}{dx}(\rho u^2 A) = 0 \tag{3.4}$$

$$\frac{d}{dt}(\rho u A) + \frac{d}{dx}(\rho u^2 A) + A\frac{dp}{dx} = \overline{f} \tag{3.5}$$

$$\rho C_v\left(\frac{\partial T}{\partial t} + u\frac{\partial T}{\partial x}\right) + k\frac{\partial^2 T}{\partial x^2} + p\frac{\partial u}{\partial x} + \eta\frac{\partial u}{\partial x} \tag{3.6}$$

where ρ is the varying fluid density, u axial fluid velocity, A cross – sectional area of the tube, p the pressure difference across the wall of the tube, and F the frictional force per unit length of the tube, k thermal diffusivity, T temperature, η Stress force, Cv specific heat at constant volume. The difference between equation (3.6) and the general energy equation is the inclusion of the term $p\frac{\partial u}{\partial x}$ called the thermal effect. This gives the assumption that the energy stored in the elastic walls of the arteries is accompanied by thermal effect.

Since the arteries are distensible and tapered, the cross – sectional areas vary with pressure and instantaneously to the pressure changes in the fluid. Hence,
A = A(p, x) (3.7)

Defining the local speed of sound as

$$c_0^2 = \frac{\partial \rho}{\partial p} \tag{3.8}$$

and using it in equation (3.4), we have

$$\frac{\partial p}{\partial t} + u\frac{\partial u}{\partial x} + \rho c_0^2 \frac{\partial u}{\partial x} = -\rho c_0^2 \frac{u}{A}\frac{\partial A}{\partial x} \tag{3.9}$$

Again by equation (3.4), equations (3.5) can be written as

$$\frac{\partial u}{\partial t} + u\frac{\partial u}{\partial x} + \frac{1}{p}\frac{\partial p}{\partial x} = f(u, A) \tag{3.10}$$

where $f = \frac{\overline{f}}{\rho A}$

Making the following replacements:

$$k\frac{\partial^2 T}{\partial x^2} = 2\xi\left(\frac{\pi}{A}\right)^{1/2}(T - T_0),\ \eta\frac{\partial u}{\partial x} = -2\overline{\mu}\left(\frac{\partial u}{\partial x}\right)^2,$$

$$\overline{\mu} = \mu(T) = \mu[1 - \alpha(T - T_0)]$$

(where ξ is the heat transfer coefficient, α is a position constant) in equation (3.6), we have

$$\begin{aligned}&\rho C_V\left(\frac{\partial T}{\partial t} + u\frac{\partial T}{\partial x}\right) + 2\xi\left(\frac{\pi}{A}\right)^{1/2}(T - T_0) + \\ &p\frac{\partial u}{\partial x} - 2\left(\frac{\partial u}{\partial x}\right)^2 \mu[1 - \alpha(T - T_0)] = 0\end{aligned} \tag{3.11}$$

Equations (3.9) and (3.10) are wave equations. Combining them we have their characteristics forms as:

$$\left\{\frac{\partial}{\partial t} + (u + c)\frac{\partial}{\partial x}\right\}(u + F) = f - \frac{c\ u}{A}\frac{\partial A}{\partial x} \tag{3.12}$$

$$\left\{\frac{\partial}{\partial t} + (u - c)\frac{\partial}{\partial x}\right\}(u - F) = f + \frac{cu}{A}\frac{\partial A}{\partial x} \tag{3.13}$$

where F = $\int_{p_0}^{p} \frac{dp}{\rho c}$

These characteristics equations show the possibility that discontinues in the form of shock waves develop in the flow

Inviscid Flow through a uniform elastic tube

For an Inviscid flow through a uniform elastic tube, f = 0, $\frac{\partial A}{dx} = 0$. Equations (3.12) and (3.13) reduce to:

$$\left\{\frac{\partial}{\partial t} + (u + c_0)\frac{\partial}{\partial x}\right\}(u + F) = 0 \tag{3.14}$$

$$\left\{\frac{\partial}{\partial t} + (u - c_0)\frac{\partial}{\partial x}\right\}(u - F) = 0 \tag{3.15}$$

showing that (u + F) and (u – F) are invariant on C+ and C- characteristics given by

C+: $\frac{\partial x}{dt} = u + c$

C-: $\frac{\partial x}{dt} = u - c$

Equations (3.14) and (3.15) have simple wave solutions. For a semi-infinite tube (x ≥ 0), which is initially undisturbed, we have

p0 = p(x, 0) = constant, u(x, 0) = 0, $\rho_0 = \rho_1(x,0) =$ constant, T0 = T(x,0) = constant. (3.16)

At x = 0, t ≥ 0, we shall assume
p(0,t) = p0 + rt + O(t2), r > 0 (3.17)

Since u = 0 in the undisturbed region (x, t ≥ 0)
U – F = - F0 = constant (3.18)

Now combining equations (3.9) and (3.10) we have

$$\left\{\frac{\partial}{\partial t} + (u + c)\frac{\partial}{\partial x}\right\}p = 0 \tag{3.19}$$

This implies that p is constant on c^+ characteristics given by

$$\frac{\partial x}{dt} = u + c = F(p) - F(p_0) + c(p) \tag{3.20}$$

C^+ are straight lines and in particular C_o^+ is the straight line x = c_ot

Discontinuities in the first derivatives occur along the wavefront characteristics c_o^+ emanating into the region x, t > 0. If the strength of the discontinuity becomes infinite at some point (x_s, t_s) on c_o^+, a shock is fitted into the solution, for x ≥ x_s, t ≥ t_s, to avoid a multivalued solution. The point (x_s, t_s) is the point nearest to origin on the envelop formed by the characteristics starting from (0, t) on the positive t - axis.

In this paper, we are not interested in the time and location where the shocks are developed.

METHOD OF SOLUTION

We shall consider viscous flow in a non-uniform elastic tube. We have seen that our governing equations are wave equations. However, an elementary solution like those of the simple wave equations will not be possible here. Hence, we shall use the wavefront expansions method, wherein we consider the flow as a perturbation of the undisturbed state.

The jump in the first derivative of the solution propagates along a wavefront characteristic, C_0^+ through the origin, and which may become infinite at some point (xs, ts) and hence, we have the formation of shock waves

The $C^{\pm}$ characteristics are given by $\frac{dx}{dt} = u \pm c$. The wavefront characteristic, C_0^+ separates the undisturbed region in the x, t – plane from the disturbed region. Thus, along

C_0^+ : u = 0, p = p0, $\rho = \rho_0$, T = T0, A = A0.

The variables with subscripts zero are constants.

We shall introduce new variables T and τ, where t = T (x) on C_0^+,

$$T(x) = \int_{p_0}^{p} \frac{d\zeta}{c(p_0,\zeta)} \tag{4.1}$$

and $\tau = t - T = t - \frac{x}{C_0}$, $\quad c_0 = c(p_0)$

On the C_0^+, τ = 0, gives x = c0t. In the undisturbed region, τ < 0, while in the disturbed region, τ > 0.
In the immediate neighbourhood of co+ we shall assume the following wavefront expansions:

For $\tau > 0$.
For $\tau < 0 : u = 0, p = p_0$, the disturbed region

$$p = p_0 + \tau p_1(t) + \frac{\tau^2}{2} p_2(t) + \ldots\ldots$$

$$\rho = \rho_0 + \tau\rho_1(t) + \frac{\tau^2}{2}\rho_2(t) + \tag{4.2}$$

$$u = u_0 + \tau u_1(t) + \frac{\tau^2}{2} u_2(t) + \ldots\ldots.$$

T = T0 + τ T1 (t) + $\frac{\tau^2}{2}$ T2 (t) +…
where ρ_1, p1, u1 and T1 are the measure of jumps in the normal derivatives of ρ, p, u, and T, respectively.

Furthermore, we consider the following notations, expansions and transformations:

c (po, x(t)) = co

$$\frac{\partial c}{\partial p}(p_{0,} x(t)) = c_P(p_{o,} x(t) = c_p^o$$

$$\frac{\partial c}{\partial x}(p_{0,} x(t)) = c_x(p_{o,} x(t) = c_x^o$$

A(po, x(t)) = Ao

$$\frac{\partial A}{\partial x}(p_{0,} x(t)) = A_x(p_{o,} x(t) = A_x^o$$

$$A(p, x(t)) = A_o + \tau(p_1(t)A_p^o - c_o A_x^o) + \ldots.$$

$$A_x(p, x(t)) = A_x^o + \tau(p_1(t)A_{px}^o - c_o A_{xx}^o) + \ldots.$$

$$c(p, x(t)) = c_o + \tau(p_1(t)c_p^o - c_o c_x^o) + \ldots.$$

$$f(u, A) = f^o + uf_u^o + (\tau u_1(t) + \frac{\tau^2}{2}u_2(t) + \ldots)f_u^o + (p_1(t)A_p^o - c_0 A_x^o)f_A^o$$

$$\frac{\partial}{\partial t} = \frac{\partial}{\partial t} + \frac{\partial}{\partial \tau}, \quad \frac{\partial}{\partial x} = -\frac{1}{c_o}\frac{\partial}{\partial \tau} \tag{4.3}$$

Using equations (4.2) and (4.3) in equations (3.9) - (3.11) respectively, and equating the coefficients of the powers of τ to zero, we have for

For τ^o :

$$p_1 - \rho_0 c_0 u_1 = 0 \tag{4.4}$$

$$p_1^1 + p_2 - \frac{p_1 u_1}{c_0} + 2\rho_0 c_0 u_1 c_x^0 - 2\rho_0 u_1 c_p^0 p_1 - \rho_1 c_0 u_1 - \rho_1 c_0 u_2 + \frac{\rho_0 c_0^2 u_1 A_x^0}{A_0} = 0 \tag{4.5}$$

$$\rho_0 C_V T_1 - \frac{p_0 u_1}{c_0} - \frac{2\mu u_1^2}{c_0^2} = 0 \tag{4.6}$$

For τ :

$$p_1 - \rho_0 c_0 u_1 = 0$$

$$\rho_0 c_0 u_1^1 + \rho_0 c_0 u_2 + \rho_1 c_0 u_1 - \rho_0 u_1^2 - p_2 - \rho_0 c_0 (p_1 A_p^0 - c_0 A_x^0) f_A^0 - \rho_1 c_0 u_1 f_u^0 = 0 \tag{4.7}$$

$$\rho_0 C_V T_1^1 + \rho_1 C_V - \rho_0 \frac{C_V u_1}{c_0} + 2\mu \frac{u_1^2 \alpha}{c_0^2} - 2\xi(\frac{\pi}{A})^{1/2} T_1 - \rho_0 C_v T_2 - \left(\frac{p_0 u_2}{c_0} + \frac{p_1 u_1}{c_0} + \frac{4\mu u_1 u_2}{c_0^2} \right) = 0 \tag{4.8}$$

Using equation (4.4), substituting u1 in terms of p1 into equations (4.5) and (4.7) and combining the results, p2 and u2 are eliminated, and we have

$$p_1^1 - \frac{p_1^2}{2c_0}\left(\frac{1}{\rho_0 c_0} + 2c_P^0 \right) + \frac{p_1}{2}\left(2c_x^0 + \frac{c_0 A_x}{A_0} - \rho_0 c_0 A_P^0 f_A^0 - f_u^0 \right) + \frac{\rho_0 c_0^2}{2} A_x^0 f_A^0 = 0 \tag{4.9}$$

This equation has the form of the Riccatti equation. This equation must satisfy the initial condition p1 (0) = r, (where $r = \frac{dp}{dt}$ is the rate of pressure rise in the ventricle at the moment when the aortic valve opens, and p is the ventricular pressure)

Also, from equation (4.6), we have

$$T_1 = \frac{p_0 u_1}{\rho_0 c_0 C_V} - \frac{2\mu u_1^2}{\rho_0 c_0^2 C_V} \qquad (4.10)$$

Specific Cases of Flow

Inviscid Flow in exponentially tapered tubes

Here, $\mu = 0$, hence, $f_A^0 = 0, c_x^0 = 0, A(p,x) = A_P e^{-\beta x}$, where $-\beta = \frac{A_x}{A_0}$, (β is a measure of the tapering of the tube. β > 0 corresponds to tubes which becomes narrower as the axial distance increases, as for blood flow in the systemic arteries, and β < 0 is for tubes which becomes wider as the axial distance increases, as for blood flow in the pulmonary arteries.)

By these, equation (4.9) reduces to:

$$\frac{dp_1}{dt} - \alpha p_1^2 - \lambda_1 p_1 = 0, \quad \text{P1 (0) = r} \qquad (4.11)$$

where $\lambda_1 = -\frac{c_0 \beta}{2}$, $\alpha = \frac{1}{2c_0}\left(\frac{1}{\rho_0 c_0} + 2c_p^0\right)$

The solution is $\frac{1}{p_{1(1)}} = \frac{1}{r} e^{\lambda_1 t} - \frac{\alpha}{\lambda_1}(e^{\lambda_1 t} - 1)$ (4.12)

Viscous flow in exponentially tapered tubes

Here, using the well known Hagen – Poiseuille formula for frictional force in laminar flow to approximate the frictional force, f≠ 0, $f_u^0 = -\frac{8\pi\mu}{\rho_0 A_0}$, μ > 0, $f_A^0 = 0$, $c_x^0 = 0$,

A (p, x) = $A_{(P)} e^{-\beta x}$

By these, equation (4.9) becomes

$$\frac{dp_1}{dt} - \alpha p_1^2 + \lambda_2 p_1 = 0, \quad \text{p1(0) = r} \qquad (4.13)$$

where $\lambda_2 = \left(\frac{4\pi\mu}{\rho_0 A_0} - \frac{c_0 \beta}{2}\right)$

The solution is $\frac{1}{p_{1(2)}(t)} = \frac{1}{r} e^{\lambda_2 t} - \frac{\alpha}{\lambda_2}(e^{\lambda_2 t} - 1)$ (4.14)

(The second subscripts attached to the p1's denote the flow cases considered)

RESULTS

A comparison of the equations (4.12) with (4.14) shows that:

$$\frac{1}{p_{1(2)}} > \frac{1}{p_{1(1)}}$$

yielding

p1(2) < p1(1)

u1(2) <u1(1) u = u (p, t) (5.1)

By equation (5.1), equation (4.10) gives

$T_{1(2)} < T_{1(1)}$ (5.2)

Discussion of results

The primary aim of this study is to investigate the effect of viscosity on the flow of blood in the artery (where arterial side branches are neglected) in relation to hypertension. Therefore, in this section, we shall look at the effect of viscosity on the flow, dynamically and clinically.

Equation (5.1) shows that the pressure in the viscous flow is less than that in the inviscid flow, and hence, the velocity in the viscous flow is less than that in the inviscid flow. From equation (4.10), since the temperature is also velocity – dependent, it follows that the temperature in the viscous flow is less than that in the inviscid flow. This yields equation (5.2)

From the foregoing, there is a clinical implication. With drugs capable of raising appreciably the viscosity of blood of the hypertension patient, the problem of hypertension will be ameliorated

CONCLUSION

The analysis shows that the viscosity of blood reduces the pressure, and hence, the velocity and temperature of the arterial blood flow. No doubt, our results will be of great importance to the biomedical and pharmacological scientists.

ACKNOWLEDGEMENT

We acknowledged the fatherly gesture of Prof. Akinrelere, E.A.

REFERENCES

[1] Akinrelere, E.A and Ayeni, R.O (1983): Shock waves in arterial blood flow, Journal of Nigerian Mathematical Society, vol 2, P. 91 – 98.

[2] Anliker, M., Rockwell, R.L, and Ogden, E (1971): Nonliner analysis of pulses and shock waves in the arteries, Journal of Applied Mathematics and Physics (ZAMP), Vol 22, pg. 217 – 245.

[3] Ayeni, R.O and Akinrelere E.A (1984): On temperature factor and the effect of viscosity on blood temperature in the arteries, Journal of Theoretical Biology, Vol. 109, pg. 479 – 487.

[4] Hoogstraten, H.W and Smit, C.H (1978): A mathematical theory of shock waves formation in the arterial blood flow, ACTA MECHANICA, vol 30, p. 145 – 153.

[5] Liepmann, H.W and Roshko, A (1957): Element of gas dynamics, John Wiley and Sons, Inc., New York.

[6] Lighthill, M.J (1972): Physiological fluid dynamics a survey, Journal of fluid Mechanics, vol 52, P. 478 – 495

[7] Lighthill, J.M (1973): Mathematical biofluid dynamics, Society of Industrial and Applied Mathematics, Philadelphia, Pennsylvania, 19103, U.S.A

[8] Pedley, T.J (1980): The fluid mechanics of large vessels, Cambridge University Press, Cambridge, U.K

[9] Richard Skalak, Nihat Ozkaya and Thomas C. Skalak (1989): Biofluid mechanics, Annual review fluid mechanics, Vol 21, P. 169 – 204

[10] Rudinger George (1970): Shock waves in mathematical model of the aorta, International Congress of Applied Mechanics, Stanford University, P. 1 – 14.

[11] Simt, C.H (1981): On modeling distributed outflow in one – dimensional model of arterial blood flow, Journal of Applied Mathematics and Physics (ZAMP),vol 32, P. 408 – 420.

[12] Streeter, V.L, Keitzer, W.F and Bohr, D.F (1963): Pulsatile Pressure and flow through distensible vessels, Circulation Research, Vol. 13, P. 3 – 20.

[13] Sundukov, A.N., Postnikova, M.A., Zvereva, K.V and Ivanov, P.A. (1978): Heat Transfer (Soviet Research) 10, 96.

[14] Van der Werff, T.J (1974): Significant parameters in arterial pressure and velocity developments, Journal of Mechanics, vol 7, p. 437 – 497

[15] Wilmer, W.N and Michael E.O. Rourke (1980): McDonald’s blood flow in arteries, Edward Arnold, London, U. K

[16] Whitham, G. B (1974): Linear and nonlinear waves, Wiley Interscience, New York, U. S. A.

African Journal of Science and Technology (AJST)
Science and Engineering Series Vol. 12, No. 2, pp. 105 - 115

ANALYSIS OF THE WELD STRENGTH OF THE HIGH DENSITY POLYETHYLENE (HDPE) DAM LINER

Mbuge, D.O.[1], Gumbe, L.O.[1] and Rading G.O.[3]
[1]Department of Environmental and Biosystems Engineering
[2]Department of Mechanical and Manufacturing Engineering
University of Nairobi
P.O. Box 30917, Nairobi, Kenya.

Email: dmbuge@yahoo.com

ABSTRACT: *An analysis was carried out to determine the strength of welded joints in High Density Polyethylene (HDPE) dam liners. Samples were collected of welded joints and subjected to tensile tests and creep test. It was observed that the welded joints from field welded samples were much weaker and had a very low straining capacity than the un-welded material. The field welded specimens registered average strengths of 5 MPa as compared to 12 MPa of un-welded specimens and a maximum strain at fracture of 0.5 as compared to 3.5 of un-welded specimens. As a result of the weak welds it was found necessary to conduct further research into the best welds possible and a protocol for hot air and hot knife welding was developed. It was shown that for hot air welding while holding the width of the weld, applied pressure and dwell time of the pressure constant at 2.6cm, 0.3 MPa and 60 s, the recommended temperature of the hot air to achieve the strongest weld was 176 and for hot knife welding the recommended temperature of the knife was 400°C*

INTRODUCTION

In the world today, there is a big shortage of potable water for domestic use as well as agricultural water for irrigation and this has led to much suffering for many people in the world [1, 2]. The most important factor that undermines the availability of water is the prohibitive cost of water storage structures. In systems that depend on rainwater harvesting for example, water security and availability lies squarely on how much water one can store [3]. This is because rainfall patterns are such that it rains unexpectedly, and the total seasonal rainfall is concentrated in two to three week episodes. Also, the commencement of the rains is unpredictable. It is therefore important for water users to collect as much water as they can during these short rainy seasons and store it for use in times when there is no rainfall. This calls for large water storage structures, which most water users cannot afford due to their high costs [3].

It is in recognition of this that there is need to develop cheaper alternatives for water storage. Already a lot of work has been done in this line which has led to the development of new products such as plastic tanks. A more recent introduction to Kenya is the plastic lined water reservoir for storage of water for both domestic and agricultural use. Using this technology, it is possible to store water at about one tenth of the cost of the conventional water storage structures such as ferro-cement tanks and plastic tanks. It also offers a unique opportunity to make collapsible tanks, which are vital in refugee camps and other conditions, which involve temporary settlement [3].

One of the more popular materials used in the fabrication of these plastic lined reservoirs is High Density Polyethylene (HDPE). It is normally extruded from the factories as 50 m long and 2 m. wide sheets and needs to be welded to cover the reservoir. The welded joints were observed to be a common failure point and there was need to study them so as to find out the problems and recommend remedies.

A linear polymer, HDPE is prepared from ethylene by a catalytic process. The absence of branching results in a more closely packed structure with a higher density and somewhat higher chemical resistance than LDPE. HDPE is also harder and more opaque than LDPE. It has a melting point that ranges from 130°C to 137°C, a maximum continued use temperature of 65^{o}C and a glass transition temperature of between -110°C to -125°C. It has a density of about 0.941 - 1.45 g/cm^3, a coefficient of thermal expansion of 100 - 220 x 10^{-6} per °C, a tensile strength of 15 - 40 MPa, a flexural modulus of 1.2GN/m^2, Young's modulus of 0.7 GN/m^2 , Brinnel hardness of 2 and an elongation of 150%-500% at failure [4, 5, 6, 7]When used for lining reservoirs, HDPE sheeting does not require soil cover unlike the other materials which are readily degraded if not covered. Installation is generally undertaken using fusion-weld joining equipment. Thickness range is 0.4 to 2.5 mm. It would be used on sites where puncturing of cheaper products cannot be avoided or where steep slopes (steeper than 2:1) preclude the use of other products [8].

HDPE is the most widely used geomembrane in the world and is used more commonly internationally due to its availability and relatively low material cost. HDPE is an excellent product for large dam applications that require UV and ozone resistance, chemical resistance or high-quality installations. The sheets are delivered in large rolls and may be heat welded in the field by trained technicians. This product has been used in landfills, wastewater treatment lagoons, animal waste lagoons, mining applications and for water storage [8].

Welding in polymers is done in order to produce seals or joints of sufficient strength to survive the work environments. When these polymer surfaces are brought into intimate contact and are partially molten, a bond is achieved. In order to achieve a realistic bond, the surfaces are pressed together for a period of time sufficient for the polymer chains to diffuse across the interface and form connecting bridges. The formation of these bridges is a function of the material being welded and at a given thickness is a function of the material composition, average molecular weight, molecular weight distribution, and thermal conductivity [9].

A weld seal is usually obtained by sealing like materials together. Weld seals are based on obtaining the strongest seal such that the material fails before the seal. The method of sealing, in particular how heat sealing is achieved, can be carried out by using different techniques like jaw-type bar sealers, rotary sealers, band rotary sealers, impulse sealers, bead sealers, hot knife, or side weld sealers. The basic process involves the welding of two polymer films when forced into intimate contact while they are in at least their semi-molten state. The two main sealing parameters that affect the heat seal quality are the interfacial temperature and sealing time. Therefore, in order to assess effectiveness of a welded joint in a polymeric material, it is very important to determine the interfacial temperature and heat sealing time that will result in a desirable seal. Many instruments have been developed, but no instrument or technique is capable of assessing these conditions yet [9].

The guiding principles of creating welded joints have been presented in part by some references [9]. They stated that when two pieces of a plastic film are heat sealed, there is an inflection point in the sealing time–temperature profiles of the materials. The inflection point occurs at a temperature below the melting point of the materials as measured by the Differential Scanning Calorimeter (DSC) technique. It was also found that pressure has limited effect on the sealing properties of the sealed films. The highest peel seal strength is achieved at a temperature near the fusion point. Seals made above the fusion point result in a weld seal that is not separable by the peel test [9].

Three main design guidelines that should be considered when designing welded or adhesive joints as [10]:

1. Maximizing Shear and minimizing peel and cleavage
2. Maximizing compression and minimizing tensile pull
3. Joint width is more important than overlap length and as a general rule it would be more feasible to increase the joint width rather than the overlap length.

Adhesives have been used successfully in joining plastics. However, the use of adhesives for joining HDPE sheets rather than welding is deemed as difficult, unsuccessful or complicated. Because of their non-polar nature, polyethylene requires an oxidation treatment using flames, plasma treatment, or chemical etching to enhance the adhesive bond). Some references have listed HDPE as one of the hard-to-bond plastics alongside LDPE, polypropylene and Teflon [10, 11]. The use of adhesives for joining HDPE was therefore not considered in this research study.

The broad objective of the study was to determine the expected lifespan of High Density Polyethylene (HDPE) and the specific objective was to determine the effect of welding HDPE on the expected lifespan.

MATERIALS AND METHODS

The specimens used in this project were obtained from HDPE plastic dam liner manufactured by A-Plus Ltd. in Nairobi. The material is available commercially in four classes with regard to the thickness ranging from 0.5 mm to 1.2 mm. The material used in the tests was 0.8mm thick, manufactured at 15–30 MPa extrusion pressure, the die temperature ranging from 131 °C to 139 °C and a rotation speed of 15 rpm. It had a melting temperature of 135 °C. The rest of the dimensions are as shown in Figure 1 as per [12] for Type II specimens.

There were three sets of samples. The first batch consisted of samples with welded joints of width 1.3 cm. Collected from 5 reservoirs made from the HDPE lining material from the same supplier of equal thickness of 8 mm, installed within one week of the test. Test specimens were then prepared from these samples such that the welded section fell in the middle of the narrow section of the dumbbell shaped test piece. These specimens were then subjected to the tensile test as well as the creep test at different expected operating temperatures. It was ascertained that all the samples had been welded using the hot air technique. The samples under this category were called 'field welded' samples.

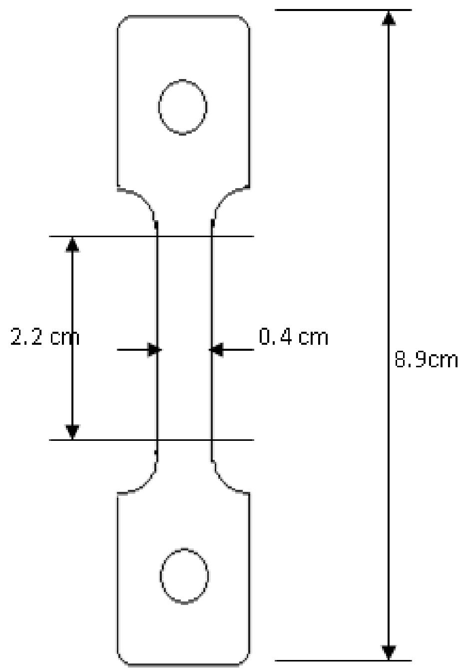

Figure 1: Specimen Geometry – Die Type II Dimensions used in the research study

The second batch of samples was obtained from un-welded pieces from the same reservoirs used to obtain the first batch of samples. Hence the punched dumbbell specimen did not have a welded joint and were called ‘un-welded’ samples.

The third batch of samples was obtained from the same reservoirs as in the first and second batch and did not have any welded joints, but was welded under laboratory conditions to obtain the best weld possible. They were called ‘laboratory welded’ samples. To obtain ‘laboratory welded’ specimens, the joints were first welded on large pieces and then the required specimens were punched at random locations along the welded joint. The punching was done so that the welded section fell at the centre of the narrow section of the dumbbell specimen.

The specimens from all three categories were then tested in tensile creep at temperatures of 30°C, 40°C and 50°C and stresses of 0.78MPa, 0.94MPa and 1.56MPa. The methods used in these test was similar to that described by [9]. All the welded joints were lap joints. Two popular field welding techniques namely the hot air and hot-knife techniques were used for the ‘laboratory welded’ specimens. The pressure applied on the welded joint and the dwell time of the pressure were held constant at 0.3MPa and 10s respectively from [9]. A variation was also made in the width of the welded joint from the ‘field welded’ dimension of 1.3 cm. to 2.6 cm. The tensile and creep tests were done on the specimens.

Hot air welding was simulated in the laboratory by heating the oven to the desired temperature. The specimens to be welded were prepared by covering the sections not to be melted with flat wood as insulation. The specimens were then placed in the oven for 10 s. The sections to be joined were placed together and pressure applied.

The hot knife welding was done by incubating flat bars of width 1.3 cm. and 2.6 cm. in the oven at a given temperature for 20 minutes. Two pieces of the material to be welded were placed to form a welded joint and the hot flat bar passed in the lap joint at the rate of 1cm/s for a weld piece of 10 cm. length. Pressure was then applied for 10 s. Specimens for subsequent tests were then prepared with a dumbbell cutter, with the welded section at the centre of the specimen.

RESULTS AND DISCUSSIONS

Tensile Test Results

It was necessary to compare the strength parameters of field welded specimens and un-welded specimens. The tensile tests carried out on the various types of specimens yielded the results presented in Table 1. All the experiments were carried out at a room temperature of 23ºC and relative humidity of 50% on specimens subjected to hot air welding. The tensile strength and the maximum strain at fracture were the main parameters for comparing the welded specimens and specimens without welded joints.

Table 1: Results for tensile test

Specimen Type	Tensile strength (MPa)	Maximum Strain (mm/mm)
Un-welded specimen	12	3.5
Field Welded with 1.3 cm welded joint	5	1.2
Field Welded with 2.6 cm welded joint	11	0.5

* Each result is the average of 5 specimens

By this test it was confirmed that indeed the welded joint is a weak point in the dam liner assembly not just by the figures but by the fact that all the failures occurred either on the welded joint or near it. Placing the un-welded joint as the standard, it can be seen from Table 1 that all the welded joints fell far short of this standard in both the strength and the maximum strain at fracture, both of which are important parameters in the operation of dam liners and flexible tanks. From the results, it was interesting to note that increasing the width of the weld more than doubled the tensile strength from 5 MPa. to 11 MPa. However, the effect on the maximum strain at fracture was the opposite, decreasing from 1.2 to 0.5. It may thus be concluded that in general, increasing the welding width of this material increases the strength of the welded joint but reduces its elasticity. It is possible that during welding, which involves a rapid temperature increase in the prescence of oxygen, certain reactions occur to modify the material on and around the welded joint. Hence a lager welded section is stronger but has a larger section rendered inelastic, with reduced straining capacity. In practical terms dam liners and other applications using this product should be designed on the asis of strength and strain values.

Creep Data for Un-welded Specimens

Curves in Figure 2(a) through Figure 2(c) are the creep curves obtained for un-welded specimens (material without a welded joint) tested under three different stresses at three different temperatures of 30ºC, 40ºC and 50ºC. From these results, the set of master curves presented in Figure 2 (d) was developed according to the principles of time-temperature superposition presented by many authors such as [13, 14, 15]. These corves are the benchmarks against which the creep curves of the field welded specimens, presented in Figure 3 (a) through Figure 3 (c) would be compared.

Creep Curves for Field Welded Specimens

Tests were done to determine the behaviour of test pieces with machine welded joints in tensile creep over time. In all instances the specimens obtained from the field failed at the welded joint. The failure was observed to result from shear between the welded surfaces. The curves of strain versus time for welded specimens under tensile creep are presented in Figure 3 (a - c).

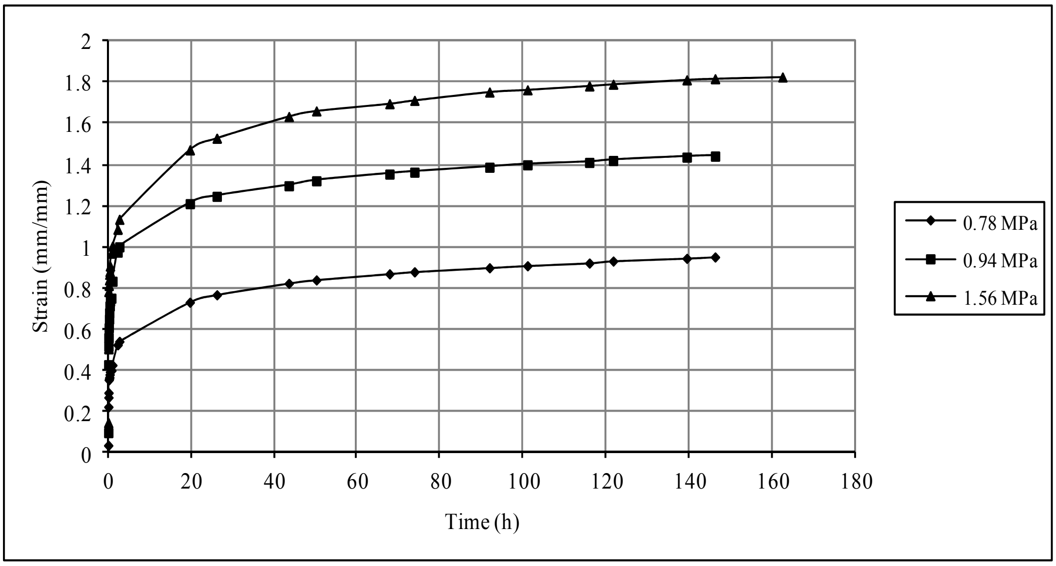

Figure 2 (a): Constant Temperature Creep Curves at 30°C

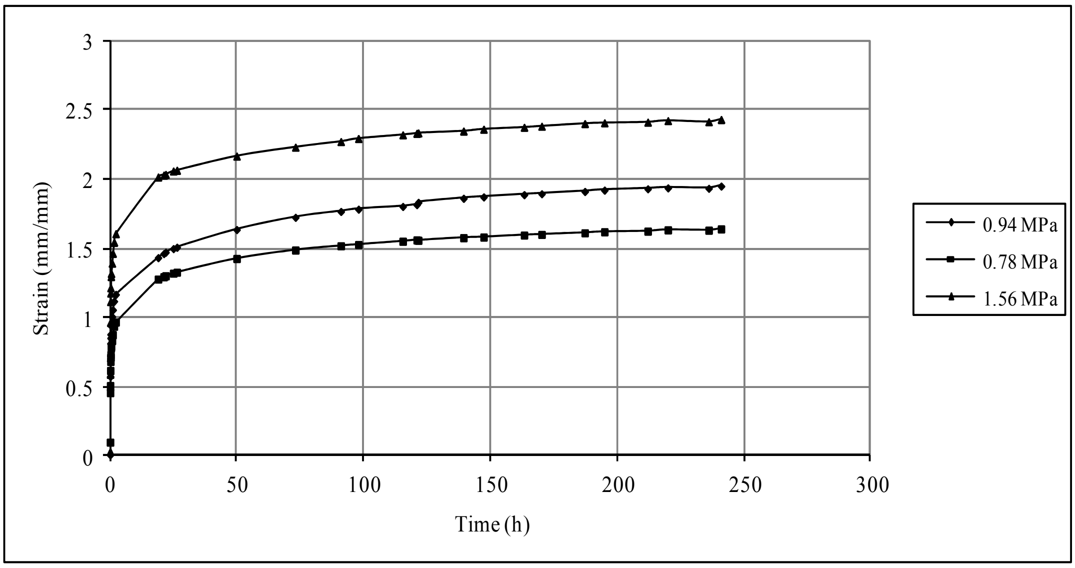

Figure 2 (b): Constant Temperature Creep Curves at 40°C

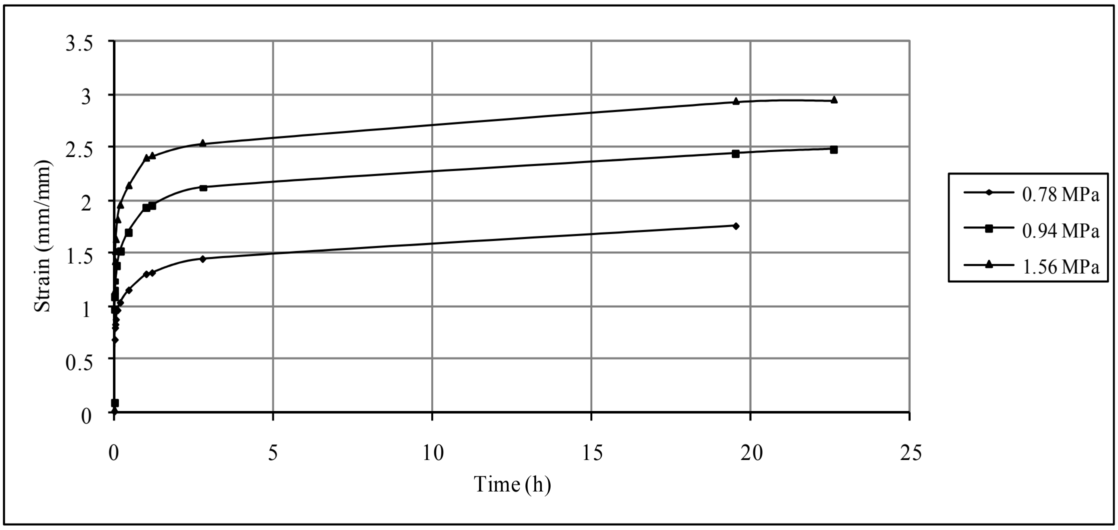

Figure 2 (c): Constant Temperature Creep Curves at 50°C

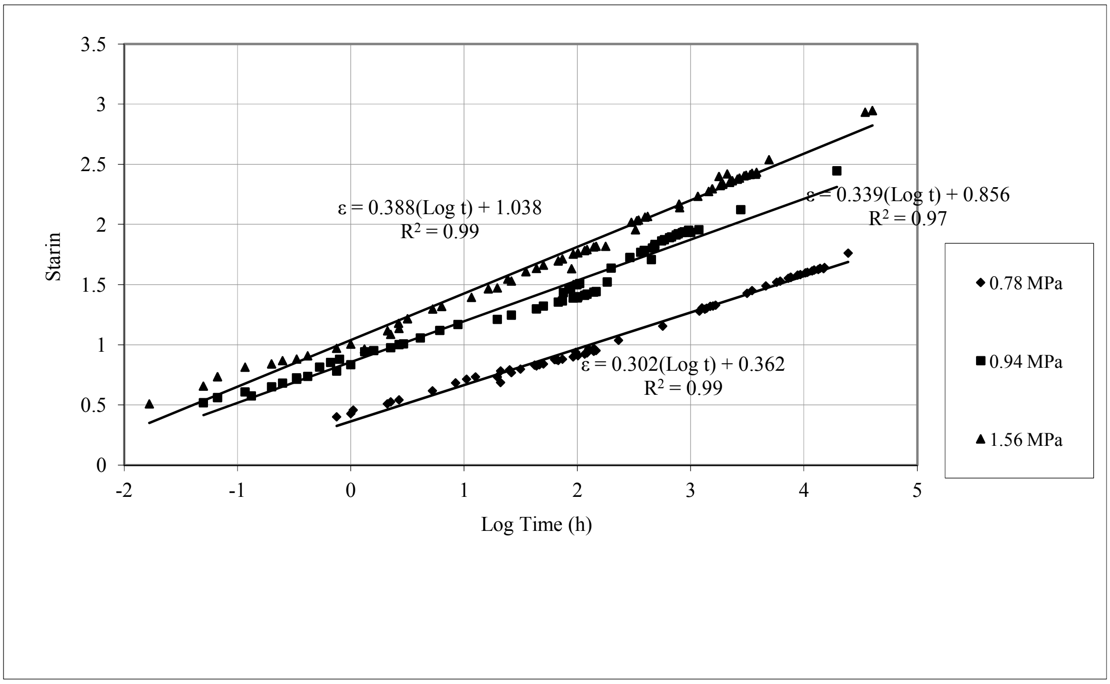

Figure 2 (d): Consolidated graph of master curves at 0.78 MPa, 0.94 MPa and 1.56 MPa.

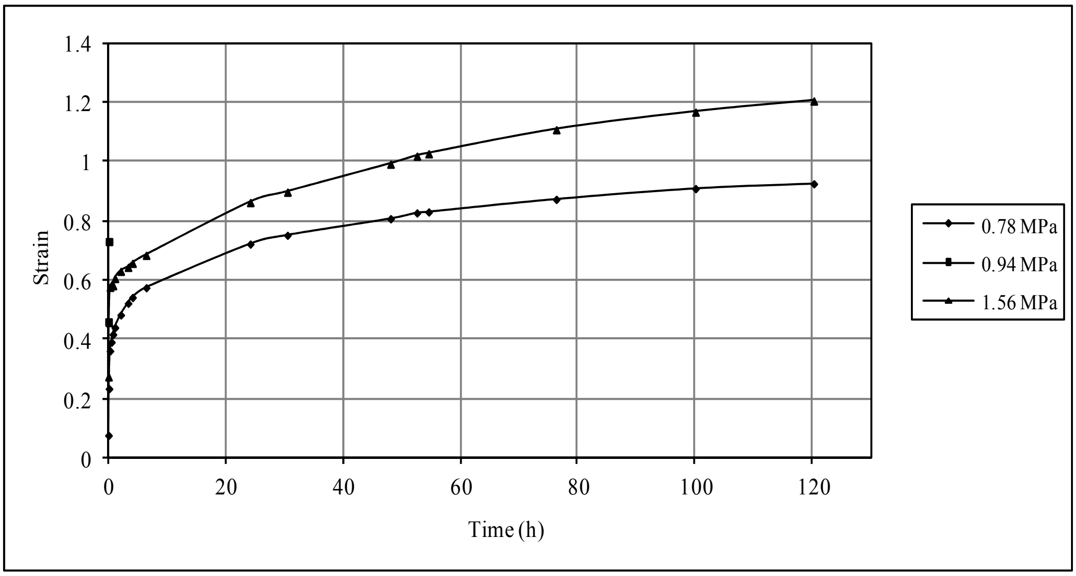

Figure 3 (a): Constant temperature hot-air machine welded specimen creep curves at 30ºc

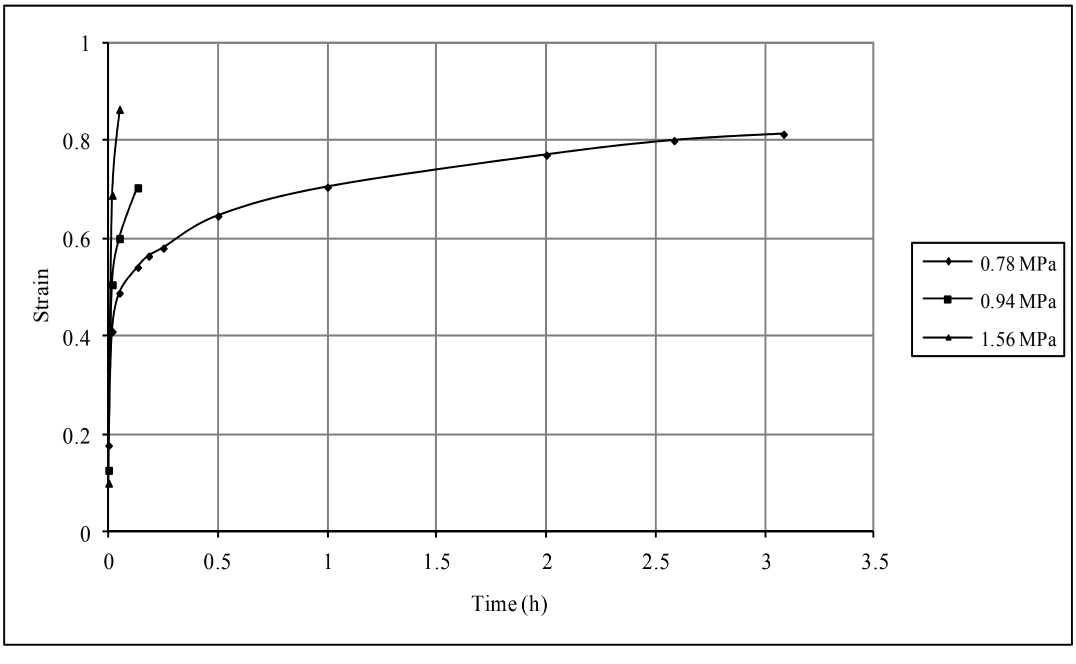

Figure 3 (b): Constant temperature hot-air machine welded specimen creep curves at 40ºC

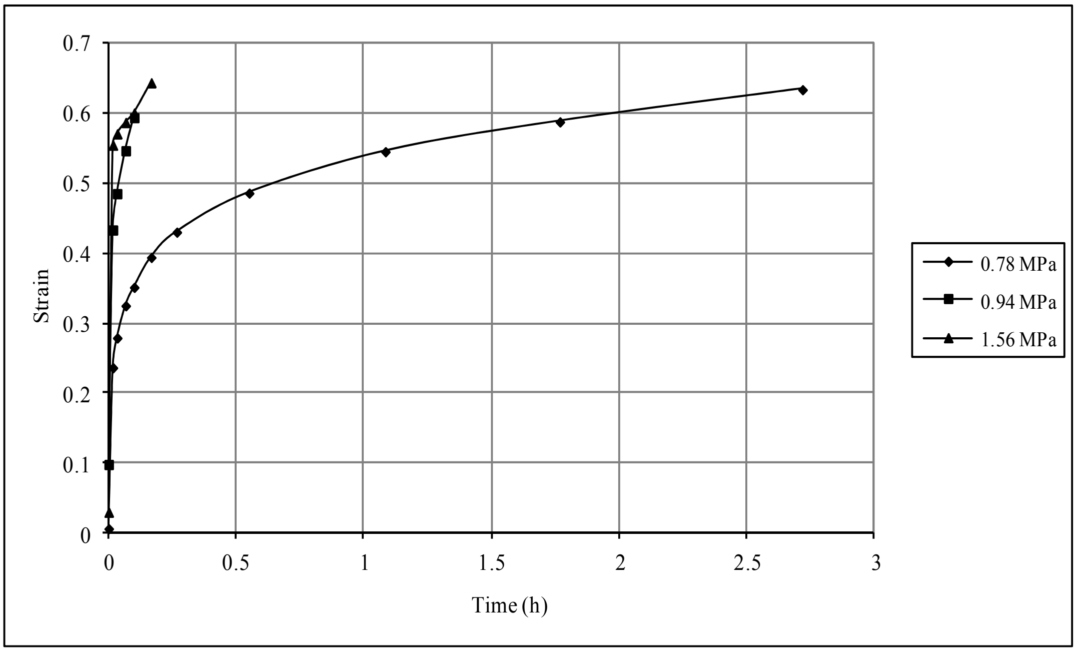

Figure 3 (c): Constant temperature hot-air machine welded specimen creep curves at 50ºC

Table 2: Summary of welded joint maximum strains at fracture, time to failure and point of failure

Temperature (ºC)	Stress applied (MPa)	Maximum strain obtained	Time to failure (h)	Point of failure
30	0.78	0.9	120	Welded joint
	1.56	1.2	120	Welded joint
40	0.78	0.8	3.1	Welded joint
	0.94	0.7	0.2	Welded joint
	1.56	0.9	0.1	Welded joint
50	0.78	0.6	2.7	Welded joint
	0.94	0.6	0.1	Welded joint
	1.56	0.6	0.2	Welded joint

The figures 3 (a – c) represent creep curves for field welded (1.3 cm width of weld) specimens subjected to the creep test at *30℃, 40℃* and fresh specimens at *50℃* respectively, all of which had been welded in the field. Table 2 gives a summary of the results obtained from figures 3 (a – c) as well as visual observations made. It was observed in all cases considered (Table 3) that the welded joint is generally a weak point. In all the experiments done, it was observed that the specimens failed on the welded joint and in much shorter times than in other experiments with clear specimens, with the highest time recorded being 120 hours and many of the specimens failing below 3 hours. The failure in all cases was in shear at the welded joint. This was an indication that in most of the specimens, complete fusion had not been attained during the initial welding.

In all the curves, failure in welded specimens was seen likely to occur as the applied stress was increased. In allthe curves, those specimens that were stressed at 0.78MPa persisted much longer than those loaded at higher stresses. The highest strain level attained for any welded specimen was 1.2. When this strain level (see dotted line in Figure 2 (d)) was superimposed on the master curves it was found that the material would fail at a maximum of 1 year (10,000 hours) when loaded at 0.78 MPa and a minimum of less than one hour when loaded at 1.56 MPa. It is clear that the welded joint is definitely a weak point in the installed dam liner exposed to tensile stresses.

With such high failure rates in welded joints, an alternative joining method was sought. But from literature it was seen that it is even more difficult to join HDPE by adhesives than by welding due to the non-polar nature of polyethylene [9]. Polyethylene is in fact listed in many sources as one of several plastics that cannot easily be joined by adhesives.

Literature points to strengths of up to 80% in the welded joints, it seems that the reason for such low strains in samples obtained from the field is poor workmanship that resulted in weak welded joints [9]. The feasible remedy is therefore factory welding of the dam liner before transportation to the field for installation. Alternatively, field welding may be done under controlled conditions particularly with regard to the welding temperature to ensure that the material is in a semi-molten state during the operation, the time and magnitude of pressure applied. It was also noted that the width of the welded joints obtained from the field was relatively small, about 1.3 cm. This had been listed in literature as another constraining factor on the strength of the welded joint apart from welding temperature, applied pressure and pressure dwell time [9].

Further tests were done in an attempt to find the conditions under which the strongest weld may be attained in HDPE. In the tests, the following parameters, earlier investigated by other researchers and found not to be significant beyond certain reasonable levels were held constant:

- Rate of heat application at 1cm/s for a width of 2.6 cm. and length of 10 cm. for hot knife welding and 10 s. of heating of the surfaces to be welded in the oven for hot air welding.
- Magnitude of pressure applied at 0.3 MPa. Pressure higher than 0.3 MPa was observed to deform the specimen.
- Dwell time of the applied pressure at 60 seconds followed by natural cooling to room temperature.

The results for hot air welding while holding the width of the weld, applied pressure and dwell time of the pressure constant at 2.6cm, 0.3 MPa and 60 s. respectively are presented in Table 3.

Table 3: Effect of temperature on the strength of hot air welded joints

Temperature (ºC)	**Peel test result (Failure strength and description)**	**Conclusion**
135	0.5 MPa - Readily failed at the welded lap joint in shear	Despite being the welding point, a weak weld is formed with incomplete fusion. There is need to increase temperature.
150	1 MPa - Readily failed at the welded lap joint in shear	Weak weld with incomplete fusion
160	1 MPa - Readily failed at the welded lap joint in shear	Weak weld with incomplete fusion, slightly stronger than previous welds
165	2 MPa - Readily failed at the welded lap joint in shear	Weak weld with incomplete fusion, still stronger than previous welds
170	5 MPa - Failed at the welded lap joint in shear	Strong weld but still with almost complete fusion
175	9 MPa - Failed at the welded joint in shear	Strong weld but still with almost complete fusion. There was now need to increase the temperature by units of 1 ºC
176	11 MPa - Failure outside the welded joint, while the welded joint remained intact for five specimens tested	Complete fusion was attained at this temperature
177	The exposed section of the material melted very fast and was easily distorted. No readings were taken from the damaged specimen.	It was difficult to obtain a weld at this temperature
178	The exposed section of the material melted very fast and was easily distorted	Any further increase in temperature would only cause distortion in the material structure due to excess heat and the tests were stopped

Table 4: Effect of temperature on the strength of hot knife welded joints

Temperature (ºC)	**Peel test result (MPa)**	**Important observations**	**Conclusion**
135(mp)- 350	1.5 (Average)	Readily failed at the welded joint in shear. Almost no melting of the material. The knife tended to stick to the material and caused distortion.	While the knife has been heated to the material melting point, a lot of the heat is lost to raise the temperature of the material from room temperature to its melting point. The knife must be significantly hotter than the melting point of the material.
360	2	Failed at the welded lap joint in shear Stickiness of the knife still experienced	Weak weld with incomplete fusion
370	2	Failed at the welded lap joint in shear Stickiness of the knife still experienced	Weak weld with incomplete fusion
380	5	Failed at the welded lap joint in shear Stickiness of the knife still experienced	Weak weld with incomplete fusion
390	8	Failed at the welded lap joint in shear slight stickiness experienced	Strong weld with almost complete fusion. There was now need to increase the temperature by units of 1 ºC
400	11	Failed outside the lap joint. No stickiness of the knife experienced	Failure outside the welded joint indicates a strong weld. This was the best result that was obtained.
401	-	Beyond 400°C the material began to burn and the surface was too damaged to be welded	It was not possible to obtain a results beyond 400C

In hot air welding, particular attention was given to the width of the weld, which was doubled to 2.6 cm. It was also necessary to find the temperature of air that would cause the material to melt. Temperature was progressively increased from 135 °C (the average melting point of HDPE) upwards with very weak welds obtained up to 176 °C. At 176 °C, it was found that there formed enough welded material to form a strong joint within at the constant conditions specified. This was higher than the melting point of the plastic, (135 °C) to supply latent heat required for melting in a relatively short time of 10 s. and due to the inefficiency of convection heat transfer from the hot air to the plastic. Any temperature below 176°C was not capable of melting enough material to obtain the required fusion at the specified constant conditions. The simple peel test suggested by Aithani et al (2006) was used to determine whether the joint formed was strong enough. Failure (peeling) at the welded joint suggested a weak joint and failure away from the welded joint denoted a strong joint where complete fusion had occurred. In all the tested specimens prepared by hot air fusion at 176°C, failure occurred outside the welded joint.

The hot knife welding technique was also tested. The detailed results for the tests on the hot air welding technique are presented in Table 4.7. A flat bar of width 2.6 cm was heated in an oven to a constant temperature and used to weld two flaps of the lap joint together by sliding the flat bat between them at high temperature. The flat bar was incubated in an oven to acquire the required working temperature before being used for welding. It was found that at temperatures below 350°C of the flat bar, it was not possible to obtain a well fused joint at the constant conditions, since the degree of melt and quantity of molten material yielded was not adequate to create a strong joint as determined by the peel test.

Another problem at temperatures below 350°C was the fact that the hot bar tended to stick to the material, making it difficult to obtain a joint with even dimensions. This indicated that the heat energy stored by the hot knife was not adequate to maintain the material in the molten state long enough. The material therefore solidified and adhered to the knife. Temperatures between 350°C and 400°C may be described as transitory since there was still stickiness of the knife and the joints were not completely fused but the joints formed were much stronger than those formed below 350°C. However, when the bar was heated at 400°C, the sticking of the bar was no longer experienced instead the material melted readily and produced adequate melt to sustain a strong joint. Heating the flat bar beyond 400°C, resulted in the material burning and puncturing as the flat bar was slid through the joint. This indicates a need for good temperature control during welding.

The results of tensile tests on specimens made by the hot knife welding method are presented in Table 2 alongside other tensile test results and the creep test in Figure 4.

The strains in Figure 4 and Table 1 for welded joints are relatively lower than other results in the same table as a result of the increased thickness of the welded specimen (almost twice) the as a result of the lap joint. The shape of the creep curve at the beginning of the creep test in Figure 4 is also not as steep as the other curves in Figure 2 (a – c) due to the increased specimen thickness. It was concluded from these results that to obtain a strong joint, the temperature that will cause adequate melting by conduction or convection must be met by the agent causing melting. It was also observed that stronger joints are obtained with larger widths of the welded joint.

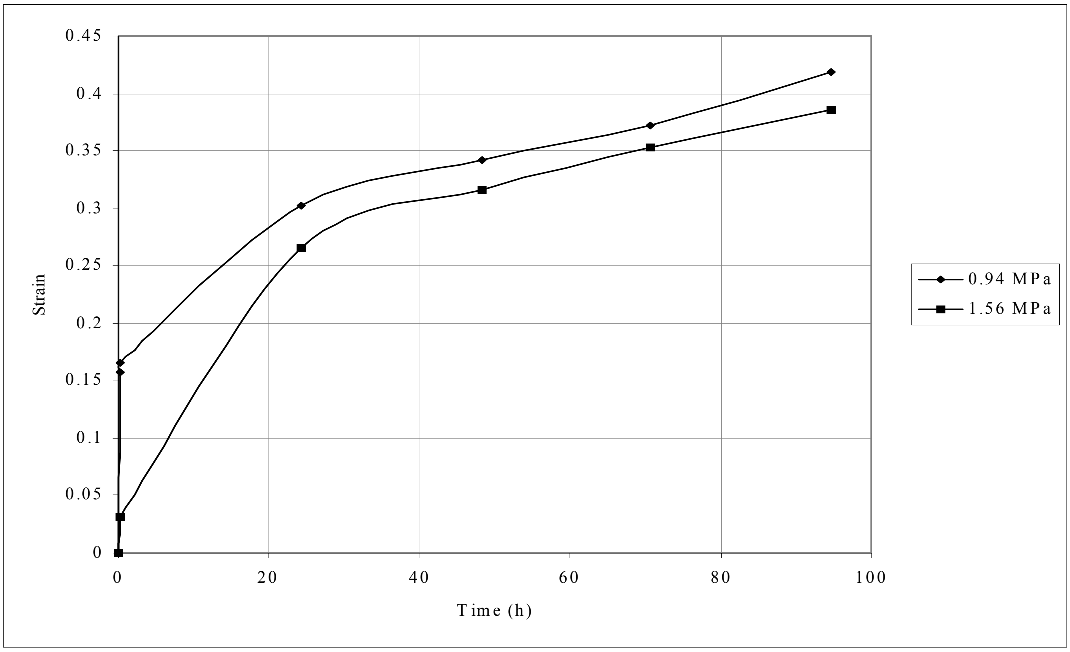

Figure 4: Laboratory welded fresh specimen creep curves at room temperature

CONCLUSIONS

It was concluded that the welded joint of samples collected from the field is the weakest point in the liner. The strength of the welded joint may be improved by correct selection of welding parameters (width of welded joint, joining pressure, dwell time of the pressure and temperature).

It is recommended for more research to be conducted with regard to developing welding devices that can satisfy the optimum conditions demonstrated in the laboratory during field welding, particularly with regard to temperature and pressure control.

REFERENCES

1. UNEP, Water – 2 Billon People are Dying for it, Nairobi (2003).
2. M.K. Tolba, O.A. El -Kholy, E.EL-Hinnawi, M.W. Holdgate, D.F. McMichael and R.E Munn, The World Environment 1972-1992. UNEP & Chapman & Hall, London (1992).
3. D.M Onyango, Women at the Source of Life: The Experience of Kenya Rainwater Association, FAO Dimitra Newsletter, 8, Brussels, Belgium (2003).
4. Sigmaaldrich, Aldrich Polymer Products Application & Reference Information, (2008).
5. Netzsch Applications Laboratory Newsletter, Characterization of Polyethylene with Differential Scanning Calorimetry (2005).
6. R.J. Crawford, Plastics Engineering, Elsevier, Butterworth Heinemann, UK (1998).
7. J.D. Idol and R.L. Lehman, "Polymers," in The CRC Handbook of Mechanical Engineering, Chapter 12, F. Kreith and Y. Goswami, Eds., CRC Press, London (2004).
8. Colorado Lining, Geomembranes / HDPE, Product Manual, (2007).

9. D. Aithani, H. Lockhart, R. Auras and K. Tanprasert, Predicting the Strongest Peelable Seal for 'Easy-Open' Packaging Applications, Journal of Plastic Film & Sheeting, Vol. 22, Pp 247-263, October 2006.

10. Illinois Tool Works, 2007. Plexus Guide to Bonding Plastics, Composites and Metals, www.itwplexus.com (Accessed in May 2008)

11. Salerni, C., 2007. Adhesive Technologies For the Assembly of Hard-to-Bond Plastics, Technical Briefs - Issue No.4, www.akd-tools.gr (Accessed in May 2008)

12. ASTM D638-2003 Standard Test Method for Tensile Properties of Plastics, ASTM International, West Conshohocken, PA, www.astm.org.

13. Kwan, M. K., T. H.C., Lin, and S. L.Y. Woo, 1993, On the Viscoelastic Properties of the Anteromedial Bundle of the Anterior Cruciate Ligament, Journal of Biomechanics, Vol. 26, pp. 447-452.

14. Pioletti, D. P., L. R. Rakotomanana, J. F. Benvenuti, P. F. Leyvraz, 1998. Viscoelastic Constitutive Law in Large Deformations: Application to Human Knee Ligaments and Tendons. J Biomech, 31(8):753-757.

15. Johnson, G. A., G. A. Livesay, S. L-Y. Woo and K. R. Rajagopal, 1996. A Single Integral Finite Strain Viscoelastic Model of Ligaments and Tendons, ASME Journal of Biomechanical Engineering, Vol. 118, pp. 221-226.

INSTRUCTIONS FOR AUTHORS

Please read carefully and adhere strictly to these instructions to ensure that the review and publication of yhour paper is as quick and efficient as possible.

Scope and policy of the African Journal of Science and Technology

The African Journal of Science and Technology is an interdisciplinary journal devoted to all aspects of research in science and technology on the African continent. Papers submitted for review should report original and unpublished work, which is not under consideration for publication elsewhere in any language.

The paper should be written in clear and concise English or French. Copies of the manuscript should be submitted electronically, as a MSWORD document attachment to: opiyo-akech@uonbi.ac.ke

The journal aims to publish as soon as possible after submission. For this purpose papers received by as an attachment on **e-mail** or submitted on diskette with the address, telephone and fax number provided will have the best turn around time. **The receipt of the email will be acknowledged by e-mail.**

Preparation of manuscripts

On preparation as a WORD document the papers must conform to A4 paper in 12-point type size in single spacing. Margins of 25 mm should be left at the sides.
If the figures are sent separately, the position for inserting a figure should be marked clearly and space for it to be inserted left in the text.

The first text page should contain the title of the paper, the name(s) of the author(s), their institutional address(es), and an abstract not exceeding 200 words. This should outline the aims, scope and conclusions of the paper.

Main body of the paper should be subdivided into first, second and third order headings. Any numeral or letters must not precede headings.

Illustrations

All illustrations are termed 'Figures' and referred to as such in the manuscript.
To ensure that the artwork will print to a high standard, we request the following:

** **Size**
Figures if submitted separately should be submitted at the final desired printed size of one or two column width.

- **Line weights**
  Use 0.5 point or 0.7 point for 'ordinary lines', such as the outlines of boxes, axes of graphs; use 1 point lines for more important lines, such as the curve plotted on a graph and use 1.5 very sparingly for emphasis. These line weights are for the final size of the drawing. Never use hairlines. They may break up when printed.
- **Labelling**
  All lettering should be inside the frame
  Use a sans serif medium typeface, such as Helvetica, Univers or Arial, in upper and lower case limited to three sizes 8 or 9 pt and 10pt and 12 pt for labels. Please keep labelling to a minimum to avoid confusion and check it reproduces legibly on a photocopier. These sizes are for the final size of the drawing. (See below Extra).
- **Keys**
  Keys should be drawn within the artwork area as part of the illustration (not as part of the caption). i.e. they should be within the frame.
- **Computer generated artwork**
  If the artwork is computer generated, avoid tints. They will not print evenly. Please use different types of cross-hatching and stippling. We shall try to open the artwork on disk here, but it is not always possible, so please use a laser printer of 600 dpi to print out in black and white on good quality paper for the hard copy. The printout must be as clear and black as possible and in the final desired printed size. **Dot matrix printers are not suitable**.

INSTRUCTIONS FOR AUTHORS

Graphs
All graphs should have scale bars inside the graph.

Photographs
Sharp glossy black and white prints of the final printed size should be provided. Photographs are regarded as figures, do not use the term plate. A definitive scale should be indicated using an item of stated dimensions, or by adding a calibrated bar.

Unless specifically requested, artwork will not be returned to authors after publication.

Acknowledgements:
These should be included at the end of the text and not in footnotes. Personal acknowledgements should precede those of institutions or agencies.

Handling of manuscripts
A manuscript will be acknowledged by e-mail. It will be passed to two reviewers for refereeing. On receipt of the two reports from referees, the author will be contacted and as soon as possible and asked:

- to make minor revisions (and a copyright form for completion enclosed)
- or major revisions (which will have to be returned to the original reviewers for checking before the paper can be accepted)
- or to rethink and rewrite the paper and resubmit it at a later date
- or the paper may be rejected on scientific grounds.

If the author supplies an e-mail number, progress reports can be given as soon as they are received.

INSTRUCTIONS AUX COLLABORATEURS

Veuillez lire attentivement ces instructions et les observer strictement pour s'assurer que l'examen et la publication de vos documents soit aussi rapide et efficace que possible.

Politique et domaine du Journal Africain pour la Science et la Technologie
Le journal Africain pour la Science et la Technologie est un journal interdisciplinaire consacré à tous les aspects des recherches scientifiques et technologiques sur le continent africain. Les documents soumis pour examen doivent porter sur des oeuvres originelles et non publiées, qui ne sont pas considérées pour publication dans une autre langue dans le monde.

Les documents doivent être rédigés en Anglais ou en Français d'une manière concise et claire. Des copies du projet de texte doivent être soumises par le biais du courrier électronique, sous forme d'un document joint en annexe en MS-WORD à l'adresse suivante: «injilah@uycdc.uninet.cm» et « opiyo-akech@uonbi.ac.ke »

Le but du journal est de publier des documents dès que possible après soumission. A cet effet, les documents reçus en annexe par courrier électronique ou sur disquette y compris l'adresse, les numéros de téléphone et de télécopieuse, seront considérés en priorité. Un accusé de reception du projet de texte sera fait par courrier électronique.

Préparation du projet de texte
La préparation du document en WORD doit se conformer au format A4 de caractère 12 avec une seule interligne d'espacement. Les marges doivent être de 12mm de tous côtés. Si des schémas (images) sont transmis séparément, l'endroit d'insertion des schémas doit être bien marqué à cet effet à la marge.

La première page du texte doit contenir le titre du document, le(s) nom(s) des auteurs, leurs adresses de service et un résumé n'excédant pas 200 mots. Ceci doit illustrer les objectifs, le domaine et les conclusions du document.

Le corps principal du texte doit être subdivisé en trois sous-titres par ordre croissant. Aucun numéro ou lettre ne doit précéder les sous-titres.

Illustrations
Toutes les illustrations sont appelées 'schémas' et des références sont faites dans le projet de texte.

En vue de s'assurer que l'impression du document d'exécution sera d'un modèle de haute qualité, nous exigeons ce qui suit:

* **Format**
Si des schémas ou images sont séparément soumises, elles doivent être soumises à l'état final de format d'impression voulue, large d'une ou de deux colonnes.

* **L'épaisseur des lignes**
Utiliser 0,5 point ou 0,7 pour les 'lignes ordinaires'; par exemple pour les lignes d'encadrement, les axes des graphiques; utiliser des lignes de 1 point pour des lignes très importantes, telles que des courbes sur les graphiques et 1,5 point très modérément pour souligner. Le poids de ces lignes sont convenables pour le format final des dessins. Il ne faut jamais utiliser des lignes fines. Elles peuvent se casser pendant l'impression.

* **Marquage**
Toute lettre doit être à l'intérieur du cadre. Veuillez utiliser des caractères moyens comme Helvetica, Univers ou Arial en lettre Capitale et petite limitée aux caractères 8 ou 9 points, 10 et 12 points pour les titres. Veuillez minimiser le marquage pour éviter toute confusion et vérifier qu'il se reproduise lisiblement sur une photocopie. Ces formats sont définitifs pour le dessin; (*voir ci-dessous*).

* **Les indicatifs**
Les indicatifs doivent être ébauchés au sein du texte comme faisant partie de l'illustration (et non pas comme faisant partie des sous-titres), c'est-à-dire qu'ils doivent être placés au sein du cadre.

* **Oeuvre élaborée sur ordinateur**

INSTRUCTIONS AUX COLLABORATEURS

Si l'oeuvre est effectuée sur l'ordinateur, veuillez éviter les teintes. Elles n'apparaîtront pas régulièrement. Veuillez utiliser de différents systèmes de croisées et de pointillages. Nous essayerons d'ouvrir le texte sur disquette ici, mais ce n'est pas toujours possible; alors veuillez utiliser une imprimante à laser de 600dpi pour imprimer en noir et blanc sur des papiers de bonne qualité. Les copies imprimées doivent être aussi claires et noires que possible dans le format définitif. **Les imprimantes à matrice (de points) ne sont pas convenables**.

* **Graphiques**

Tous les graphiques doivent avoir des barres de graduation à l'intérieur du graphique.

* **Photos**

Des imprimés en noir et blanc léger du format définitif doivent être fournis. Les photos sont considérées comme des images; il ne faut pas utiliser le terme plaque. Une échelle définitive doit être indiquée en utilisant un objet de dimensions mentionnées ou en ajoutant une barre graduée.

Les oeuvres ne seront pas retournées aux auteurs à moins qu'une demande spéciale soit faite.

Remerciements

Les remerciements (ou reconnaissances) doivent être placés à la fin du texte et non pas comme une note au bas de page. Les remerciements personnels doivent précéder ceux des institutions ou agences.

Traitement des projets de texte

L'accusé de réception d'un projet de texte sera effectué par courrier électronique. Il sera approuvé par deux responsables chargés de l'approbation. A la réception des deux rapports des responsables, l'auteur sera contacté aussitôt que possible pour:

- faire de petites corrections (et un formulaire de droit d'auteur à remplir et à joindre),
- ou faire une révision générale (qui doit être retournée aux responsables chargées de l'approbation pour vérification avant que le document ne soit accepté),
- ou reprendre tout le document et le présenter à une date ultérieure,
- ou le document peut être rejeté pour des raisons scientifiques. Si l'adresse électronique de l'auteur est disponible, les rapports d'avancement peuvent être transmis dès leur réception.

For subscription and frurther information contact:

Pour tout renseignement complémentaire s'adresser au:

ANSTI/RAIST Secretariat
UNESCO Regional Office in Nairobi
P.O. Box 30952 - 00100 Nairobi, Kenya
Telephone: +254 20 7622619/20
E-mail:info@ansti.org